

Assessment of the Utility of Laplace's Equation for Modeling of Localized Corrosion

A Dissertation

Presented to

the faculty of the School of Engineering and Applied Science

University of Virginia

in partial fulfillment
of the requirements for the degree

Doctor of Philosophy

by

Chao Liu

December 2018

APPROVAL SHEET

This Dissertation
is submitted in partial fulfillment of the requirements
for the degree of
Doctor of Philosophy

Author Signature: Chao Liu

This Dissertation has been read and approved by the examining committee:

Advisor: Dr. Robert G. Kelly

Committee Member: Dr. Elizabeth J. Opila

Committee Member: Dr. Gary M. Koenig

Committee Member: Dr. James T. Burns

Committee Member: Dr. Stephen J. McDonnell

Committee Member: _____

Accepted for the School of Engineering and Applied Science:



Craig H. Benson, School of Engineering and Applied Science

December 2018

Executive Summary

Connection between dissimilar materials are frequently encountered in complex structures involved in aviation and aerospace industry. In a typical aircraft structure, aluminum-alloy-based airframe component and noble fasteners such as stainless steel is one of the most common couples encountered. When the aircraft is exposed in an aggressive moisture environment such as rainfall, fog, splash, or salt-enabled deliquescence, a thin layer of electrolyte or droplet can be established on the dissimilar materials assembly surface. If the assembly has a fastener-hole geometric configuration, it can assist trapping or wicking of surface electrolyte into the tight crevice between the fastener and the airframe component once breakdown happens on the protective coating above the assembly, resulting in a localized galvanic corrosion environment in which Al-alloy based component is the corroding anode, whereas the stainless steel fastener is the cathode. This phenomenon can further lead to pit-to-fatigue crack initiation on the Al-alloy based component which deteriorates its structural integrity and shortens the lifespan. The main goal of this dissertation is to investigate the galvanic-coupling induced localized corrosion distribution along AA7050-T7451 with a fastener-hole configuration between AA7050-T7451 and SS316L in a simulated environment representative of atmospheric corrosion. This goal is fulfilled by the following tasks: (1) develop a robust finite-element-method (FEM) based modeling approach based on Laplace's Equation to accurately predict corrosion distributions and bound the application of this modeling framework within its limitation by providing reasonable assumptions; (2) utilize FEM modeling approach, electrochemical techniques, and pertinent instrumental characterization tools to systematically investigate the effect of electrolyte layer thickness, solution chemistry, materials surface properties, and galvanic coupling geometry on the electrochemical

and corrosion distributions in the galvanic coupling between AA7050 and SS316L, and capture the underlying mechanism for the dependence of corrosion distributions on each external variable.

To validate the robustness of our modeling approach, a Laplace-Equation based modeling coupled with mathematically fitted electrochemical kinetics from experiment as boundary conditions was applied to simulate galvanic corrosion between Zn plate and SS 316 rods under thin layer electrolyte condition. The modeling results were also compared with experimental results from a four-day modified B117 test. It shows that: electrolyte layer thickness (WL)=3,500~4,000 μm would be the appropriate WL range formed on the sample surface during modified B117 salt fog testing; the robustness of Laplace-Equation based modeling is highly dependent on the boundary conditions, experimentally determined electrochemical kinetics as boundary conditions can truly reflect the electrochemical response of anode/cathode to the surrounding solution environment, which in turn yields the simulated results mostly close to experimental measurement.

In the study of the effect of electrolyte layer thickness, the total cathode current capacity of a surface on the electrolyte film thickness and cathode size in a galvanic couple to support the corrosion of AA7050 were accessed. The total cathode current capacity spans the range of WL thickness from full immersion conditions (where the total cathode current scales with cathode size) to the thin film regime in which the WL is the diffusion boundary layer thickness. In order to fully assess the transition from thin film to thick film condition, an understanding of the natural convection layer thickness is required. For the conditions studied here, the natural convection boundary layer was found to be close to 800 μm . The WL thickness, cathode length and electrochemical kinetics interact to create four regimes of total cathode current as a function of WL thickness.

In the study of the solution chemistry effect, the effect of solution pH, conductivity, pertinent cation species (Al^{3+} , Zn^{2+} and Mg^{2+}) on the electrochemical and galvanic corrosion distributions between SS316L and AA7050 was well studied. For the aspect of solution pH and conductivity, a FEM based modeling approach with experimentally determined electrochemical kinetics as boundary conditions was used to simulate potential and current density distributions in the galvanic coupling with a simulated fastener-hole configuration based on different pH and conductivity assumptions in the solution. Acidic crevice solution at the mouth leads to more severe corrosion at the occluded site of the crevice than mild alkaline crevice solution. The linear conductivity assumption is good enough to represent the effect of varying conductivity on electrochemical distributions and reflect corrosion behavior along the anode. As for the aspect of pertinent metallic cation, Zn^{2+} and Mg^{2+} show inhibitive effect due to formation of precipitate on Cu-containing intermetallic compound (IMC) embedded in the AA7050 surface thus impeding oxygen reduction reaction (ORR) activity; whereas Al^{3+} shows promotive effect on hydrogen evolution reaction (HER) cathodic kinetics due to enhanced proton diffusivity, this effect is not only observed on Al alloys, but also on Pt and stainless steel. The cation study for the galvanic couple indicates that Al^{3+} is galvanic corrosion accelerator, and Mg^{2+} is the corrosion inhibitor.

The effect of oxide film properties (thickness, composition, and resistivity) on the cathodic kinetics of stainless steel were investigated. It can be concluded that: (1) when the passive oxide film is thin ($\sim 2\text{nm}$), the effect of electrolyte layer thickness overwhelms that of oxide film thickness in terms of ORR cathodic kinetics as long as electrolyte layer thickness is larger than $36\ \mu\text{m}$; below this critical electrolyte layer thickness, the effect of oxide film becomes comparable to that of electrolyte layer thickness and has lower cathodic limiting current density compared to the scenario in which only electrolyte layer thickness matters; (2) the effect of oxide film properties

at various pre-oxidation potentials on the cathodic kinetics during ORR potential range of SS304L and SS316L was investigated: for both steels, as oxidation potential increases, the amount of Cr^{3+} in oxide film initially increases from corrosion potential to 0~0.4 V_{SCE} , and then decreases over increasing potential and is oxidized to Cr^{6+} once the potential is higher than 0.63 V_{SCE} ; the amount of Fe^{3+} in general increases with ascending potential; at transpassive potential, although film has the largest thickness but its resistivity is lowest. A higher Fe^{3+} content in the oxide film during oxidation stage will result in a larger cathodic current density due to larger Fe^{3+} -to- Fe^{2+} reduction current density during the scan in the negative potential direction, and provide more Fe^{2+} sites for larger ORR cathodic kinetics during the scan in the reverse direction, since active Fe^{2+} site is believed to facilitate ORR.

At last, in the study of geometric parameter effect, the area ratio of cathode to anode, and crevice geometry were investigated. In the study of area ratio, a galvanic crevice former between AA7050 and SS316L was utilized to evaluate the dependence of pH and dissolution current density of AA7050 on the cathode-to-anode ratio. It shows that higher area ratio (>1:1) geometry leads to more severe corrosion focused at the crevice mouth, resulting in larger potential and pH variation from crevice center to mouth as well as higher anodic current density. In the study of the scaling law for a galvanic-coupling induced crevice, the effect of electrolyte layer over the external SS cathode surface, crevice solution chemistry and wall condition of internal SS cathode were considered in the study. It is found that L_{crit}^2/G is more applicable to galvanic-coupling induced crevice than L_{crit}/G , but L_{crit}^2/G varies with WL and internal SS wall condition.

This dissertation developed a fundamental understanding of the effect of several pertinent variables on the galvanic-coupling induced localized corrosion of Al alloy, provided an approachable modeling means to predict corrosion distribution at given conditions in a timely

fashion as well as develop corresponding corrosion mitigation strategies for NAVAIR, and complemented continuum/meso-scale atmospheric corrosion modeling studies in this field. Electrochemistry and characterization studies in this dissertation also provided meaningful supplementary information for better understanding of corrosion protection mechanism of metal-rich primers, as well as utilization of passive/transpassive characteristics of noble stainless steel to control cathode current availability of sustaining localized corrosion of Al alloy.

Acknowledgements

I would like firstly to thank my advisor, Dr. Rob Kelly, for his genuine guidance and countless support through the years of my PhD study. He has not only taught me how to become an independent researcher, but also cared about my life like a friend, sometimes a father. Thank you for the wonderful mentorship, encouragement and caring these years; you are the role model in my life and future career.

I would also like to sincerely thank and acknowledge the members in my dissertation committee: Dr. Beth Opila, Dr. Jimmy Burns, Dr. Stephen McDonnell, and Dr. Gary Koenig for their time and valuable assistance with my dissertation research. A special thanks is given to my research collaborators from the NAVAIR project: Dr. John Scully, Dr Jimmy Burns, Dr. Veronica Rafla, Dr. Noelle Co, and program manager Mr. Bill Nickerson.

I would like to thank the other collaborators involved in my research studies: Dr. Eric Schindelholz at Sandia National Lab, Dr. Christopher Alexander at the University of South Florida, Dr. Jayendran Srinivasan, Dr. Marybeth Parker, Dr. Piyush Khullar, Miss Lindsey Blohm, Miss Cathy Dukes, Mr. Ryan Katona, Mr. R.J. Santucci, Dr. Carol Glover, Dr. Mary Lyn Lim, Dr. Yijing Shi and my undergraduate researchers Victor Yang and Ali Alshanoon. Their collaboration and advice are greatly appreciated. Also, I would like to acknowledge and thank all the past and present members of the Center for Electrochemical Science and Engineering from whom I have learned so much. Another special thanks go to my favorite staff at MSE Department: Ms. Kim Fitzhugh, Ms. Sherri Sullivan, Mr. Eric Newsome, Mr. Richard White and Mr. Tanner Fitzgerald.

Finally, I would like to thank my mom and dad for their endless support and encouragement during my overseas study in the past few years. I am hoping my achievements will make them feel

proud. At the very last I would also like to thank my lovely girlfriend, Hongxu Dong for being always ready to give me a warm hug whenever I am happy or down.

All hail the power of Jesus' name!

Bibliography

The publications that resulted/will result from this dissertation are listed below

1. **C. Liu** and R.G. Kelly, “The Use of Finite Element Methods (FEM) in the Modeling of Localized Corrosion”, *The Electrochemical Society Interface*, 23 (2014): p 47-51.
2. **C. Liu**, V.N. Rafla, J.R. Scully, R.G. Kelly, “Mathematical Modeling of Potential and Current Distributions for Atmospheric Corrosion of Galvanic Coupling in Airframe Components”, *CORROSION 2015* (Houston, TX: NACE, 2015).
3. **C. Liu**, R.G. Kelly, “Mathematical Modeling of Effect of pH and Conductivity on Electrochemical Distributions in Galvanic Coupling in Airframe Components”, DoD Corrosion Conference 2015, Pittsburgh, PA, November 15-19, 2015.
4. J. Srinivasan, **C. Liu**, R.G. Kelly, “Geometric Evolution of Flux from a Corroding One-Dimensional Pit and Its Implications on the Evaluation of Kinetic Parameters for Pit Stability”. *Journal of the Electrochemical Society*, 163 (2016): p.C694-C703.
5. **C. Liu**, J. Srinivasan, and R.G. Kelly, “Editors' Choice—Electrolyte Film Thickness Effects on the Cathodic Current Availability in a Galvanic Couple”, *Journal of the Electrochemical Society*, 164 (2017): p.C845-C855.
6. C.L. Alexander, **C. Liu**, A. Alshanoon, R.M. Katona, R.G. Kelly, J. Carpenter, C. Bryan, and E. Schindelholz, “Oxygen Reduction on Stainless Steel in Concentrated Chloride Media”, *Journal of the Electrochemical Society*, 165 (2018): p.C869-C877.
7. **C. Liu**, G. Kubacki, and R.G. Kelly, “Application of Laplace-Equation Based Modeling into Corrosion Damage Prediction for Galvanic Couple between Zn Plate and Stainless Steel Rods under a Thin Film Electrolyte”, Accepted by *Corrosion*.
8. **C. Liu**, and R.G. Kelly, “A Review of the Application of Finite Element Method (FEM) to Localized Corrosion Modeling”, *Corrosion Review*.
9. **C. Liu**, V. Yang, and R.G. Kelly, “The Cathodic Inhibition Effect of $[Zn^{2+}]$ and $[Mg^{2+}]$ on Cathodic Kinetics of AA7050-T7451”, *Journal of the Electrochemical Society*.
10. **C. Liu**, P. Khullar, and R.G. Kelly, “The Cathodic Promotive Effect of $[Al^{3+}]$ on Cathodic Kinetics of Aluminum Alloys”, *Journal of the Electrochemical Society*.
11. **C. Liu**, and R.G. Kelly, “The Effect of Oxide Film Properties on Oxygen Reduction Reaction of Stainless Steels in Sulfate Solution”, *Corrosion*.
12. L.M. Blohm, **C. Liu**, R.G. Kelly, “A Combined Experiment and Modeling Analysis of ASTM G85 WB Accelerated Corrosion Testing of Galvanically Coupled Sensitized AA5456-H116 and CDA 706 Cupronickel”, *Corrosion*.

Table of Contents

Executive Summary	i
Acknowledgements.....	vi
Bibliography	viii
List of Figures.....	xvi
List of Tables	xxix
List of Symbols	xxxii
1. Introduction.....	1
1.1 An Overview of Dissertation Problem	1
1.2 Background.....	2
1.2.1 Atmospheric Corrosion vs. Submerged Corrosion	2
1.2.2 Al-Zn 7xxx Alloys	4
1.2.3 Localized Corrosion Damage Induced by Galvanic Coupling	5
1.2.4 Variables Affecting Localized Corrosion in Atmospheric Conditions	7
1.2.5 Application of Finite Element Method in Localized Corrosion Modeling Study ...	11
1.3 Overarching Research Questions.....	18
1.4 Objectives	19
1.5 Organization of Dissertation.....	19
1.6 References	22

2. Verification of the Robustness of Laplace-Equation Based Modeling into Corrosion Prediction	27
2.1 Abstract	28
2.2 Hypothesis	28
2.3 Introduction	29
2.4 Experimental Procedure	31
2.4.1 Mathematical Development	31
2.4.2 Model Implementation	32
2.4.3 Electrochemical Kinetics.....	34
2.4.4 Modified ASTM B-117 Salt Fog Testing	35
2.5 Results and Discussions	36
2.5.1 Electrochemical Kinetics of SS and Zn	36
2.5.2 Modeling Studies to Investigate the Effect of Pertinent Parameters	37
2.5.3 Comparison of Results between Salt Fog Testing and Modeling Prediction.....	44
2.5.4 Evaluation of the Effect of Boundary Conditions on the Modeling Predictions.....	48
2.6 Conclusions	51
2.7 Acknowledgement	53
2.8 References	53
3. Electrolyte Film Thickness Effect on the Cathodic Current Availability in Galvanic Couple.....	56

3.1	Abstract	57
3.2	Hypothesis:	57
3.3	Introduction	58
3.4	Methodology.....	61
3.4.1	Sample Preparation	61
3.4.2	Electrochemical Kinetics.....	62
3.4.3	Finite Element Method (FEM) Modeling	63
3.5	Results	65
3.5.1	Determination of Critical Electrolyte Layer Thickness for Natural Convection.....	66
3.5.2	Electrochemical Kinetics of SS 316L and AA7050-T7451	68
3.5.3	Effect of Area Ratio of Anode to Cathode on Total Cathodic Current	70
3.5.4	I_c/W on SS 316L Coupled with AA7050 versus WL as a Function of L_c	71
3.6	Discussions	74
3.6.1	Determination of the Thickness of the Natural Convection Layer	75
3.6.2	Different Regimes of Dependence of Cathodic Current on Film Thickness are Clearly Distinguishable	76
3.6.3	The Linear Dependence of Total Current on the Logarithm of the WL Thickness for Small WL and Its Independence of Cathode Length	83
3.6.4	Implications and Limitations	85
3.7	Conclusions	88

3.8	Acknowledgement	88
3.9	References	89
4.	Effect of Solution Chemistry (pH, Conductivity and Dissolved Metal Species) on the Distribution of Localized Corrosion in AA7050/SS316L Couple	92
4.1	Abstract	93
4.2	Hypothesis	94
4.3	Part 1: Mathematical Modeling of Effects of pH and Conductivity on Electrochemical Distributions in Galvanic Coupling in Airframe Components	94
4.3.1	Introduction	94
4.3.2	Methodology.....	96
4.3.3	Results and Discussion.....	102
4.3.4	Conclusion.....	110
4.3.5	Acknowledgements.....	110
4.3.6	References	111
4.4	Part 2: The Cathodic Inhibition Effect of $[Zn^{2+}]$ and $[Mg^{2+}]$ on Cathodic Kinetics of AA7050- T7451	112
4.4.1	Introduction	112
4.4.2	Methodology.....	114
4.4.3	Results	116
4.4.4	Discussions	132

4.4.5	Conclusions:	134
4.4.6	References	134
4.5	Part 3: Promotive Effect of Al ³⁺ on the Cathodic Kinetics of Aluminum Alloys	137
4.5.1	Introduction	137
4.5.2	Experimental Methods	139
4.5.3	Results	141
4.5.4	Discussions	151
4.5.5	Conclusions	158
4.5.6	References	159
4.6	Part 4: Effect of Solution Chemistry on Galvanic Coupling between AA7050-T7451 and SS316L: Experimental Approach and Modeling Validation.....	161
4.6.1	Introduction	161
4.6.2	Experimental Approach	163
4.6.3	Results and Discussions	165
4.6.4	Conclusions	176
4.6.5	References	177
4.7	Acknowledgements.....	178
5.	The Effect of Materials Properties (Oxide Film Composition and Thickness) on the Corrosion Kinetics of the Materials Involved in the Galvanic Couple	179
5.1	Abstract	180

5.2	Introduction	180
5.3	Hypothesis	183
5.4	Methodology.....	183
5.4.1	Effect of Surface Treatment	183
5.4.2	Comparative Study of Effect of Pre-Oxidation Potential Between SS316L and SS314L	184
5.5	Results and Discussions.....	186
5.5.1	RDE Studies to Investigate the Effect of Surface Treatment on ORR Cathodic Kinetic	186
5.5.2	Comparative Study of Effect of Pre-Oxidized Potential on Cathodic ORR Kinetics Between SS316L and SS314L	189
5.6	Conclusions:	211
5.7	Acknowledgements	212
5.8	References.....	212
6.	The Effect of Geometric Parameters on the Extent of Localized Corrosion of AA7050-T7451 Galvanically Coupled to SS316L Fastener.....	215
6.1	Abstract	215
6.2	Hypothesis	216
6.3	Part 1: Effect of Cathode-to-Anode Area Ratio on Potential, Current and pH Distribution in the Crevice Formed in Galvanic Coupling Between AA7050-T7451 and SS316L	217
6.3.1	Introduction:	217

6.3.2	Experimental Approaches	218
6.3.3	Results and Discussions	221
6.3.4	Conclusions	226
6.4	Part 2: A Modeling Study of Exploring the Scaling Law in the Galvanic-Coupling Induced Corrosion of AA7050-T7451	226
6.4.1	Introduction	226
6.4.2	Experimental Approaches	229
6.4.3	Results and Discussions	232
6.4.4	Conclusions	241
6.5	Acknowledgements.....	241
6.6	References	241
7	Summary and Recommended Future work	243
7.1	Summary	243
7.2	Recommended Future Work.....	247

List of Figures

Figure 1.1: A schematic representation of galvanic couple between AA7050-T7451 airframe component and SS316L fastener with fastener-hole configuration.	2
Figure 1.2: A schematic comparison between atmospheric corrosion and submerged corrosion with fastner-hole configuration: a) atmospheric corrosion and b) submerged corrosion.	3
Figure 1.3: a) Schematic representation of development of critical crevice solution in a corroding crevice geometry; b) IR drop theory based on a crevice geometry, after Shu et al. ¹⁶	6
Figure 1.4: Corrosion Rate as a function of thickness of moisture layer. I) Region of dry atmospheric corrosion; II) region of humid atmospheric corrosion; III) region of wet atmospheric corrosion; IV) region of complete immersion. After Tomashov. ²⁰	9
Figure 1.5: An example to show discrepancies in potential distributions by selecting different reference ions.....	14
Figure 1.6: Schematic representation of FEM based model geometry a) materials and electrolyte conditions studied and b) assumptions of boundary conditions, after King et al. ⁷⁵	18
Figure 2.1: Configurations of two types of Zn/SS galvanic couple: a) SS rod in center of Zn plate in Configuration 1; b) Two SS rods (one stayed in center) with spacing equal to 1.5, 2.5 and 4cm respectively in Configuration 2.....	34
Figure 2.2: Original and fitted polarization curves of SS and Zn for 0.6 M NaCl.	37
Figure 2.3: Comparison of current density distribution between Configuration 1 and Configuration 2 with three different spacing.	38
Figure 2.4: Current density distributions as a function of solution conductivities for WL=4,000 μm	39

Figure 2.5: a) current density distributions as a function of solution conductivities for $WL=50\mu\text{m}$; b) zoom-in of Figure 2.5a at the interface area.....40

Figure 2.6: Comparison of current density distributions for: a) 5.5 S/m and b) 0.5 S/m as a function of WLs; for c) $WL=4,000$ and d) $WL= 50 \mu\text{m}$ as a function of conductivities.....41

Figure 2.7: A comparison of average inter-cathode dissolution current densities as a function of WLs for three different spacings.....43

Figure 2.8: Comparison of Zn dissolution current map on the plate in terms of cathode current availability on SS from a): 100%, to b): 50% and c): 10%. In this comparison, $WL=200 \mu\text{m}$, spacing= 1.5 cm and solution conductivity= 5.5 S/m.44

Figure 2.9: Original and fitted polarization curves of SS and Zn in 0.6M NaCl+0.04M $\text{K}_2\text{S}_2\text{O}_8$ solution.45

Figure 2.10: a) Top view and b) 3D view of corrosion morphology in the vicinity of Zn/SS interface measured by Zygo optical profilometer for samples with Configuration 1 after modified B-117 Test.46

Figure 2.11: a) comparison of corrosion depth distance away the Zn/SS interface from three different samples; b) comparison between experimental and modeling result; c) zoomed in near interface shown in Figure 2.11b; d) residual analysis between experimental results and simulated results when $WL=3,000 \mu\text{m}$, $3,500 \mu\text{m}$ and $4,000 \mu\text{m}$ respectively.47

Figure 2.12: a) Comparison of SS316L kinetics in different forms; b) comparison of simulated corrosion depth distributions away from Zn/SS interface in Configuration 1 based on different forms of SS316L cathodic kinetics at the same $WL=3500 \mu\text{m}$; c) comparison of simulated corrosion depth distributions away from Zn/SS interface in Configuration 1: $WL=3500 \mu\text{m}$ for experimental determined kinetics, $WL=1\text{m}$ for B-V kinetics, and $WL=1 \mu\text{m}$ for linear kinetics.51

Figure 3.1: Schematic configuration of the interaction between thin film electrolyte and galvanic couple (316L cathode with AA7050 anode in this study). Width of anode/cathode is normal to x-y plane.	64
Figure 3.2: Polarization curves of Pt RDE as a function of rotation speed (rpm).	67
Figure 3.3: (a) Limiting current density (i_{lim}) at $-0.75 V_{SCE}$ vs $1/\delta$; (b) Zoom-in of thick WL regime to exhibit critical natural convection electrolyte layer thickness (δ_{nc}). Blue dash line represents the value for cathodic limiting current density of Pt in full immersion condition.	68
Figure 3.4: Polarization curves of 316L as a function of rotation speed.	69
Figure 3.5: Comparison of i_{lim} vs. $1/WL$ between Pt and 316L.	69
Figure 3.6: Tafel-fitting for anodic kinetics of both AA7050-T7451.	70
Figure 3.7: I_C/W vs. area ratio of anode to cathode for AA/SS galvanic couple, assuming fixed length of anode when $WL=1$ mm.	71
Figure 3.8: Boundary conditions for modeling between AA/SS galvanic couple under different δ	72
Figure 3.9: (a) I_C/W vs. WL as a function of cathode length (L_C) in linear scale; (b) I_C/W vs. WL as a function of L_C in semi-logarithm scale; (c) I_C/W vs. L_C as a function of WL	73
Figure 3.10: I_C/W over a range of $WL \leq 1$ mm for $L_C =$: (a) 1 cm; (b) 5 cm; (c) 9.25 cm; (d): 10 cm.	74
Figure 3.11: (a) Four different regimes in I_C/W vs. WL ; (b) Corresponding percentage of length of cathode within mass-transfer limited (ORR) kinetics in each of four regimes. Note that percentage of length of cathode within M-T limited kinetics means that electrochemical kinetics thrown upon this part of cathode is mass-transfer controlled, the rest of the cathode is under either activation or mixed control.	77

Figure 3.12: Comparison of I_C/W vs. WL among three different scenarios: I_C/W affected by (1) both ohmic drop and M-T limited kinetics; (2) by ohmic drop only; (3) by M-T limited kinetics.80

Figure 3.13: (a) Four different regimes in I_C/W vs. WL; (b) Corresponding percentage of length of cathode within mass-transfer limited (ORR) kinetics in each of four regimes.82

Figure 3.14: (a) Three different regimes in I_C/W vs. WL; (b) Corresponding percentage of length of cathode within mass-transfer limited (ORR) kinetics in each of two regimes.83

Figure 3.15: Comparisons of cathodic current density (absolute value) distributions along the length of cathode for the length of cathode=5, 10, 20, 40 cm for a WL = 89 μ m.84

Figure 4.1: a) Simplified geometry of fastener hole configuration involving SS fastener (UNS S30400), Al alloy (UNS A97050), coating and electrolyte. All pertinent geometric parameters and indicating points are included; b) Screenshot of mesh of electrolyte domain in the modeling software.99

Figure 4.2: a) Geometry and boundary conditions in the modeling; b) First type of electrochemical kinetics (boundary conditions) of Al Alloy and SS; c) Second type of electrochemical kinetics (boundary conditions) of Al Alloy and SS. Solid lines of Al alloy represent reverse scans after reaching highest current density limit during the cyclic potentiodynamic polarizations. 101

Figure 4.3: Comparisons of a) potential distributions and b) current density distributions along the anodic boundaries between alkaline crevice mouth (case 1) and acidic crevice mouth (case 2) solution assumptions. 103

Figure 4.4: a) Potential distribution considering repassivation potentials in aerated and deaerated solutions in case 1; b) Potential distribution considering repassivation potentials in aerated and deaerated solution in case 2; c) Generic illustration to show passive-active transition behavior

along Al alloy surface in case 1; d) Generic illustration to show passive-active transition behavior along Al alloy surface in case 2. 105

Figure 4.5: a) a schematic diagram of galvanic coupling between a SS rivet and an AA7050-T7451 under a droplet; b) a typical XCT result to show the distribution of corrosion fissures in AA7050 (Red) along the SS rivet (Blue); c) corrosion fissure area bars for the 4 fissures observed in AA7050 in the 4M NaCl exposure after 62 hours as a function of rivet depth. 106

Figure 4.6: Comparison of conductivity distributions under three different assumptions along the cathodic boundaries. 107

Figure 4.7: a) Comparison of potential distributions along cathodic boundaries; b) Comparison of potential distribution along anodic boundaries; c) Comparison of current density distributions along cathodic boundaries; d) Comparison of current density distributions along anodic boundaries. 108

Figure 4.8: Comparison of a) potential and b) current density distributions along the anodic boundaries 6-7-8 under different conductivity assumptions. 109

Figure 4.9: a) Cathodic polarization curves of AA7050-T7451 in 0.6M NaCl with addition of different concentration of MgSO₄; b) Cathodic polarization curves of AA7050-T7451 in 0.6M NaCl with addition of different concentration of ZnSO₄; c) Comparison of i_{lim} as a function of metal ion concentration between Zn²⁺ and Mg²⁺. 118

Figure 4.10: a) SEM image of Al₇Cu₂Fe covered by corrosion product in 0.6M NaCl+ 0.1M MgSO₄ solution; EDS spectrum and composition (atomic percent) of b) location A and c) location B. 119

Figure 4.11: a) SEM image of Al₇Cu₂Fe covered by corrosion product in 0.6M NaCl+0.1M ZnSO₄ solution; EDS spectrum and composition (atomic percent) of b) location A and c) location B. 120

Figure 4.12: a) Overlaid x-ray reference intensity vs. 2θ plots of precipitate-coated AA7050 from MgSO_4 containing solution, as-polished AA7050 and pure Mg(OH)_2 ⁵⁰; b) overlaid x-ray reference intensity vs. 2θ plots of precipitate-coated AA7050 from ZnSO_4 containing solution, as-polished AA7050 and $\text{NaZn}_4(\text{SO}_4)(\text{OH})_6\text{Cl}\cdot 6\text{H}_2\text{O}$ ⁵⁰. 122

Figure 4.13: a) Overlaid Raman reference intensity vs. Raman shift plots of precipitate-coated AA7050 from MgSO_4 containing solution, and pure Mg(OH)_2 ⁵⁰; b) overlaid Raman reference intensity vs. Raman shift plots of precipitate coated AA7050 from ZnSO_4 containing solution and $\text{NaZn}_4(\text{SO}_4)(\text{OH})_6\text{Cl}\cdot 6\text{H}_2\text{O}$ ⁵⁰. 123

Figure 4.14: Equivalent circuit model to fit EIS spectra of AA7050 in pure 0.6M NaCl, and 0.6M NaCl+ Mg^{2+} 125

Figure 4.15: a) Nyquist plot as a function of immersion time; b) Bode impedance vs. frequency as a function of immersion time; c) phase angle vs. frequency as a function of immersion time for AA7050 immersed in 0.6M NaCl. 126

Figure 4.16: a) Nyquist plot as a function of immersion time; b) Bode impedance vs. frequency as a function of immersion time; c) phase angle vs. frequency as a function of immersion time for AA7050 immersed in 0.6M NaCl+0.1M MgSO_4 127

Figure 4.17: Equivalent circuit model for AA7050 in 0.6M NaCl+0.1M ZnSO_4 128

Figure 4.18: a) Nyquist plot as a function of immersion time; b) Bode impedance vs. frequency as a function of immersion time; c) phase angle vs. frequency as a function of immersion time for AA7050 immersed in 0.6M NaCl+0.1M ZnSO_4 128

Figure 4.19: a) Comparison of a) R_{film} , b) CPE_{film} and c) $C_{\text{eff, film}}$ as a function of immersion time in three different solutions. 130

Figure 4.20: a) SEM images of AA7050 surface prior to HNO₃ treatment after 120hr-immersion in a) 0.6M NaCl solution; b) SEM image of AA7050 surface in 0.6M NaCl +0.1M MgSO₄ solution; c) SEM image of AA7050 surface in 0.6M NaCl+0.1M ZnSO₄ solution; d) a zoom-in of a); e) a zoom-in of b); f) a zoom-in of c). 131

Figure 4.21: SEM image of AA7050 surface with HNO₃ cleaning the surface after 120hr-immersion in a) 0.6M NaCl solution; b) 0.6M NaCl +0.1M MgSO₄ solution; c) 0.6M NaCl+0.1M ZnSO₄ solution..... 132

Figure 4.22: a) Comparison of film RC products between Zn²⁺ and Mg²⁺ containing solutions as a function of immersion time; b) Comparison of total resistance between Zn²⁺ and Mg²⁺ containing solutions as a function of immersion time. 133

Figure 4.23: a) Comparison of cathodic polarization curves of AA7050 as a function of [Al³⁺]; b) *i*_{lim} vs. [Al³⁺] at a reference potential -1.05 V_{SCE}. 142

Figure 4.24: Comparisons of cathodic kinetics of AA7050, AA5083 and AA2024 in 0.6M NaCl and 0.3M NaCl+0.1M AlCl₃ 143

Figure 4.25: A comparison of cathodic kinetics of AA7050 in 0.6M NaCl (pH=5.6), 0.6M NaCl (pH=3.01), and 0.3M NaCl + 0.1M AlCl₃ (pH=3.01). 144

Figure 4.26: a) A comparison of full polarization curves of AA7050 as a function of [Al³⁺]; b) schematic polarization curve to show the controlling factors for E_{Corr} based on the Mixed Potential Theory. 145

Figure 4.27: a) Nyquist Plots of AA7050 as a function of [Al³⁺]; b) Bode impedance vs. Frequency as a function of [Al³⁺]; c) phase angle vs. Frequency as a function of [Al³⁺]. 148

Figure 4.28: a) equivalent circuit model to fit data in 0.6M NaCl solution; b) in NaCl+AlCl₃ solution. 148

Figure 4.29: a) $R_{\text{film}}C_{\text{eff, film}}$ product vs. $[\text{Al}^{3+}]$ and b) R_{total} vs. $[\text{Al}^{3+}]$ for AA7050 from EIS analysis.
..... 149

Figure 4.30: Comparison of cathodic polarization curves of a) SS316L, and b) Pt in 0.6M NaCl (natural pH), 0.6M NaCl (pH=3.01), and 0.3M NaCl+0.1M AlCl_3 (pH=3.01, additional test in deaerated solution for Pt)..... 151

Figure 4.31: a) SEM image , b) layered EDS map, c) O elemental EDS map and d) Al elemental map of film covered on the Pt surface after cathodic polarization in 0.3M NaCl+0.1M AlCl_3 solution. 152

Figure 4.32: Repeated cathodic polarization scans of Pt in 0.3M NaCl+0.1M AlCl_3 154

Figure 4.33: RDE tests of Pt in both 0.6M NaCl pH3.01 and 0.3M AlCl_3 +0.1M AlCl_3 (pH=3.01) with rotation speed= 100, 200, 500 and 1000 rpm respectively. 155

Figure 4.34: Levich Plots for Pt in 0.6M NaCl pH3.01 and 0.3M AlCl_3 +0.1M AlCl_3 (pH=3.01).
..... 156

Figure 4.35: Proton Transport in: a) purely acidified NaCl solution and b) Al^{3+} containing solution based on Grotthuss Theory^{42,43}. 158

Figure 4.36: A schematic diagram to show the solution chemistry environment between a generic SS316L fastener and MgRP coated AA7050-T7451. 163

Figure 4.37: Dimension of galvanic coupling between SS316L and AA7050-T7451 for SVET measurements..... 164

Figure 4.38: a) Geometry setup for the 1st set of modeling, typical of SVET sample's geometry; b) geometry setup for the 2nd set of modeling, the dimension was identical to a), but half of the surface was covered by MgRP..... 165

Figure 4.39: Distributions of pertinent stable species as a function of pH during metal cation hydrolysis were generated for a) Mg^{2+} and b) for Al^{3+} by OLI software..... 166

Figure 4.40: Comparisons of polarization curves of SS316L and AA7050 as a function of $[Mg^{2+}]$ at a) pH=5.5, b) pH=4 and c) pH=3; d) comparison of galvanic coupling current density vs. $[Mg^{2+}]$ for different pHs..... 168

Figure 4.41: a) Comparisons of polarization curves of SS316L and AA7050 as a function of $[Al^{3+}]$ at pH=3; b) comparison of galvanic coupling current density vs. $[Mg^{2+}]$ at pH=3..... 169

Figure 4.42: SVET measurement in 0.6M NaCl pH=5.6 solution at a) 0 hrs, b) 3.2 hrs, c) 3.3 hrs, d) 3.5 hrs, and e) 24hrs. f) optical micrograph of galvanic coupling after 24hr-SVET measurement. 170

Figure 4.43: SVET measurement in 0.6M NaCl+0.05M $Al_2(SO_4)_3$ pH=3 solution at a) 0 hr, b) 2 hrs, c) 3.2 hrs, d) 7 hrs, and e) 24 hrs. f) optical micrograph of galvanic coupling after 24hr-SVET measurement. 170

Figure 4.44: SVET measurement in 0.6M NaCl+0.1M $MgSO_4$ pH=4 solution at a) 0 hr, b) 6 hrs, c) 12 hrs, d) 18 hrs, and e) 24 hrs. f) optical micrograph of galvanic coupling after 24hr-SVET measurement. 171

Figure 4.45: SEM characterizations of corrosion damage on the surface in the vicinity of SS316L/AA7050 interface after 24-hr SVET tests for a) 0.6M NaCl pH=5.6, b) 0.6M NaCl+0.05M $Al_2(SO_4)_3$ pH=3, and c) 0.6M NaCl+0.1M $MgSO_4$ pH=4. 172

Figure 4.46: a) Boundary conditions used for bare galvanic coupling configuration shown in Figure 4.38a in three different SVET test solutions; b) comparison of current density distributions along the distance from the SS rod center to the AA7050 edge in three different solutions. 174

Figure 4.47: a) Comparison of average anodic current density from SVET as a function of immersion time for three different solutions; b) comparison of maximum anodic current density between modeling prediction and SVET results for three different solutions.174

Figure 4.48: Boundary conditions for half-coated galvanic coupling in a) 0.6M NaCl pH=5.6, b) 0.6M NaCl+0.05M Al₂(SO₄)₃ pH=3, and c) 0.6M NaCl+0.1M MgSO₄ pH=4; d) direction for potential distribution along the galvanic coupling surface.....175

Figure 4.49: a) Potential distributions along the distance from the left edge of MgRP to the right edge of AA7050 (Figure 4.48d) for three different solutions; display of the simulated potential on AA7050 (dashed line) over the electrochemical kinetics diagram in b) 0.6M NaCl pH=5.6, c) 0.6M NaCl+0.05M Al₂(SO₄)₃ pH=3, and d) 0.6M NaCl+0.1M MgSO₄ pH=4.....176

Figure 5.1: Cathodic polarization curves of a) Pt, b) cathodically pre-reduced SS316L, c) 1.5-hr OCP treated SS316L and d) chemical treated SS316L in 0.6M NaCl as a function of rotation speed.187

Figure 5.2: Levich plots for Pt and SS316L with three different surface treatments in which i_{lim} is a function of reciprocal of simulated electrolyte layer thickness.188

Figure 5.3: Theoretical calculation of $D_{O_2} C_{bulk,O_2}$ product as a function of [Na₂SO₄] and that in 0.6M NaCl; b) cathodic kinetics of SS304L and SS316L in 0.3M Na₂SO₄ and 0.6M NaCl, as well as Pt in 0.3M Na₂SO₄.190

Figure 5.4: Comparison of full electrochemical kinetics of SS304L and SS316L in 0.3M Na₂SO₄.190

Figure 5.5: XPS spectra and deconvolution of Fe 2p_{3/2} at pre-oxidation potential a) E_{corr}; b) 0 V_{SCE}; c) 0.4 V_{SCE}; d) 0.9 V_{SCE} and e) 1.4 V_{SCE} for SS304L and f) E_{corr}; g) 0 V_{SCE}; h) 0.4 V_{SCE}; i) 0.9 V_{SCE} and j) 1.4 V_{SCE} for SS316L.....193

Figure 5.6: XPS spectra and deconvolution of Cr 2p _{3/2} at pre-oxidation potential a) E_{corr} ;b) 0 V_{SCE}; c) 0.4 V_{SCE}; d) 0.9 V_{SCE} and e) 1.4 V_{SCE} for SS304L and f) E_{corr} ;g) 0 V_{SCE}; h) 0.4 V_{SCE}; i) 0.9 V_{SCE} and j) 1.4 V_{SCE} for SS3316L.195

Figure 5.7: XPS spectra and deconvolution of Ni 2p _{3/2} at pre-oxidation potential a) E_{corr} ;b) 0 V_{SCE}; c) 0.4 V_{SCE}; d) 0.9 V_{SCE} and e) 1.4 V_{SCE} for SS304L and f) E_{corr} ;g) 0 V_{SCE}; h) 0.4 V_{SCE}; i) 0.9 V_{SCE} and j) 1.4 V_{SCE} for SS3316L.....197

Figure 5.8: XPS spectra and deconvolution of Mo 3d at pre-oxidation potential a) E_{corr} ;b) 0 V_{SCE}; c) 0.4 V_{SCE}; d) 0.9 V_{SCE} and e) 1.4 V_{SCE} for SS316L.198

Figure 5.9: Comparisons of ratio of each oxidized a) Fe and b) Cr species to the total amount of all oxidized species (Fe+Cr+Ni+Mo) between SS314L and SS316L as a function of applied potential; c) Mo species ratio vs. applied potential for SS316L.....201

Figure 5.10: Comparison of depth profile in terms of ratio of Fe 2p _{3/2} to the sum of Fe 2p _{3/2} and Cr 2p _{3/2} as a function of applied potential for a) SS304L and b) SS316L; c) comparison of oxide film thickness vs applied potential for 304L(solid square) and 316L(hollow circle) from this study and SS316L from Nicić and Macdonald’s work³⁸ (solid triangle).203

Figure 5.11: a) Comparisons of cathodic kinetics of SS304L in negative and positive directions as a function of applied potential; b) comparisons of cathodic kinetics of SS316L in negative and positive directions at a function of applied potential.205

Figure 5.12: Comparison of i_{cathodic} at -0.8V_{SCE} in both negative and positive direction as a function of applied potential for both SS304L and SS316L.205

Figure 5.13: Equivalent circuit models used to fit EIS data of SS304L and SS316L at a) applied potential=E_{corr}, 0, 0.4, and 0.9V_{SCE}; b) 1.4 V_{SCE}.....206

Figure 5.14: a) Bode Impedance response and b) phase angle response of SS304L in 0.3M Na₂SO₄ for different applied potentials; c) Bode Impedance response and d) phase angle response of SS316L in 0.3M Na₂SO₄ for different applied potentials. All solid lines represented the fit using the equivalent circuit models in **Figure 5.13**.207

Figure 5.15: Comparison of a) effective oxide film capacitances ($C_{\text{film,eff}}$), b) total resistance ($R_{\text{film}}+R_{\text{ct}}$) and c) $R_{\text{film}}C_{\text{film,eff}}$ product between SS304L and SS316L as a function of applied potential.208

Figure 6.1: A schematic representation of crevice assembly between AA7050 and SS 316L from a) side view and b) from top view, and c) snapshot of testing crevice assembly.219

Figure 6.2: Geometry Setup of Crevice Assembly in COMSOL™221

Figure 6.3: pH distribution in the crevice for area ratio =1:1 and 8:1 after 8-week testing.222

Figure 6.4: a) Optical profilometry of corrosion distribution around the crevice mouth when area ratio=8:1; b) False color expression of a); c) Corrosion depth profile along the direction in b). 222

Figure 6.5: Comparison of maximum corrosion depth for area ratio ranging from 1:1 to 8:1...223

Figure 6.6: Boundary conditions used in the modeling study.223

Figure 6.7: An example to show Cu (within the yellow circle) replated on AA7050 after 8-week immersion testing when area ratio of cathode to anode is 8:1.....224

Figure 6.8: Boundary conditions setup for a) AA7050 side; b) SS316L side.224

Figure 6.9: Comparison of potential distributions for different area ratios.....225

Figure 6.10: Current density vs. distance along the direction 1 as a function of area ratio.225

Figure 6.11: A schematic representation of a generic crevice geometry involving two pertinent crevice geometric parameters¹².....227

Figure 6.12: Comparison of modeling and experimental results for Ni200 in 0.5M H ₂ SO ₄ : a) for linear scaling law; b) quadratic scaling law ¹²	228
Figure 6.13: A schematic geometry of axisymmetric galvanic coupling between SS316L fastener and AA7050-T7451 plate in the modeling.....	231
Figure 6.14: a) Electrochemical kinetics of SS316L and AA7050-T7451 in different solutions; b) boundary conditions in Case 1&2; c) boundary conditions in Case 3&4.	233
Figure 6.15: a) Potential distributions and b) anodic current density distributions along the AA7050 in the crevice as a function of G when T _{plate} =10 mm and WL= 1000 μm in Case 1: internal passive SS wall.	234
Figure 6.16: Comparison of a) potential distribution and b) anodic current density distribution along the AA7050 in the crevice as a function of WL between Case 1: passive SS wall and Case 2: active SS wall.....	236
Figure 6.17: Comparison of simulated data and linear fit as a function of G plotted on a) linear scale L _{crit} and b) quadratic scale L _{crit} ²	237
Figure 6.18: Comparisons of L _{crit} ² /G as a function of WLs for two different internal SS wall conditions.	239
Figure 6.19: Comparison of potential distributions along AA7050 in the crevice as a function of WL when the internal SS wall is a) passive and b) negative. This figure has the same geometry configuration as Figure 6.16	239
Figure 6.20: Comparison of potential distributions along AA7050 between WL=1000 and 100 μm when T _{plate} =150 mm and G=10 μm in Case 4.	240

List of Tables

Table 2.1: Nominal composition of UNS S31600 alloy (wt%)	35
Table 2.2: Electrochemical Parameters Fitted from Experimentally Determined Cathodic Kinetics of SS316L via EC-Lab Software.	49
Table 3.1: Composition of the SS316L disk used (all values in weight percent)	62
Table 3.2: Composition of the AA7050-T7451 used (all values in weight percent)	62
Table 3.3: Percentage of ratio of I_C/W for the first 5cm of L_c to that for the entire cathode for $L_c = 5, 10, 20, 40$ cm	85
Table 3.4: The pertinent parameters of persulfate ion, hydrogen peroxide and dissolved oxygen in 1M NaCl ³⁸ and calculated <i>ilim</i> for $S_2O_8^{2-}$, H_2O_2 and O_2	87
Table 4.1: Bulk composition of UNS A97050.....	97
Table 4.2: Compsotion of UNS S30400.....	97
Table 4.3: Range of Values of All Pertinent Geometric Parameters.....	99
Table 4.4: Boundary Conditions in First Type of Boundary Condition.....	101
Table 4.5: Boundary Conditions in Second Type of Boundary Condition.....	101
Table 4.6: Repassivation Potentials of Al Alloy in Case 1&2.....	104
Table 4.7: Film Resistivity and dielectric constant of MgO, ZnO and Al_2O_3 ⁵⁶	125
Table 4.8: Fitted EIS parameters for AA7050 in 0.6M NaCl solution in different immersion time	126
Table 4.9: Fitted EIS parameters for AA7050 in 0.6M NaCl+0.1M $MgSO_4$ solution in different immersion time.	127
Table 4.10: Fitted EIS parameters for AA7050 in 0.6M NaCl+0.1M $ZnSO_4$ solution in different immersion time	129

Table 4.11: Composition of AA7050-T7451, AA5083-H131 and AA2024-T351 (All values in weight percent)	139
Table 4.12: pH of each test solution.....	140
Table 4.13: A list of Fitted Electrochemical Parameters for AA7050 as a function of $[Al^{3+}]$ in solutions.....	145
Table 4.14: Fitted EIS parameters as a function of $[Al^{3+}]$ for AA7050	149
Table 5.1: Composition of SS304L and SS316L in Atomic Weight Percent (%)	184
Table 5.2: List of binding energies for different states of each primary element appeared in the oxide film of steels ³³⁻³⁵	199
Table 5.3: List of values of $C_{film, eff}$, R_{film} and R_{ct} . for both SS304L and SS316L in 0.3M Na_2SO_4	207
Table 6.1: Comparison between different area ratios in terms of ratio of max anodic current density (from modeling) and maximum corrosion depth (from measurement)	226
Table 6.2: Boundary condition assignments for four different modeling case studies.	231
Table 6.3: A list of comparisons between L_{crit}^2/G and L_{crit}/G in terms of R^2 values in different WL and internal SS wall conditions.	238

List of Symbols

AA	Aluminum alloy
C_j	Concentration of species
CPE	Constant phase element
CV	Cyclic voltammetry
D	Diffusivity
E_{corr}	Corrosion potential
E_{galv}	Galvanic coupling potential
EDS	Energy dispersive spectroscopy
F	Faraday constant
FEM	Finite element method
G	Crevice gap width
HER	Hydrogen evolution reaction
i	Current density
$i_{cathodic}$	General cathodic current density
i_{galv}	Galvanic coupling current density
i_{lim}	Cathodic limiting current density
i_o	Exchange current density
I_c	Total cathode current
IR	Potential due to ohmic resistance
L_{crit}	Critical crevice length
N-P	Nernst-Planck Equation
N_j	Mass flux of species
OCP	Open circuit potential
ORR	Oxygen reduction reaction
Q	Electricity charge
SEM	Scanning electron microscopy
SS	Stainless steel
SVET	Scanning vibrating electrode technique
V_{SCE}	Electrode potential in terms of saturated calomel reference electrode
v	Electrolyte flow velocity
WL	Electrolyte/ water layer thickness
W	Warburg impedance
XPS	X-ray photoelectron spectroscopy
XRD	X-ray diffraction
z	Number of electron transferred
α_a	Anodic charge transfer coefficient
α_c	Cathodic charge transfer coefficient
β_a	Anodic Tafel slope
β_c	Cathodic Tafel slope
δ	Boundary layer thickness

δ_{nc}	Critical boundary layer thickness
κ	Electrolyte conductivity
ε	Dielectric constant
ε_0	Vacuum permittivity
Φ_l	Electrolyte potential
ν	Viscosity
ρ	Resistivity

1. Introduction

1.1 An Overview of Dissertation Problem

Connections between dissimilar materials are frequently encountered in complex structures involved in aviation and aerospace industry. In a typical aircraft structure, aluminum-alloy-based airframe component and noble fasteners such as stainless steel is one of the most common couples encountered. When the aircraft is exposed in an aggressive moisture environment such as rainfall, fog, splash, salt-enabled deliquescence, a thin layer of electrolyte or droplet can be established on the dissimilar materials assembly surface. If the assembly has a fastener-hole geometric configuration, it can assist trapping or wicking of surface electrolyte into the tight crevice between the fastener and the airframe component once breakdown happens on the protective coating above the assembly, resulting in a localized galvanic corrosion environment in which Al-alloy based component is the corroding anode, whereas the stainless steel fastener is the cathode (Figure 1.1), this phenomenon can further lead to pit-to-fatigue crack initiation on the Al-alloy based component which deteriorate its structural integrity and shorten the lifespan.

It should be noted that there are three key elements identified in this problem: dissimilar materials, external environment, and geometry. There have been numerous previous research studies focusing on interaction between galvanic couple and external environment or geometry, however research effort towards interaction among all three elements is rare in literature, especially one with complicated geometry makes the in-situ experimental measurement more difficult to be achieved. Modeling approach provides an alternative to interrogate the underlying corrosion mechanism of galvanic-coupling induced Al alloy as a function of environmental variables involved in a complicated geometry. By utilizing modeling approach, one can target the essential environmental and geometric variable (s) that controls the corrosion rate of Al alloy and

predict its in-service lifetime in a timely fashion. Nevertheless, most of galvanic corrosion modeling work especially in continuum or meso-scale falls short of careful consideration of environmental variables, let alone one with complicated geometry.

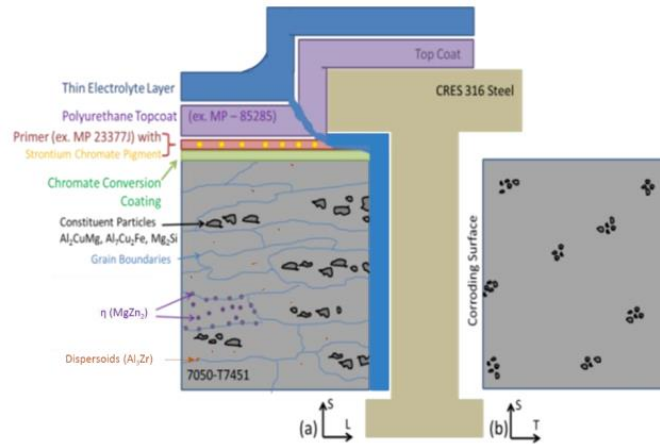


Figure 1.1: A schematic representation of galvanic couple between AA7050-T7451 airframe component and SS316L fastener with fastener-hole configuration.

1.2 Background

1.2.1 Atmospheric Corrosion vs. Submerged Corrosion

The type and rate of corrosion depend on the environment that is in contact with the material of interest. One way of categorizing corrosion is by the nature of the environmental exposure. All exposures can be classified into two types: atmospheric corrosion and submerged corrosion (corrosion under full immersion¹). Atmospheric corrosion refers to the corrosive action that occurs on the surface of a metal in an atmospheric environment (rain, fog, dew, etc.)². Specifically, when a metallic material is exposed in a marine environment, a thin layer of electrolyte will form on the top surface of the material due to the splash, rain water, and salt enabled deliquescence. This situation creates the ionic conditions needed for the occurrence of corrosion. There are several differences in corrosion behavior between atmospheric corrosion and submerged corrosion (a schematic comparison is illustrated in Figure 1.2): (1) atmospheric corrosion in

general is not a continuous process because of the existence of wet-dry cycles due to diurnal changes in temperature and relative humidity, but submerged corrosion can proceed continuously for a long period due to the constant presence of bulk solution; (2) there is an accumulation of dissolved species in atmospheric conditions due to the limited volume of electrolyte available, leading to dramatic change in the solution chemistry in contact with the surface. However, for submerged corrosion, the concentration of dissolved species does not significantly change in light of the large bulk solution volume, and chemistry at the metal surface will be generally stable; (3) during the wet stage of atmospheric corrosion, the electrolyte layer thickness does not stay at a constant value, and its changes in thickness can impact the mass-transfer limited electrochemical kinetics of the corroding metal. But for submerged corrosion, mass-transfer limited kinetics will be stabilized once the corrosion process reaches steady state; It is important to think about the choice of applying either atmospheric corrosion kinetics or submerged corrosion kinetics when it comes to corrosion modeling studies.

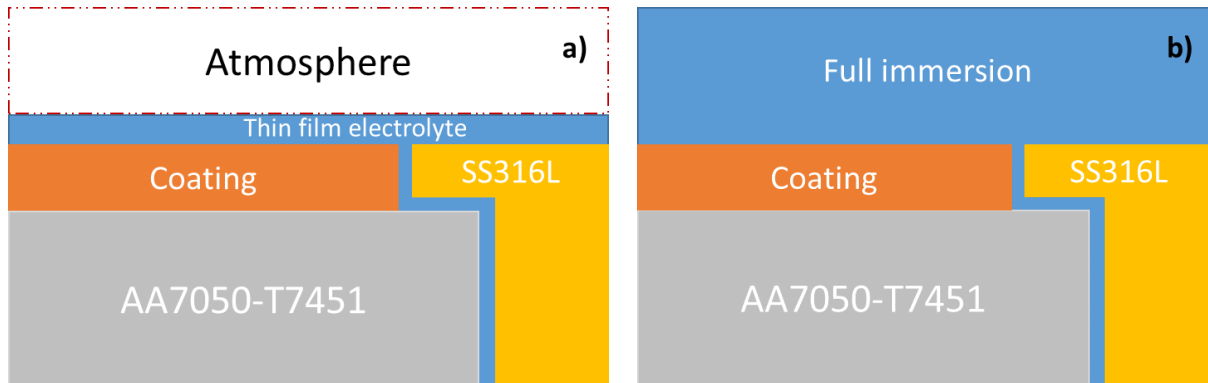


Figure 1.2: A schematic comparison between atmospheric corrosion and submerged corrosion with fastner-hole configuration: a) atmospheric corrosion and b) submerged corrosion.

1.2.2 Al-Zn 7xxx Alloys

With the advantage of high strength-to-weight ratios, low density and excellent fabricability, aluminum (Al) alloys are widely applied in aerospace and military applications. 7xxx Al alloys are very strong heat treatable alloys which can be strengthened by precipitation hardening based on the combination of zinc (mostly between 4~6 wt%), magnesium (range 1~3 wt%), and copper (range 0.1~2.4 wt%)³. 7xxx Al alloys have highly heterogeneous microstructures which feature^{4,5}: (1) Al-matrix grains, (2) porosity, (3) inclusion (oxides of aluminum and magnesium), (4) constituent particles (generally insoluble particles formed by eutectic reaction during solidification with sizes ranging from 0.5 μ m to 500 μ m), (5) dispersoids (fine precipitates with limited solubility in Al-matrix formed during either solidification or ingot preheating, with sizes ranging from 50 nm to 400 nm, comprised of Cr, Zr and Mn), (6) aging hardening precipitates (fine precipitates formed at low temperature with sizes ranging from 10 nm to 200 nm, generally as a consequence of high solute supersaturation resulting from a solution heat treatment and quench), and (7) grain boundary regions, including grain boundary (G.B.) precipitates and precipitate free zones (regions adjacent to the grain boundaries resulting from a depletion of both vacancies and solute in this region). Usually, constituent particles, dispersoids and age hardening precipitates can be categorized as intermetallic particles/compounds (IMP/IMCs). This microstructural heterogeneity is the fundamental source of the localization of corrosion damage that is typical of 7xxx Al Alloy.

Common localized corrosion forms that happen in 7xxx Al Alloys are¹: pitting corrosion, crevice corrosion, intergranular corrosion (IGC), exfoliation corrosion, and environmentally assisted cracking (e.g., stress-corrosion cracking (SCC)). In this work, pitting corrosion and crevice corrosion will be the localized corrosion forms of interest along the surface of AA7050-

T7451 galvanically coupled with SS316L. Constituent particles are the dominant microstructural features that cause pitting corrosion. Large and irregularly shaped constituent particles tend to break up and align into bands along the rolling direction within the Al-matrix. They can be either cathodic (e.g., $\text{Al}_7\text{Cu}_2\text{Fe}$, $(\text{Al,Cu})_6(\text{Fe,Cu})$, Al_3Fe)⁶⁻⁸, or anodic (e.g. Mg_2Si , Al_2CuMg)^{8,9}, with respect to Al-matrix, where these micro-galvanic corrosion couplings can be formed which initiates pitting corrosion of Al alloy. Crevice corrosion¹ generally occurs if an electrolyte is present in a region between two faying surfaces. Since the amount of dissolved oxygen is plentiful outside the crevice mouth (cathodic area) whilst the oxygen content is limited in the crevice (anodic area) due to sluggish diffusion into tight crevice, a differential aeration cell is formed as a result. Once the crevice attack has initiated, cathodic areas becomes alkaline and the anodic areas turn acidic. Details of the mechanism of crevice corrosion introduced by the galvanic couple will be discussed in Section 1.2.3.

1.2.3 Localized Corrosion Damage Induced by Galvanic Coupling

There are two prevailing theories used to better understand the underlying mechanisms of crevice corrosion: the critical crevice solution (CCS) theory and critical potential drop (IR) theory. Oldfield and Sutton^{10,11} developed the first mathematical modeling to express the crevice corrosion for stainless steel in seawater. In the CCS theory (Figure 1.3a), mass transport of species is limited by the occluded geometry of a crevice, which leads to a difference in solution chemistry between the bulk solution near the crevice mouth and the crevice solution in the occluded region. The crevice solution generally develops a low pH, and high $[\text{Cl}^-]$ due to hydrolysis of dissolved metal species as well as migration of $[\text{Cl}^-]$ into the crevice to maintain charge neutrality. When the crevice solution chemistry passes a critical composition, the passive film breaks down and results in onset of the localized corrosion. Pickering *et al.*¹²⁻¹⁵ proposed the IR mechanism in which a

large potential drop occurs within the crevice solution is caused by the restricted geometry which is a barrier to electrical flux (Figure 1.3b). At the location where the potential drops below the critical value E_{crit} in the crevice, the corrosion rate is accelerated due to the presence of an active/passive transition. In reality, it is likely that both theories are relevant.

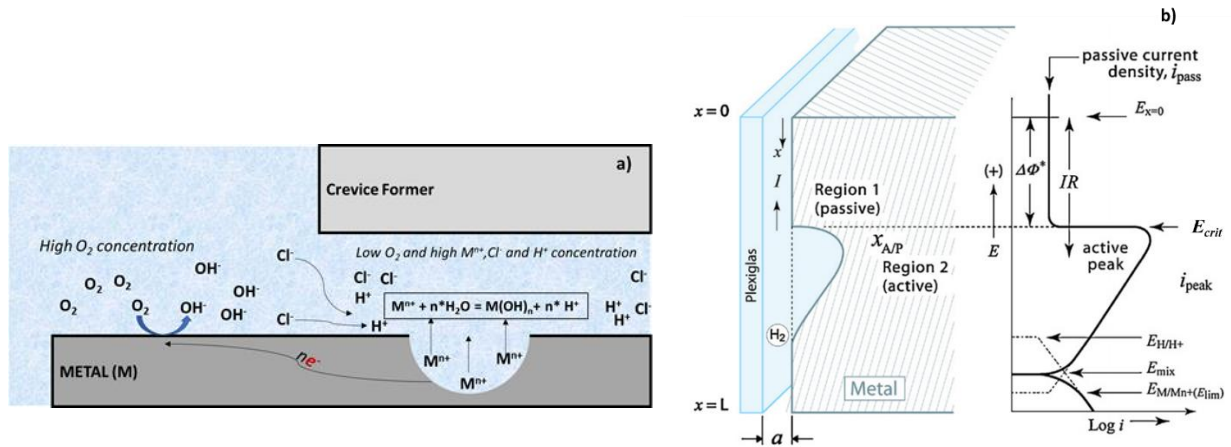


Figure 1.3: a) Schematic representation of development of critical crevice solution in a corroding crevice geometry; b) IR drop theory based on a crevice geometry, after Shu *et al.*¹⁶.

When a metal is in electrical contact with a more noble metal or nonmetallic conductor in a conductive environment, the corrosion rate of the less noble metal can be accelerated due to the formation of the galvanic cell. This phenomenon is called galvanic corrosion². This corrosion damage can be further aggravated if there is a crevice formed between the two materials. In this dissertation work, the assumed breakdown of a corrosion protective coating will facilitate the trapping/wicking of the electrolyte on the materials surface into the tight crevice in the galvanic coupling between AA7050 based airframe component and SS316 fastener with a fastener-hole configuration (Figure 1.1)¹⁷. The difference in the content of dissolved oxygen between the solution at the crevice mouth and the most occluded region of the crevice leads to the formation of crevice corrosion on AA7050, exacerbated by the effect of anodic polarization of AA7050 by SS 316L fastener. A potential distribution that develops along the AA7050 surface, together with

the solution chemistry variation from crevice mouth to the most occluded region, will result in the localized corrosion (pitting corrosion) at locations where the critical conditions occur. The localized corrosion happening in the crevice introduced by the galvanic couple is the major corrosion form that the dissertation work investigated.

1.2.4 Variables Affecting Localized Corrosion in Atmospheric Conditions

Atmospheric corrosion is an interdisciplinary subject that combines atmospheric chemistry and surface science. It is a complex corrosion process involving several factors including environmental, geometric and materials aspects.

1.2.4.1 Environmental Factors

Time of Wetness. Atmospheric corrosion happens in the presence of a thin film electrolyte. The source of the electrolyte comes from rain, fog, dew, melting snow or high humidity¹⁸. However, the electrolyte is not always present on the materials surface, making atmospheric corrosion a discontinuous process. The concept of “time of wetness” was introduced to describe the effective time period when atmospheric corrosion takes place. Time of wetness refers to the length of time during which the material surface is covered by a film of water that renders significant atmospheric corrosion possible¹⁸. It is often defined as a function of other environmental factors, such as relative humidity (RH) and temperature¹⁹. In some models, the total corrosion effect as a result of taking into account time of wetness can be expressed as¹⁸

$$K = \sum_{i=1}^n t_n v_k (n) \quad (1.1)$$

where K is the total corrosion effect, t_n is time of wetness, and v_k is the average corrosion rate during the individual periods of wetness.

Electrolyte Layer Thickness (WL). Atmospheric corrosion proceeds in the presence of thin film electrolyte. Variation in the thicknesses of electrolyte layer can affect some pertinent processes, e.g., dissolved oxygen transport, solubility of some corrosion product. Tomashov²⁰ proposed a theory to describe the effect of electrolyte layer thickness on the corrosion rate of metals, in which he divided moisture layer thickness into four different regions as shown in Figure 1.4: I) Region of dry atmospheric corrosion, $WL < 10 \text{ nm}$; II) region of humid atmospheric corrosion, $10 \text{ nm} < WL < 1 \text{ }\mu\text{m}$; III) region of wet atmospheric corrosion, $1 \text{ }\mu\text{m} < WL < 1 \text{ mm}$; IV) region of complete immersion, $WL > 1 \text{ mm}$. Region I leads to a minimum corrosion rate since the adsorbed water molecules cannot form a continuous water layer, according to Tomashov. In Region II, the corrosion rate is limited by anodic kinetics, and the reduction in WL results in the decrease in corrosion rate due to lack of water molecules needed for dissolving metal ions, In Region III, a smaller WL lead to higher corrosion rates since oxygen transport through the layer can occur more rapidly. Region IV proceeds equivalently to the corrosion under full immersion condition. Tomashov's theory provides a conceptual description of the dependence of atmospheric corrosion on electrolyte thickness, but the critical thickness of each region is not well characterized. More accurate and quantitative characterization of this dependence has been the focus of many researchers, as will be explicitly discussed in Chapter 3.

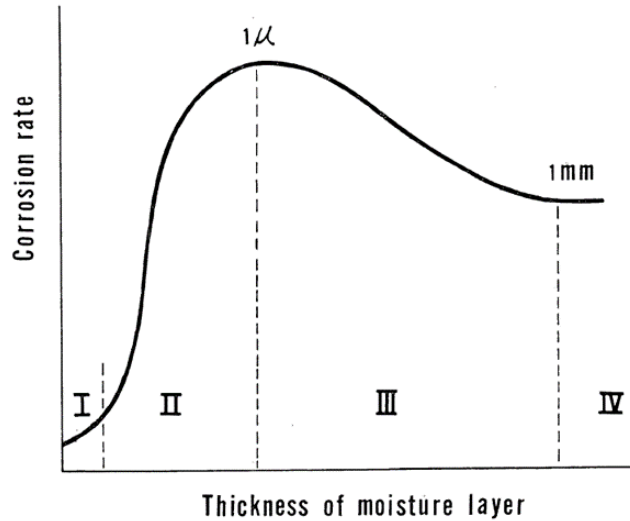


Figure 1.4: Corrosion Rate as a function of thickness of moisture layer. I) Region of dry atmospheric corrosion; II) region of humid atmospheric corrosion; III) region of wet atmospheric corrosion; IV) region of complete immersion. After Tomashov.²⁰

Thin Film Solution Chemistry. Another important factor influencing atmospheric corrosion rate is the thin film solution chemistry. There are mainly two sources contributing to the composition of thin film solution^{21,22}: dissolved metal ions from the corrosion product, and anions (Cl^- , SO_3^{2-} , SO_4^{2-} , CO_3^{2-} , etc.) from the environment (rain, fog, dew, splash, gas phase, etc.). Furthermore, decreases in pH from hydrolysis of metal ions at anodic sites, as well as the increase in pH from oxygen reduction reaction at cathodic sites can be dramatic due to very limited volume of thin film solution. This aggressive solution environment can be very detrimental to the surface structure of the metallic materials, making them be prone to localized corrosion. Details in the effect of thin film solution chemistry will be discussed in Chapter 4.

1.2.4.2 Materials

Some internal variables pertinent to the surface properties of the materials can also significantly impact the degree of localized corrosion damage, e.g., polarization behaviors of anode/cathode, presence/absence of the corrosion protective coating, breakdown of oxide film above bare metal

surface, and spatial distributions of intermetallic particles (discussed in Section 1.2.2). Note that the polarization behaviors of the anode and cathode in atmospheric conditions will be different from those for the submerged condition if the electrochemical kinetics are mass transfer limited. For the corrosion protective coating, besides a number of studies regarding metallic coating in atmospheric conditions²³⁻²⁵, localized corrosion introduced by defects in organic coating is another focus in atmospheric corrosion study^{26,27}. As for the oxide film, concentrated aggressive species in the thin film electrolyte can breakdown the film and bring in pitting corrosion^{28,29}. A detailed study focused on the surface properties of stainless steel fastener will be elaborated in Chapter 5.

1.2.4.3 Geometry

The geometry of anode and cathode in a corrosion system can be significant in determining the degree of localized corrosion damage. The area ratio of cathode to anode and/or the size of the external cathode are the geometric factors that many corrosion researchers have investigated extensively. From the perspective of cathode-to-anode ratio, it has been shown that larger cathode-to-anode ratio results in larger corrosion damage on the anodic materials³⁰⁻³³. Furthermore, if a crevice was introduced into assembly of anode and cathode, the fully exposed area along the external cathode would experience a different corrosion environment from the most occluded region of the crevice between the internal cathode and anode, and this discrepancy in corrosion environment due to the geometry arrangement has been investigated by several researchers^{10,11,34,35}. By considering atmospheric conditions, more focused corrosion at the anode/cathode interface could be actually escalated due to enhanced mass-transferred kinetics of the cathode on the premise of large cathode-to-anode area ratio. A careful study regarding the effect of geometry will be presented in Chapter 6.

1.2.5 Application of Finite Element Method in Localized Corrosion Modeling Study

As mentioned earlier, computational modeling can also play an important role in improving the understanding of localized corrosion process, in particular when it is coupled with experimental research that accurately quantifies the important characteristics that control corrosion rate and resultant morphology. There are many modeling methods that can be applied, with the choice of method driven by the goal of the modeling exercise.

Empirical models³⁶ can be used to predict performance within the parameter space for which they are created. Such models can provide insight into what kinds of processes might be dominating the corrosion process, but further dissection of controlling factors is more difficult. Numerical modeling, in which the concentration, potential and current distributions are calculated, plays an important role in helping understand controlling factors. There are several numerical methods in continuum- or meso-scale that have been implemented by corrosion scientists and engineers: the finite difference method (FDM)³⁷⁻⁴⁰, the boundary element method (BEM)⁴¹⁻⁴⁵, the finite volume method (FVM)⁴⁶⁻⁴⁸, Peridynamics (PD)⁴⁹⁻⁵¹ and the finite element method (FEM). Among those, FEM has been the most widely used to investigate transport phenomena in the corrosion systems due to its advantages of dealing with arbitrary shapes, and accessible solution evaluation at any point within the domain without losing much accuracy.

FEM is a numerical technique used to obtain approximate solutions to the differential equations based on different types of discretizations in which the domain of interest is divided into different types of elements. These discretization methods approximate the differential equations with numerical model equations and provide a numerical solution to the equations. These differential equations can describe a wide variety of physical phenomena, ranging from electrical and mechanical systems to chemical and fluid flow problems. Generally, FEM establishes credible

stability criteria and provides more flexibility (e.g., in handling inhomogeneity and complex geometries) compared to other numerical modeling method such as finite difference methods (FDM).

1.2.5.1 Prevailing Governing Equations in FEM-Based Corrosion Modeling

In FEM-based computational study for transport phenomena in the corrosion system, there are two prevailing modeling approaches: Nernst-Planck-Equation (N-P) based approach and Laplace-Equation based approach.

The Nernst-Planck Equation is the most complete means to describe the materials balance of each charged species (j) in a system. It is formulated as a summation of diffusion, migration and convection and homogeneous reaction terms⁵²:

$$\frac{\partial C_j}{\partial t} = -\nabla \cdot N_j + R_j = -\nabla \cdot (D_j \nabla C_j) + \frac{z_j F}{RT} \nabla \cdot (D_j C_j \nabla \Phi_l) - \nabla \cdot (C_j v) + R_j \quad (1.2)$$

where N_j is the mass flux (mole/(m²·s)), C_j is the concentration (mole/m³), z_j is the number of charges, D_j is the diffusivity (m²/s), Φ_l is the electrolytic potential (V), F is the Faraday's constant (96,485 C/mole), v is the fluid velocity (m/s) and R_j is the homogeneous production of species j (mole/(m³·s)). If the number of charged species is n , a system of n equations in form of Equation 1.2 can be obtained. It should be noted that there are $(n+1)$ variables in this system of equations: Φ_l and C_j (j from 1 to n). Thus, in order to find the solution of this system, an $(n+1)$ th equation is needed, which in electrochemical systems is most often found by the application of the electroneutrality assumption in the electrolyte domain:

$$\sum z_j C_j = 0 \quad (1.3)$$

As a result, the electrolyte potential as well as concentration of each charged species are obtained.

As for the current density distribution, in the electrolyte domain, the total current density i_l can be expressed as

$$i_l = -F \sum z_j D_j \nabla C_j - \frac{F^2}{RT} \nabla \Phi_l \sum z_j^2 D_j C_j + Fv \sum z_j C_j \quad (1.4)$$

The last term (convection) in Equation 1.4 is cancelled out due to the electroneutrality assumption.

By combining conservation of charge

$$\nabla \cdot i_l = 0 \quad (1.5)$$

The electrolyte current density i_l can be obtained eventually.

The solution to the Nernst-Planck Equation results in full transient descriptions of the distributions of chemical composition, potential, and current density. The costs of obtaining this complete data set are computational complexity and time. The wide range of time scales that must be considered in modeling localized corrosion include very fast processes (ion reaction and response to potential gradients) and slow processes (diffusion of species under a concentration gradient). This range of timescales, combined with the mathematical difficulties in dealing with highly nonlinear boundary conditions (i.e., electrochemical kinetics) make the calculations very difficult, requiring very small-time steps and highly refined spatial meshing. In practice, to use the Nernst-Planck equation in combination with the electroneutrality condition, at each time step for each spatial element, a “make-up” ion is selected to enforce electroneutrality. There is concern that this lacks a defensible physical basis, particularly when it is not obvious which ion should be selected. In some cases, negative concentrations can be predicted^{53,54}. An example is shown in Figure 1.5 in which different choices of “reference ion” can lead to a discrepancy in potential distributions across the electrolyte between two parallel planar Al electrodes in two-dimensional configuration.

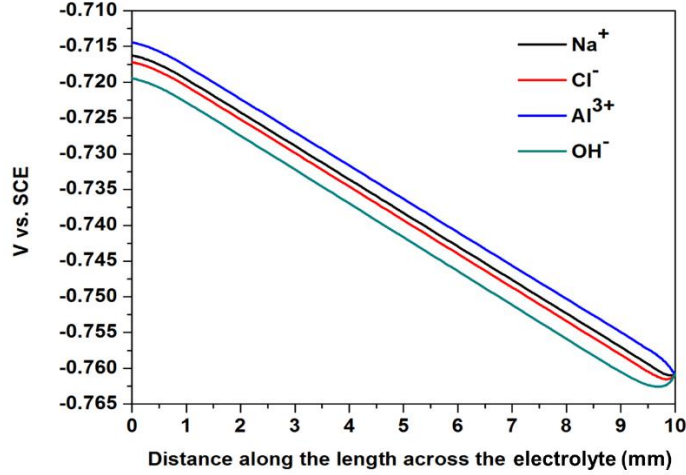


Figure 1.5: An example to show discrepancies in potential distributions by selecting different reference ions.

An alternative approach is to use Laplace's Equation as the governing equation. In this approach, it is assumed that the solution is well mixed and there is no bulk motion of the fluid such that the first and last terms in Equation 1.4 are cancelled out, as a result, Equation 1.4 is reduced to Equation 1.6:

$$i_l = -\kappa \nabla \Phi_l \quad (1.6)$$

where conductivity $\kappa = F^2 \sum z_j^2 D_j C_j$. By applying charge conservation (Equation 1.5), one can obtain the Laplace Equation

$$\nabla^2 \Phi_l = 0 \quad (1.7)$$

Rather than solving for the full transient, the use of the Laplace's Equation approach relies instead on a knowledge or estimation of the electrolyte characteristics (primarily conductivity) and its dependence on position and other experimental variables, which is the governing equation used in the dissertation work. However, one of the biggest disadvantages regarding this approach is that it loses numerical accuracy in the system if diffusive and convective transport are significant.

In both approaches, the boundary conditions describe the electrochemical kinetics (i.e., current density is a function of applied potential, $i(E)$) of the reactions which are generally highly nonlinear. These nonlinear boundary conditions can be described mathematically in some cases (e.g., via the Butler-Volmer equation for cathodic/anodic that are both under charge-transfer control) although very often the polarization behaviors measured do not follow any prescribed law, for example, for a system containing an active-passive transition. In these and other cases, a description of the kinetics via numerical fits to the polarization behavior is needed for both the anodic and cathodic reactions. Independent of the means by which the electrochemical kinetics are described, they serve as the most important aspect of the problem statement.

1.2.5.2 A Literature Review on the Application of FEM in Galvanic Corrosion Modeling

In this subsection, two types of galvanic corrosion will be discussed explicitly: micro-scale galvanic corrosion, and large scale (beyond meso-scale) galvanic corrosion.

Aluminum and magnesium alloys have very heterogeneous microstructures which include a number of different intermetallic compounds (IMC) which can serve as initiation sites for localized corrosion (pitting or intergranular corrosion) of these alloys⁵⁵⁻⁶³. The accepted mechanism for the location of the initiation sites is based on microgalvanic couples in which the alloy matrix can be either the anode or cathode with respect to the adjacent IMC. Besides FEM based modeling study which mainly focused on the potential, current and pH distributions on the engineered galvanic couple in a very simple configuration set at micro-scale^{64,65}, there are a number of numerical efforts aiming to determine corrosion morphology evolution introduced by the IMC. Deshpande⁶⁶ developed a novel model to simulate the evolution of micro-galvanic corrosion between α (AM30 alloy) and β ($Mg_{17}Al_{12}$) phases in AZ91D alloy. The two-dimensional modeling was based on the Laplace's Equation, with experimentally measured

polarization curves of α and β phases rather than analytical expression (e.g., Butler-Volmer or Tafel kinetics) as anodic and cathodic boundary conditions. The movement of corrosion front and interface velocity were determined by Arbitrary Lagrangian Eulerian (ALE) method. A network of β phases was created according the pertinent SEM image to represent the distribution of this phase in the real microstructure, and this scenario was compared to a single β phase case. It was found that β -phase-network scenario resulted in more accelerated corrosion of α phase than a single- β -phase one due to larger cathode-to-anode area ratio. About the same time, Xiao and Chaudhuri⁶⁷ advanced the development of micro-galvanic corrosion modeling framework based on the N-P Equation and proposed a predictive model to rigorously study the connection among the Al alloy matrix, microstructure, and electrode/electrolyte conditions. The highlight of this modeling framework is that boundary conditions can be adaptive to the changes in chemistry or surface property that occurred in the previous time step. However, this modeling only focused on the interaction between a single IMC and Al-matrix, a future work for the interaction between multiple IMCs and Al-matrix is needed. A recent series of modeling studies performed by Yin *et al.*⁶⁸⁻⁷⁰ and Wang *et al.*⁷¹ systematically studied the effect of bulk & local solution chemistry (pH, dissolved oxygen and carbon dioxide, and etc.), the condition of corrosion product (structure, surface coverage, and etc.), and geometric factors (radius of IMC and initial pit ring size) on the pit morphology development in a single-IMC (Al₃Fe)/ AA7075-matrix micro-galvanic corrosion system, and also confirmed through both modeling and in-situ AFM measurement of the deposition of Al(OH)₃ on the localized corrosion site and its blocking effect.

The discussion above focuses on the galvanic corrosion at a very localized site on the materials surface. Actually, FEM based modeling can also provide a holistic view of corrosion distribution for an engineering metal/alloy such as aluminum or magnesium alloys which are prone

to localized corrosion when galvanically coupled with a noble material at a larger scale. Deshpande^{72,73} used a Laplace-Equation-based modeling approach to study localized corrosion current density distribution along Mg Alloy AE44 when it was galvanically coupled with either mild steel or Al alloy AA6063 in full immersion conditions and then compared the modeling results with experimental measurements from the scanning vibrating electrode technique (SVET). The comparison showed that maximum corrosion rate for AE44/mild steel couple was eight times higher than that for AE44/AA6063 couple from modeling prediction. Trinh *et al.*⁷⁴ extended Deshpande's framework by re-examining the galvanic couple between AE44/mild steel, but with the materials embedded in epoxy to create surrounding insulated edge. From both modeling and SVET measurements, they showed that the localized corrosion rate and overall corrosion rate were enhanced by existence of insulated edge, compared with the no-edge scenario.

FEM Modeling can also provide insight for the performance of sacrificial metallic coatings that protect the underlying materials substrate⁷⁵⁻⁸¹. An example application can be demonstrated by Cui *et al.*⁷⁶, in which they used a combined numerical and experimental approach to examine the throwing power (distance from the farthest protected point to the edge of aluminum cladding along the AA2024 substrate) of aluminum cladding for protecting underlying AA2024 within a scratch, and they found that the throwing power is a function of electrolyte layer thickness over the materials surface, scratch size, chloride concentration, cathodic limiting current density of substrate as well as passive current density of clad. In order to achieve comparable results to the outdoor exposed sample whose exposure environment was hard to estimate, a modeling condition of 1M sodium chloride thin film electrolyte layer with thickness=25 μm should be applied. King *et al.*⁷⁵ simulated the current and potential distribution in a galvanic couple between Mg rich primer and its protected AA2024-T351 (Figure 1.6), they took into account polymer resistance of the

primer by defining a term representative of potential drop across the primer film and incorporated it into the boundary conditions. A study for the effect of polymer resistance showed that increased polymer resistance can gradually decouple AA2024 from Mg rich primer electrochemically, making it less protected.

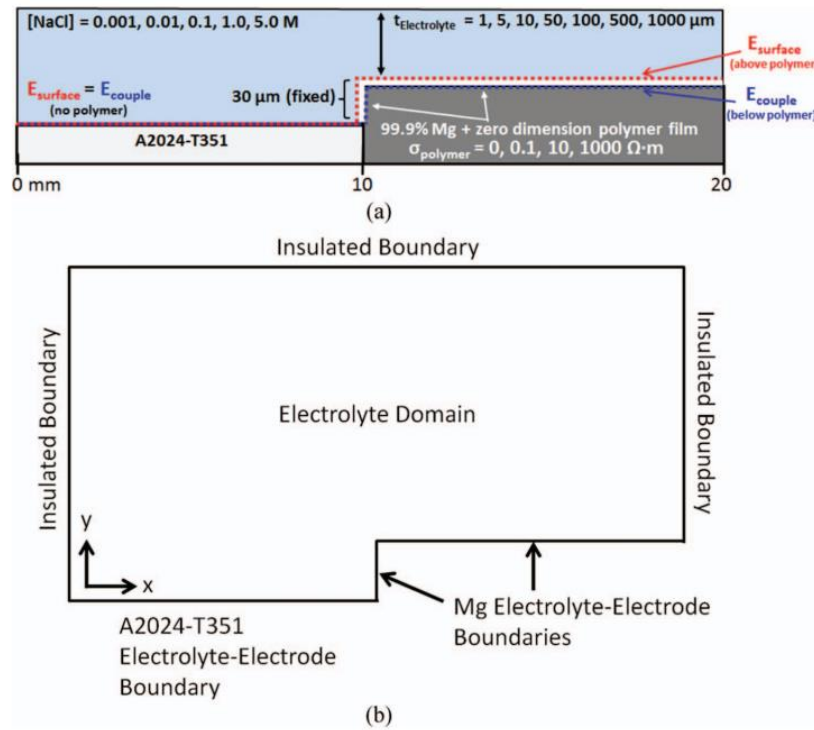


Figure 1.6: Schematic representation of FEM based model geometry a) materials and electrolyte conditions studied and b) assumptions of boundary conditions, after King *et al.*⁷⁵

1.3 Overarching Research Questions

The overarching research question in this dissertation work is: how can we develop robust computational modeling to predict localized corrosion as a function of environmental variables related to atmospheric environment, materials properties and geometry of relevant corroding structures? Two explicit questions will be addressed: (1) under what circumstances can Laplace’s Equation be used to evaluate electrochemical distributions instead of the Nernst-Planck Equation?

(2) What mechanisms control how external (solution environment, geometry) and internal (materials) factors affect electrochemical and localized corrosion distributions for a galvanic couple between SS316 and AA7050 involving a fastener-hole configuration?

1.4 Objectives

The main goal of this dissertation is to investigate the galvanic-coupling induced localized corrosion distribution along AA7050-T7451 with a fastener-hole configuration between AA7050-T7451 and SS316L in a simulated environment representative of atmospheric corrosion. This goal is fulfilled by the following tasks:

- Develop a robust finite-element modeling approach based on Laplace's Equation to accurately predict corrosion distributions and bound the application of this modeling framework within its limitation by providing reasonable assumptions.
- Utilize FEM modeling approach, electrochemical techniques, and pertinent instrumental characterization tools to systematically investigate the effect of electrolyte layer thickness, solution chemistry, materials surface properties, and galvanic coupling geometry on the electrochemical and corrosion distributions in the galvanic coupling between AA7050 and SS316L, and capture the underlying mechanism for the dependence of corrosion distributions on each external variable.

1.5 Organization of Dissertation

This dissertation is divided into 7 chapters (Chapter 1: introduction; Chapter 2: verification of Laplace-Equation based modeling into corrosion modeling; Chapter 3: electrolyte layer thickness effect study; Chapter 4: solution chemistry effect study; Chapter 5: surface property effect Study; Chapter 6: corrosion geometry effect study; Chapter 7: conclusions and recommended future work).

Chapter 1 provided a literature review of several external variables pertinent to corrosion issues in this dissertation work and gave a brief introduction to mathematical basis of finite-element based modeling and its application to galvanic corrosion modeling. The latter part is based on our published work: **C. Liu** and R.G. Kelly, “The Use of Finite Element Methods (FEM) in the Modeling of Localized Corrosion”, *The Electrochemical Society Interface*, 23 (2014): p 47-51. Another publication based on the literature review will be submitted to *Corrosion Reviews*.

Chapter 2 presented an example in which Laplace-Equation based modeling coupled with accurately experimentally determined electrochemical kinetics as boundary conditions was utilized to simulate galvanic corrosion distribution between Zn plate and SS rods and predict the electrolyte layer thickness during ASTM B-117 salt spray testing. Another example was shown to demonstrate the robustness of our modeling approach is based on well determined boundary conditions. This chapter is based on our published work: **C. Liu**, G. Kubacki, and R.G. Kelly, “Application of Laplace-Equation Based Modeling into Corrosion Damage Prediction for Galvanic Couple between Zn Plate and Stainless Steel Rods under a Thin Film Electrolyte”, Accepted by Corrosion.

Chapter 3 studied the effect of electrolyte layer thickness on the galvanic corrosion between SS316L and AA7050 and provided a mathematical modeling approach to determine the critical value of electrolyte layer thickness below which full immersion condition transitions into thin film conditions, and parse dependence of cathodic current capacity of SS cathode to support AA7050 anode corrode on electrolyte film thickness, electrolyte resistance and cathode-to-anode area ratio in thin film condition. This chapter is based on the published work: **C. Liu**, J. Srinivasan, and R.G. Kelly, “Editors' Choice—Electrolyte Film Thickness Effects on the Cathodic Current Availability in a Galvanic Couple”. *Journal of the Electrochemical Society*, 164 (2017): p.C845-C855.

Chapter 4 investigated the effect of solution chemistry on the galvanic corrosion distribution. This chapter consists of four parts: (1) the effect of pH and conductivity on the electrochemical distributions in AA7050/SS316L with as fastener-hole configuration was investigated in Part 1; (2,3) Part 2&3 investigated the effect of Zn^{2+} & Mg^{2+} (Part 2), and Al^{3+} (Part 3) on the cathodic kinetics of AA7050 as a function of concentration and immersion time, assuming there was no galvanic coupling between AA7050 and SS316L such that AA7050 was the cathode and metal-richer primer was the anode; (4) Part 4 combined the study from Part 2 and 3 to investigate the effect of Al^{3+} and Mg^{2+} on the galvanic corrosion distribution between SS316L and AA7050 without and with metal-rich primer involved. Part 1 is based on the published work: **C. Liu**, R.G. Kelly, “Mathematical Modeling of Effect of pH and Conductivity on Electrochemical Distributions in Galvanic Coupling in Airframe Components”, DoD Corrosion Conference 2015, Pittsburgh, PA, November 15-19, 2015. Part 2 and 3 will be turned into another two publications which will be submitted to *Journal of Electrochemical Society*.

Chapter 5 studied the effect of surface properties on the cathodic kinetics of stainless steel. Three different studies were presented in this chapter: (1) the effect of surface treatment on the ORR cathodic kinetics of stainless steel in a simulated thin film electrolyte condition; (2) comparative study of the effect of oxide film composition at various pre-oxidation potentials on the cathodic kinetics between SS304L and SS316L. The work in this chapter will be submitted to *Corrosion*.

Chapter 6 presented a combined experimental and modeling approach to study the effect of galvanic coupling geometry on the galvanic corrosion distributions. Two different studies were performed: (1) the electrochemical and corrosion distributions in the crevice formed in galvanic coupling between AA7050 and SS316L as a function of cathode-to-anode area ratio were studied

experimentally and numerically; (2) the effect of crevice geometry on the galvanic-coupling induced crevice corrosion of AA7050 was explored, and validation of application of typical crevice scaling law for the crevice between the galvanic couple was also examined.

Chapter 7 provided a summary of conclusions from each chapter and recommended future works for this dissertation research.

1.6 References

1. J.R. Davis, *Corrosion of Aluminum and Aluminum Alloys*, ASM International, (1999).
2. D.A. Jones, *Principles and Prevention of Corrosion*, Prentice Hall, (1996).
3. S.D. Cramer and B.S. Covino, Jr, *ASM Handbook: Vol. 13B, Corrosion: Materials*, ASM International, (2003).
4. J. E. Hatch, *Aluminum: Properties and Physical Metallurgy*, ASM International, (1984).
5. G. E. Totten and D. S. MacKenzie, *Handbook of Aluminum: Vol. 1: Physical Metallurgy and Processes*, p. 1314, CRC Press, (2003).
6. F. Andreatta, H. Terryn, and J. H. W. de Wit, *Corrosion Science*, **45**, 1733–1746 (2003).
7. F. Andreatta, H. Terryn, and J. H. W. de Wit, *Electrochimica Acta*, **49**, 2851–2862 (2004).
8. N. Birbilis and R. G. Buchheit, *J. Electrochem. Soc.*, **152**, B140–B151 (2005).
9. J. Wloka and S. Virtanen, *J. Electrochem. Soc.*, **154**, C411–C423 (2007).
10. J. W. Oldfield and W. H. Sutton, *British Corrosion Journal*, **13**, 13–22 (1978).
11. J. W. Oldfield and W. H. Sutton, *British Corrosion Journal*, **13**, 104–111 (1978).
12. H. W. Pickering, *Corrosion Science*, **29**, 325–341 (1989).
13. Y. Xu and H. W. Pickering, *J. Electrochem. Soc.*, **140**, 658–668 (1993).
14. M. Wang, H. W. Pickering, and Y. Xu, *J. Electrochem. Soc.*, **142**, 2986–2995 (1995).
15. H. W. Pickering, *J. Electrochem. Soc.*, **150**, K1–K13 (2003).
16. H.-K. Shu, F. M. Al-Faqeer, and H. W. Pickering, *Electrochimica Acta*, **56**, 1719–1728 (2011).

17. C. Liu, V. N. Rafla, J. R. Scully, and R. G. Kelly, "Mathematical Modeling of Potential and Current Distributions for Atmospheric Corrosion of Galvanic Coupling in Airframe Components," NACE International (2015).
18. P. A. S. P.E, *Atmospheric Degradation and Corrosion Control*, CRC Press, (1999).
19. E. Schindelholz, R. G. Kelly, I. S. Cole, W. D. Ganther, and T. H. Muster, *Corrosion Science*, **67**, 233–241 (2013).
20. N. D. Tomashov, *Corrosion*, **20**, 7t-14t (1964).
21. H. E. Townsend, *Outdoor Atmospheric Corrosion*, ASTM International, (2002).
22. P. Marcus, *Corrosion Mechanisms in Theory and Practice, Third Edition*, CRC Press, (2011).
23. R. Ramanauskas, P. Quintana, P. Bartolo-Pérez, and L. Díaz-Ballote, *Corrosion*, **56**, 588–597 (2000).
24. E. Palma, J. M. Puente, and M. Morcillo, *Corrosion Science*, **40**, 61–68 (1998).
25. J. J. Friel, *Corrosion*, **42**, 422–426 (1986).
26. J. E. Gray and B. Luan, *Journal of Alloys and Compounds*, **336**, 88–113 (2002).
27. S. J. Oh, D. C. Cook, and H. E. Townsend, *Corrosion Science*, **41**, 1687–1702 (1999).
28. G. S. Frankel, *J. Electrochem. Soc.*, **145**, 2186–2198 (1998).
29. Z. Szklarska-Smialowska, *Corrosion Science*, **41**, 1743–1767 (1999).
30. F. Mansfeld, *Corrosion*, **27**, 436–442 (1971).
31. F. Mansfeld and J. V. Kenkel, *Corrosion Science*, **16**, 111–122 (1976).
32. Z. Y. Chen, F. Cui, and R. G. Kelly, *J. Electrochem. Soc.*, **155**, C360–C368 (2008).
33. Z. Y. Chen and R. G. Kelly, *J. Electrochem. Soc.*, **157**, C69–C78 (2010).
34. A. Alavi and R. A. Cottis, *Corrosion Science*, **27**, 443–451 (1987).
35. K. Hebert and R. Alkire, *J. Electrochem. Soc.*, **130**, 1001–1007 (1983).
36. M.L.C. Lim, J.R. Scully, and R.G. Kelly, *Corrosion*, **69**, 35–47 (2012).
37. P. Doig and P. E. J. Flewitt, *J. Electrochem. Soc.*, **126**, 2057–2063 (1979).
38. K. L. Heppner, R. W. Evitts, and J. Postlethwaite, *The Canadian Journal of Chemical Engineering*, **80**, 849–856.

39. K. L. Heppner, R. W. Evitts, and J. Postlethwaite, *The Canadian Journal of Chemical Engineering*, **80**, 857–864 (2002).
40. G. F. Kennell, R. W. Evitts, and K. L. Heppner, *Corrosion Science*, **50**, 1716–1725 (2008).
41. S. Aoki and K. Kishimoto, *Mathematical and Computer Modelling*, **15**, 11–22 (1991).
42. R. Adey and S. Niku, in *Computer Modeling in Corrosion*, R. Munn, Editor, ASTM International (1992)
43. F. E. Varela, Y. Kurata, and N. Sanada, *Corrosion Science*, **39**, 775–788 (1997).
44. K. Amaya and S. Aoki, *Engineering Analysis with Boundary Elements*, **27**, 507–519 (2003).
45. J.-F. Yan, S.N.R. Pakalapati, T.V. Nguyen, R.E. White and R.B. Griffin, *J. Electrochem. Soc.*, **139**, 1932-1936 (1992)
46. S. Scheiner and C. Hellmich, *Corrosion Science*, **49**, 319–346 (2007).
47. S. Scheiner and C. Hellmich, *Computer Methods in Applied Mechanics and Engineering*, **198**, 2898–2910 (2009).
48. Y. Onishi, J. Takiyasu, K. Amaya, H. Yakuwa, and K. Hayabusa, *Corrosion Science*, **63**, 210–224 (2012).
49. Z. Chen and F. Bobaru, *Journal of the Mechanics and Physics of Solids*, **78**, 352–381 (2015).
50. Z. Chen, G. Zhang, and F. Bobaru, *J. Electrochem. Soc.*, **163**, C19–C24 (2016).
51. S. Jafarzadeh, Z. Chen, and F. Bobaru, *CORROSION*, **74**, 393–414 (2017).
52. J. Newman and K. E. Thomas-Alyea, *Electrochemical Systems*, John Wiley & Sons (2004).
53. S. Sarkar and W. Aquino, *Electrochimica Acta*, **56**, 8969–8978 (2011).
54. K. C. Stewart, University of Virginia, VA, *Ph.D. Dissertation* (1999)
55. R. Ambat, N. N. Aung, and W. Zhou, *Corrosion Science*, **42**, 1433–1455 (2000).
56. G. Baril, C. Blanc, and N. Pébère, *J. Electrochem. Soc.*, **148**, B489–B496 (2001).
57. R. G. Buchheit, J. P. Moran, and G. E. Stoner, *CORROSION*, **46**, 610–617 (1990).
58. M. Shao, Y. Fu, R. Hu, and C. Lin, *Materials Science and Engineering: A*, **344**, 323–327 (2003).
59. P. Campestrini, E. P. M. van Westing, H. W. van Rooijen, and J. H. W. de Wit, *Corrosion Science*, **42**, 1853–1861 (2000).

60. R.G. Buchheit, R.P. Grant, P.F. Hlava, B. Mckenzie and G.L. Zender, *J. Electrochem. Soc.*, **144**, 2621-2628 (1997)
61. N. Birbilis, M. K. Cavanaugh, and R. G. Buchheit, *Corrosion Science*, **48**, 4202–4215 (2006).
62. S. Jain, M. L. C. Lim, J. L. Hudson, and J. R. Scully, *Corrosion Science*, **59**, 136–147 (2012).
63. M. L.C. Lim, R. G. Kelly, and J. R. Scully, *CORROSION*, **72**, 198–220 (2015).
64. J.-B. Jorcin, C. Blanc, N. Pébère, B. Tribollet, and V. Vivier, *J. Electrochem. Soc.*, **155**, C46–C51 (2008).
65. N. Murer, N. A. Missert, and R. G. Buchheit, *J. Electrochem. Soc.*, **159**, C265–C276 (2012).
66. K. B. Deshpande, *Electrochimica Acta*, **56**, 1737–1745 (2011).
67. J. Xiao and S. Chaudhuri, *Electrochimica Acta*, **56**, 5630–5641 (2011).
68. L. Yin, Y. Jin, C. Leygraf, and J. Pan, *Electrochimica Acta*, **192**, 310–318 (2016).
69. L. Yin, Y. Jin, C. Leygraf, N. Birbilis, and J. Pan, *J. Electrochem. Soc.*, **164**, C75–C84 (2017).
70. L. Yin, Y. Jin, C. Leygraf, and J. Pan, *J. Electrochem. Soc.*, **164**, C768–C778 (2017).
71. Y. Wang, L. Yin, Y. Jin, J. Pan, and C. Leygraf, *J. Electrochem. Soc.*, **164**, C1035–C1043 (2017).
72. K. B. Deshpande, *Corrosion Science*, **52**, 2819–2826 (2010).
73. K. B. Deshpande, *Corrosion Science*, **52**, 3514–3522 (2010).
74. D. Trinh, P. Dauphin Ducharme, U. Mengesha Tefashe, J. R. Kish, and J. Mauzeroll, *Anal. Chem.*, **84**, 9899–9906 (2012).
75. A. D. King, J. S. Lee, and J. R. Scully, *J. Electrochem. Soc.*, **163**, C342–C356 (2016).
76. F. Cui, F. J. Presuel-Moreno, and R. G. Kelly, *Corrosion*, **62**, 251–263 (2006).
77. F. Thébault, B. Vuillemin, R. Oltra, K. Ogle, and C. Allely, *Electrochimica Acta*, **53**, 5226–5234 (2008).
78. F. J. Presuel-Moreno, M. E. Goldman, R. G. Kelly, and J. R. Scully, *J. Electrochem. Soc.*, **152**, B302–B310 (2005).
79. S. R. Cross, R. Woollam, S. Shademan, and C. A. Schuh, *Corrosion Science*, **77**, 297–307 (2013).

80. S. R. Cross, S. Gollapudi, and C. A. Schuh, *Corrosion Science*, **88**, 226–233 (2014).
81. S. R. Cross and C. A. Schuh, *Corrosion Science*, **116**, 53–65 (2017).

2. Verification of the Robustness of Laplace-Equation Based Modeling into Corrosion Prediction

Summary:

In this chapter, the robustness of Laplace-Equation based FEM modeling was verified by investigating the galvanic corrosion between a zinc plate and stainless steel (SS) 316L rods. The purpose of using zinc as anode materials is two-fold: (1) zinc is the principal alloying element of 7xxx series Al alloy; (2) Al and Al alloys are prone to localized corrosion in chloride containing solution, whereas zinc generally experiences uniform corrosion which can make the post corrosion damage easier to measure and easily perform direct comparison with modeling prediction. In this work, the effect of electrolyte layer thickness, solution conductivity as well as geometric spacing between SS rods on the corrosion current distribution was investigated, the modeling prediction was also compared with experimental results from laboratory scale salt fog test to back calculate the electrolyte layer thickness assuming a constant thin electrolyte layer was maintained on the surface during the exposure. Analysis of the effect of types of boundary conditions on the modeling predictions was examined to demonstrate that the robustness of Laplace-Equation based modeling is highly dependent on the use of accurate boundary conditions.

The work presented in this chapter has been reported in the following publication:

- **C. Liu**, G. Kubacki, and R.G. Kelly, “Application of Laplace-Equation Based Modeling into Corrosion Damage Prediction for Galvanic Couple between Zn Plate and Stainless Steel Rods under a Thin Film Electrolyte”, Accepted by *Corrosion*.

2.1 Abstract

Connections between dissimilar materials are frequently encountered in aviation and marine structures. When two types of materials are exposed to a moist atmospheric condition, there is a high possibility that a corrosion cell can be established due to galvanic coupling via the creation of either a droplet or a thin film electrolyte. Experimental measurements under such conditions are challenging. Computational modeling can complement experimental characterization to achieve a better understanding of corrosion susceptibilities and the dependence on external variables in atmospheric conditions. In this work, a finite element modeling approach based on the Laplace Equation with mathematically fitted electrochemical kinetics from experiment was developed to simulate electrochemical and corrosion distributions along a Zn plate with inserted SS rods under thin film electrolyte conditions. Modeling results were then compared with accelerated exposure testing results to demonstrate the ability of Laplace-Equation based modeling to predict corrosion damage under thin electrolyte conditions. Comparison of modeling and measurement of damage along the Zn plate and showed the electrolyte layer thickness was about 3,500~4,000 μm on the surface during modified ASTM B117 test assuming a constant thin electrolyte layer was maintained on the surface during the exposure.

2.2 Hypothesis

Laplace-Equation based approach can accurately predict corrosion damage from experiment, as long as boundary conditions are bounded by well-defined solution chemistry, electrolyte layer thickness, as well as geometries of anode and cathode.

2.3 Introduction

Connections between dissimilar materials are frequently encountered in aviation and marine structures, and thus there is an increase in the likelihood of galvanic corrosion when an ionically conductive solution is present. There have been extensive experimental investigations of galvanic corrosion between dissimilar metals or alloys, but many of them used full immersion conditions to simulate an atmospheric corrosion environment. This approach may fail to fully capture the important characteristics of atmospheric exposures. Atmospheric corrosion is a complicated phenomenon affected by multiple external variables¹ (e.g., relative humidity, solution chemistry, electrolyte layer thickness/droplet size), and when galvanic coupling with a complicated geometry is involved, conventional experimental characterization on galvanic-couple-induced atmospheric corrosion is difficult.

Computational modeling can be combined with experimental characterization to increase the understanding of the dependence of the corrosion susceptibility on external variables. This complementary computational and experimental approach quantifies the important characteristics that control corrosion rate and resultant corrosion morphology. There are several computational modeling approaches available for corrosion studies, but among these, the finite element method (FEM) has been most widely used to study potential and current distributions, as well as transport phenomena in corroding systems^{2,3}. There are two prevailing approaches in FEM-based corrosion modeling which are differentiated based on the governing equation used: the Nernst-Planck Equation or the Laplace Equation. The Nernst-Planck Equation takes into account all the contributions from diffusion, migration and convection. The solution to Nernst-Planck Equation results in a full transient expression of the distributions of concentration, potential, and current, but at the cost of very long processing time and increases computational complexity. Recent work⁴

⁹ has demonstrated the utility of the use of Laplace's Equation in the modeling of electrochemical distributions by coupling it with experimentally-derived electrochemical kinetics as boundary conditions along with estimations of the electrolyte conductivity. However, the accuracy of numerical solutions by Laplace Equation needs to be assessed for predicting realistic experimental results.

Stainless steel (SS) is a typical cathode material involved in a number of galvanic coupling systems such as aluminum alloy (AA)/ SS¹⁰⁻¹³, zinc (Zn)/SS^{14,15}, and magnesium alloy /SS¹⁶⁻¹⁸. Especially for AA/SS or Zn /SS galvanic couple, the galvanic coupling potential is usually located at the cathodic mass-transfer-limited region of SS based on the Mixed Potential Theory assuming cathode-to-anode area ratio is 1:1^{4,19}, which implies cathodic diffusional kinetics of oxygen reduction reaction (ORR) for noble SS can further impact the degree of galvanic corrosion if corrosion exposure environment can affect mass transfer of dissolved oxygen in the electrolyte. Zinc (Zn) is an electrochemically-active metal material which generally experiences uniform corrosion when coupled with noble materials in saline solutions, leading to corrosion damage that is more straightforward to assess as compared to materials such as aluminum alloys which are prone to localized corrosion. There have been a number of reported studies focusing on exploring the electrochemical, chemical and corrosion distributions for Zn/noble material couples. Tahara *et al.*²⁰ utilized a Kelvin probe to measure the potential distribution along the Zn/SS couple under a thin layer of electrolyte, and they found that the effective galvanic corrosion distance along the Zn away from the Zn/SS interface was proportional to electrolytic resistance and water layer thickness. Tada *et al.*^{21,22} developed both [Zn²⁺] and pH sensors to determine [Zn²⁺] and pH distributions along a Zn/Steel couple in 0.01M NaCl. Simões *et al.*¹⁵ applied both the scanning vibrating electrode technique (SVET) and the scanning electrochemical microscope (SECM) to investigate

current distribution along a Fe-Zn cell. As for modeling efforts, Lee²³ used the Laplace Equation to solve for the potential distribution along the Zn/SS galvanic couple interface under a thin layer electrolyte and concluded that the degree of corrosion is affected by electrolyte thickness, conductivity, and the properties of surface.

The objective of this study is to assess the application of the Laplace Equation for the prediction of potential, current, and corrosion distributions along a Zn plate with SS rods in the plate under a controlled simulated thin layer electrolyte. The galvanic corrosion as a function of electrolytic conductivity, electrolyte layer thickness, and spacing between two adjacent SS rods has been evaluated numerically. Experimentally determined kinetics of each material serve as boundary conditions. ASTM B117 testing for Zn plate/SS rods galvanic couple followed by optical profilometry was conducted to utilize the numerically predicted results to estimate the electrolyte layer thickness during a modified ASTM B117 testing. The effect of types of boundary conditions on the modeling prediction was also investigated to demonstrate the robustness of Laplace-Equation based modeling approach is highly dependent on the use of appropriate boundary conditions.

2.4 Experimental Procedure

2.4.1 Mathematical Development

In a dilute electrolyte, the current density can be expressed as²⁴

$$i = -F \sum_j z_j D_j \nabla c_j - F^2 \nabla \phi \sum_j z_j^2 u_j c_j + Fv \sum_j z_j c_j \quad (2.1)$$

diffusion
migration
convection

where c_j is the concentration of species j , D_j is the diffusivity of species i , z_j is the charge number of species j , F is Faraday's constant, ϕ is the electric potential, u_j is the electrochemical potential of species j , and v is the fluid velocity.

Three assumptions are typically made in order to simplify the solution to this equation. The first is electroneutrality, which is shown in Equation 2.2:

$$\sum_{j=1}^n z_j c_j = 0 \quad (2.2)$$

The second assumption is that the migration term overwhelms diffusion term in Equation 1, and finally, there is no convection motion in bulk solution. Hence, Equation 2.1 is simplified to Equation 2.3:

$$i = -\kappa \nabla \phi \quad (2.3)$$

where conductivity (κ) = $F^2 \sum_j z_j^2 u_j c_j$. By enforcing the conservation of charge (Equation 2.4),

$$\nabla \cdot i = 0 \quad (2.4)$$

the Laplace Equation can be obtained, which is the governing equation used in the modeling framework

$$\nabla \phi^2 = 0 \quad (2.5)$$

2.4.2 Model Implementation

A Workstation with Quad-core processor and 8 GB of RAM was used to perform the mathematical modeling in this work. The Secondary Current Distribution Module at steady state

in COMSOL™ Multiphysics software (version 5.3a) was applied to calculate electrochemical distributions in the simulated geometry of the galvanic couple. The modeling domain of interest is the electrolyte only. Two objectives were the focus of the modeling: (1) to investigate the influence of solution parameters (electrolyte layer thickness and solution conductivity) and geometric parameters on electrochemical distributions along the galvanic couple surface; (2) to compare the modeling results with those from exposure testing to demonstrate the application of the Laplace Equation for corrosion distribution prediction. Two configurations were used in the first modeling category. A single SS rod was set at the center of the Zn plate in Configuration 1, whereas two SS rods were set at the center and side of the plate in Configuration 2. The details of dimensions of two configurations are shown in Figure 2.1. The electrolyte layer thickness ranged from $5\text{E-}3$ cm ($50\ \mu\text{m}$) to 0.4 cm, and solution conductivity ranged from 0.5 S/m to 5.5 S/m. For spacing between the centers of two SS rods in Configuration 2, three different values were chosen: 1.5cm (short), 2.5cm (medium), and 4cm (long). Electrochemical kinetics of the Zn and SS were mathematically fitted to facilitate the boundary condition implementation. Anodic kinetics of Zn was applied on the Zn plate as the boundary condition, whereas the cathodic kinetics of SS was applied on the SS rod(s) as the boundary condition for those areas.

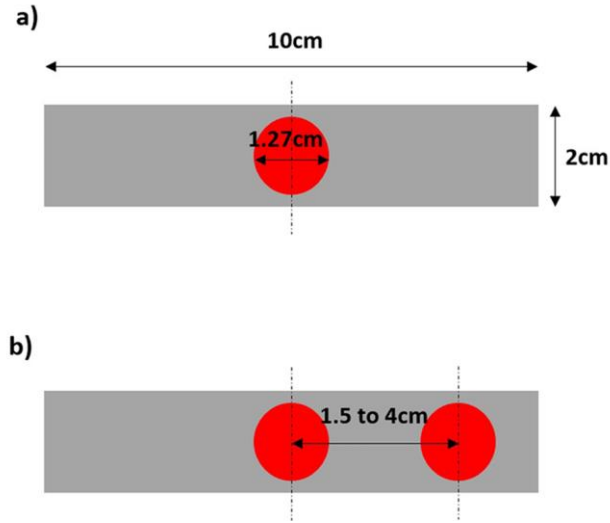


Figure 2.1: Configurations of two types of Zn/SS galvanic couple: a) SS rod in center of Zn plate in Configuration 1; b) Two SS rods (one stayed in center) with spacing equal to 1.5, 2.5 and 4cm respectively in Configuration 2.

2.4.3 Electrochemical Kinetics

Stainless steel (SS) UNS S31600 (composition shown in Table 2.1) and 99.9%wt pure Zn were used in this work. They were prepared into 2cm x 2cm square coupons and ground to a surface finish of 600 grit with silicon carbide paper. All the electrochemical measurements were conducted using a Bio-Logic™ SP200 potentiostat in a three-electrode cell configuration with a SS (or Zn) coupon as the working electrode (WE, exposure area=1cm²), a platinum-niobium mesh as the counter electrode (CE), and a saturated calomel electrode (SCE) as the reference electrode (RE). Potentiodynamic polarization measurements were performed at a scan rate= 0.167 mV/s after 1-hour open circuit potential (OCP) stabilization. For SS, the scan started 100 mV above OCP before reaching the final potential of -1400 mV_{SCE}; for Zn, the scan began 100 mV below OCP and ended at 300 mV above OCP. Two types of solutions were tested at 35°C: 0.6M NaCl, and 0.6M NaCl + 0.04M K₂S₂O₈. The latter solution with potassium persulfate added was used to accelerate the galvanic corrosion rate in the salt spray testing described in the following subsection.

Table 2.1: Nominal composition of UNS S31600 alloy (wt%)

Element Present									
Composition	C	Mn	Si	P	S	Cr	Ni	N	Fe
Avg. Mass%	0.08	2.0	0.75	0.045	0.03	20.0	10.5	0.1	balance

2.4.4 Modified ASTM B-117 Salt Fog Testing

Zn/SS galvanic couples in Configuration 1 with surface finish equal to 320 grit were tested in the experiment. Optical microscope was used to ensure that no crevice appeared in the interface between SS rod and the Zn surrounding. All the test samples were horizontally placed in the slots of test rack in a salt fog testing chamber, with a tilt angle equal to 30 degree with respect to the rack bottom.

A modified salt fog test was utilized in which the testing solution was 0.6M NaCl with addition of 0.04M $K_2S_2O_8$ and the temperature was set at 35°C. A 96hr test with constant salt spray was conducted with a 5-minute interruption every 24hrs to remove accumulated corrosion products. During this interval, testing specimens were sonicated in ammonium persulfate solution (10 wt%) for 1 minute to remove the majority of the corrosion products accumulated on the Zn plate. The purpose of this treatment was to mitigate the effect of corrosion products on the thin film electrolyte layer on the testing specimens, and to maintain a relatively uniform testing solution composition on the specimen surfaces during the entire testing period. The testing samples were thoroughly cleaned with 10wt% ammonium persulfate solution for 5mins and rinsed with DI water at the end of the salt fog testing. The corrosion damage was then measured using Zygo NewView™ 7300 Optical Surface Profiler.

2.5 Results and Discussions

2.5.1 Electrochemical Kinetics of SS and Zn

Polarization curves of both Zn and SS were mathematically fitted using EC-lab software (Ver.11.01) shown in Figure 2.2. For Zn, only anodic kinetics portion was taken into account from E_{corr} to $-0.95 V_{\text{SCE}}$. As for SS the fitted region started from $-0.3 V_{\text{SCE}}$ down to $-1.4 V_{\text{SCE}}$. This fitting allowed the removal of the effects of uncompensated IR drop during the generation of the Zn polarization curve at high current density as well as allowing representation of mass transfer limited cathodic kinetics of SS as a function of thin film electrolyte layer thickness. Specifically, the cathodic limiting current density ($i_{\text{lim},WL}$) was determined via Equation 2.6, by knowing the value in quiescent solution from the original curve

$$\frac{i_{\text{lim},\text{quiescent}}}{i_{\text{lim},WL}} = \frac{WL}{800\mu\text{m}} \quad (2.6)$$

where a reduction in the electrolyte layer thickness on the SS surface increases the pertinent $i_{\text{lim},WL}$. Actually, $i_{\text{lim},WL}$ is proportional to reciprocal of WL according to Fick's 1st Law,

$$i_{\text{lim},WL} = \frac{nFDC_{O_2,\text{bulk}}}{WL} \quad (2.7)$$

but $800 \mu\text{m}$ was chosen for the critical natural convection diffusional layer thickness for quiescent solution due to the inevitable natural convection phenomenon in thick electrolyte films^{1,25}. The determination of this value has been discussed elsewhere⁴. The net result of the natural convection limit is that the dependence of the diffusion limited current density can be described by Fick's 1st Law as long as WL is smaller than $800\mu\text{m}$, whereas it is a constant regardless of WL thickness above that value. It should be also noted that only mass transfer limited cathodic kinetics of SS in terms of ORR were fitted and extrapolated since the activation region of ORR is not affected by

the WL. These fitted and extrapolated electrochemical kinetics of Zn and SS were assigned as anodic (Zn) and cathodic (SS) boundary conditions in the modeling work.

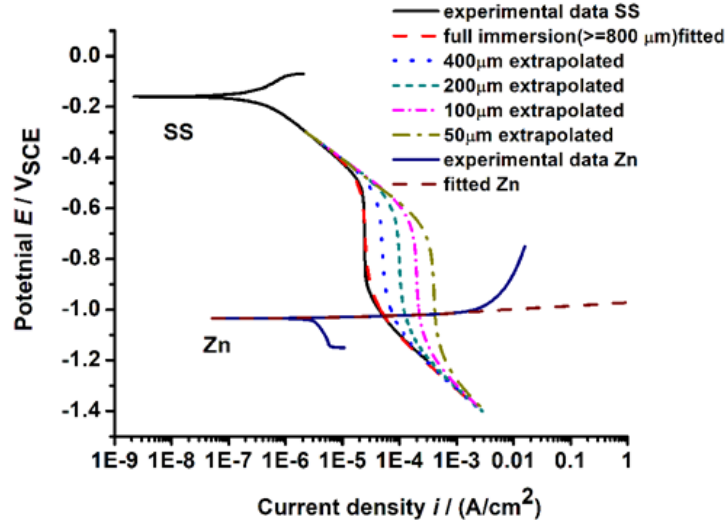


Figure 2.2: Original and fitted polarization curves of SS and Zn for 0.6 M NaCl.

2.5.2 Modeling Studies to Investigate the Effect of Pertinent Parameters

2.5.2.1 Geometric Parameters

In this subsection, the effects of spacing and the number of SS rods are addressed. For this portion of the work, the WL was set equal to 800 μm and was uniformly distributed across the galvanic couple surface. The conductivity was set to 5.5 S/m. In Configuration 1, the peak current density is at the SS/Zn interface, as expected, with the current density decreasing towards a steady state with increasing distance. This steady state is due to the high conductivity and thickness of the WL. A comparison of dissolution current density distribution away from the center of centric SS rod (center of Zn plate) along the Zn plate, between Configuration 1 and Configuration 2 with three different spacings is shown in Figure 2.3. When a second SS rod was introduced (Configuration 2), the average dissolution current density between the two SS rods increased relative to Configuration 1. As the spacing between the two SS rods decreased, the average

dissolution current density became more intensified, implying the most severe corrosion damage would appear between the two SS rods in the short spacing scenario. Furthermore, the decay in current density away from the Zn/SS interface within the spacing was steeper as the spacing became longer. The peak current density appeared at Zn/SS interface and did not change significantly when the spacing changed from 4 cm to 2.5 cm, and then rose up when the spacing shrank to 1.5 cm, which was nearly 1.5 times that for medium or short spacing scenario.

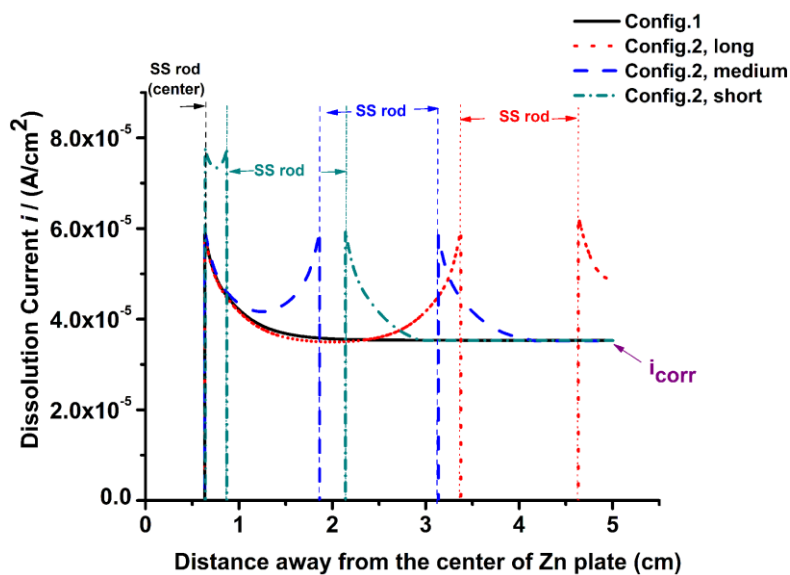


Figure 2.3: Comparison of current density distribution between Configuration 1 and Configuration 2 with three different spacing.

2.5.2.2 Electrolyte Parameters

Solution conductivity and electrolyte layer thickness (WL) are the two main electrolyte parameters studied in this subsection. An assumption was made under which electrolytic conductivity is independent of the concentration of solution (fixed at 0.6M NaCl during the simulation). Although it is not physically true since solution conductivity is a function of solution chemistry, the purpose of this study is to concentrate on the effect of solution conductivity on the

potential and current density distributions in the galvanic coupling, making this assumption reasonable for a decent range of solution conductivity which was from 0.5 to 5.5 S/m.

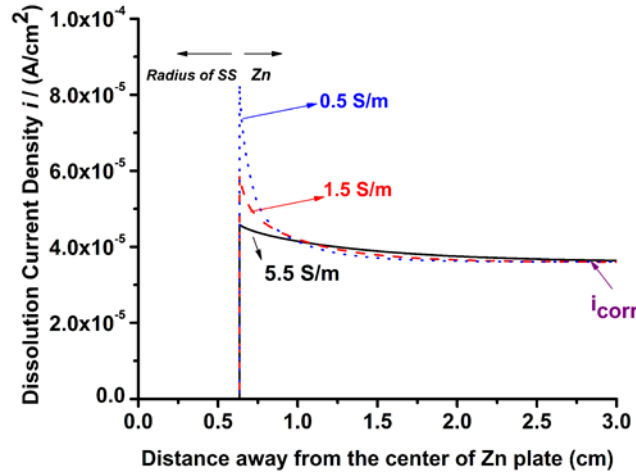


Figure 2.4: Current density distributions as a function of solution conductivities for $WL=4,000 \mu\text{m}$

For Configuration 1, the current density distribution as a function of solution conductivity for two different WL s is shown in Figure 2.4 ($4,000 \mu\text{m}$) and Figure 2.5 ($50 \mu\text{m}$) respectively. When $WL=4,000 \mu\text{m}$, the lowest solution conductivity (0.5 S/m) resulted in the highest peak current density at the SS/Zn interface, with the current density decaying sharply with distance from the interface, compared to a more sluggish decay when the conductivity was equal to 5.5 S/m, the peak current density for 0.5 S/m was almost twice that for 5.5 S/m. Whereas when $WL=50 \mu\text{m}$ (Figure 2.5), the highest peak current density (0.5 S/m) was more than four times that for 5.5 S/m, a sharper drop in current density occurred, and the large dissolution current density was constrained to a shorter distance away from the interface compared to $WL=4000 \mu\text{m}$, implying that larger ohmic resistance brought by thinner WL electrolyte layer resulted in more severe corrosion attack focused at the interface before decaying dramatically, and the corrosion attack at the interface became more obvious at lower solution conductivity.

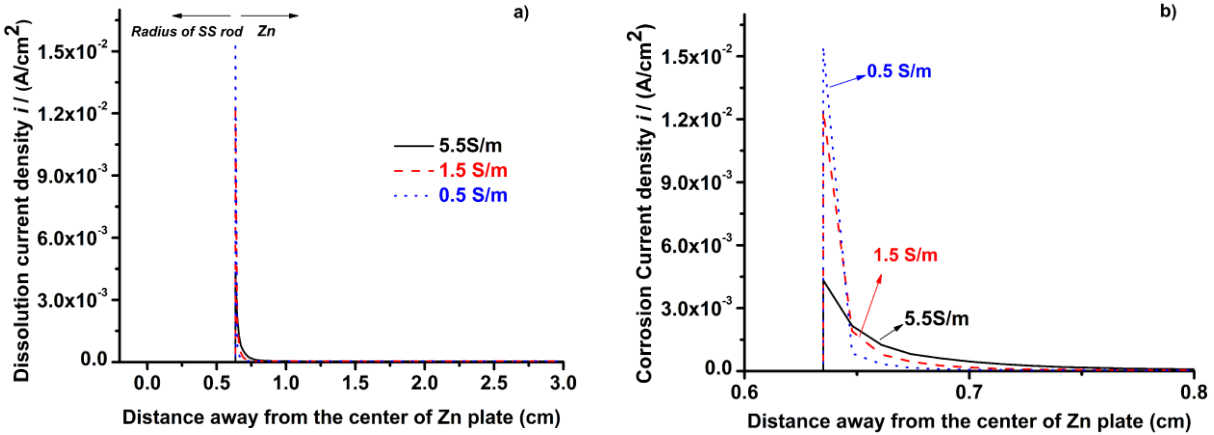


Figure 2.5: a) current density distributions as a function of solution conductivities for $WL=50\mu\text{m}$; b) zoom-in of Figure 2.5a at the interface area.

As for Configuration 2, the case of short spacing was analyzed. A comparison of current density distributions as a function of WL s for two different solution conductivities is shown in Figure 2.6a & b. For a solution conductivity of 5.5 S/m, a flat current density distribution between the two SS is observed, and the average current density increased mildly as WL decreased from 4,000 μm to 800 μm . As the WL decreased from 800 μm to 50 μm , a non-uniform current density distribution appeared in which peak current density was at Zn/SS interface and a minimum in current density was at the center of the spacing. Overall, the minimum current density increased as the WL decreased for a conductivity of 5.5 S/cm. However, when conductivity was decreased to 0.5 S/m, although the peak current densities at the Zn/SS interface were all higher than those under 5.5 S/m, the minimum current density decreased with decreasing WL from 200 to 50 μm , resulting in a lower minimum for $WL=50\mu\text{m}$ than for $WL=4,000\mu\text{m}$. This phenomenon indicates that although lower WL resulted in enhanced cathode delivery capacity of SS rod (due to higher diffusion limited cathodic current densities) which intensified corrosion damage at the Zn/SS interface, the high ohmic resistance due to a thin WL and low solution conductivities prevented the cathode from delivering current far from the interface. This situation can be confirmed from the comparison of current density distributions as a function of solution conductivity for $WL=4,000$

μm and $50 \mu\text{m}$ respectively (Figure 2.6c &d). Both the peak current density and the minimum current density increased as the solution conductivity decreased when $WL=4,000 \mu\text{m}$, whereas when $WL=50 \mu\text{m}$, the minimum current density as well as average current density decreased as conductivity decreased.

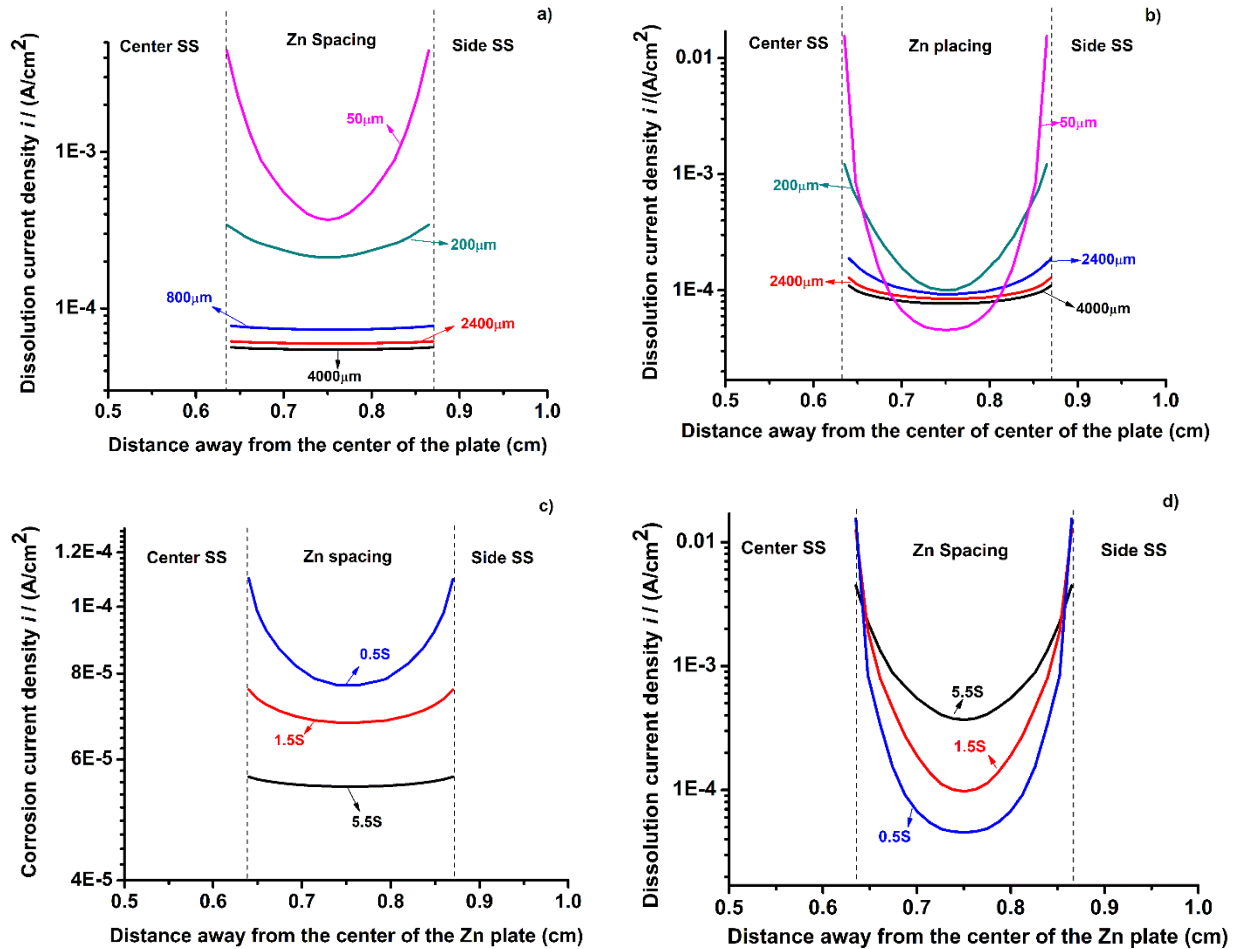


Figure 2.6: Comparison of current density distributions for: a) 5.5 S/m and b) 0.5 S/m as a function of WL s; for c) $WL=4,000$ and d) $WL= 50 \mu\text{m}$ as a function of conductivities.

2.5.2.3 Combined Effect of SS Rod Spacing and WL

To explore the combined effects of geometric and electrolyte parameters on the galvanic corrosion damage, an example will be discussed in this subsection to demonstrate how spacing between two SS rods and WL affected the average dissolution current density between the two rods

in Configuration 2. The definition of average current density is the integral of current density along the length of the Zn spacing divided by the total length of the Zn spacing. The solution conductivity was set at 5.5 S/m. It should be noted that the long, medium and short spacing were assigned to be 4, 2.5 and 1.5 cm specified previously. A comparison of average current densities as a function of WL for three different spacings is shown in Figure 2.7. Under the same WL , the average current density increased with reduced spacing due to the more effective interaction between Zn/SS brought by the shortened ohmic resistance distance (spacing), the degree of this increase became more significant as WL decreased below $800\ \mu\text{m}$, owing to enhanced cathodic kinetics of SS rod brought by enhanced mass transfer of oxygen. For the same spacing, an almost constant average current density was found for the long spacing above $800\ \mu\text{m}$. It then rose gradually as the WL kept decreasing. The medium spacing experienced a similar change in average current density, except that average current density started to increase once WL was thinner than $2400\ \mu\text{m}$. For the short spacing, the average current density increased for all decreased WL , and the degree of increase was more dramatic once WL was below $800\ \mu\text{m}$. It can be concluded that the lowest electrolytic ohmic resistance from short spacing resulted in more interaction between two SS rods and the Zn portion in between, and the galvanic corrosion became more significant as WL went below $800\ \mu\text{m}$, thanks to the enhanced mass transfer limited cathodic kinetics from SS cathode to provide more cathode current to maintain the corrosion of Zn.

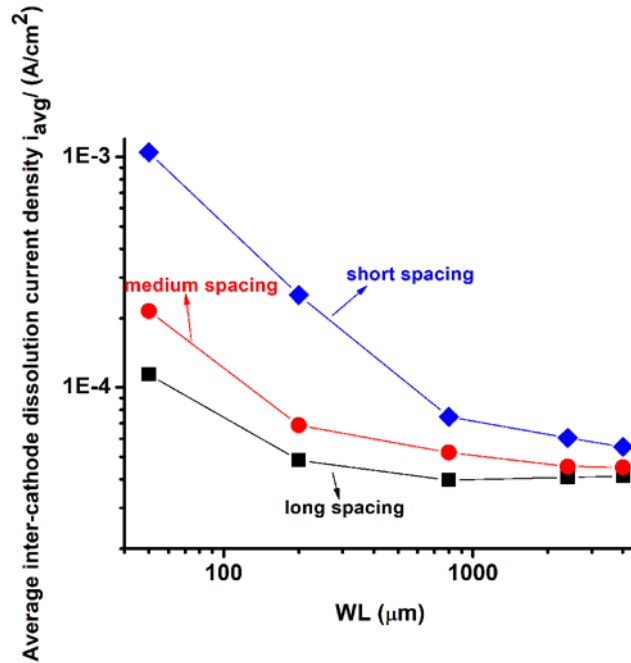


Figure 2.7: A comparison of average inter-cathode dissolution current densities as a function of WLs for three different spacings.

2.5.2.4 Cathode Current Availability

This subsection focuses on the effect of cathode current availability from SS rod on the galvanic corrosion. Changes in cathode kinetics could occur due to a change in the surface property of SS, or the presence of corrosion products, or an insulating coating. To assess such effects, a comparison of Zn dissolution current map on the plate from the top view is shown in Figure 2.8, in which the cathode current from SS was reduced from 100% (Figure 2.8a) to 50% (Figure 2.8b), and 10% (Figure 2.8c) of its original value. The WL was set equal to 200 μm , and solution conductivity was set to be 5.5 S/m. It can be seen that: for Configuration 2 with a short spacing =1.5cm between the SS, as the cathode current availability decreased, the interaction between Zn and SS rods within the spacing become disconnected. The reduced cathode current delivery capacity hence made the effective area ratio of cathode to anode smaller than the one with full current delivery capacity, resulting in less corrosion-attacked phenomenon taking place at the Zn/SS interface. Although the IR drop between two cathodes became smaller which would have

led to more galvanic corrosion in between because of reduced IR, the effect of significant reduction in cathodic current availability overwhelmed the reduced IR drop effect which made the area and degree of galvanic corrosion dramatically decreased. This also implied that a corrosion product build-up as well as protective coatings on the cathode can actually mitigate the corrosion damage.

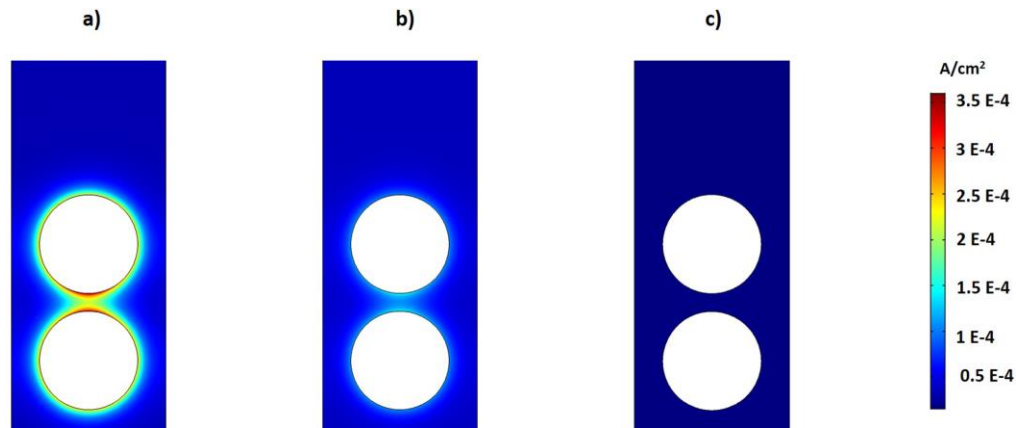


Figure 2.8: Comparison of Zn dissolution current map on the plate in terms of cathode current availability on SS from a): 100%, to b): 50% and c): 10%. In this comparison, WL=200 μm , spacing= 1.5 cm and solution conductivity= 5.5 S/m.

2.5.3 Comparison of Results between Salt Fog Testing and Modeling Prediction

In order to validate the application of the Laplace's Equation based modeling work to corrosion damage distribution prediction, the corrosion damage occurring on the Zn surface near the SS rods after 96 hrs. salt fog testing was compared to the modeling results in Configuration 1. The main goal of this comparison is to back calculate the estimated electrolyte layer thickness during B-117 test through modeling approach, due to the technical difficulty of monitoring and measuring the real electrolyte layer thickness during the experimental test.

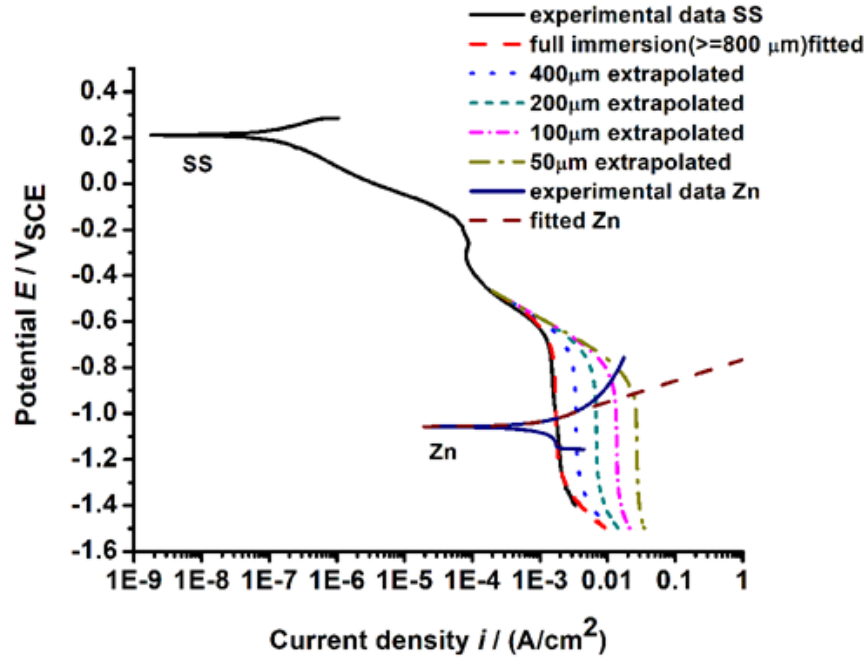


Figure 2.9: Original and fitted polarization curves of SS and Zn in 0.6M NaCl+0.04M $K_2S_2O_8$ solution.

Modeling work in this section used electrochemical kinetics of Zn and SS in 0.6M NaCl+0.04M $K_2S_2O_8$ as new boundary conditions which are shown in Figure 2.9. It can be seen that in quiescent solution, the mass transfer limited cathodic current density was about 100 times that observed in 0.6 M NaCl solution, which is the main reason why persulfate species was added into NaCl solution as it would be expected to accelerate the galvanic corrosion damage during 96hrs salt spray testing so as to obtain measurable corrosion damage on the Zn plate. In the simulation, a parametric sweep in terms of WL from 4 mm to 50 μm at a fixed conductivity of 5.5 S/m was performed to obtain a series of dissolution current density distributions and then found out under what WL the modeling result matched well with experimental results.

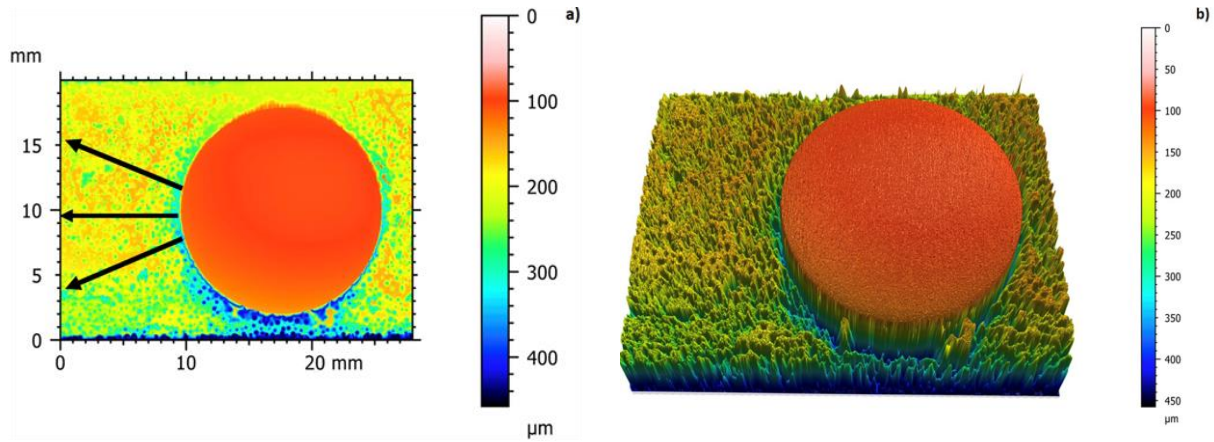


Figure 2.10: a) Top view and b) 3D view of corrosion morphology in the vicinity of Zn/SS interface measured by Zygo optical profilometer for samples with Configuration 1 after modified B-117 Test.

The resultant top view and 3D view of corrosion depth distribution of Zn plate in the vicinity of center SS rod were shown in Figure 2.10. A comparison of corrosion depth distributions for three samples which were obtained by averaging the depth distributions along the three directions in each sample (shown in Figure 2.10a) was displayed in Figure 2.11a. The average corrosion depth profile based on measurements from these three samples then compared with modeling results, in which current density profiles were converted into corrosion depth profile using Faraday's Law

$$\frac{iM_{Zn}t}{n\rho_{Zn}F} = x \quad (2.8)$$

where i is the current density, M_{Zn} is the molar mass of Zn ($M_{Zn} = 65.38$ g/mol), n is the number of electron transferred ($n=2$), t is the exposure time ($t=4*24*3600=345,600$ s), ρ_{Zn} is the density of Zn ($\rho_{Zn}=7140$ kg/m³), F is the Faraday's constant ($F=96,485$ C/mol), and x is the corrosion depth. The comparison is shown in Figure 2.11b. From the modeling prediction, the corrosion depth distribution at each WL decreased quickly from the SS/Zn interface until approximately 0.1cm, and then kept decreasing slowly afterwards. A zoom-in of Figure 2.11b focusing on the

first 0.1cm away from the interface is available in Figure 2.11c. It is shown that experimental result falls within the range of simulated results between $WL=3,000 \mu\text{m}$ and $4,000 \mu\text{m}$. To find the appropriate WL range, residual analysis is performed between experimental results and simulated results when $WL=3,000 \mu\text{m}$, $3,500 \mu\text{m}$ and $4,000 \mu\text{m}$ respectively shown in Figure 2.11d. The calculated residual areas based on this figure are: -0.175 m^2 ($WL=3,000 \mu\text{m}$), $-1.28\text{E}-2 \text{ m}^2$ ($WL=3,500 \mu\text{m}$), and 0.109 m^2 ($WL=4,000 \mu\text{m}$) respectively. As a result, $WL=3,500\sim 4,000 \mu\text{m}$ would be the appropriate WL range formed on the sample surface during salt fog testing as it best matches the profile for the majority of the distribution. Close to the interface it is likely that rapid formation of corrosion products limited the attack.

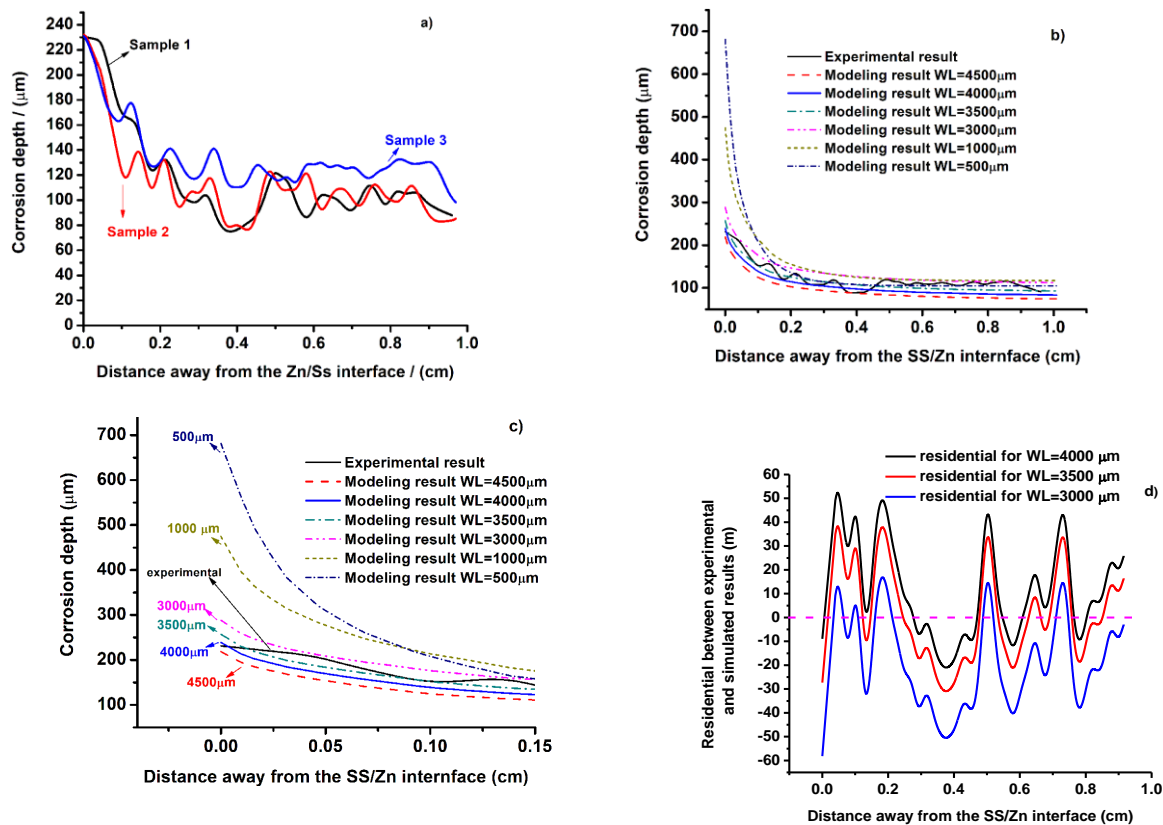


Figure 2.11: a) comparison of corrosion depth distance away the Zn/SS interface from three different samples; b) comparison between experimental and modeling result; c) zoomed in near interface shown in Figure 2.11b; d) residual analysis between experimental results and simulated results when $WL=3,000 \mu\text{m}$, $3,500 \mu\text{m}$ and $4,000 \mu\text{m}$ respectively.

It should be noted that one cannot calculate the exact WL thickness in a simulated B-117 testing environment from the modeling framework in this study since WL is not the direct modeling output, but potential and current density as well as corrosion depth are. Instead, the appropriate WL range pertinent to B-117 environment can be back calculated by matching the experimental results with simulated one under different WL assumptions as shown in Figure 2.11. Since the in-situ measurement of WL above the sample surface during B-117 test is difficult to be achieved experimentally, modeling prediction can provide alternative way to predict WL thickness range, which in turn validates the application of our modeling approach into localized corrosion distribution prediction. Furthermore, the predicted WL range for the modified B-117 test in this study is 3,500~4,000 μm (3.5~4 mm), the rationality that WL thickness is on the order of millimeters during constant salt spray test or even wet-dry cyclic salt spray test can be verified by Skelton and Kelly's work²⁶ (WL~4mm during ASTM B-117 test) and Blohm's work²⁷ (WL~4mm during modified ASTM G85 test involving wet-dry cycling).

2.5.4 Evaluation of the Effect of Boundary Conditions on the Modeling Predictions

Besides the actual electrochemical response of materials to the testing solution (experimentally determined electrochemical kinetics) as boundary conditions in the FEM based corrosion modeling, one can also use equation-based electrochemical kinetics as boundary conditions such as Butler-Volmer-Equation²⁸⁻³⁰, and linear electrode kinetics³¹. This discussion is aimed to illustrate that inappropriate estimation of electrode kinetics as boundary conditions can lead to a false prediction of corrosion damage largely different from one based on experimentally determined electrode kinetics.

In previous section, experimentally determined electrochemical kinetics of SS316L as well as Zn in 0.6M NaCl+0.04M $\text{K}_2\text{S}_2\text{O}_8$ solution were used as cathodic and anodic boundary

conditions in the modeling work to simulate corrosion damage distribution along the distance away from the Zn/SS interface in Configuration 1. Here Butler-Volmer Equation and linear electrode kinetics were both applied to estimate the kinetics of SS316L compared to the experimentally determined one. For Butler-Volmer Equation, the response of current density to the applied potential is

$$i = i_o \left\{ \exp \left[\frac{\alpha_a n F (E - E_{corr})}{RT} \right] - \exp \left[\frac{-\alpha_c n F (E - E_{corr})}{RT} \right] \right\} \quad (2.9)$$

Or it can be expressed in terms of Tafel form

$$i = i_o \left(10^{\frac{E - E_{corr}}{\beta_a}} - 10^{\frac{E - E_{corr}}{-\beta_c}} \right) \quad (2.10)$$

where i_o is the exchange current density, E_{corr} is the corrosion potential, n is the number of electrons transferred, α_a is the anodic charge transfer coefficient, α_c is the cathodic charge transfer coefficient, β_a is anodic Tafel slope and β_c is the cathodic Tafel slope. As for linear electrode kinetics, one can express it as

$$i = -i_o \frac{F(E - E_{corr})}{RT} \quad (2.11)$$

It should be noted that the evaluation of electrochemical parameters in either Butler-Volmer or linear electrode kinetics is based on the potential region in vicinity of corrosion potential E_{corr} . By utilizing EC-lab software, one can obtain these pertinent electrochemical parameters shown in Table 2.2.

Table 2.2: Electrochemical Parameters Fitted from Experimentally Determined Cathodic Kinetics of SS316L via EC-Lab Software.

Electrochemical Parameters			
i_o	E_{corr}	β_a	β_c
9.4E-9 A/cm ²	0.222 V _{SCE}	138 mV/dec	77.6 mV/dec

By plugging these values into Equation 2.10 and 2.11, the pertinent Butler-Volmer and linear kinetics of SS316L were plotted together with experimentally determined one in Figure 2.12a. Assuming the cathode to anode area ratio was 1:1, one can observe that the galvanic coupling potential (E_{galvanic}) based on Butler-Volmer equation was more positive and led to much higher galvanic corrosion current (i_{galvanic}) than experimentally determined one, whereas E_{galvanic} based on linear kinetics was more negative ($\sim E_{\text{corr}}$ of Zn) which resulted in much lower i_{galvanic} . A comparison of simulation results of corrosion damage distributions away from the Zn/SS interface based on three different cathodic boundary conditions when $WL=3,500 \mu\text{m}$ is shown in Figure 2.12b. It can be clearly seen that: Butler-Volmer-Equation based kinetics extensively overestimated the corrosion damage across the entire length, especially the corrosion depth right at the interface was about $240000 \mu\text{m}$ which was nearly 800 times higher than experimental kinetics; linear kinetics however underestimated the corrosion damage to a large degree such that the corrosion depth at the interface was $0.9 \mu\text{m}$, which was only 0.3% of that for experimental kinetics. Since higher WL leads to shallower corrosion depth and lower WL leads to deeper one as discussed earlier, we increased WL for Butler-Volmer Equation based kinetics to 1m and decreased that for linear kinetics to $1 \mu\text{m}$, however neither of their results became comparable to that for $WL=3,500 \mu\text{m}$ with experimental kinetics which was most relevant to experimental measurement result (Figure 2.12c). From this case study, one can conclude that: the robustness of Laplace-Equation based modeling is highly dependent on the boundary conditions, experimentally determined electrochemical kinetics as boundary conditions can truly reflect the electrochemical response of anode/cathode to the surrounding solution environment, which in turn yields the simulated results mostly close to experimental measurement.

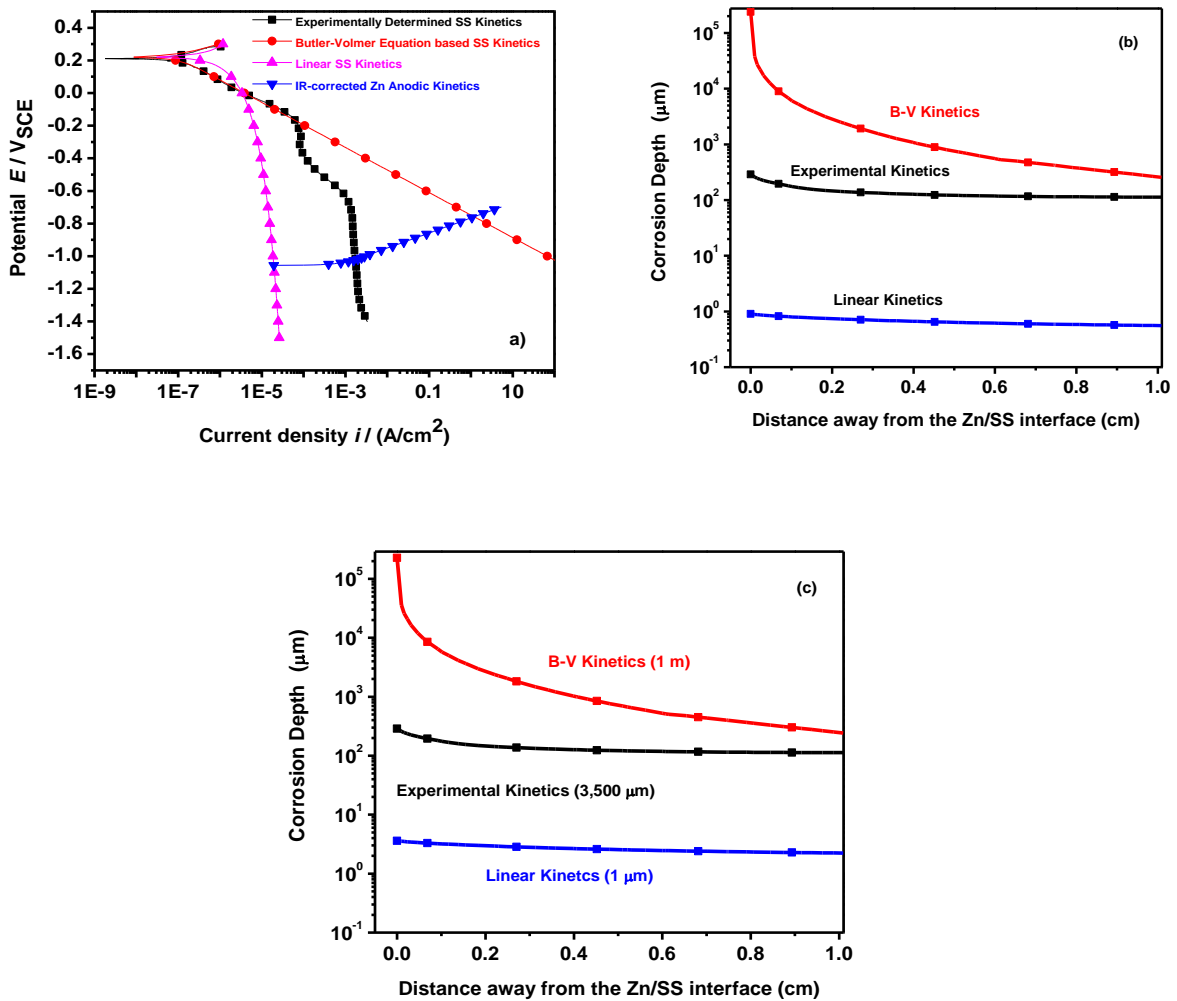


Figure 2.12: a) Comparison of SS316L kinetics in different forms; b) comparison of simulated corrosion depth distributions away from Zn/SS interface in Configuration 1 based on different forms of SS316L cathodic kinetics at the same $WL=3500 \mu\text{m}$; c) comparison of simulated corrosion depth distributions away from Zn/SS interface in Configuration 1: $WL=3500 \mu\text{m}$ for experimental determined kinetics, $WL=1\text{m}$ for B-V kinetics, and $WL=1 \mu\text{m}$ for linear kinetics.

2.6 Conclusions

Laplace-Equation based modeling coupled with mathematically fitted electrochemical kinetics from experiment as boundary conditions was applied to simulate galvanic corrosion between Zn plate and SS 316 rods under thin layer electrolyte condition. The effect of geometric, electrolytic parameters on the corrosion distribution had been examined. The modeling results

were then compared with experimental results from a four-day modified B117 test by adding sodium persulfate to predict the thickness of thin film electrolyte during the test from modeling.

- For geometric parameters, Increasing the number of cathode rod (SS) resulted in higher current density (corrosion) on the anode (Zn) due to higher cathode-to-anode ratio; Shorter spacing between two adjacent SS rods resulted in more severe corrosion damage.
- For electrolytic parameters, the high ohmic resistance due to thin WL and low solution conductivities prevented the cathode from delivering current far away from the interface.
- For a combined effect of both geometric and electrolytic parameters, the lowest electrolytic ohmic resistance from shortest spacing resulted in more interaction between two SS rods and the Zn portion in between, and the galvanic corrosion became more significant as *WL* went below 800 μm , due to the enhanced mass transfer limited cathodic kinetics from SS cathode to provide more cathode current to maintain the corrosion of Zn.
- $WL=3,500\sim 4,000\ \mu\text{m}$ would be the appropriate *WL* range formed on the sample surface during modified B117 salt fog testing.
- The robustness of Laplace-Equation based modeling is highly dependent on the boundary conditions, experimentally determined electrochemical kinetics as boundary conditions can truly reflect the electrochemical response of anode/cathode to the surrounding solution environment, which in turn yields the simulated results mostly close to experimental measurement.

2.7 Acknowledgement

The financial support from Office of Naval Research (ONR) via Grants N00014-14-1-0012 and N00014-17-1-2033, Sea-Based Aviation Program, William Nickerson, Program Manager is gratefully acknowledged. The author also would love to acknowledgement experimental assistance from Dr. Greg Kubacki at the University of Virginia.

2.8 References

1. N.D. Tomashov, "Development of the Electrochemical Theory of Metallic Corrosion", *Corrosion* 20 (1964): p. 7t-14t.
2. C. Liu, V.N. Rafla, J.R. Scully, R.G. Kelly, "Mathematical Modeling of Potential and Current Distributions for Atmospheric Corrosion of Galvanic Coupling in Airframe Components", CORROSION 2015 (Houston, TX: NACE, 2015)
3. C. Liu, R.G. Kelly, " The Use of Finite Element Methods (FEM) in the Modeling of Localized Corrosion", *Electrochemical Society Interface* 23 (2014): p. 47–51.
4. C. Liu., J. Srinivasan, R.G. Kelly, " Electrolyte Film Thickness Effects on the Cathodic Current Availability in a Galvanic Couple", *Journal of Electrochemical Society* 164 (2017): p. C845–C855.
5. F. Thébault, B. Vuillemin, R. Oltra, C. Allely, K. Ogle, " Modeling bimetallic corrosion under thin electrolyte films", *Corrosion Science* 53 (2011): p. 201–207.
6. G. Song, "Potential and Current Distributions of One-Dimensional Galvanic Corrosion Systems " *Corrosion Science*, 52 (2010): p. 455-480.
7. M. Verbrugge," Galvanic Corrosion over a Semi-Infinite Planar Surface", *Corrosion Science* 48 (2006): p. 3489–3512.
8. F. Cui, F.J. Presuel-Moreno, R.G. Kelly, "Experimental and Computational Evaluation of the Protection Provided by an Aluminum Cladding to AA2024-T3 Exposed at a Seacoast Environment", *Corrosion* 62 (2006): p. 251–263.
9. F.J. Presuel-Moreno, H. Wang, M.A. Jakab, R.G. Kelly, J.R. Scully," Computational Modeling of Active Corrosion Inhibitor Release from an Al-Co-Ce Metallic Coating", *Journal of Electrochemical Society* 153 (2006): p. B486–B498.
10. C.A. Matzdof, W.C. Nickerson, B.C. Rincon Troconis, G.S. Frankel, L. Li, and R.G. Buchheit, "Galvanic Test Panels for Accelerated Corrosion Testing of Coated Al Alloys: Part 1—Concept", *Corrosion* 69 (2013): p. 1240-1246.

11. Z. Feng, and G.S. Frankel, " Accelerated Corrosion Testing of Coated Al Alloys: Part 2— Measurement of Galvanic Interaction", *Corrosion* 70 (2013): p. 95-106.
12. Z. Feng, G.S. Frankel, and C.A. Matzdorf. "Quantification of Accelerated Corrosion Testing of Coated AA7075-T6", *Journal of Electrochemical Society* 161 (2014): p. C42-49.
13. V.N. Rafla, A.D. King, S. Glanvill, A. Parsons, A. Davenport, and J.R. Scully, " Operando Observation of Galvanic Corrosion Between Aluminum Alloy 7050-T7451 and 304 Stainless Steel in a Simulated Fastener Arrangement Using X-Ray Tomography". *Corrosion* 71 (2015): p. 1171-1176.
14. X.G. Zhang, "Galvanic Corrosion of Zinc and Its Alloys", *Journal of Electrochemical Society* 143 (1996): p. 1472-1484.
15. A.M. Simões, A.C. Bastos, M.G. Ferreira, Y. González-García, S. González, R.M. Souto, " Use of SVET and SECM to Study the Galvanic Corrosion of an Iron–Zinc Cell", *Corrosion Science* 49 (2007): p. 726–739.
16. J. X. Jia, G.L. Song, and A. Atrens, "Influence of Geometry on Galvanic Corrosion of AZ91D Coupled to Steel", *Corrosion Science* 48 (2016): p. 2133-2153.
17. J.X. Jia, G.L. Song, and A. Atrens, " Experimental Measurement and Computer Simulation of Galvanic Corrosion of Magnesium Coupled to Steel", *Advanced Engineering Materials* 9 (2007): p. 65-74.
18. K.B. Deshpande, " Validated Numerical Modelling of Galvanic Corrosion for Couples: Magnesium Alloy (AE44)–Mild Steel and AE44–Aluminium Alloy (AA6063) in Brine Solution", *Corrosion Science* 52 (2010): p 3514-3522.
19. F. Thébault, B. Vuillemin, R. Oltra, K. Ogle and C. Allely, " Investigation of Self-Healing Mechanism on Galvanized Steels Cut Edges by Coupling SVET and Numerical Modeling", *Electrochimica Acta* 53 (2008): p. 5226-5234.
20. A. Tahara, T. Kodama, " Potential Distribution Measurement in Galvanic Corrosion of Zn/Fe Couple by Means of Kelvin Probe", *Corrosion Science* 42 (2000): p. 655–673.
21. E Tada, K. Sugawara, H. Kaneko, " Potential Distribution Measurement in Galvanic Corrosion of Zn/Fe Couple by Means of Kelvin Probe", *Electrochimica Acta* 49 (2004): p. 1019–1026.
22. E. Tada, E., S. Satoh, H. Kaneko, " The Spatial Distribution of Zn²⁺ during Galvanic Corrosion of a Zn/Steel Couple", *Electrochimica Acta* 49 (2004): p. 2279–2285.
23. J.-M., Lee, " Numerical Analysis of Galvanic Corrosion of Zn/Fe Interface beneath a Thin Electrolyte", *Electrochimica Acta* 51 (2006): p. 3256–3260.

24. J. Newman, K.E. Thomas-Alyea, *Electrochemical Systems* 3rd ed. (Hoboken, N.J.: John Wiley & Sons, 2004).
25. A. Nishikata, Y. Ichihara, Y. Hayashi, T. Tsuru, "Influence of Electrolyte Layer Thickness and pH on the Initial Stage of the Atmospheric Corrosion of Iron", *Journal of Electrochemical Society* 144 (1997): p. 1244–1252.
26. R.J. Skelton, and R. G. Kelly, "Investigation of Galvanic Coupling on AA7075-T6 NAVAIR Plate Inside Fastener Hole", ECS 234th Meeting (Cancun, Mexico: ECS 2018).
27. L.M. Blohm, "Galvanic Coupling of AA5xxx-H116 and CDA 706 Utilizing Laboratory, Outdoor, and Accelerated Testing", University of Virginia, Charlottesville, VA, M.S. Thesis (2018).
28. Wong, K.P., and R.C. Alkire, "Effect of Fluid Flow on Convective Transport in Small Cavities", *J. Electrochem. Soc.* 137 (1990): pp. 3010–3015.
29. Harb, J.N., and R.C. Alkire, "Transport and Reaction during Pitting Corrosion of Ni in 0.5M NaCl 1: Stagnant Fluid", *J. Electrochem. Soc.* 138 (1991): pp. 2594–2600.
30. Harb, J.N., and R.C. Alkire, "Transport and Reaction during Pitting Corrosion of Ni in 0.5M NaCl 1: Flowing Fluid " *J. Electrochem. Soc.* 138 (1991): pp. 3568–3575.
31. R.C. Alkire, T. Bergh, and R.L. Sani, "Predicting Electrode Shape Change with Use of Finite Element Methods" *J. Electrochem. Soc.* 125 (1978): pp. 1981–1988.

3. Electrolyte Film Thickness Effect on the Cathodic Current Availability in Galvanic Couple

Summary:

There have been a number of corrosion modeling work in which electrochemical kinetics in full immersion were used as boundary conditions, which cannot fully capture the characteristics of atmospheric corrosion, especially the one under a thin layer of electrolyte. It is well known that natural convection boundary layer exists when the solution stays in quiescent condition, however, the exact value of this natural convection layer is vague in literature, and transition of corrosion distributions in a galvanic coupling from a full immersion condition into true thin film condition by taking into account natural convection remains as a knowledge gap, let alone the ohmic drop introduced by thin film electrolyte between the anode and the cathode in the galvanic coupling. This chapter is aimed to determine the critical value of electrolyte layer thickness below which full immersion condition transitions into thin film conditions, and parse the dependence of cathodic current capacity of SS cathode to support AA7050 anode corrode on electrolyte film thickness, electrolyte resistance and cathode-to-anode ratio in thin film condition.

The work presented in this chapter has been reported in the following publication:

C. Liu, J. Srinivasan, and R.G. Kelly, "Editors' Choice—Electrolyte Film Thickness Effects on the Cathodic Current Availability in a Galvanic Couple". *Journal of the Electrochemical Society*, 164 (2017): p.C845-C855.

3.1 Abstract

A combined modeling and experimental study was performed to understand the dependence of the cathodic current delivery capacity on the electrolyte film thickness and cathode size in a galvanic couple. The appropriate cathodic kinetics for the modeling were generated by use of a rotating disk electrode to simulate the electrolyte film thickness. These results provided boundary conditions for a finite element model which calculated the potential distribution along a metallic surface and the associated cathodic current supplied for electrolyte layers of varying thickness. The total cathodic current was then calculated through integration of the current density across the surface. Electrolyte layer domains were delineated by three limits which described, in order of decreasing film thickness, i) transition in exposure condition from full immersion to thick film, ii) the hydrodynamic boundary layer due to natural convection which defined the upper limit of the thin film regime, and iii) the relative dominance of ohmic resistance over mass transport in determining the total current output. This study also showed that for sufficiently thin films, this total current was independent of the size of the cathode and the nature of kinetics at the electrochemical interface, being solely driven by the ohmic resistance in solution.

3.2 Hypothesis:

The cathodic current availability from the SS316L cathode should be a function of electrolyte layer thickness and cathode length. Electrolyte layer thickness affects ORR cathodic kinetics and electrolyte ohmic resistance, and cathode length only affects ohmic resistance. There should be a critical electrolyte layer thickness and cathode length existed beyond which cathodic current availability would be a monotonic function of ohmic resistance.

3.3 Introduction

Dissimilar engineering alloys in close proximity and in electrical contact are frequently encountered in the architecture of high-value structural assets in the transportation, aerospace, and marine industries. In service, these structures are often exposed to atmospheric environments, such as sea spray, that result in the formation of a thin electrolyte layer on the surface sufficient to allow the dissimilar alloys to form galvanic couples. Under atmospheric conditions, the electrolyte can also form via deliquescence of salt as either a droplet or a thin film on the alloy surface, leading to the establishment of a corrosion cell. The extent of galvanic corrosion on the anode that results depends on a number of environmental, physicochemical, and geometric variables, which include relative humidity, temperature, electrolyte conductivity, electrolyte film thickness, in addition to the electrochemical kinetics on the alloy surface.¹⁻⁷ Different exposure conditions can be modeled by varying the thickness of the electrolyte film (also termed the water layer, *WL*), which in turn affects solution resistance as well as cathodic kinetics, thus having a direct effect on the total cathodic current available to support corrosion of the galvanic system.

The effects of the electrolyte film thickness on corrosion rate were recognized initially by Tomashov,² who qualitatively identified four regions of *WL* corresponding to different types of reaction control. As film thickness decreased, a transition from a plateau in corrosion rate when a constant diffusion layer was attained (conditions of full immersion) to cathodically controlled corrosion limited by diffusion of dissolved oxygen to the reaction surface (the corrosion rate increased as film thickness decreased under this condition, governed by Fickian mass transport behavior), before transitioning into reduced dissolution (termed anodic control) owing to lower corrosion product solubility in a smaller solution volume. Finally, an extreme region was reached which had the very low corrosion rate of dry chemical oxidation due to the lack of a continuous

film. While useful conceptually, this outline lacked any quantitative, mechanistic description or validation of the relationship between electrochemical kinetics and the film thickness. Attempts to develop a rigorous study of this dependence have since been made by a number of researchers⁸⁻²². Nishikata *et al.*^{14,15}, in their experimental studies on the oxygen reduction reaction (ORR) cathodic kinetics of both iron and platinum under an electrolyte thin film, observed a one-dimensional, Fickian relationship between the limiting current density for ORR and the film thickness over the range 20 μm to 1 mm. This study posited that a critical electrolyte thickness exists in the vicinity of 1 mm. For films thicker than this critical value, the limiting current density would be constant, no longer obeying the inverse relationship of Fickian diffusion. This critical value thus denoted the minimum thickness at which the boundary layer established by natural convection dictates mass transport. Experimental work by Stratmann *et al.*¹⁰⁻¹² and Frankel *et al.*¹⁶ concurred regarding the presence of such a critical film thickness between 500 μm to 1 mm. However, the exact value for this critical water layer thickness for natural convection is still unknown.

Recently there have been modeling studies¹⁸⁻²⁴ that have focused on corrosion under an electrolyte thin film instead of full immersion. Dolgikh *et al.*²⁴ performed a combined experimental and modeling study which incorporated the idea that convective flux could be expressed in terms of an analogous diffusion term²⁵. They proposed that the critical water layer thickness for natural convection is on the order of 250 μm which is in line with the suggestion of Gileadi²⁶. It should be noted that the geometry used in that work consisted of a band electrode 1mm x 10 mm, resulting in 2D diffusion which would inherently lead to higher currents and thus lower estimates for the natural convection layer (termed the “micro-convection layer” by Dolgikh *et al.*²⁴).

Galvanic corrosion under a thin film electrolyte is modulated by the WL thickness due to the impact of *WL* on both diffusional kinetics at the cathode and ohmic drop in solution between

the anode and cathode. Both of these aspects can affect the total amount of cathodic current available to drive dissolution at the anode. However, work to date has focused primarily on either one or the other of these two effects, which may often be synergistic. For instance, King *et al.*²³ investigated the effect of electrolyte layer thickness on the galvanic throwing power for a Mg-rich primer/AA2024-T351 couple, wherein an increase in electrolyte layer thickness was observed to lead to a smaller ohmic drop in solution and consequently a smaller potential difference between the anode and cathode sites. The effect of film thickness on mass transport-limited kinetics was not addressed in this study because in the potential range considered, as the cathodic kinetics accessible to the galvanic couple were in the activation-controlled region. Kelly and coworkers^{27,28} utilized a charge conservation-based argument to develop a model that permitted the numerical computation of the maximum current delivery capacity of a finite cathode under a thin electrolyte film as part of a model used to predict the maximum pit size that could form. The ohmic drop in solution delineated the potential gradient across the cathode, which in combination with kinetics information from experiment would then provide the total current available to support corrosion on the coupled anode (i.e., the pit). The dependence of the current on the electrolyte film as a consequence of changes in relative humidity, loading density, and solution concentration was discussed. The experimental kinetics data used in this study were measured in full-immersion experiments and the value of the limiting current density in the simulations was modified assuming that the diffusion layer thickness was equal to the *WL* (all of which were below 1 mm). No studies have investigated the total cathodic current that a surface can supply over the range of *WL* spanning from thin films to full immersion.

The rotating disk electrode (RDE) technique provides a means to investigate the effects of *WL* thickness on the electrochemical kinetics under thin electrolytes. It utilizes hydrodynamic

forces to create a constant diffusional boundary layer near the electrode surface. Thus, the rotation rate can be used to define a diffusional boundary layer thickness to represent the effect of the *WL* thickness on the diffusion of oxygen. This quantitative control of the diffusional boundary layer avoids some of the difficulties inherent in making electrochemical measurements in thin electrolyte layers^{14,29}. Panali *et al.*²¹ used electrochemical kinetics of both AA2024 and CFRP generated with RDE as boundary conditions in their modeling of galvanic corrosion between AA2024 and CFRP under a thin layer of electrolyte with varying thickness. In the present study, the RDE was utilized to achieve two goals: RDE testing on Pt was used to determine the critical water layer thickness beyond which natural convection controls the diffusional boundary layer; RDE testing of SS 316L after different periods at OCP was used to determine the effects of both water layer thickness and oxide film on cathodic limiting current density.

The galvanic couple between stainless steel (SS) Type 316L cathode and the aluminum alloy (AA) 7050-T7451 anode (hereafter referred to AA|SS) formed the central focus of this study due to its widespread occurrence in aerospace repairs. This chapter quantitatively determines and mechanistically interprets the effects of electrolyte film thickness on the total cathodic current available to support galvanic corrosion. The results of this study identify the exposure conditions under which the total cathodic current can be the controlling factor in the extent and distribution of dissolution on the anode.

3.4 Methodology

3.4.1 Sample Preparation

The cathode sample used in the study was a rotating disk electrode (RDE) constructed from a cylinder of Type 316L stainless steel (McMaster-Carr Supply Company, Elmhurst, IL) of diameter 0.5 inches (1.27 cm) (embedded in a PTFE holder with an internal electrical contact)

which resulted in an area of 1.27 cm² exposed to the electrolyte. The anode samples – AA7050-T7451 (ALCOA, Pittsburgh, PA) – consisted of rectangular coupons of exposed area 1 cm². Experiments were also performed on a platinum rotating disk electrode (Pine Research Instrumentation, Inc., Durham, NC) of diameter 0.5 cm (exposed area 0.2 cm²). The compositions of 316L and AA7075-T7451 are listed in Table 3.1 and Table 3.2 respectively. All samples were ground to a surface finish of 1200 grit with SiC paper. After grinding, the cathode surface was examined with an optical microscope to ensure that it was flush with the PTFE holder. The electrode surfaces were finally rinsed thoroughly with acetone and then with deionized water before use in the experiment.

Table 3.1: Composition of the SS316L disk used (all values in weight percent)

C	Mn	P	S	Si	Cr	Ni	Mo	N	Cu	Fe
0.019	1.750	0.039	0.028	0.460	17.03	10.160	2.050	0.071	0.440	Balance

Table 3.2: Composition of the AA7050-T7451 used (all values in weight percent)

Si	Fe	Cu	Mn	Mg	Cr	Zn	Ti	Zr	Al
0.12	0.15	2.6	0.1	2.6	0.04	6.7	0.06	0.15	Balance

3.4.2 Electrochemical Kinetics

Cathodic kinetics were determined in a three-electrode electrochemical cell set up with the stainless steel or platinum RDE as the working electrode actuated by a Pine Instruments ASR rotator (Pine Research Instrumentation, Inc., Durham, NC), saturated calomel reference electrode (SCE) and a platinum-niobium mesh as the counter electrode. The experiments were performed at a scan rate of 1 mV/s with the RDE at various rotation speeds ranging from 0 to 2000rpm. Following 15 minutes of open circuit potential (OCP) measurement, the potential scan started

10mV above OCP, and ended at $-1.6 V_{SCE}$ for Pt and $-1.2 V_{SCE}$ for 316L. The current at a reference potential of $-0.75 V_{SCE}$ was used to assess the relationship between cathodic limiting current density due to ORR and electrolyte layer thickness (δ) on each of Pt, and a reference potential of $-0.85 V_{SCE}$ was used for the 316L polarization curves.

Electrochemical kinetics of AA7050 were measured by recording potentiodynamic polarization data of the coupons as working electrodes with a saturated calomel reference electrode (SCE) and a platinum-niobium mesh counter electrode. The experiments were performed with the exposed surface of the coupon fully immersed in quiescent solution after 1 hour at OCP, scanning at a rate of 0.2 mV/s from $-1.55 V_{SCE}$ to $-0.7 V_{SCE}$.

All measurements were recorded in unbuffered 0.6 M NaCl. All experiments were performed on a Bio-Logic SP-200 (Bio-Logic SAS, Claix, France) potentiostat running EC-Lab (Version 11.01) software. The kinetics for the AA7050 were characterized quantitatively for the model via the Tafel fitting module of the anodic slope using the EC-lab software. The slope of the fitted curves was 23 mV/decade. Although active localized corrosion precludes any mechanistic interpretation of the slope, for determination of the current and potential distributions, such mechanistic information is not required. All that is required is the empirical relationship between potential and current density.

3.4.3 Finite Element Method (FEM) Modeling

The modeling framework is based on Laplace's Equation^{30,31}, and the elaborated mathematical development of the modeling framework used has been described elsewhere^{32,33}. COMSOL Multiphysics v5.3 (COMSOL, Inc., Burlington, MA) software was used for two types of modeling work in this study. In this first type, the potential and current distributions along a 316L cathode coupled galvanically with AA7050-T7451 were modeled using a simplified two-

dimensional geometry which represented the cross-section of the couple under a layer of electrolyte, as depicted in Figure 3.1. The anode-to-cathode area ratio of the system was varied by changing the length of the cathode with the anode length kept constant. The width of both electrodes was considered identical, obviating the necessity for a three-dimensional model. For the major modeling study in which cathodic current availability was the focus, the anode length was fixed at 1 cm, and the range of cathode lengths considered in this study varied from 1 cm to 40 cm, corresponding to an area ratio of 1:1 to 1:40, respectively. The thickness of the electrolyte film was varied across four orders of magnitude from 13.8 μm to 5 cm in order to provide a sufficiently wide range to capture exposure conditions representative of thin film and full immersion at either limit. The second type of modeling was carried out to investigate the effect of area ratio of anode to cathode, in which cathode length was fixed at 10cm with constant $WL=1\text{mm}$ on the surface, and the area ratio of anode to cathode varied from 0.1 to 10. Simulations using the model geometry were run to convergence such that differences in calculations from consecutive iterations were less than the error tolerance limit of 0.1%.

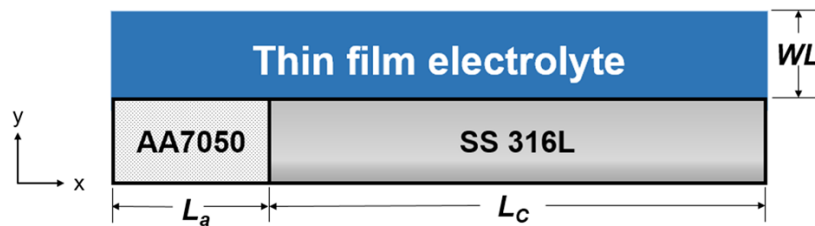


Figure 3.1: Schematic configuration of the interaction between thin film electrolyte and galvanic couple (316L cathode with AA7050 anode in this study). Width of anode/cathode is normal to x-y plane.

The model results shown here are based on the use of the Laplace equation as the governing equation rather than implementing the full Nernst-Planck equation with consideration of ion-ion interactions. The latter is extraordinarily computationally expensive, and for the goals of this work, unnecessary. The Laplace approach provided a straightforward framework to calculate the spatial

distribution of electrochemical variables on the cathode surface, relying instead on the knowledge of the physicochemical characteristics of the electrolyte such as the conductivity estimated from thermodynamic solution modeling³¹. The value used for κ throughout this study was that of 0.6 M NaCl, 5.5 S/m. Boundary conditions (B.C.) were anodic kinetics of AA7050 (anodic B.C.) and cathodic kinetics of SS 316L (cathodic B.C.). All the calculations assumed steady state.

The absolute value of the total cathodic current per unit width (I_C/W) from a surface surrounding a finite anode under thin film conditions is dependent on the WL thickness, solution conductivity (κ), cathodic and anodic kinetics, and length of cathode (L_C). WL thickness and κ affect the ohmic resistance of the electrolyte per unit length of cathode, WL thickness and kinetics control the current-potential behavior of the galvanic couple, and L_C fixes the maximum cathode length available for current supply. The WL thickness is a function of both loading density ($LD =$ amount of salt deposited per unit area), and the relative humidity (RH). The calculations of cathodic current availability were performed for electrolyte properties corresponding to 0.6 M NaCl, which would be in equilibrium with a RH of 98% at 25 °C as representative of atmospheric exposure conditions. Different WL thicknesses modeled in the study therefore correspond to different amounts of NaCl deposited on the metal surface. Furthermore, a constant RH values fixes the equilibrium concentration of salt thus decoupling κ from its dependence on varying WL thickness.

3.5 Results

The total cathodic current available to support galvanic corrosion across different cathode lengths under varying WL thicknesses was computed from the solution of the Laplace equation for the model geometry with the boundary conditions described previously. The experimental RDE cathodic kinetics data were analyzed to extract the value of the boundary layer thickness due to

natural convection as well as identify any effects on the diffusion limited current density due to the presence of a native oxide film. In order to evaluate the effects of both mass transport-limited kinetics as well as the ohmic resistance in solution on the total current delivery capacity of the finite cathode, the simulated data were assessed in terms of the total cathodic current output versus the electrolyte film thickness for a range of cathode lengths.

3.5.1 Determination of Critical Electrolyte Layer Thickness for Natural Convection

The RDE technique provides an experimental methodology to study the effect of varying the thickness of the diffusional boundary layer on kinetics. The Levich Equation³⁴ quantitatively describes the convective motion at a RDE, utilizing hydrodynamic forces to control the boundary layer thickness, which is related to the angular velocity of rotation as shown in Equation 3.1:

$$\delta = 1.61D^{1/3} \nu^{1/6} \left(\frac{2\pi}{60} rpm \right)^{-1/2} \quad (3.1)$$

where δ is the thickness of hydrodynamic boundary layer or diffusional layer, D is the diffusivity of dissolved oxygen at 25°C ($D=2.1E-9$ m²/s, calculated by OLI Analyzer Studio 9.2), ν is the kinematic viscosity of 0.6M NaCl solution ($\nu=9.2E-7$ m²/s, calculated by OLI Analyzer Studio 9.2), and rpm is the rotation speed of the RDE. δ can be obtained for corresponding rotation speed by using Equation 3.1 (e.g., 0, 10, 50, 200, 720, and 2000 rpm represent full immersion, and δ equal to 200 μ m, 89 μ m, 44.5 μ m, 23.5 μ m, and 13.8 μ m, respectively). Figure 3.2 shows cathodic polarization curves of Pt RDE in 0.6 M NaCl as a function of rotation speed. According to the expression of the steady state, one-dimensional diffusion limited current density,

$$i_{\text{lim}} = \frac{nFD_{O_2} (C_{O_2, \text{bulk}} - C_{O_2, \text{electrode_surface}})}{\delta} \quad (3.2)$$

the limiting current density is inversely proportional to δ . However, the diffusional layer thickness cannot continue to increase without bound, because at some thickness, natural convection¹⁴ will

cause mixing and thus terminate the concentration gradient. Otherwise, there would be zero current at steady state in full immersion because δ would go to infinity if it were not bounded.

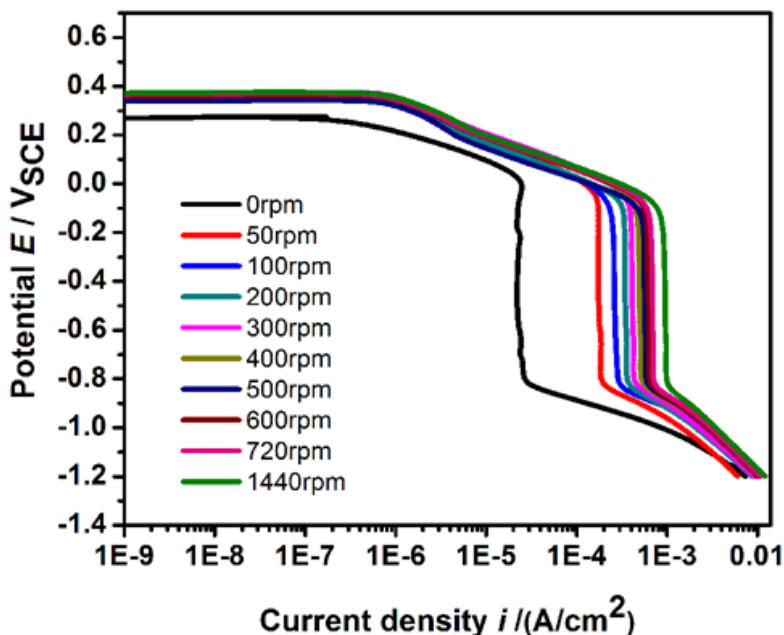


Figure 3.2: Polarization curves of Pt RDE as a function of rotation speed (rpm).

Figure 3.3a shows the Levich plot for the Pt RDE experiments. The value of i_{lim} measured under quiescent conditions in full immersion (i.e., 0 rpm, referred to as $i_{lim,nc}$) can be used in conjunction with the RDE data to determine the location of critical electrolyte layer thickness for natural convection (δ_{nc}). The intersection of the $i_{lim,nc}$ with the line describing the Levich equation (see Figure 3.3b) identifies the natural convection boundary layer for the bulk electrolyte in full immersion condition. It is the lowest diffusion limited current density predicted, indicating that no diffusion layer larger than δ_{nc} was obtainable. From these experiments, the critical electrolyte layer thickness for natural convection (δ_{nc}) in terms of dissolved oxygen was found to be equal to

797 \approx 800 μm . It is also implied that δ is equal to the WL thickness as long as WL is less than or equal to δ_{nc} .

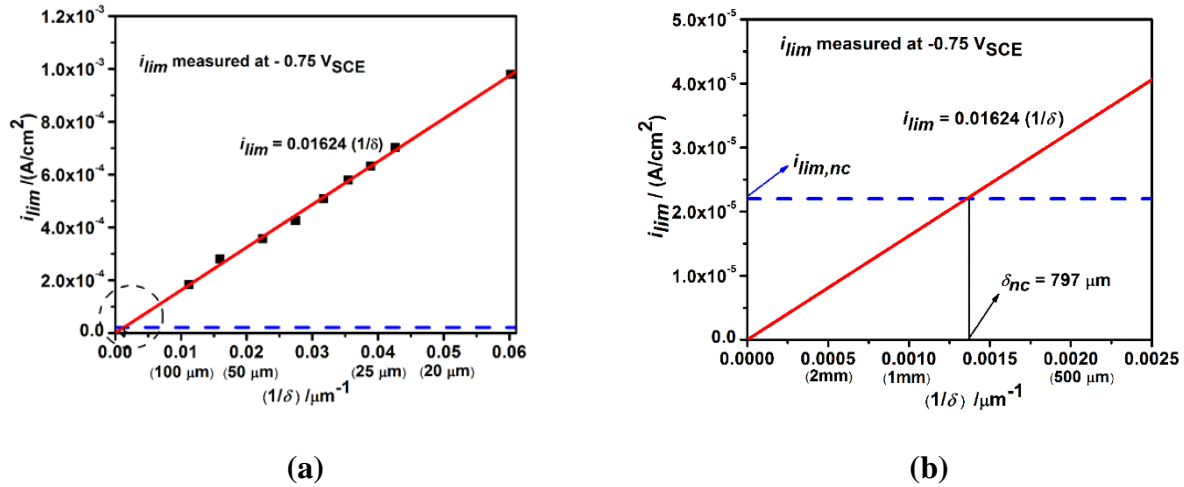


Figure 3.3: (a) Limiting current density (i_{lim}) at $-0.75 \text{ V}_{\text{SCE}}$ vs $1/\delta$; (b) Zoom-in of thick WL regime to exhibit critical natural convection electrolyte layer thickness (δ_{nc}). Blue dash line represents the value for cathodic limiting current density of Pt in full immersion condition.

3.5.2 Electrochemical Kinetics of SS 316L and AA7050-T7451

Polarization curves of SS 316L using the RDE are displayed as a function of rotation speed from 0 to 2000 rpm in Figure 3.4. The cathodic limiting current density on 316L increased with increasing rotation speed, showing the same tendency as the Pt RDE data. Figure 3.5 compares the Levich plots for the Pt (i_{lim} at $-0.75 \text{ V}_{\text{SCE}}$) and 316L (i_{lim} at $-0.85 \text{ V}_{\text{SCE}}$) data. For δ thicker than 36.4 μm , the limiting current densities for 316L were almost identical with those for Pt. For thinner δ , there was discrepancy between limiting current densities for Pt and 316L, and the discrepancy became larger as the boundary layer continued to decrease. This might imply the effect of oxide film become significant under very thin electrolyte thickness, but the mechanism behind it is out of research scope in this work and will be elaborated later.

Anodic electrochemical kinetics of AA7050 were measured under full immersion and are displayed in Figure 3.6, with Tafel fits to the anodic branches of AA7050 shown in the same figure. AA7050 had fairly flat anodic kinetics with the anodic pseudo-Tafel slope of 23 mV/decade, indicating the low polarizability of an active localized corrosion.

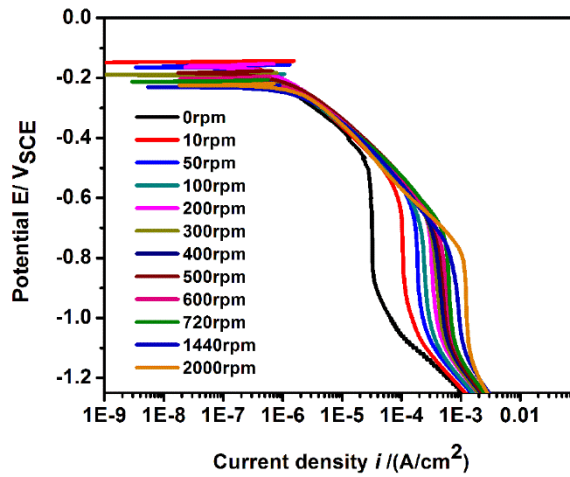


Figure 3.4: Polarization curves of 316L as a function of rotation speed.

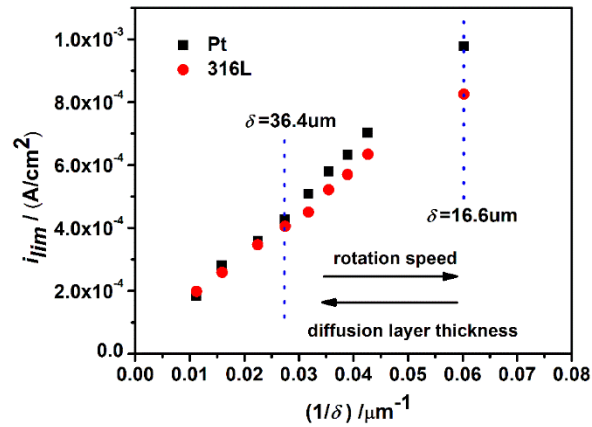


Figure 3.5: Comparison of i_{lim} vs. $1/WL$ between Pt and 316L.

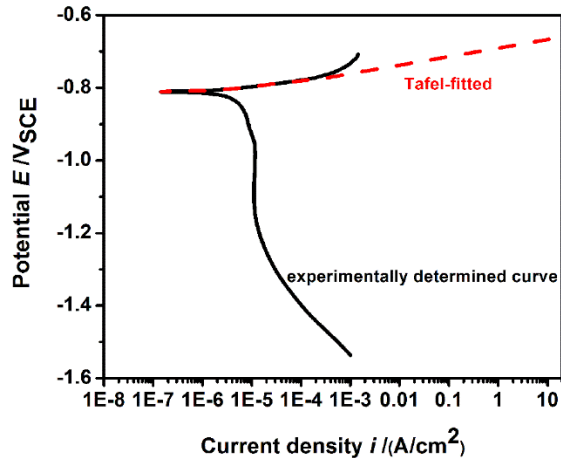


Figure 3.6: Tafel-fitting for anodic kinetics of both AA7050-T7451

3.5.3 Effect of Area Ratio of Anode to Cathode on Total Cathodic Current

The majority of the modeling results for the galvanic couple between AA7050 and SS316L used a fixed length of the anode (AA). However, it is of importance to demonstrate the application of this modeling study is not applicable only to the length of anode used here (i.e., 1 cm), but rather is applicable as long as the anodic materials has electrochemical kinetics with limited polarizability and the galvanic coupling potential for a 1:1 cathode: anode area ratio is located in the region of diffusion controlled cathodic kinetics. Under these conditions, the variation in area ratio has a negligible effect on total cathodic current per width. An example for a WL of 1mm is shown in Figure 3.7, in which a fixed length of cathode (SS) equal to 1 cm was coupled with different lengths of anode (AA). It is clearly seen that total cathodic current per unit width was invariant to the change in the length of anode over an area ratio range of at least 0.1 to 10. Although varying the exposure area of anode changed the potential at the SS/AA interface slightly, it was still located in the diffusion-controlled kinetics region of 316L, so the current was almost a constant in this scenario due to fixed length (surface area) of 316L (cathode). The almost non-polarizable electrochemical kinetics of AA7050 led to only a subtle change of the galvanic couple potential

when varying the area ratio. As a result of these two effects, the total cathodic current per length of SS316L was a constant regardless of the length of the coupled AA7050.

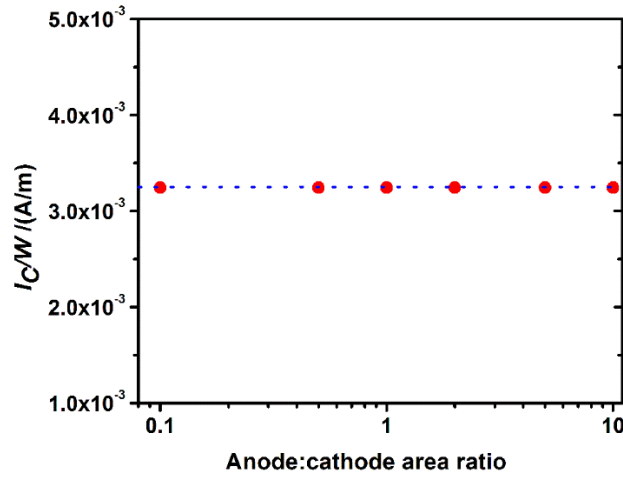


Figure 3.7: I_c/W vs. area ratio of anode to cathode for AA/SS galvanic couple, assuming fixed length of anode when $WL=1$ mm

3.5.4 I_c/W on SS 316L Coupled with AA7050 versus WL as a Function of L_c

In this section, results from studies of a galvanic couple between AA7050 with fixed length (1 cm) and 316L with length ranging from 1 to 40 cm are described. In addition to the experimentally determined cathodic kinetics, simulated cathodic kinetics with an equivalent WL of 400 μm was created, as the minimum rotation speed available experimentally was 10 rpm, which implies that the maximum equivalent was 200 μm . The boundary conditions are shown in Figure 3.8.

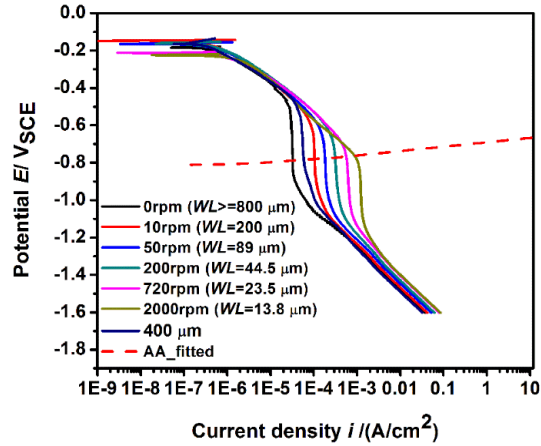


Figure 3.8: Boundary conditions for modeling between AA/SS galvanic couple under different δ .

The total cathodic currents per width (I_C/W) for a 316L cathode versus WL as a function of the length of cathode (L_C) are plotted in Figure 3.9. The linear scale of Figure 3.9a shows that the I_C/W became a constant after a critical WL for each L_C , and this constant total current increased with L_C . A semi-log scale plot allows better inspection of the I_C/W in the thin electrolyte layer (<1 mm) region, shown in Figure 3.9b. For short L_C (<9.25 cm), the I_C/W initially increased with WL , then decreased to an intermediate minimum at $\delta_{nc} = 800$ μm before reaching a plateau. For a cathode length of 9.25 cm, I_C/W grew before reaching a first plateau with WL from 400 μm to 800 μm , and then again increased with WL until reaching a second plateau. For cathode lengths larger than 9.25 cm, the total I_C/W did not have an intermediate minimum, instead it increased with increasing WL until reaching a plateau albeit with an inflection point at 800 μm . Figure 3.9c shows that for sufficiently thick WL (5 cm), there was a linear relationship between I_C/W and L_C , the criterion for considering a galvanic couple to be under full immersion conditions. The I_C/W over a range of WL smaller than 1mm for four cases in which cathode length is equal to 1, 5, 9.25, and 10 cm is displayed in Figure 3.10, showing the existence of this intermediate minimum for L_C less than 9.25 cm.

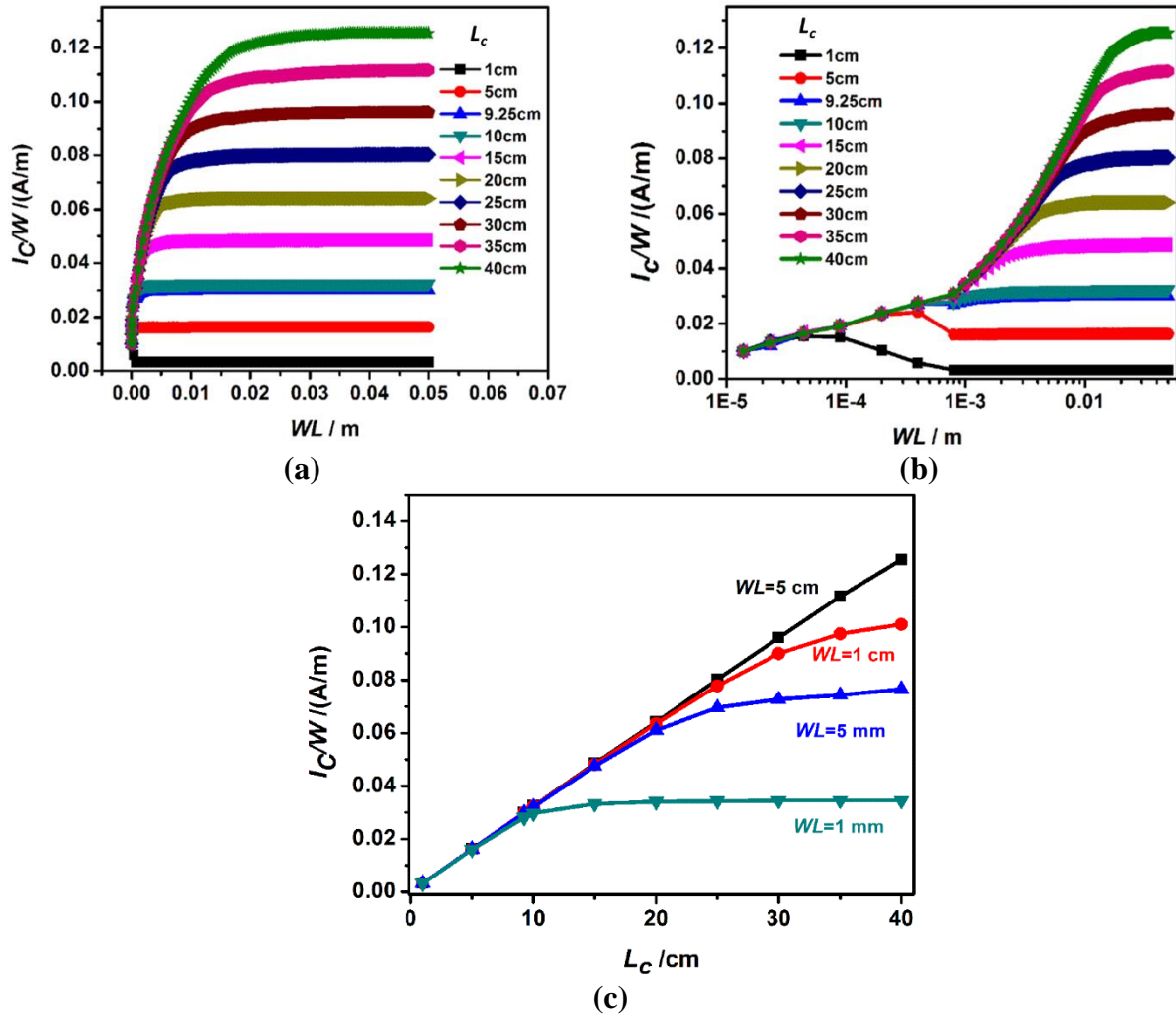


Figure 3.9: (a) I_C/W vs. WL as a function of cathode length (L_C) in linear scale; (b) I_C/W vs. WL as a function of L_C in semi-logarithm scale; (c) I_C/W vs. L_C as a function of WL .

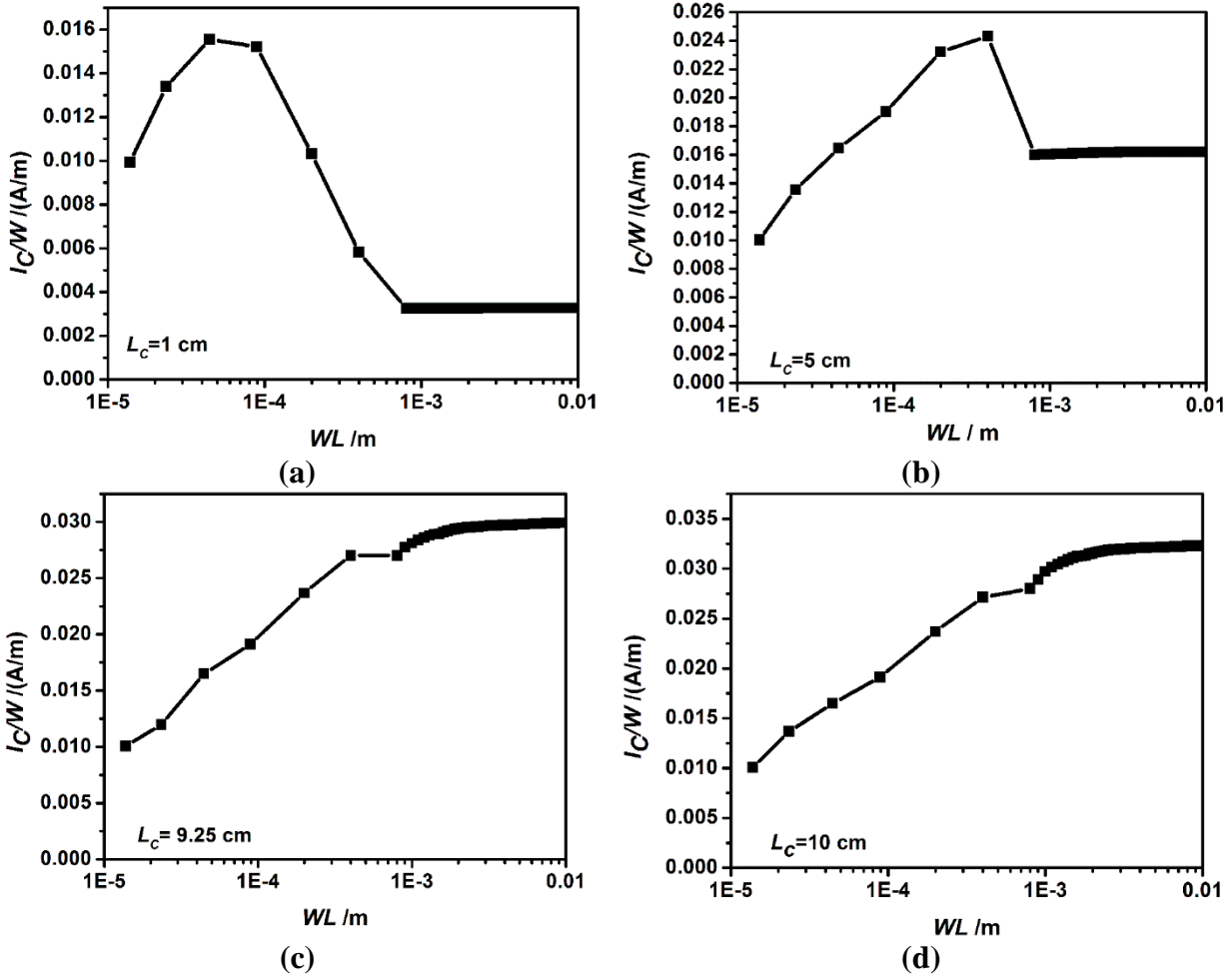


Figure 3.10: I_C/W over a range of $WL \leq 1$ mm for $L_C =$: (a) 1 cm; (b) 5 cm; (c) 9.25 cm; (d): 10 cm.

3.6 Discussions

This work presents the results of a finite-element based modeling approach to understand the effects of electrolyte layer thickness (WL) on galvanic corrosion between AA7050-T7451 and SS 316L with different area ratios in thin film electrolyte conditions, as might be expected during atmospheric exposure of many structures. The critical question of when an electrolyte layer can be treated as a thin film, a thick film and full immersion is addressed. The first section describes the experimental determination of the thickness of the natural convection layer, δ_{nc} , which defines the WL thickness above which the diffusion-limited current density becomes independent of WL thickness. It can also be considered the WL thickness below which true thin film electrolyte

conditions occur. The second section describes the dependence of the total cathodic current from a surface exposed to an electrolyte film available to drive galvanic corrosion. The dependences of this total current on *WL* thickness and cathode length are quantified and rationalized. The effects of *WL* thickness can be viewed as a competition between the ohmic resistance of the electrolyte and diffusion-controlled cathodic kinetics of the cathode as will be discussed in detailing in the following section. The results as a function of cathode length can be parsed into two categories according which parameter controls the available cathodic current capacity. Both modeling and experiment data in literature are also compared to validate our simulated results. The logarithmic relationship between the *WL* thickness and the total cathode current is shown to be independent of cathode length under thin film conditions. There also exists an ohmic-resistance affected thin film condition above which true full immersions are realized in that the total cathode current scales linearly with the size of the cathode. Finally, the implications of the work as well as its limitations are discussed.

3.6.1 Determination of the Thickness of the Natural Convection Layer

Natural (or free) convection is the spontaneous fluid flow created by density gradients^{26,35}. In the present case, this flow prevents the oxygen concentration gradient from extending to large distances away from the electrode. The most obvious manifestation of the presence of a natural convection layer is the presence of a non-zero diffusion-limited current density at steady state under quiescent conditions, as illustrated in Figure 3.2 and Figure 3.4 for the 0 rpm case of ORR on Pt and 316L, respectively. In the absence of natural convection, the diffusion boundary layer would continuously increase with time, lowering the diffusion-limited current density continuously as well. Instead, a well-defined, diffusion-limited current for oxygen reduction is found of approximately $22 \mu\text{A}/\text{cm}^2$. Either through the use of Equation 3.2, or the construction of

the intersection of the lines in Figure 3.3, a natural convection boundary layer of approximately 800 μm is observed for the system studied here. Although natural convection in electrochemical systems has been discussed in texts^{26,35}, there has been a limited amount of experimental work aimed at determining the actual thickness of this layer. The literature^{2,14,16,22,29,36} cites values of δ_{nc} from 250 μm to 1 mm. Tomashov² estimated that thin film conditions could be considered to apply for $WL < 1$ mm. Amatore *et al.*²⁵ described a micro-convection approach in which a diffusion-like term was used to account for natural convection. They estimated a δ_{nc} of 230 μm , which Dolgikh *et al.*²⁴ also used in their extension of this approach from consideration of a single species to multi-ion environments. This value is also similar to that stated in Gileadi's text²⁶. The present work describes both a rigorous experimental method for measurement of δ_{nc} and data demonstrating its use. It should be noted that different systems (i.e., electrolytes, temperatures, diffusing species, geometries) may have other values of the natural convection layer, but the method used in this work provides a means to determine the value unambiguously, even without specific knowledge of the diffusivity and kinematic viscosity (as needed in Equation 3.2).

3.6.2 Different Regimes of Dependence of Cathodic Current on Film Thickness are Clearly Distinguishable

Based on L_C , distinct regimes arise that delineate the dependence of cathode current on film thickness. The potential along the cathode rose from that at the AA/SS interface towards the open circuit potential of the cathode (SS). The extent of potential rise and its distribution is determined by the ohmic drop in solution along the cathode. This ohmic drop is determined by the WL thickness, the current/potential relationship and the cathode length. The net effects of these variables are the existence of four regimes of behavior for WL , with the particulars of the regimes depending on the cathode length

3.6.2.1 $L_c < 9.25 \text{ cm}$

In the small cathode-to-anode area ratio region, the total cathodic current available exhibited four distinct WL thickness regimes. This behavior is illustrated using the results for the 5 cm long cathode (Figure 3.11).

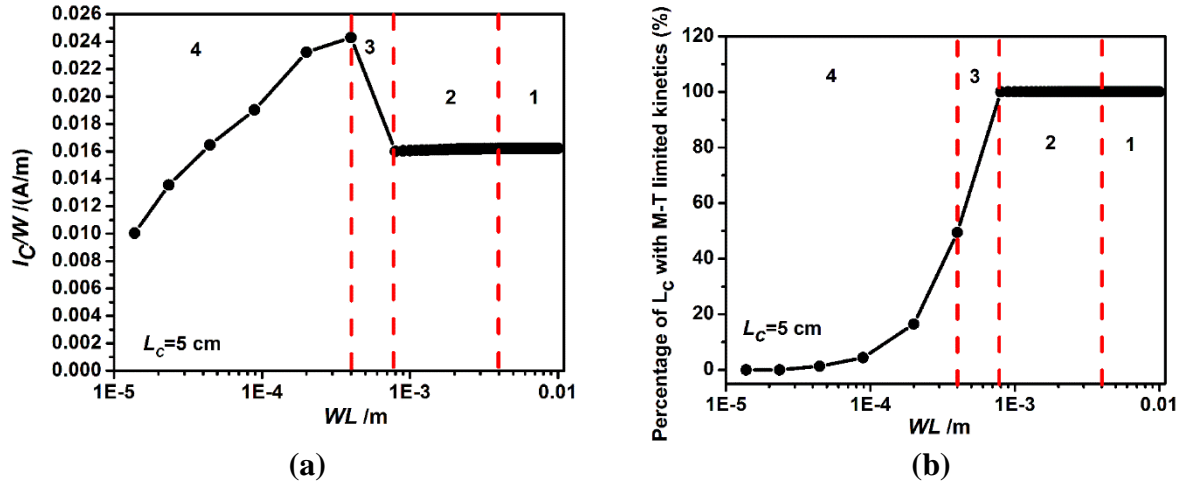


Figure 3.11: (a) Four different regimes in I_C/W vs. WL ; (b) Corresponding percentage of length of cathode within mass-transfer limited (ORR) kinetics in each of four regimes. Note that percentage of length of cathode within M-T limited kinetics means that electrochemical kinetics thrown upon this part of cathode is mass-transfer controlled, the rest of the cathode is under either activation or mixed control.

Regime 1 – $WL \geq 4 \text{ mm}$: For the large WL thicknesses in this regime, the couple was essentially under full immersion conditions, and the ohmic drop across the entire cathode was negligible. Thus, the two electrodes were not polarized appreciably from the coupling potential predicted from Mixed Potential Theory ignoring ohmic drop taking into account the cathode-to-anode area ratio. Consequently, the cathodic current density at all points is equal to the coupling current density (for the AA/SS couple, this is the mass transport-limited cathodic current density when $WL = 800 \mu\text{m}$) and I_C is simply $i_{lim} \cdot L_C$. As shown in Figure 3.9c, the total cathode current scales linearly with L_C . In this regime, the system behaves as if it is fully immersed in the electrolyte.

Regime 2 – δ_{nc} (800 μm) \leq $WL < 4$ mm: The role of the ohmic drop in this second regime was small, but not completely negligible, causing only minor polarization from the coupling potential. Moreover, polarization of the cathode away from the coupling potential resulted in a current density still in the mass transfer-limited region shown in Figure 3.11b. Therefore, the I_c/W available was only marginally smaller than that available under very thick WL conditions (Regime 1). Kinetics data generated in quiescent full immersion conditions informed the calculation of the potential distribution and the cathodic current density at each point on the cathode. The diffusion distance controlling the cathodic kinetics in this regime was the hydrodynamic boundary layer associated with natural convection (δ_{nc}). The value of δ_{nc} will determine at what WL thickness the transition occurs, but will not qualitatively affect the existence of such behavior. It should be noted that the more noble portion of the potential range associated with mass transfer limitation is, in fact, mixed activation/diffusion control, so the current density is slightly lower than the limiting current density, especially for longer cathodes. A decrease in total cathodic current can be resulted if the potential range associated with mass transport control is narrow, and consequently even a low ohmic drop can result in the sufficiently distant points on the cathode displaying kinetics associated with the mixed activation/diffusion-limited region.

Regime 3 – $400 \mu\text{m} \leq WL < \delta_{nc}$: In Regime 3, the diffusion distance controlling the cathodic kinetics was the water layer thickness (WL) itself. Calculations of the cathodic current density in this regime used kinetic information obtained from RDE studies in which decreasing WL thickness was simulated by the increasing the rotation speed of the RDE to reduce the diffusional boundary layer in a calculable manner. Although the effect of ohmic resistance was still significant, it did not become the dominant factor controlling the relationship between I_c/W and WL as long as the percentage of the cathode length under mass-transfer (M-T) limited kinetics

was above 50%, as illustrated in Figure 3.11b. As a result, the total cathodic current showed a sharp rise with decreasing WL thickness because of the inverse relationship between the cathodic limiting current density and the WL thickness.

Regime 4 – $WL < 400 \mu\text{m}$: At sufficiently thin WL thicknesses, the ohmic drop was substantial, with less than 10% of length of cathode within the M-T limited kinetics portion of the polarization in this regime (see Figure 3.11b). The vast majority of the cathode experienced potentials in the mixed or activation region of the polarization curve. A precipitous drop in the total cathodic current occurred at smaller WL thicknesses. If WL was sufficiently small, the ohmic drop would be so large such that every point on the cathode would be at its OCP and there would be no net current to the anode. Under the conditions studied here, even a $13.8 \mu\text{m}$ WL allowed some interaction between the cathode and anode, as demonstrated by a non-zero value of I_C/W .

To better understand the competitive nature of relationship between ohmic drop and M-T limited kinetics on I_C/W in thin electrolytes, Figure 3.12 compares the result in Figure 3.11a with I_C/W vs. WL affected by either only ohmic drop or only M-T limited kinetics. To do so, the ability of computational studies to isolate individual parameters was exploited by performing one set of calculations in which the M-T kinetics were made very rapid, allowing the effects of WL on ohmic drop (and I_C/W) alone to be studied, and performing another set of calculations in which the ohmic drop was maintained at a low level, allowing the effects of WL on M-T (and I_C/W) alone to be studied. The circular symbols are the results for ohmic drop control, whereas the triangles are the results for the M-T limited kinetics control. The line with the circular symbols assumed that the cathodic kinetics for $WL=13.8 \mu\text{m}$ applied to the calculation of I_C/W for all WL cases, and thus changing the thickness of electrolyte layer only varied the amount of ohmic drop. As for the line with triangle symbols, it was assumed that the WL during the simulation was equal to $800 \mu\text{m}$ to

fix the ohmic resistance, and the M-T limited kinetics was varied to test the effects of the diffusion layer alone.

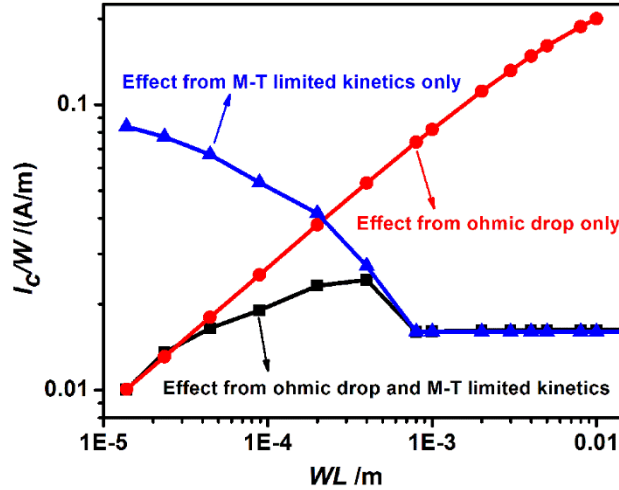


Figure 3.12: Comparison of I_C/W vs. WL among three different scenarios: I_C/W affected by (1) both ohmic drop and M-T limited kinetics; (2) by ohmic drop only; (3) by M-T limited kinetics.

As shown in Figure 3.12, as the WL thickness increased, the ohmic drop decreased linearly, and thus the total cathodic current increased linearly. Conversely, the M-T controlled current decreased with increasing WL thickness as the increasing boundary layer increased the diffusion distance until the natural convection WL thickness was achieved. For WL thickness larger than δ_{nc} , the current did not change as the current density was limited by δ_{nc} .

The behavior of the combined system (illustrated by the squares) can be understood by noting that the ohmic and M-T processes occur in series. At low WL thickness, the current was controlled by the ohmic drop; the M-T limited kinetics at these WL thicknesses was very high and would thus allow much larger currents, then those allowed by the ohmic drop limitation. At large WL thicknesses, the current was controlled by the M-T kinetics. In the intermediate region, both processes were important and their resistances effectively added, suppressing the current to values below either limiting behavior.

As the length of the cathode increased, the total current in Regimes 1 and 2 increased due to the larger area. The ohmically-controlled Regime 4 was unchanged with increasing cathode length as for these small WL , only the small portion of the cathode nearest the anode/cathode interface contributed current. Regime 3, in which the transition from ohmic to M-T control occurred, also shrank until it disappeared as the L_c increased to the critical value=9.25 cm.

3.6.2.2 Critical $L_c=9.25\text{cm}$

The results for L_C of 9.25 cm also show 4 different regimes in Figure 3.13 like what are shown in Figure 3.11 for the shorter cathodes. The dominant factors controlling the patterns in Regime 1' ($WL \geq 8$ mm) and Regime 2' ($\delta_{nc} \leq WL < 8$ mm) were the same as Regime 1 and 2 for smaller cathode scenario in Figure 3.11, respectively. However, there was a difference between Regime 3' (Figure 3.13) and Regime 3 (Figure 3.11) within the same range of WL ($400 \mu\text{m} \leq WL < \delta_{nc}$). For Regime 3', although the M-T limited cathodic kinetics at a WL thickness of $400 \mu\text{m}$ was twice as large as at a WL thickness of $800 \mu\text{m}$, these faster cathodic kinetics covered only about 20% of the length of cathode for $WL=400 \mu\text{m}$ compared to 60% of the length covered by smaller kinetics for $WL=800 \mu\text{m}$. Thus, the effect of the larger ohmic resistance of the smaller WL ($400 \mu\text{m}$) nulled the effects of enhanced M-T limited cathodic kinetics at the same WL . As a result, I_c/W at $WL=400 \mu\text{m}$ was identical to $WL=800 \mu\text{m}$ in Regime 3', which did not show the same pattern in Regime 3. Regime 4' was identical to Regime 4 (Figure 3.11) for the case of smaller cathode which has been discussed above.

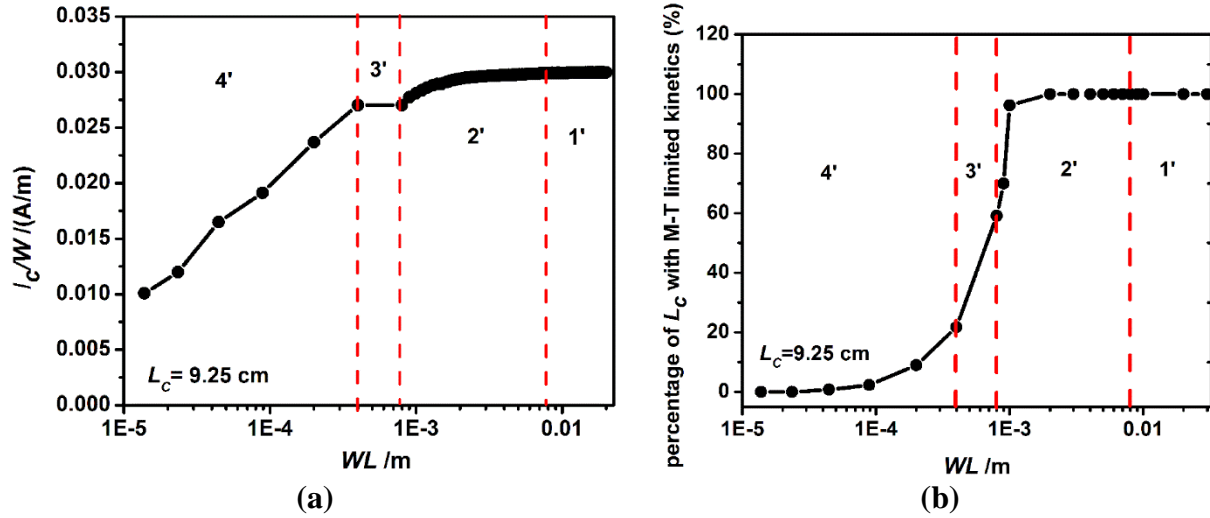


Figure 3.13: (a) Four different regimes in I_c/W vs. WL ; (b) Corresponding percentage of length of cathode within mass-transfer limited (ORR) kinetics in each of four regimes.

3.6.2.3 $L_c > 9.25$ cm

For large cathodes, four regimes were observed, but some were qualitatively different than observed for shorter cathodes. Results from a cathode length of 40cm are shown in Figure 3.14. Regime 1'' ($WL \geq 3.2$ cm) was similar to Regime 1 in Figure 3.11 and Regime 1' in Figure 3.13, and Regime 2'' ($2 \text{ cm} \leq WL < 3.2$ cm) is similar to Regime 2 in Figure 3.11 and 2' in Figure 3.13, in which potential range across the entire cathode length was within M-T limited region (as demonstrated in Figure 3.14b), but the average cathodic current density was closer to the value at the beginning of mass-transfer limited region, making I_c/W slightly smaller. In Regime 3'' ($\delta_{nc} \leq WL < 2$ cm), the dominant controlling factor was the same as Regime 2'', except that the percentage of L_c within M-T limited kinetics was reduced with decreased WL , causing the rate of decrease in I_c/W with decreasing WL to be larger than in Regime 2''. Regime 4'' ($WL \leq \delta_{nc}$) was similar to Regime 4 (Figure 3.11) and 4' (Figure 3.13) as the ohmic drop was so dominant, that cathode length was irrelevant.

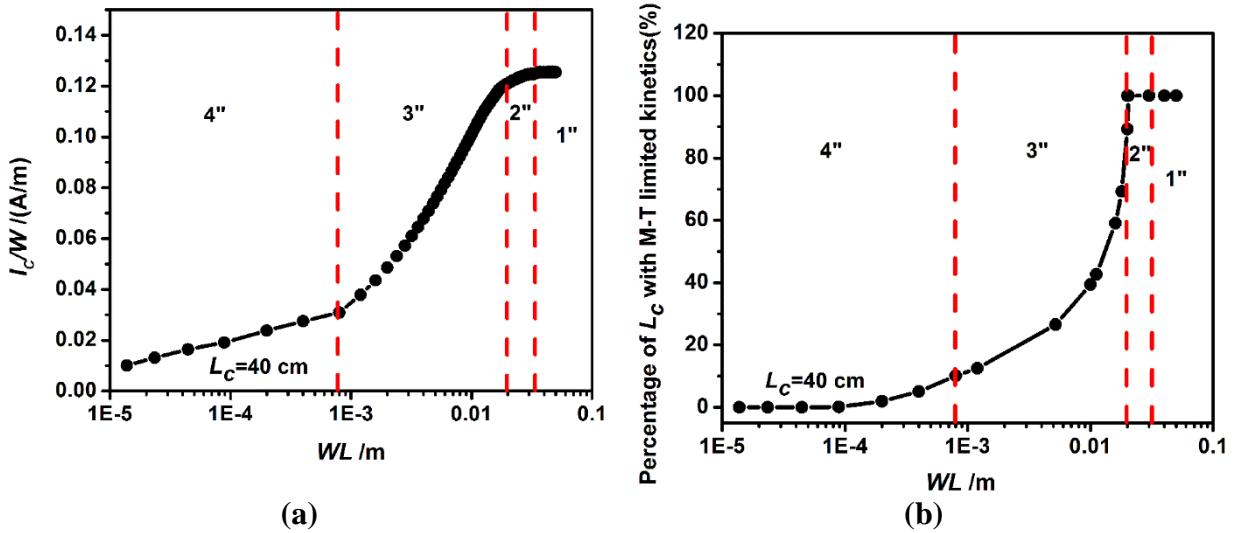


Figure 3.14: (a) Three different regimes in I_c/W vs. WL ; (b) Corresponding percentage of length of cathode within mass-transfer limited (ORR) kinetics in each of two regimes.

3.6.3 The Linear Dependence of Total Current on the Logarithm of the WL Thickness for Small WL and Its Independence of Cathode Length

As shown in Figure 3.9b, the data of total cathodic current versus the logarithm of WL thickness for very thin films fit a straight line with a slope that was independent of cathode length over this range of WL thicknesses. The WL range across which this linear dependence was observed expands when more cathode was available, reaching nearly the value of the boundary layer for natural convection (δ_{nc}) for the largest cathode length studied. Similar trends have been reported from experiment as well as modeling^{8,21,37}. The particular values of the slope and the intercept for this linear fit vary from study to study as the quantitative parameters are determined by the specific kinetics considered. For instance, Palani *et al.*²¹ considered ORR kinetics on carbon fiber reinforced polymer in contrast to this work on 316L stainless steel. This linear relationship between I_{cath} and $\log WL$ was also present across similar film thicknesses in the work of McCafferty data³⁷ as well as the finite element modeling study by Morris and Smyrl⁸; however, the polarization parameters considered in those studies were extracted in the linear limit of kinetics near the open circuit potential. This analysis therefore yields another important insight; the nature of the kinetics

itself does not affect the observation of a linear relationship between total cathodic current and logarithm of the WL thickness across a certain range of WL thicknesses lower than the boundary layer for natural convection (δ_{nc}). However, the particular numerical values that the slope and the intercept of the linear fit assume are dependent on the specific polarization kinetics chosen.

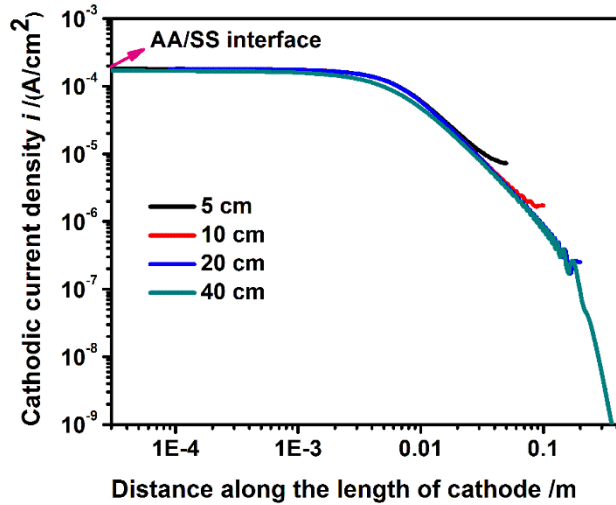


Figure 3.15: Comparisons of cathodic current density (absolute value) distributions along the length of cathode for the length of cathode=5, 10, 20, 40 cm for a $WL = 89 \mu\text{m}$.

In order to justify the independence of I_C/W on L_C for a limited range of WL , comparisons of current density distributions along the length of cathode for cathodes ranging from 5 to 40 cm when $WL=89 \mu\text{m}$ was presented in Figure 3.15. Cathodic current densities were highest and stayed as a constant along the first 3 mm of the cathode from the interface because this region on all of the cathodes was under M-T controlled kinetics, before decaying at an almost same rate along the rest of the cathode for all four cases. Analysis shows that for the L_c studied, more than 90% of the I_C/W resulted from the first 5 cm of the cathode (shown in Table 3.3). In addition, the current densities over the first 800 μm from the AA/SS interface along the length of the cathode were virtually identical for all L_c in Figure 3.15, thus it is not surprising that the total current at low WL thicknesses was independent of the cathode length.

Table 3.3: Percentage of ratio of I_C/W for the first 5cm of L_c to that for the entire cathode for $L_c = 5, 10, 20, 40\text{cm}$

L_c (cm)	Percentage (%)
5	100
10	94.2
20	93.5
40	92.5

3.6.4 Implications and Limitations

As with all models, the modeling approach used here has several limitations. The most important are: 1) the assumption of a uniform thin layer of electrolyte across the entire galvanic couple, which is not always the case due to imperfect wetting, especially at the edge of the cathode/anode. This imperfect wetting would lead to a shorter effective length of cathode available. The effect on the total current would depend on what regime(s) are sampled by the droplet and will be reported in future work, 2) the assumption of a static, stagnant, and uniform electrolyte layer with constant chemical concentration and conductivity neglects the fact of changes in chemical (solution chemistry, corrosion products), electrochemical (corrosion kinetics) and physical (evaporation, temperature) conditions can and do occur in reality; 3) The current work focused on the contribution from cathode, using an anode that is largely non-polarizable, 4) the assumption of steady-state is made in the study, neglecting the time-evolution of cathodic current available and 5) only ohmic drop is considered, which is an intrinsic limitation of the use of Laplace's Equation-based modeling, with diffusion effects being captured through the effects on cathodic kinetics.

It should be also noted that the limiting current density i_{lim} in this study is obtained based on mass-transfer limited cathodic kinetics pertinent to oxygen reduction reaction when the dominant oxidizer in the solution is dissolved oxygen only. There might be some uncertainty

brought by different oxidizer species in terms of critical natural convection boundary layer thickness. To evaluate the effect of oxidizer species on this critical thickness value during their reduction reaction at the same species concentration and number of electrons transferred, two other oxidizer species persulfate ion ($S_2O_8^{2-}$), and hydrogen peroxide (H_2O_2) are introduced to compare with oxygen. The former species was used in modified ASTM B-117 test in Chapter 2, and the latter one is a typical intermediate during ORR reaction. By combining Equation 3.1 and 3.2, one can obtain Levich Equation assuming concentration of oxidizer at the electrode surface equal to 0:

$$i_{lim} = 0.620nFD_{oxidizer}^{2/3} \nu^{-1/6} C_{oxidizer,bulk} \left(\frac{2\pi}{60} rpm \right)^{0.5} \quad (3.3)$$

The pertinent parameters of persulfate ion, hydrogen peroxide and dissolved oxygen in 1M NaCl³⁸ and calculated i_{lim} for these three species when rpm = 100 are listed in Table 3.4, assuming concentration of all the species is equal to equilibrium concentration of dissolved oxygen in 1M NaCl. One can see that i_{lim} of these species at the same rpm follows this order: $S_2O_8^{2-} < H_2O_2 < O_2$. Unfortunately, we do not have experimental data of cathodic kinetics with respect to $S_2O_8^{2-}/H_2O_2$ reduction in quiescent 0.6M NaCl in order to obtain the critical natural convection layer thickness as we did for oxygen shown in Figure 3.3, but one can postulate that the i_{lim} of these species in the quiescent solution would also follow this order: $S_2O_8^{2-} < H_2O_2 < O_2$, so that corresponding natural convection boundary layer thickness would be the same assuming all the species have the same concentration. RDE studies in $S_2O_8^{2-}$ and H_2O_2 containing sodium chloride solution will be performed in the future work.

Table 3.4: The pertinent parameters of persulfate ion, hydrogen peroxide and dissolved oxygen in 1M NaCl³⁸ and calculated i_{lim} for $S_2O_8^{2-}$, H_2O_2 and O_2 .

Species	ν (m ² /s)	D (m ² /s)	$C_{oxidizer,bulk}$ (M)	n	i_{lim} (A/cm ²)
$S_2O_8^{2-}$	9.95×10^{-7}	8×10^{-10}	0.00021	2	7.02×10^{-5}
H_2O_2	1.01×10^{-6}	1.4×10^{-9}	0.00021	2	1.02×10^{-4}
O_2	1.01×10^{-6}	1.9×10^{-9}	0.00021	2	1.24×10^{-4}

Despite these limitations the implications of the work should be noted. The method for determining the natural convection layer should be applicable to any system for which the hydrodynamic boundary layer can be controlled (e.g., rotating disk, rotating cylinder, flow channel, etc.). The presence of the different regimes of cathode length and WL thickness represent a key element in understanding the factors controlling galvanic interactions under atmospheric conditions. In particular, the fact that cathode length matters for $WL > 800 \mu\text{m}$ is surprising; intuition might lead one to believe that current would not be thrown through an $800 \mu\text{m}$ WL from a cathode surface 5 cm away (a L_c : WL of 125), but in fact, the current is $\sim 5x$ higher than that of a 1 cm long cathode. These longer throwing distances have important implications for the sizing of samples for chamber or outdoor testing, as samples that are too small will be non-conservative results. The decrease in total current that occurs for small cathodes (< 9.25 cm in the present case) at larger WL highlights the importance of considering the interplay between ohmic drop and mass transport for cathodic reactions when considering galvanic interactions under atmospheric conditions. In addition, the observation of oxide film effects on the diffusion limited current density at thin ($< 40 \mu\text{m}$ in the cases studied here) is important as otherwise, the amount of cathodic current available will be overestimated under these conditions, which would lead to substantial errors, particularly in cases of wetting and drying.

3.7 Conclusions

This study assesses how the total cathodic current capacity of a surface on the electrolyte film thickness and cathode size in a galvanic couple. It spans the range of WL thickness from full immersion conditions (where the total cathode current scales with cathode size) to the thin film regime in which the WL is the diffusion boundary layer thickness. In order to fully assess the transition from thin film to thick film condition, an understanding of the natural convection layer thickness is required. The natural convection layer defines the upper limit for true thin film behavior for atmospheric corrosion, and it can be experimentally determined by combining RDE experiments with data from quiescent conditions. For the conditions studied here, the natural convection boundary layer was found to be close to 800 μm . For very thin electrolyte layers, it was shown that oxide films can limit cathodic kinetics which will have important implications for galvanic corrosion productions under wetting and drying. The WL thickness, cathode length and electrochemical kinetics interact to create four regimes of total cathode current as a function of WL thickness. The prediction of a decrease in total available cathodic current from stainless steel upon an increase in WL thickness for small ($L_c < 9.25$ cm) is unique and has implications both for corrosion testing and corrosion prediction. The dependences can be understood by considering the competitive effects of ohmic drop and mass transport of oxygen on the total current for different cathode lengths.

3.8 Acknowledgement

The financial support from Office of Naval Research (ONR) via Grants N00014-14-1-0012 and N00014-17-1-2033, Sea-Based Aviation Program, Mr. William Nickerson, Program Manager is gratefully acknowledged.

3.9 References

1. C. Leygraf, I. O. Wallinder, J. Tidblad, and T. Graedel, *Atmospheric Corrosion*, John Wiley & Sons, Inc., (2016).
2. N. D. Tomashov, *Corrosion*, **20**, 7t–14t (1964).
3. M. Stratmann, *Berichte der Bunsengesellschaft für physikalische Chemie*, **94**, 626–639 (1990).
4. P. R. Roberge, R. D. Klassen, and P. W. Haberecht, *Mater. Des.*, **23**, 321–330 (2002).
5. E. Schindelholz and R. G. Kelly, *Corros. Rev.*, **30**, 135–170 (2012).
6. G. S. Frankel, *J. Electrochem. Soc.*, **145**, 2186–2198 (1998).
7. I. S. Cole, N. S. Azmat, A. Kanta, and M. Venkatraman, *Int. Mater. Rev.*, **54**, 117–133 (2009).
8. R. Morris and W. Smyrl, *J. Electrochem. Soc.*, **136**, 3229–3236 (1989).
9. M. Stratmann, *Corros. Sci.*, **27**, 869–872 (1987).
10. M. Stratmann and H. Streckel, *Corros. Sci.*, **30**, 681–696 (1990).
11. M. Stratmann and H. Streckel, *Corros. Sci.*, **30**, 697–714 (1990).
12. M. Stratmann, H. Streckel, K. T. Kim, and S. Crockett, *Corros. Sci.*, **30**, 715–734 (1990).
13. A. Nishikata, Y. Ichihara, and T. Tsuru, *Corros. Sci.*, **37**, 897–911 (1995).
14. A. Nishikata, Y. Ichihara, Y. Hayashi, and T. Tsuru, *J. Electrochem. Soc.*, **144**, 1244–1252 (1997).
15. A. Nishikata, Y. Ichihara, and T. Tsuru, *Corros. Sci.*, **37**, 897–911 (1995).
16. G. S. Frankel, M. Stratmann, M. Rohwerder, A. Michalik, B. Maier, J. Dora, and M. Wicinski, *Corros. Sci.*, **49**, 2021–2036 (2007).
17. A. P. Yadav, H. Katayama, K. Noda, H. Masuda, A. Nishikata, and T. Tsuru, *Electrochim. Acta*, **52**, 3121–3129 (2007).
18. F. Thébault, B. Vuillemin, R. Oltra, K. Ogle, and C. Allely, *Electrochim. Acta*, **53**, 5226–5234 (2008).

19. M. S. Venkatraman, I. S. Cole, and B. Emmanuel, *Electrochim. Acta*, **56**, 7171–7179 (2011).
20. H. Simillion, O. Dolgikh, H. Terryn, and J. Deconinck, *Corros. Rev.*, **32**, 73–100 (2014).
21. S. Palani, T. Hack, J. Deconinck, and H. Lohner, *Corros. Sci.*, **78**, 89–100 (2014).
22. O. Dolgikh, A. C. Bastos, A. Oliveira, C. Dan, and J. Deconinck, *Corros. Sci.*, **102**, 338–347 (2016).
23. A. D. King, J. S. Lee, and J. R. Scully, *J. Electrochem. Soc.*, **163**, C342–C356 (2016).
24. O. Dolgikh, A. -S. Demeter, S. V. Lamaka, M. Taryba, A. C. Bastos, M. C. Quevedo, and J. Deconinck, *Electrochim. Acta*, **203**, 379–387 (2016).
25. C. Amatore, S. Szunerits, L. Thouin, and J.-S. Warkocz, *J. Electroanal. Chem.*, **500**, 62–70 (2001).
26. E. Gileadi, *Electrode Kinetics for Chemists, Chemical Engineers, and Materials Scientists*, VCH Publishers, Inc., (1993).
27. Z. Y. Chen, F. Cui, and R. G. Kelly, *J. Electrochem. Soc.*, **155**, C360–C368 (2008).
28. Z. Y. Chen and R. G. Kelly, *J. Electrochem. Soc.*, **157**, C69–C78 (2010).
29. Y. L. Cheng, Z. Zhang, F. H. Cao, J. F. Li, J. Q. Zhang, J. M. Wang, and C. N. Cao, *Corros. Sci.*, **46**, 1649–1667 (2004).
30. C. Wagner, *J. Electrochem. Soc.*, **99**, 1-12 (1952).
31. J. T. Waber, *J. Electrochem. Soc.*, **101**, 271-276 (1954).
32. C. Liu, V. N. Rafla, J. R. Scully, and R. G. Kelly, “Mathematical Modeling of Potential and Current Distributions for Atmospheric Corrosion of Galvanic Coupling in Airframe Components,” NACE International (2015).
33. C. Liu and R. G. Kelly, *Electrochem. Soc. Interface*, **23**, 47–51 (2014).
34. A. J. Bard and L. R. Faulkner, *Electrochemical Methods: Fundamentals and Applications*, 2nd ed., John Wiley & Sons, Inc. (2000).
35. J. Newman and K. E. Thomas-Alyea, *Electrochemical Systems*, John Wiley & Sons, Inc., Hoboken, N.J., U.S. (2004).
36. S. H. Zhang and S. B. Lyon, *Corros. Sci.*, **35**, 713–718 (1993).

37. E. McCafferty, *J. Electrochem. Soc.*, **124**, 1869–1878 (1977).
38. M.E. Parker, University of Virginia, Charlottesville, Ph.D. Dissertation (2018)

4. Effect of Solution Chemistry (pH, Conductivity and Dissolved Metal Species) on the Distribution of Localized Corrosion in AA7050/SS316L Couple

Summary:

As mentioned in Chapter 2, well-defined electrochemical kinetics as boundary conditions are vital for accurate Laplace-Equation based modeling prediction. Several variables pertinent to solution chemistry such as pH and dissolved metal ion species can potentially affect electrochemical kinetics of AA7050 and SS316L. Besides these, electrolyte conductivity is another important variable which can affect electrochemical distributions in the galvanic coupling system. Dissolved metal species investigated in this chapter are Al^{3+} , Zn^{2+} and Mg^{2+} since Al, Zn and Mg are major constituent elements in AA7050 or particulates embedded in corresponding metal-rich primers, and they can be diffused into corrosion solution during the self- or galvanic-coupling induced dissolution of AA7050 substrate and/or its protective metal-rich primers. However, there is a very limited number of previous works regarding the effect of Al^{3+} , Zn^{2+} and Mg^{2+} on the electrochemical kinetics of SS316L and AA7050, let alone the effect of conductivity on the electrochemical distributions in a galvanic coupling system with complicated geometry. The structure of this chapter is laid out as: (1) the effect of pH and conductivity on the electrochemical distributions in AA7050/SS316L with as fastener-hole configuration was studied in Part 1; (2,3) Part 2&3 investigated the effect of Zn^{2+} & Mg^{2+} (Part 2), and Al^{3+} (Part 3) on the cathodic kinetics of AA7050 as a function of concentration and immersion, assuming there was no galvanic coupling between AA7050 and SS316L such that AA7050 is the cathode and metal-richer primer is the anode; (4) Part 4 combined the study from Part 2 and 3 to investigate the effect of Al^{3+} and Mg^{2+} on the galvanic corrosion distribution between SS316L and AA7050 without and with metal-rich primer involved.

4.1 Abstract

In this study, the effect of solution pH, conductivity, pertinent cation species (Al^{3+} , Zn^{2+} and Mg^{2+}) on the electrochemical and galvanic corrosion distributions between SS316L and AA7050 was well studied. For the aspect of solution pH and conductivity, a FEM based modeling approach with experimentally determined electrochemical kinetics as boundary conditions was used to simulate potential and current density distributions in the galvanic coupling with a simulated fastener-hole configuration based on different pH and conductivity assumptions in the solution. It shows that the acidic crevice solution at the mouth leads to more severe corrosion at the occluded site of the crevice than mild alkaline crevice solution. It has been indicated that linear conductivity assumption is good enough to represent the effect of varying conductivity on electrochemical distributions and reflect corrosion behavior along the anode if one focuses on the study of anode only, implying that conductivity might be a secondary factor affecting electrochemical distributions in the galvanic coupling; but the estimation of conductivity function should be within a reasonable range.

As for the aspect of pertinent metallic cation, their effect on cathodic kinetics of Al alloys and on the galvanic corrosion between the couple were both investigated by a number of electrochemical and instrumental characterization techniques. Zn^{2+} and Mg^{2+} show inhibitive effect due to formation of precipitates on Cu-containing IMCs embedded in the AA7050 surface thus impeding ORR activity; whereas Al^{3+} shows promotive effect on HER cathodic kinetics due to enhanced proton diffusivity, this effect is not only observed on Al alloys, but also on Pt and stainless steel. The cation study for the galvanic couple indicates that: addition of Al^{3+} or Mg^{2+} into NaCl solution significantly affects galvanic corrosion between AA7050/SS316L. Al^{3+} is corrosion accelerator, and Mg^{2+} is corrosion inhibitor.

4.2 Hypothesis

For pertinent solution chemistry variables: pH, solution conductivity, and M^{n+} (Zn^{2+} , Mg^{2+} , and Al^{3+} are selected since they are major constituent elements in AA7050), they are all primary factors affecting electrochemical and corrosion distributions in the AA7050/SS316L couple. A lower pH can lead to enhanced HER diffusion-limited cathodic kinetics of SS316L, resulting in a larger scale galvanic corrosion distribution; electrochemical and corrosion distributions in the galvanic coupling system are highly dependent on conductivity, and varying conductivity assumption can give different results compared to constant conductivity assumption; Zn^{2+} , Mg^{2+} , and Al^{3+} all lowers cathodic kinetics of both SS316L and AA7050 due to their depressed effect on ORR cathodic kinetics, which in turn lowers the galvanic corrosion damage between SS316L and AA7050.

4.3 Part 1: Mathematical Modeling of Effects of pH and Conductivity on Electrochemical Distributions in Galvanic Coupling in Airframe Components

The work presented in this chapter has been reported in the following publication:

C. Liu, R.G. Kelly, “Mathematical Modeling of Effect of pH and Conductivity on Electrochemical Distributions in Galvanic Coupling in Airframe Components”, DoD Corrosion Conference 2015, Pittsburgh, PA, November 15-19, 2015.

4.3.1 Introduction

Connections involving stainless steel (SS) fasteners in intimate contact with aluminum (Al)-alloy components in airframes are frequently encountered after repair. When the Al-alloy components are exposed to marine environments, splash, rainwater, or salt enabled deliquescence can lead to the formation and maintenance of a thin surface electrolyte which contains chloride species¹. This thin film/galvanic couple configuration inherently aids in the trapping/wicking of

electrolyte into a tight crevice. A localized galvanic cell between the SS fastener and Al alloy can be formed as a consequence, leading to severe corrosion on the Al-alloy.

Numerous geometric and local environmental variables could affect potential and current density distributions inside such a galvanic couple. Studying the relationship among these variables and the corrosion behaviors that are expressed in terms of potential and current distributions will allow the development of a quantitative understanding of the effects of these variables and the application of that knowledge to design corresponding mitigation strategies. In this paper, two important variables are discussed: the pH and the conductivity of the trapped solution within the crevice formed by the SS fastener and the Al alloy.

The variation of the pH within the crevice is the result of hydrolysis of the aluminum ions created by dissolution and their diffusion out of the crevice. For single corrosion pits on pure aluminum, the pH of pit solution has been measured to be between 3 and 4 ². However, the local pH within a crevice can differ from that in a corrosion pit due to its geometry. Alavi and Cottis found that although the pH at crevice mouth was about 3-4, in the most occluded crevice region, the pH was near 8 for in a corroding crevice of UNS A97475 ³. This pH discrepancy within the crevice was also reported by Cooper and Lewis ^{4,5}.

Conductivity influences ohmic resistance, causing potential drop inside a localized corrosion environment. Pickering ⁶⁻⁹ developed the IR model to illustrate how the restricted crevice geometry triggers potential (IR) drops within the crevice solution for materials that exhibit active-passive transitions. However, an ohmic drop serves to diminish the dissolution rate of materials that do not have active-passive transitions in the crevice solution, which can lead to the creation of higher pH deeper in the crevice, thereby focusing the corrosion attack near the mouth ^{10,11}.

There has been increasing demand for better characterization of the controlling parameters in localized corrosion in systems of complicated geometry. The Finite Element Method (FEM) is a numerical tool which is widely applied into localized corrosion modeling¹². In this work, FEM was used to build up the mathematical framework in order to investigate the effects of pH and conductivity on the electrochemical distributions in the crevice formed in the galvanic couple between UNS A97050 component and UNS S30400 fastener. Experimentally determined electrochemical kinetics served as boundary conditions in the modeling work.

4.3.2 Methodology

4.3.2.1 Mathematical Development

The governing equation used in this modeling work is Laplace's Equation. Details of mathematical derivation of Laplace's Equation has been discussed in Chapter 1&2.

4.3.2.2 Electrochemical Testing

Aluminum alloy UNS A97050 and stainless steel UNS S30400 were used in this work. The composition of two materials is listed in Table 4.1 and

Table 4.2, respectively. The size of each sample was 654.16 mm² (1 in²) square with a thickness of 6.35 mm (0.25 in). They were cut from the SL plane of the bulk materials. These samples were wet ground to 1200 grits with alumina paper to obtain a smooth metal surface for this study. Deionized water was used to clean the sample surface before testing. It should be noted that UNS S30400 was used rather than UNS S31603 (SS 316L) here, since this study was aimed to correlate Rafla's experimental work¹³ in which UNS30400 was utilized as cathode, pertinent discussion will be presented later.

Chemicals of analytical grade quality were used in the testing. Sodium chloride (NaCl) was used as bulk solution for this study. Different concentrations of Sodium Aluminate (NaAlO₂) or hydrochloric acid (HCl) were added to the NaCl solutions to create alkaline or acidic environment, respectively.

Table 4.1: Bulk composition of UNS A97050

Composition	Element present (wt%)									
	Si	Fe	Cu	Mn	Mg	Cr	Zn	Ti	Zr	Al
Average mass%	0.12	0.15	2.6	0.10	2.6	0.04	6.7	0.06	0.15	87.54

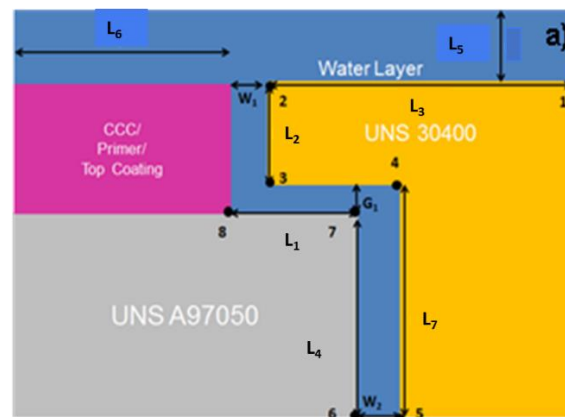
Table 4.2: Compsotion of UNS S30400

Composition	Element present (wt%)									
	C	Mn	Si	P	S	Cr	Ni	N	Fe	
Average mass %	0.08	2.0	0.75	0.045	0.030	20.0	10.5	0.1	66.49	

Full immersion measurements were made using a glass flat cell with a 1 cm² exposed area defined with a Teflon knife-edged washer to prevent crevice corrosion. A Pt counter electrode and a saturated calomel reference electrode were used. Cyclic potentiodynamic polarization experiment was carried out at a scan rate of 1 mV/s. All tests were conducted at laboratory temperature (20°C) in both quiescent and deaerated (1 hour) solutions to mimic the crevice geometry.

4.3.2.3 Modeling Setup

A Dell 3610 Workstation with Quad-core processors and 8 GB of RAM was used to perform the mathematical modeling in this work. The Secondary Current Distribution Module at steady state in COMSOL™ Multiphysics software (version 4.4) was applied to calculate electrochemical distributions in the simulated geometry of galvanic couple. The modeling domain of interest is the electrolyte only. A simplified fastener hole configuration was used in the modeling which is shown in Figure 4.1a. Figure 4.1b is a visual demonstration how COMSOL software divided electrolyte domain into fine meshes. Pertinent geometric factors in the simplified geometry are listed in Table 4.3. Eight different points along the UNS S30400 fastener and UNS A97050 component are used as points of comparison for potential and current density values.



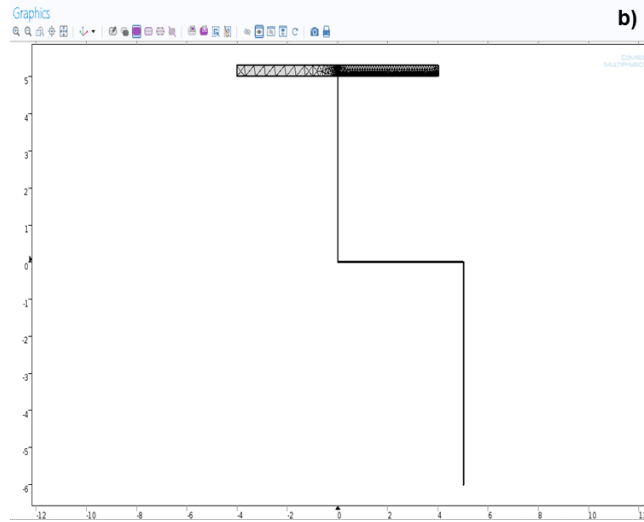


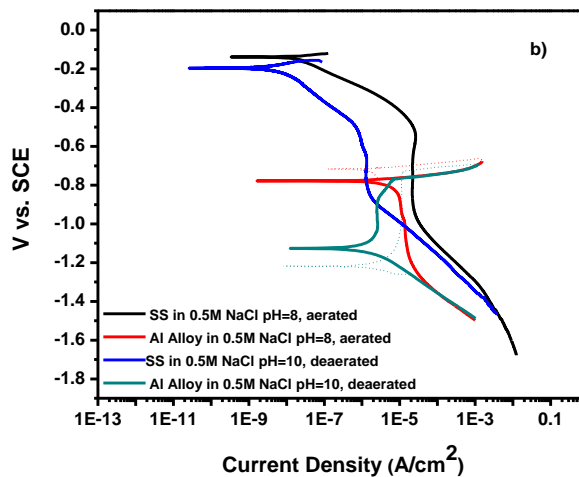
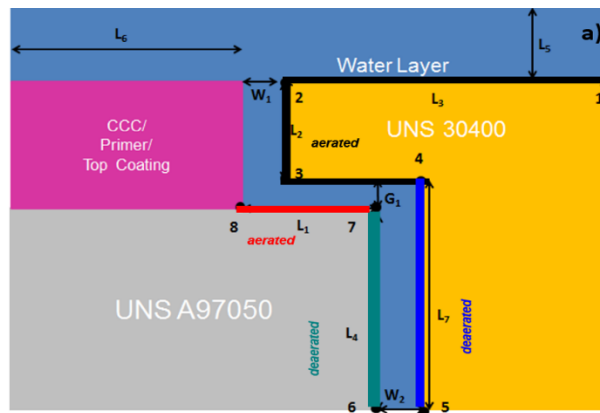
Figure 4.1: a) Simplified geometry of fastener hole configuration involving SS fastener (UNS S30400), Al alloy (UNS A97050), coating and electrolyte. All pertinent geometric parameters and indicating points are included; b) Screenshot of mesh of electrolyte domain in the modeling software.

Table 4.3: Range of Values of All Pertinent Geometric Parameters

No.	Parameter	Influencing Factor
1	W_1	Set by scribe size in coating
2	W_2	Set by tolerance, wet installation (sealant), sealant coverage
3	G_1	Set by primer and chromate conversion coating (CCC) coverage
4	L_1	Set by the fastener given
5	L_2	Set by the fastener given
6	L_3	Set by the coating coverage
7	L_4	Set by the plate thickness and sealant coverage
8	L_5	Set by loading density (L.D.) and relative humidity (R.H.)
9	L_6	Set by max cathode calculation
10	L_7	Set by the plate thickness and sealant coverage

4.3.2.4 Electrochemical Boundary Conditions

The two types of boundary conditions used in this work are shown in Figure 4.2. The first one is associated with a condition where aerated solution exists at the crevice mouth with a pH of 8, and deaerated solution exists within the occluded site of the crevice which has a pH of 10. This type of boundary condition was used in both the pH and conductivity studies. The second one is associated with a condition where aerated solution exists at the crevice mouth with a pH of 3, and deaerated solution exists at the occluded site of the crevice which has a pH of 10. The second type was used in the pH study only. Details these two boundary conditions are listed in Table 4.4 and Table 4.5, respectively.



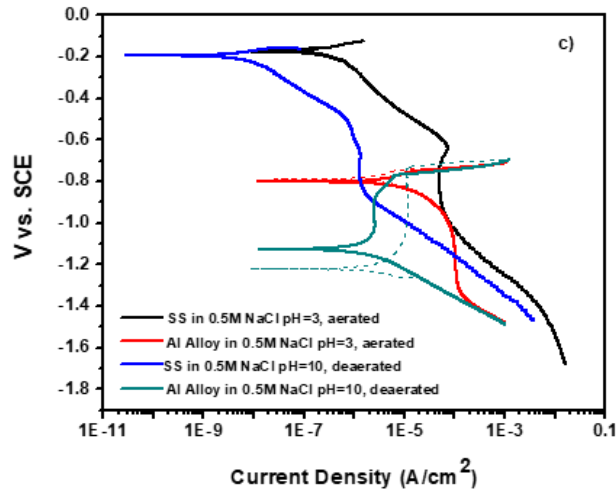


Figure 4.2: a) Geometry and boundary conditions in the modeling; b) First type of electrochemical kinetics (boundary conditions) of Al Alloy and SS; c) Second type of electrochemical kinetics (boundary conditions) of Al Alloy and SS. Solid lines of Al alloy represent reverse scans after reaching highest current density limit during the cyclic potentiodynamic polarizations.

Table 4.4: Boundary Conditions in First Type of Boundary Condition

Boundaries		Description
1	1-2-3-4	UNS S30400 in aerated 0.5M NaCl solution pH=8
2	4-5	UNS S30400 in deaerated 0.5M NaCl solution pH=10
3	5-6-7	UNS A97050 in deaerated 0.5M NaCl solution pH=10
4	7-8	UNS A97050 in aerated 0.5M NaCl solution pH=8

Table 4.5: Boundary Conditions in Second Type of Boundary Condition

Boundaries		Description
1	1-2-3-4	UNS S30400 in aerated 0.5M NaCl solution pH=3
2	4-5	UNS S30400 in deaerated 0.5M NaCl solution pH=10
3	5-6-7	UNS A97050 in deaerated 0.5M NaCl solution pH=10
4	7-8	UNS A97050 in aerated 0.5M NaCl solution pH=3

4.3.3 Results and Discussion

4.3.3.1 Effect of pH on Potential and Current Distributions

In this subsection, two distinct cases relative to the effect of pH on potential and current distributions in the galvanic coupling induced crevice are compared and discussed. In the first case, it is assumed that the amount of hydroxide ion produced from oxygen reduction reaction (ORR) at the dominant crevice cathode (i.e., the SS fastener) is more than what is needed to balance the acid produced by the hydrolysis of the aluminum ion (Al^{3+}) from anode dissolution (Al alloy). As a result, crevice solution at the crevice mouth will be alkaline (pH=8 in this case). This hydroxide production will lead to higher pH values deeper into the crevice which would in turn lead to passivation of the Al alloy deeper in the crevice. The second case is based on the experimental result from Alavi and Cottis' work ³, in which they found that solution at the crevice mouth was mildly acidic (pH 3~4), whilst it became alkaline (pH=8) when moving to the deeper parts of the crevice. This acidic-to-alkaline transition was adopted in this work, except that solution along the deeper parts was considered to be more alkaline (pH=10). The electrochemical kinetics shown in Figure 4.2b was applied to the first case as boundary conditions, while that in Figure 4.2c was applied to the second case. Note that only the reverse scans of Al alloy polarization curve were used as anodic boundary conditions (shown as solid lines in Figure 4.2b and Figure 4.2c) as these better represent the electrochemical kinetics of an established localized corrosion site than the forward scan. The geometry for the two cases was the same: $W_1=15 \mu\text{m}$, $W_2 = 15 \mu\text{m}$, $G_1= 15 \mu\text{m}$, $L_1 = 5 \text{ mm}$, $L_2 = 5 \text{ mm}$, $L_3 = 4 \text{ mm}$, $L_4 = 6 \text{ mm}$ $L_5 = 0.3 \text{ mm}$. Comparisons of potential and current density distributions along the anode (Al alloy) are shown in Figure 4.3.

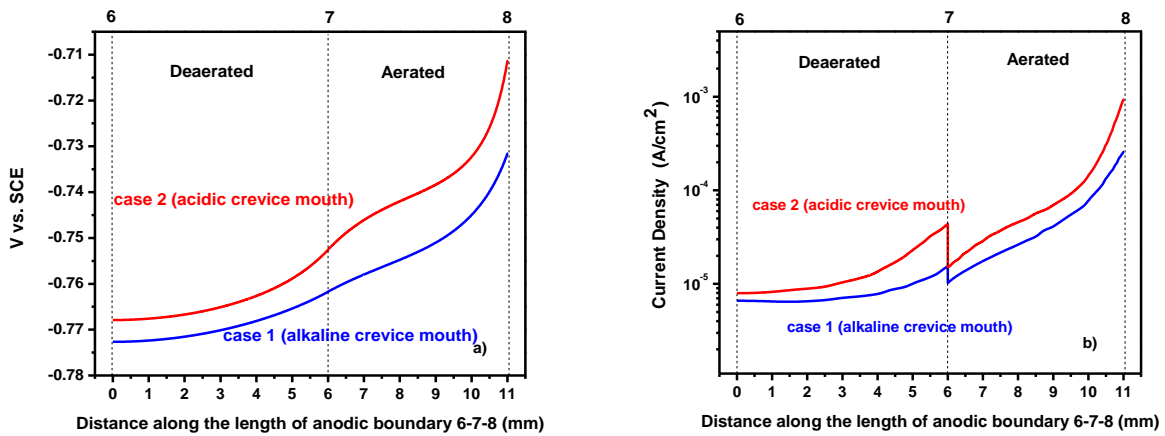


Figure 4.3: Comparisons of a) potential distributions and b) current density distributions along the anodic boundaries between alkaline crevice mouth (case 1) and acidic crevice mouth (case 2) solution assumptions.

For the potential distributions (Figure 4.3a), it can be seen that Case 1 has a relatively large potential range (from -0.768 V to -0.710 V) compared to case 2 (from -0.773 V to -0.732 V), and the potential in Case 1 is always more negative than that in Case 2. Although both cases have the same boundary conditions (SS/Al alloy in 0.5M NaCl solution with pH=10) in the deaerated region, there is a potential difference which is about 0.005V between the two cases along most of the regime until it is near to point 7. Beyond point 7, the potential difference becomes larger along the aerated region until it reaches a maximum at point 8, which is equal to ~0.022 V. As for the current density distributions (Figure 4.3b), Case 1 has smaller current densities than Case 2 along the entire anodic boundary. It is worthwhile to see that the average current density at aerated regime is larger than deaerated regime in either of cases, implying that Al alloy experiences more localized corrosion at the aerated regime than deaerated regime.

In order to investigate repassivation behavior along the anodic boundaries, the repassivation potentials of Al alloy in aerated and deaerated NaCl solutions in different pH values are needed. These values are shown in

Table 4.6. By considering repassivation potential information into potential distribution profiles of two cases, a passive-to-active transition along the anodic boundary can be predicted as shown in Figure 4.4. In Case 1 (Figure 4.4a), the potential along the entire aerated region is above $E_{rp, aerated} = -0.770$ V, whereas in the deaerated region, only a small portion of boundary 6-7 (at roughly 0.8mm below point 7 along boundary 6-7) is above $E_{rp, deaerated} = -0.765$ V. This result indicates localized corrosion is mainly focused at the crevice mouth in Case 1, which is explicitly illustrated in Figure 4.4c. In Case 2 (Figure 4.4), the potential along the aerated region is all above $E_{rp, aerated} = -0.795$ V as well, but half of the deaerated regime near point 7 is above $E_{rp, deaerated} = -0.765$ V, the rest of the deaerated regime is below $E_{rp, deaerated}$. This result shows that the degree of localized corrosion attack along the deaerated regime in Case 1 is around $\frac{3mm}{0.8mm} \approx 4 \frac{3mm}{0.8mm} \approx 4$ times that in Case 2, which is explicitly shown in Figure 4.4d.

Table 4.6: Repassivation Potentials of Al Alloy in Case 1&2

	Case 1	Case 2
$E_{rp, aerated}$	-0.770 V	-0.795 V
$E_{rp, deaerated}$	-0.765 V	-0.765 V

corrosion was more dominant at the near-crevice mouth area. However, our modeling failed to predict the localized corrosion damages inside the crevice as shown in Figure 4.5b, due to the assumption of boundary conditions that uniform electrochemical property was across the entire AA surface, whereas AA has highly microstructure heterogeneity everywhere in reality.

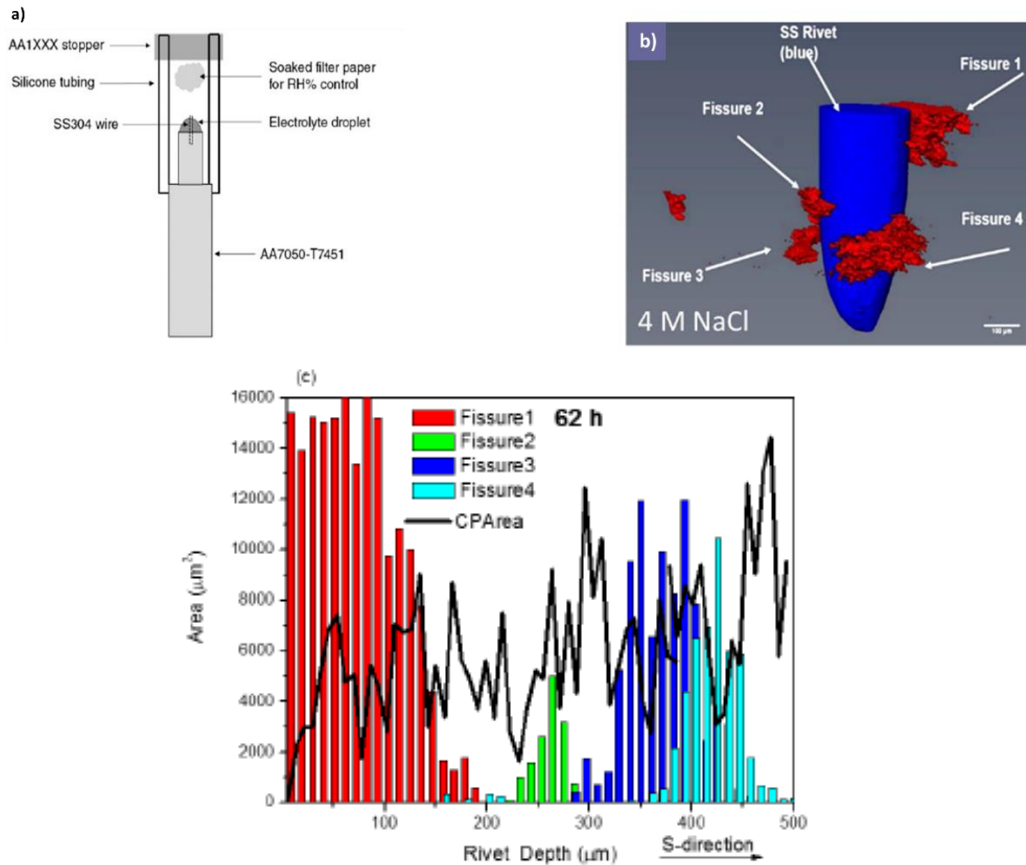


Figure 4.5: a) a schematic diagram of galvanic coupling between a SS rivet and an AA7050-T7451 under a droplet; b) a typical XCT result to show the distribution of corrosion fissures in AA7050 (Red) along the SS rivet (Blue); c) corrosion fissure area bars for the 4 fissures observed in AA7050 in the 4M NaCl exposure after 62 hours as a function of rivet depth.

4.3.3.2 Effect of Conductivity on Potential and Current Distributions

In this subsection, three different assumptions concerning the conductivity within the crevice are compared and discussed. We set the conductivity of water layer outside the crevice to be 6 S/m, but applied three distinct conductivity assumptions in the crevice solution. The first assumption is constant conductivity equal to 6 S/m throughout the entire crevice. The second one

is that crevice is treated as a pit, in which conductivity at the pit mouth is equal to 11 S/m, and linearly increases to 17 S/m at the pit bottom. The values of conductivity at pit mouth and bottom were obtained from Wong and Alkire's work². The third assumption is that conductivity distribution along the crevice is an arbitrary piecewise function with all conductivities fall within a range from 6 to 17 S/m. Conductivity distributions along the cathodic boundaries for three assumptions are shown in Figure 4.6. The geometry setup is the same as that in pH effect study.

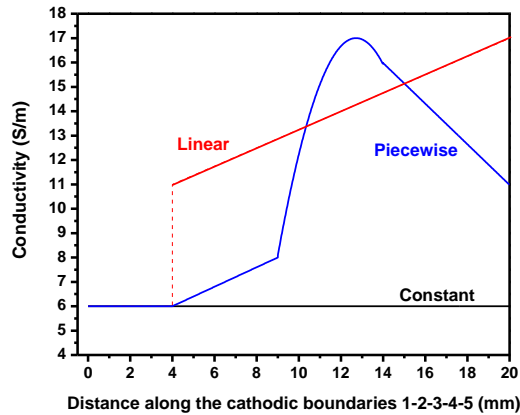


Figure 4.6: Comparison of conductivity distributions under three different assumptions along the cathodic boundaries.

Potential and current density distributions under these assumptions are shown in Figure 4.7. In Figure 4.7a, it is obvious potential differences among three assumptions appear at the crevice mouth. The difference between linear and piecewise function assumptions becomes smaller as it moves to the occluded site of the crevice, whereas, the difference between the constant assumption and the linear or piecewise function assumption is negligible in the middle region (boundary 3-4), but increases gradually as it moves to the most occluded site (boundary 4-5). In Figure 4.7b, potential distributions along the entire anodic boundaries are shown to be almost the same for the linear and piecewise function assumptions, but they are distinguishable from the constant

assumption, especially along the boundary 6-7. For the current density distributions shown in Figure 4.7c and Figure 4.7d, it can be seen that the linear and piecewise function assumptions almost overlap along the cathodic and anodic boundaries, but they still have differences with the constant conductivity assumption. This finding also overturned the hypothesis raised earlier that conductivity could significantly affect electrochemical distributions, implying that it should be a secondary factor within a reasonable range.

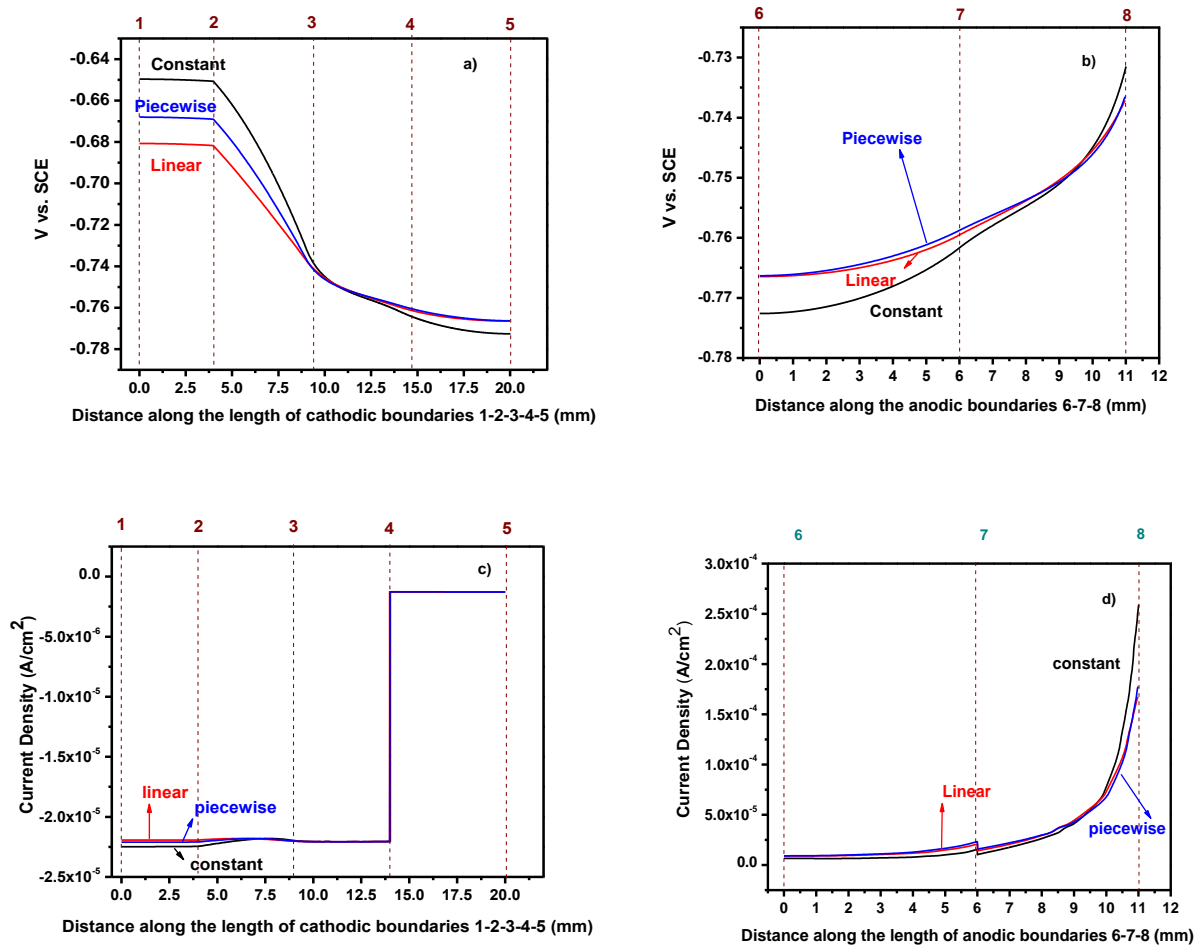


Figure 4.7: a) Comparison of potential distributions along cathodic boundaries; b) Comparison of potential distribution along anodic boundaries; c) Comparison of current density distributions along cathodic boundaries; d) Comparison of current density distributions along anodic boundaries.

A sensitivity study of the effect of conductivity on anodic current distribution along boundaries 6-7-8 is performed with conductivity ranging from 0.3 to 25 S/m. The lower limit 0.3 S/m is equivalent to conductivity of 2M AlCl₃ which has maximum Al ion concentration appearing in the Al crevice, and the upper limit 25 S/m corresponds to 5.5 M NaCl which is the saturated NaCl concentration at room temperature. Comparisons of potential and anodic current density along anodic boundaries 6-7-8 under different conductivity assumptions are displayed in Figure 4.8a&b respectively. It is clearly seen that when conductivity ranges from 1 to 17 S/m, current distributions are similar to each other; when conductivity at two extremums (0.3 and 25 S/m respectively), current density distributions have significant difference from the those at medium range, and current density near the crevice mouth (point 8) is higher for 25 S/m and is lower for 0.3 S/m compared to the medium range. These comparisons infer that the estimation of conductivity as a function of position should be made within a reasonable range, which is 1~17 S/m in this study.

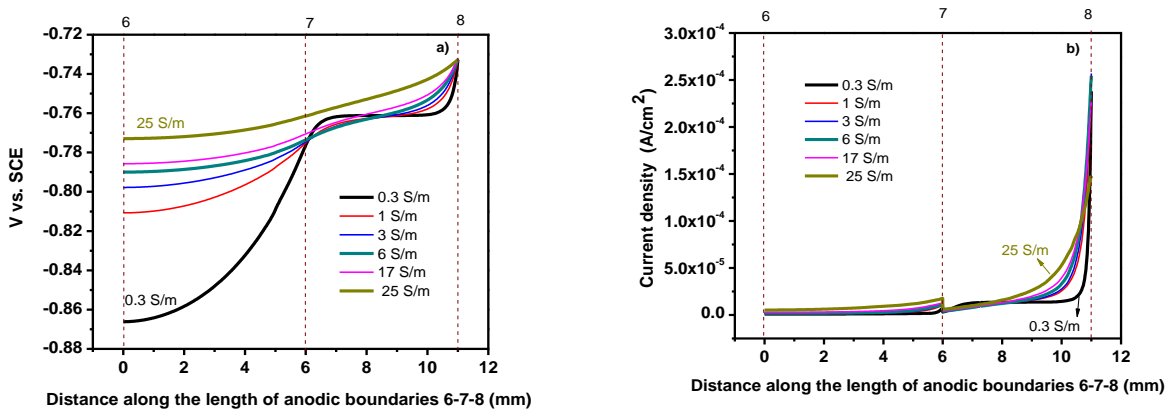


Figure 4.8: Comparison of a) potential and b) current density distributions along the anodic boundaries 6-7-8 under different conductivity assumptions.

The key points drawn from the conductivity study are: (1) the effect of varying conductivity is relatively small on the current density distributions on cathode/anode and potential distribution

on anode, compared to assuming constant conductivity; (2) Conductivity affects the cathodic potential distribution significantly, especially at the crevice mouth.; (3) if one want to make conductivity as a function of position, the estimation needs to be within a reasonable range, excessively over- or under-estimation can lead to a wrong prediction.

4.3.4 Conclusion

The effects of pH and conductivity on the potential and current distributions that develop in a fastener hole configuration involving a realistic thin film/galvanic coupling configuration between UNS A97050 component and SS fastener have been studied numerically. The modeling work was based on the Laplace Equation to simulate these electrochemical distributions under steady state. In the pH effect study, two types of boundary conditions were applied. They both have alkaline (pH=10) solution at the occluded site of the crevice, but different pH at the crevice mouth (acidic pH =3 in Case 1, and mild alkaline pH=8 in Case 2). It was shown that the acidic crevice solution at the mouth leads to more severe corrosion at the occluded site of the crevice than mild alkaline crevice solution. In conductivity study, three different conductivity assumptions were compared. It has been indicated that linear conductivity assumption is good enough to represent the effect of varying conductivity on electrochemical distributions and reflect corrosion behavior along the anode if one focus on the study of anode only, implying that conductivity might be a secondary factor affecting electrochemical distributions in the galvanic coupling; but the estimation of conductivity function should be within a reasonable range (1~17 S/m in this study).

4.3.5 Acknowledgements

We thank financial support from the Office of Naval Research (ONR) Grant N00014-14-1-0012; Mr. William Nickerson, Technical Officer, is gratefully appreciated.

4.3.6 References

1. E. Schindelholz, R.G. Kelly, "Wetting phenomena and time of wetness in atmospheric corrosion: a review," *Corrosion Reviews*, 30, 5-6 (2012): pp.135-170.
2. K.P. Wong, R.C. Alkire, "Local Chemistry and Growth of Single Corrosion Pits in Aluminum", *Journal of Electrochemical Society*, 137, 10 (1990), pp. 3010-3015.
3. A. Alavi, R.A. Cottis, "The Determination of pH, Potential and Chloride Concentration in Corroding Crevices on 304 Stainless Steel and 7475 Aluminum Alloy", *Corrosion Science*, 27, 5 (1987), pp.443-451.
4. K.R. Cooper, "Chemistry and Electrochemistry of Environment-Assisted Cracking of an Al-Zn-Mg-Cu Alloy", University of Virginia, VA, Ph.D. Dissertation (2001).
5. K.S. Lewis, "Determination of the Corrosion Conditions within Aircraft Lap-Splice Joints", University of Virginia, Charlottesville, VA, Master Thesis (1999).
6. H.W. Pickering, "The Significance of the Local Electrode Potential within Pits, Crevices and Cracks", *Corrosion Science*, 29 2-3 (1989), pp. 325-341
7. M. Wang, H.W. Pickering and Y. Xu, "Potential Distributions, Shape Evolution, and Modeling of Pits Growth for Ni in Sulfuric Acid", *Journal of Electrochemical Society*, 142, 9 (1995), pp.2986-2995
8. K. Cho, M.I. Abdulsalam, H.W. Pickering, "The Effect of Electrolyte Properties on the Mechanism of Crevice Corrosion in Pure Iron", *Journal of Electrochemical Society*, 145, 6 (1998), pp.1862-1869
9. Y. Xu, H.W. Pickering, "The Initial Potential and Current Distributions of the Crevice Corrosion Process", *Journal of Electrochemical Society*, 140, 3 (1993), pp. 658-668.
10. K.C. Stewart, "Intermediate Attack in Crevice Corrosion by Cathodic Focusing", University of Virginia, Charlottesville, VA, Ph.D. Dissertation (1999).
11. J. Lee, "Using Modeling and Microfabrication for Insights into Factors Controlling the Location of Crevice Attack", University of Virginia, Charlottesville, VA, Ph.D. Dissertation (2011).
12. C. Liu, R.G. Kelly, "The Use of Finite Element Method (FEM) in the Modeling of Localized Corrosion", *Interface*, 23, 4 (2014), pp. 47-51.
13. V.N. Rafla, "Localized Corrosion Damage Morphology and Corrosion Electrochemistry for Al-Zn-Mg-Cu Fastener Galvanic Couples in Marine Environments", University of Virginia, Charlottesville, VA, Ph.D. Dissertation (2018).

4.4 Part 2: The Cathodic Inhibition Effect of $[Zn^{2+}]$ and $[Mg^{2+}]$ on Cathodic Kinetics of AA7050- T7451

4.4.1 Introduction

Chromate-based coatings have been widely utilized in corrosion protection of aluminum alloy¹⁻⁵. Nevertheless, application of this type of coating has been limited due to the hazardous effect to the environment and human health, as a result, more environment-friendly compounds which provide chromate replacement inhibitors are being developed these years. Among these chromium-free compounds, magnesium rich primer (MgRP)⁶⁻¹² and zinc-rich primers (ZnRP)¹³⁻¹⁶ are excellent candidates providing cathodic protection to aluminum (Al) alloys. The protection mechanism of MgRP/ZnRP is that: the Mg/Zn pigment embedded in the primer matrix works as sacrificial anode and forms a galvanic couple with the Al-alloy substrate, forcing the substrate cathodically polarized below its corrosion potential. In the meantime, metallic cations (Mg^{2+} , and Zn^{2+}) produced from open circuit and sacrificial anodic dissolution are leached out of the primer matrix and diffuse into the corrosion solution, which might further impact cathodic kinetics of the Al alloy substrate. There are tremendous literature work focusing on the sacrificial-anode cathodic protection mechanism of these primers to the Al alloys¹⁷⁻²², however the following effect of the dissolved cation on the cathodic kinetics, especially mass-transfer limited region is rarely discussed in the literature, which will be addressed in this work.

An ideal paradigm of protection of Al-alloy substrate by a metal-rich primer would be: metal pigment from the primer provides active cathodic protection for the Al alloy, and then the dissolved metal cations from the pigment cathodically inhibit oxygen reduction reaction (ORR) which lowers the self-corrosion rate of the Al-alloy substrate if there was no cathodic protection

available. It is known that Cu-/Fe- containing intermetallic compounds (IMC)²³⁻²⁵, or replated Cu from dealloying²⁶, acts as a local cathodic site which increases susceptibility of localized corrosion due to microgalvanic coupling. Jakab *et al.*²⁷ used both experimental and modeling approaches to demonstrate that both charge-transfer and mass-transfer-controlled ORR reaction rates were increased with copper coverage in AA2024-T3, which inferred that the corrosion rate can be minimized by reducing copper coverage assuming it is controlled by the cathodic reaction. There are a number of literature work showing that several metallic cations cathodically inhibit oxygen reduction reaction by producing precipitates on the Fe/Cu-IMC in Al alloys. Aldykewicz *et al.*²⁸, Aballe *et al.*²⁹, Yasakau *et al.*³⁰, and Mishra *et al.*³¹ parsed the protective nature of lanthanide group (Ce, La, etc.) inhibitors via precipitating the lanthanide hydroxide compounds on Cu-IMC (AA2024, AA2014) and Fe-IMC (AA5083). Transition-metal based inhibitors such as chromate^{2,24,32}, vanadate^{33,34}, molybdate^{35,36}, and cobalt^{35,37} were also found to lower down ORR rate by forming precipitates on IMCs. However, pertinent research work focusing on the effect of Mg²⁺ or Zn²⁺ of the corrosion behavior of aluminum alloys is rare in literature, although they have demonstrated popular application in the galvanic cathodic protection of steel³⁸⁻⁴³, by directly precipitating zinc or magnesium containing corrosion products on the steel surface and causing inhibition of ORR which in turn lowers the corrosion rate. Collazo *et al.*⁴⁴ compared the corrosion behavior of AA2024-T3 in solution with and without Mg²⁺, and found that AA2024 shifted to a more extended anodic passive window and more cathodic open circuit potential as well as larger corrosion resistance by adding Mg²⁺ in the chloride containing solution. The corrosion inhibitive effect caused by addition of Mg²⁺ was explained by formation of Mg(OH)₂ which hinders the dealloying of S phase and lowers the ORR rate at the S phase site. Buchheit *et al.*⁴⁵ developed a synthesized Al-Zn-decavanadate hydrotalcite compound as inhibitor additive in the epoxy, and

discovered that the released Zn^{2+} showed mild corrosion protection behavior toward underlying 2024-T3 substrate by lowering cathodic kinetics due to ORR.

Nevertheless, all the relevant available research is only limited to 2xxx series Al alloy. Our study is aimed to extend the effect of Mg^{2+}/Zn^{2+} to 7xxx series Al alloy, focusing on AA7050-T7451. The objective of the study is to evaluate the effect of Zn^{2+} and Mg^{2+} on inhibiting ORR kinetics of AA7050-T7451, and inhibitive effect was evaluated in terms of cation concentration and immersion time.

4.4.2 Methodology

4.4.2.1 Materials Preparations

20mm x 20 mm square coupons machined from the S-L surface of a 50 mm thick rolled AA 7050-T7451 plate (ACRONIC, Pittsburgh, PA) were used in this study. The composition of AA7050-T7451 is listed in Table 4.1 in Part 1. all the testing coupons were polished to a surface finish of 1200 grit with SiC paper. After polishing, the sample surfaces were rinsed with acetone and then with de-ionized water prior to experiment.

4.4.2.2 Electrochemical Experiments

A three-electrode electrochemical cell with the AA 7050 coupon as the working electrode (exposure area: 1cm^2), a platinum-niobium mesh as the counter electrode, and saturated calomel reference electrode was used for all the electrochemical testing. In the study of the effect of concentration, the test solutions were: (1) 0.6M NaCl, (2) 0.6M NaCl+0.005M, 0.01M, 0.05M, 0.1M $ZnSO_4$, and (3) 0.6M NaCl+0.005M, 0.01M, 0.05M, and 0.1M $MgSO_4$. The pH of all the test solutions was adjusted to 6. Cathodic polarization curve measurements were obtained in each solution. For cathodic polarization experiments, 1 hour of open circuit potential (OCP) measurements were performed prior to the potential scan starting from 0 V vs. OCP to -1.15 V_{SCE}

at a scan rate of 0.2 mV/s. To produce adequate corrosion products on AA7050 during cathodic polarization for post characterization, potentiostatic experiments holding at $-0.9 V_{SCE}$ for 8 hours were performed to deposit film on the AA7050 coupons in 0.6M NaCl+0.1M ZnSO₄, and 0.6M NaCl+0.1M MgSO₄, respectively. As for the study of the immersion time, EIS measurements were performed to estimate corrosion parameters after 1, 24, 48, 96 and 120 hours of immersion time at OCP in 0.6M NaCl, 0.6M NaCl+0.1M ZnSO₄, and 0.6M NaCl+0.1M MgSO₄, respectively. A typical electrochemical impedance measurement in this part was acquired in the frequency range from 100 kHz to 10 mHz at 10 points per decade and a 10 mV AC amplitude around OCP after each pertinent immersion time. All the electrochemical experiments were carried using a Gamry Potentiostat (Ref 600/PCI 4) with Gamry Framework software.

4.4.2.3 Cleaning Procedure for Corrosion Products

All the AA7050 test coupons after 120hrs immersion time were cleaned in concentrated nitric acid (HNO₃) for 5 mins at 25°C following ASTM G1 Standard⁴⁶, and then rinsed with deionized water and air dry.

4.4.2.4 Characterizations

Corrosion products, Cu-containing intermetallic compounds (IMC) on the surface of AA7050, as well as the surface morphology of the test coupons from 120 hours of immersion time before and after nitric acid cleaning were characterized by both FEI QUANTA 200 and QUANTA 650 scanning electron microscopes (SEM) with an energy dispersive spectroscopy (EDS) detector.

Corrosion products on AA7050 from potentiostatic testing in Mg²⁺/Zn²⁺ containing solutions were also characterized with x-ray diffraction (XRD) using a PANalytical X'pert powder XRD instrument. A Cu-K α source (1.54 nm) was utilized to perform a scan from $2\theta=5^\circ$ to 80° at step size= 0.015° with a 40mA beam accelerated to 45kV. Raman Spectroscopy by Renishaw inVia

Raman microscope (Wotton-under-Edge, UK) was then applied to confirm the results from XRD. Measurements were conducted using a 200 mW 514 nm laser at 50% power under a 50× objective lens through an 1,800 L/mm visible grating.

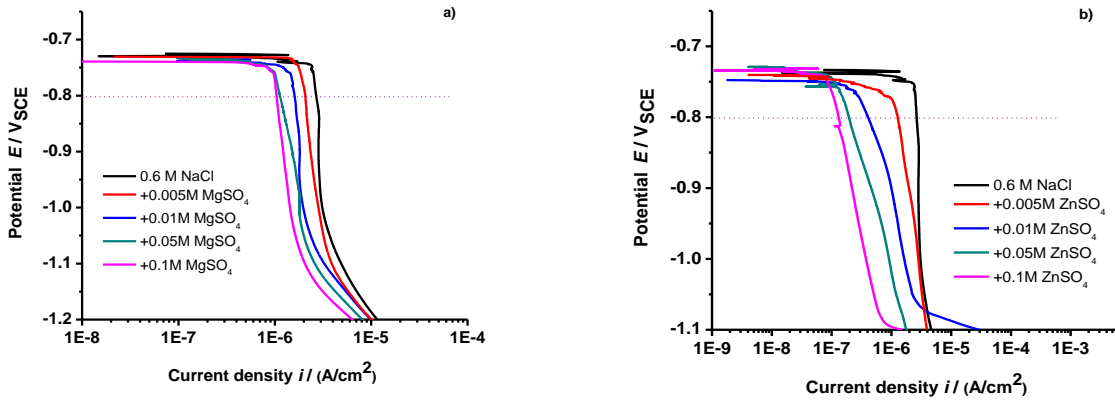
4.4.3 Results

To develop a systematic understanding of the effect of Mg^{2+}/Zn^{2+} ion on the cathodic kinetics of AA7050-T7451, and parse the underlying mechanism of corrosion inhibition of these two ions toward AA7050, the study started with determination of diffusion-limited cathodic kinetics of AA7050-T7451 in 0.6M NaCl as a function of concentration of added Mg^{2+} and Zn^{2+} . SEM/EDS was then utilized to characterize morphology and composition of IMC right after the cathodic polarization measurement. For the course of corrosion inhibitive performance of these two ions as a matter of exposure time, EIS was applied to monitor the electrochemical behavior changes with immersion time with and without addition of $Mg^{2+}/[Zn^{2+}]$, and SEM/EDS was then to compare the corresponding corrosion damage differences after 120hrs immersion time. To explore the composition of corrosion products formed through both Mg^{2+} and Zn^{2+} -containing sodium chloride solution, potentiostatic tests were performed to grow measurable amount of precipitation on the alloy surface with holding potential at diffusion limited potential region. Post XRD and Raman analysis were used to determine the corrosion product(s) at each type of solution.

4.4.3.1 Cathodic Polarization Curves of AA7050 as a Function of $[Mg^{2+}/Zn^{2+}]$

The purpose of the cathodic scan starting from E_{corr} was to maintain the surface structure of as-polished samples and avoid the effect of unwanted dissolution on the surface if the scan started from the potential above the E_{corr} . Comparisons of cathodic kinetics of AA7050-T7451 in 0.6M NaCl with addition of $MgSO_4$ or $ZnSO_4$ from 0 to 0.1 M are displayed in Figure 4.9a and 4.9b, respectively. In both the cases, cathodic kinetics of AA7050 displayed a diffusion-limited

potential window from E_{corr} to $\sim 1V_{\text{SCE}}$ in the negative direction; cathodic limiting current densities (i_{lim}) were both smaller in Mg^{2+} and Zn^{2+} containing solution than pure 0.6M NaCl solution, and the corresponding i_{lim} decreased with increasing concentration of $\text{Mg}^{2+}/\text{Zn}^{2+}$. To discern the difference in the degree of ORR inhibition between Mg^{2+} and Zn^{2+} , a comparison of i_{lim} at a reference potential = $-0.8 V_{\text{SCE}}$ as a function of ion concentration is shown in Figure 4.9c. Instead of experiencing gradual decrease in i_{lim} as increasing ion concentration for Mg^{2+} , i_{lim} plunged dramatically when just adding a little amount of Zn^{2+} till 0.01M, and then followed a slow decrease in i_{lim} . At each concentration, i_{lim} for Zn^{2+} was always lower than Mg^{2+} , and the largest difference came from 0.1M, in which i_{lim} for Zn^{2+} was only about 19% of that for Mg^{2+} , indicating Zn^{2+} demonstrated a better inhibition effect than Mg^{2+} in terms of ORR at the same concentration.



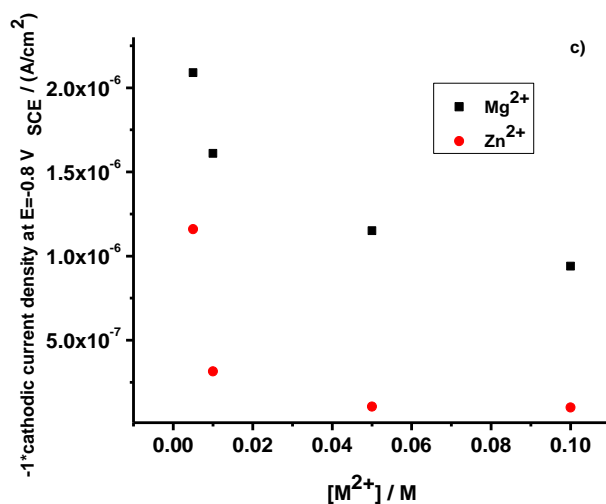


Figure 4.9: a) Cathodic polarization curves of AA7050-T7451 in 0.6M NaCl with addition of different concentration of MgSO₄; b) Cathodic polarization curves of AA7050-T7451 in 0.6M NaCl with addition of different concentration of ZnSO₄; c) Comparison of i_{lim} as a function of metal ion concentration between Zn²⁺ and Mg²⁺.

4.4.3.2 SEM and EDS Analysis for Cu-IMC after Cathodic Polarization Measurements

In order to observe if any corrosion product formed on the intermetallic compounds (IMC) of AA7050-T7451 during the cathodic polarization in either Mg²⁺ or Zn²⁺ containing solution, SEM was utilized for two different AA7050 coupons after cathodic polarizations in 0.6M NaCl+0.1M MgSO₄ and 0.6M NaCl+0.1M ZnSO₄ solutions, respectively. Figure 4.10 shows the micrograph and EDS analysis for two points at and outside the IMC after immersing in Mg²⁺. It can be clearly seen from SEM micrograph that a thin layer of corrosion product film covered on the IMC surface. EDS analysis shows that: the IMC (location A) was relatively rich in Cu and Fe compared to the matrix composition (location B), which implies this type of IMC is Al₇Cu₂Fe; huge concentration of oxygen, as well as relative high Mg concentration with respect to the matrix, indicates some magnesium oxide/hydroxide film formed during the cathodic scan.

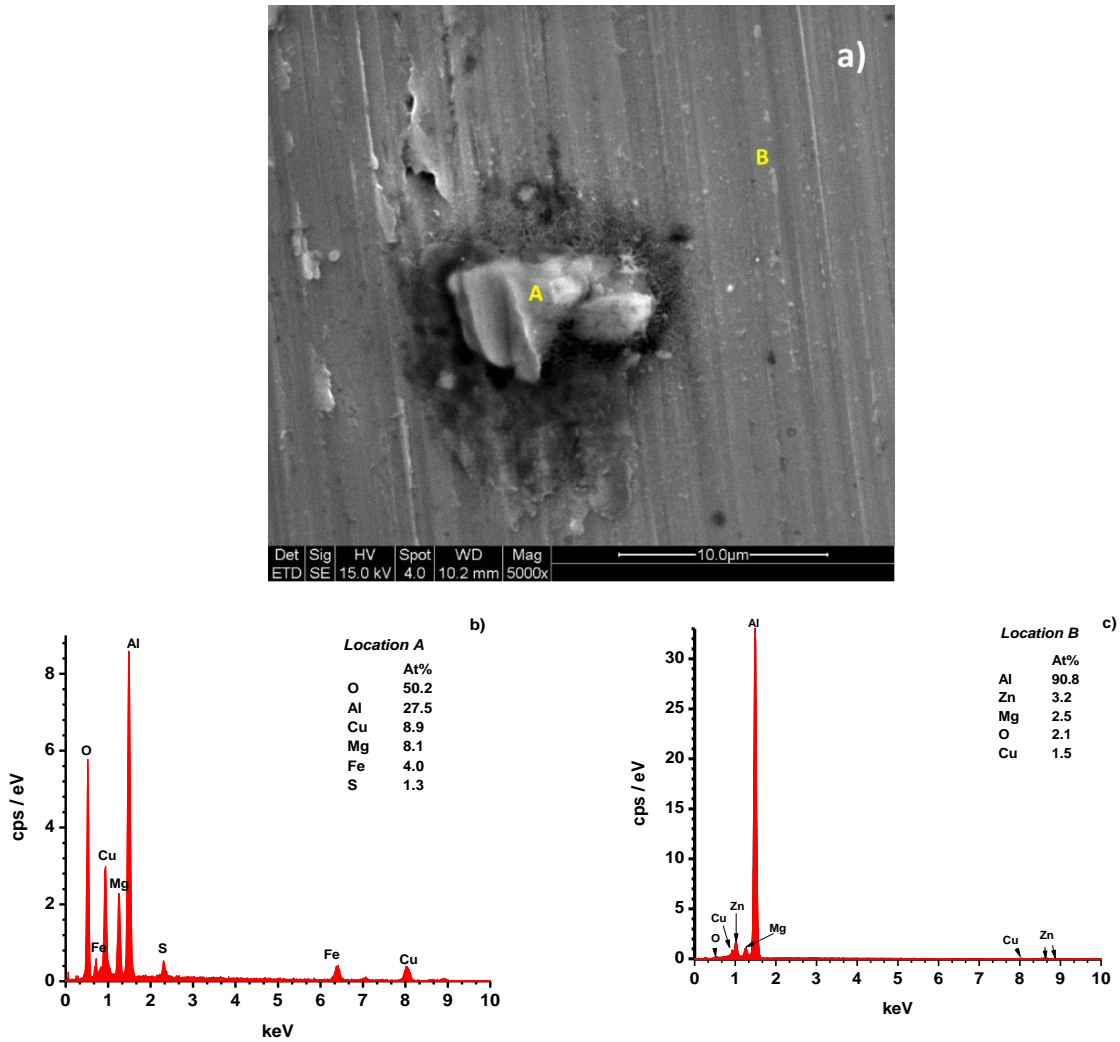


Figure 4.10: a) SEM image of $\text{Al}_7\text{Cu}_2\text{Fe}$ covered by corrosion product in 0.6M NaCl+ 0.1M MgSO_4 solution; EDS spectrum and composition (atomic percent) of b) location A and c) location B.

For the case of 0.6M NaCl+0.1M ZnSO_4 , a thicker corrosion product film was formed on the $\text{Al}_7\text{Cu}_2\text{Fe}$ (Figure 4.11a), and again some type of zinc oxide/hydroxide film was formed on the IMC (Figure 4.11b and 4.11c). The details of characterization of corrosion products during cathodic polarizations will be discussed later. It is well known that $\text{Al}_7\text{Cu}_2\text{Fe}$ IMC is one of common IMCs appeared in 2xxx and 7xxx series alloys, and is also the initiation site for localized corrosion since its cathodic polarity with respect to Al matrix^{25,47-49}, blockage of cathodic

Al₇Cu₂Fe particle can impede its ORR rate, which in turn decreases overall diffusion limited cathodic kinetics of AA7050.

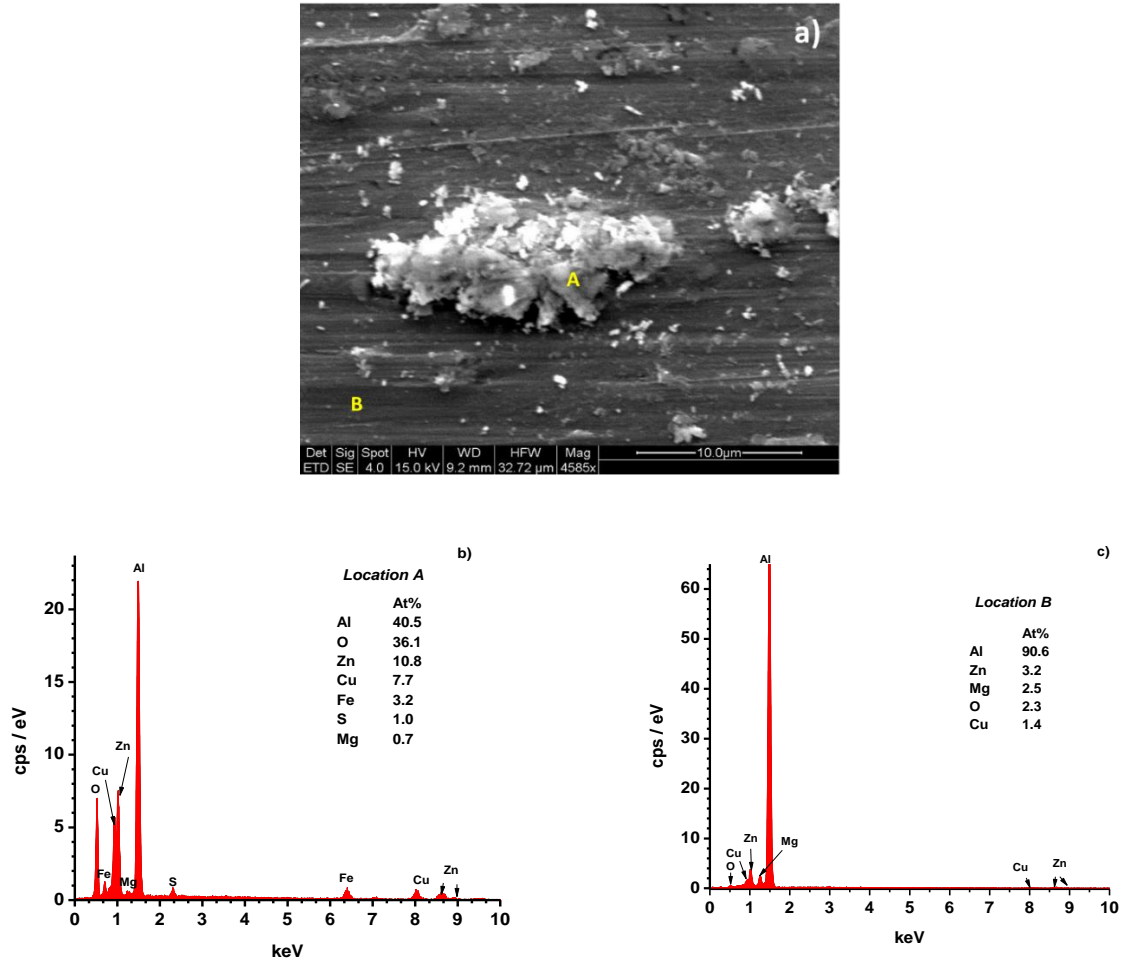


Figure 4.11: a) SEM image of Al₇Cu₂Fe covered by corrosion product in 0.6M NaCl+0.1M ZnSO₄ solution; EDS spectrum and composition (atomic percent) of b) location A and c) location B.

4.4.3.3 Corrosion Product Characterization after Potentiostatic Testing

In order to characterize the composition of precipitation/corrosion product formed on the AA7050 within the diffusion-limited potential range, potentiostatic tests were performed at -0.9 V_{SCE} for 8hrs in both 0.6M NaCl+0.1M MgSO₄ and 0.6M NaCl+0.1M ZnSO₄ solutions respectively. All the samples after the tests were sonicated in deionized water for 10mins in order to remove residual soluble salts before XRD/Raman analysis. The XRD patterns for samples taken

from two different solutions are shown in Figure 4.12. The XRD spectrum of bare AA7050 substrate was also listed to exclude the peaks from the underlying AA7050 and focus on the surface corrosion product. By searching the RRUFF Project Database⁵⁰, the composition of corrosion products for each solution has been identified: $\text{Mg}(\text{OH})_2$, and $\text{NaZn}_4(\text{SO}_4)(\text{OH})_6\text{Cl}\cdot 6\text{H}_2\text{O}$ were formed on the AA7050 in MgSO_4 and ZnSO_4 containing solutions respectively during cathodic potentiostatic hold at ORR potential. They were confirmed by complementary Raman spectra shown in Figure 4.13. The mechanism of formation of these two corrosion products will be discussed later.

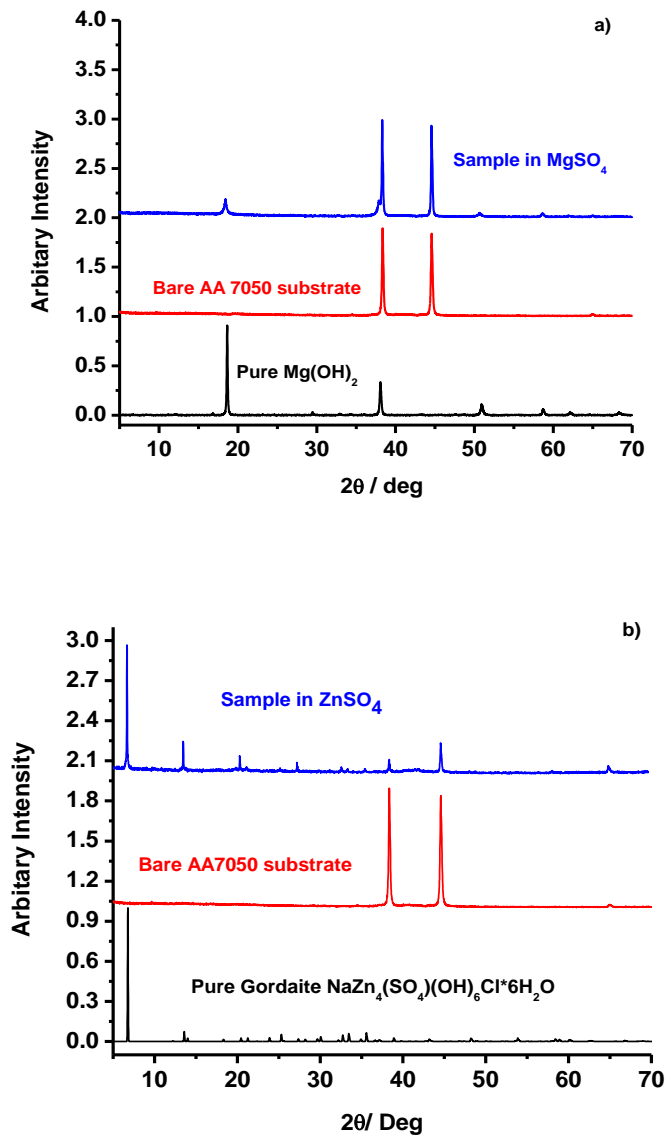


Figure 4.12: a) Overlaid x-ray reference intensity vs. 2θ plots of precipitate-coated AA7050 from MgSO₄ containing solution, as-polished AA7050 and pure Mg(OH)₂⁵⁰; b) overlaid x-ray reference intensity vs. 2θ plots of precipitate-coated AA7050 from ZnSO₄ containing solution, as-polished AA7050 and NaZn₄(SO₄)(OH)₆Cl·6H₂O⁵⁰.

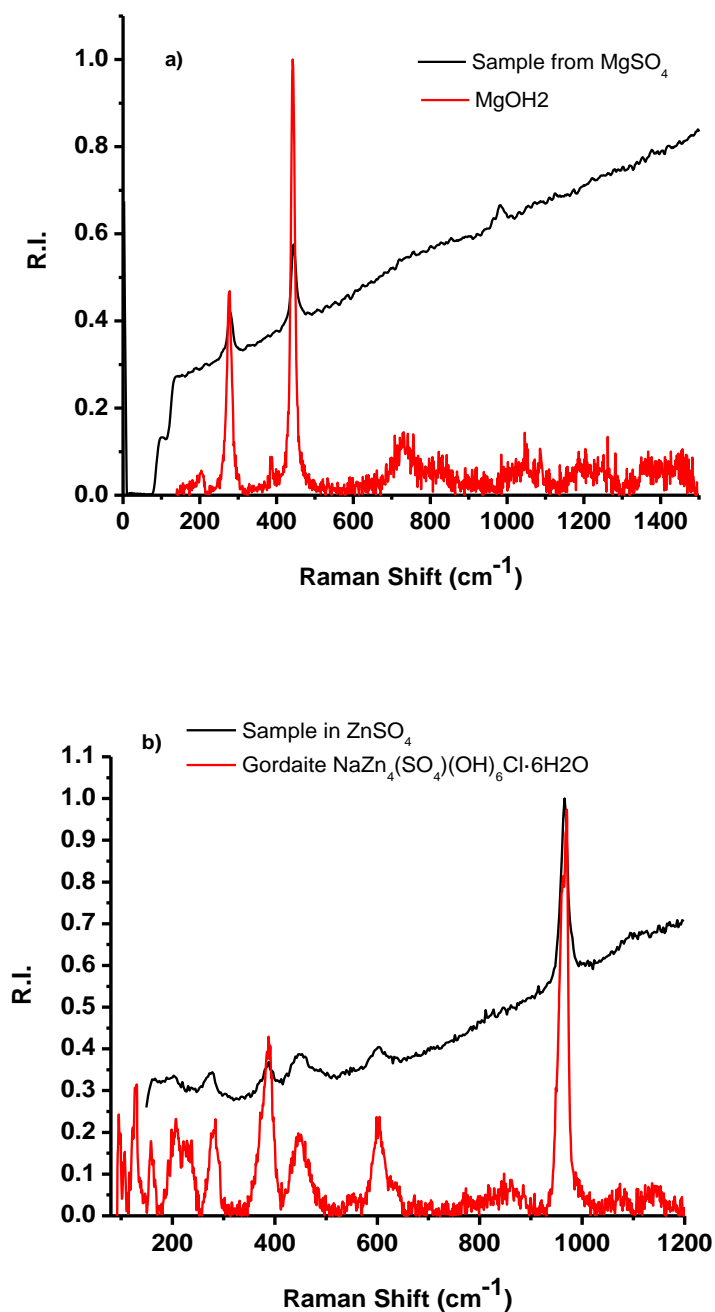


Figure 4.13: a) Overlaid Raman reference intensity vs. Raman shift plots of precipitate-coated AA7050 from MgSO₄ containing solution, and pure Mg(OH)₂⁵⁰; b) overlaid Raman reference intensity vs. Raman shift plots of precipitate coated AA7050 from ZnSO₄ containing solution and NaZn₄(SO₄)(OH)₆Cl·6H₂O⁵⁰.

4.4.3.4 EIS Analysis as a Function of Immersion Time

The main purpose of EIS analysis is to evaluate the property of the films formed by the corrosion products, as well as charge transfer resistance of the AA7050 substrate. The lower limit of EIS spectrum was 0.01 Hz due to significant noises of the scan at frequency smaller than 0.01 Hz. An equivalent circuit model with consideration of corrosion product films was utilized to fit EIS parameters (shown in Figure 4.14), which has been reported elsewhere⁵¹⁻⁵³. In this model, R_s is the solution resistance ($ohm \cdot cm^2$), CPE_{film} is the constant phase element (CPE) for the corrosion protection film ($S \cdot s^{\alpha_1}$), α_1 is the exponent parameter for CPE_{film} ($0 < \alpha_1 \leq 1$), R_{film} is the film resistance ($ohm \cdot cm^2$), CPE_{dl} is the double layer capacitance ($S \cdot s^{\alpha_2}$), α_2 is the exponent parameter for CPE_{dl} ($0 < \alpha_2 \leq 1$), R_{ct} is the charge transfer resistance ($ohm \cdot cm^2$), and W is the Warburg impedance ($S \cdot s^{0.5} \cdot cm^{-2}$). To evaluate effective oxide film capacitance from CPE value, Hirschorn *et al.*^{54,55} derived the mathematical relation between constant phase element (CPE) and effective capacitance for oxide film thickness

$$C_{eff} = gQ(\rho_{\delta}\epsilon\epsilon_0)^{1-\alpha} \quad (4.1)$$

where C_{eff} is the effective capacitance, ρ_{δ} is the film resistivity, ϵ is the dielectric constant for the film, ϵ_0 is the vacuum permittivity (8.854E-012 F/m), and g is a dimensionless number which is a function of α : $g = 1 + 2.88(1 - \alpha)^{2.375}$. Magnesium oxide (MgO), zinc oxide (ZnO) and aluminum oxide (Al_2O_3) were utilized to estimate oxide film properties, their film resistivity and dielectric constant are listed in Table 4.7

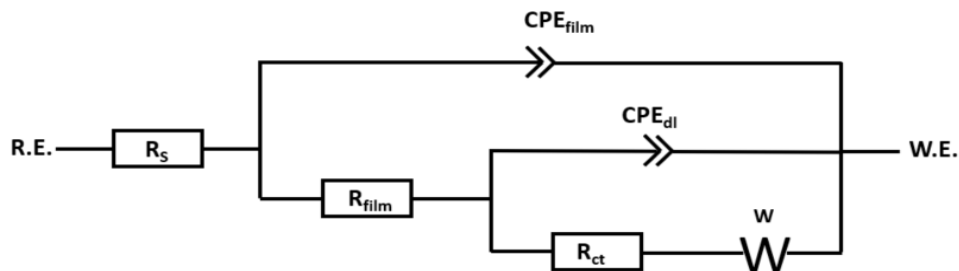


Figure 4.14: Equivalent circuit model to fit EIS spectra of AA7050 in pure 0.6M NaCl, and 0.6M NaCl+Mg²⁺.

Table 4.7: Film Resistivity and dielectric constant of MgO, ZnO and Al₂O₃⁵⁶

	MgO	ZnO	Al₂O₃
Film resistivity (<i>ohm · m</i>)	1E+12	7.5E+05	1E+12
Dielectric constant	9.5	8.5	9.1

Corresponding Nyquist and Bode plots for AA7050-T7451 in 0.6M NaCl and 0.6M NaCl+0.1M MgSO₄ after 1, 24, 48, 96 and 120 hrs are shown in Figure 4.15 and Figure 4.16. All the fitted EIS parameters are tabulated in Table 4.8 and Table 4.9. It should be noted that, the main goal of EIS analysis in this work is to extrapolate and evaluate the properties of film formed by corrosion product(s), for the analysis of EIS data in Zn²⁺ containing solutions, a different equivalent circuit model was proposed shown in Figure 4.17. In this model, all the low-frequency EIS components with respect to the interface between electrode and double layer were not displayed due to the limitation of frequency range in this work. These components might appear at lower frequency than 0.01Hz, but would experience significant noises when collecting data at extreme low frequency region, as mentioned earlier. Following the same routine, the EIS plots for and 0.6M NaCl+0.1M ZnSO₄ are shown in Figure 4.18, and the corresponding fitted EIS parameters are listed in Table 4.10.

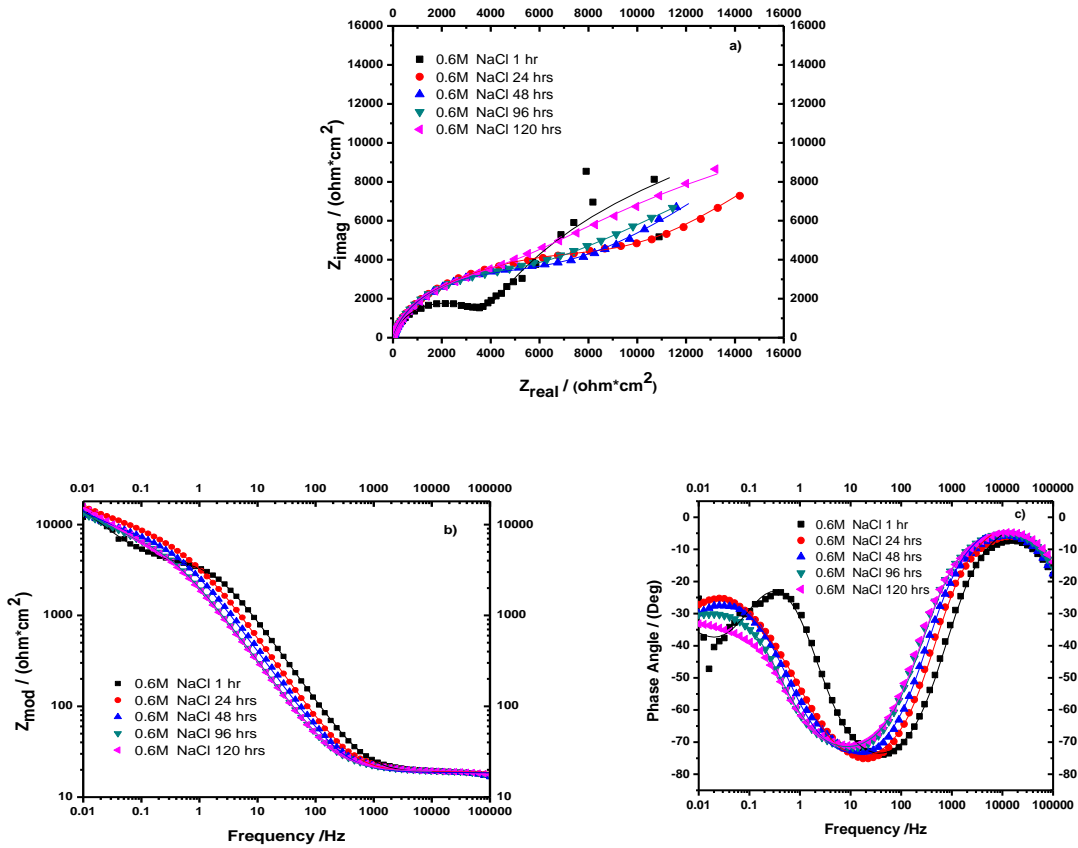


Figure 4.15: a) Nyquist plot as a function of immersion time; b) Bode impedance vs. frequency as a function of immersion time; c) phase angle vs. frequency as a function of immersion time for AA7050 immersed in 0.6M NaCl.

Table 4.8: Fitted EIS parameters for AA7050 in 0.6M NaCl solution in different immersion time

Time (Hr)	1	24	48	96	120
R_s ($ohm \cdot cm^2$)	18.57	18.86	18.55	18.98	19.1
CPE_{film} ($S \cdot s^{\alpha_1}$)	2.685E-5	4.412E-5	6.401E-5	9.063E-5	9.760E-5
α_1	0.9002	0.8917	0.882	0.8552	0.8498
$C_{film,eff}$ ($F \cdot cm^{-2}$)	4.211E-5	7.201E-5	1.094E-5	1.736E-5	1.947E-5
R_{film} ($ohm \cdot cm^2$)	4037	6340	6210	6631	6914
CPE_{dl} ($S \cdot s^{\alpha_2}$)	5.512E-4	1.260E-4	3.582E-4	4.710E-4	4.00E-4
α_2	0.8266	1	0.6022	0.645	0.7294
R_{ct} ($ohm \cdot cm^2$)	15682	2999	12000	17820	18110
W ($S \cdot s^{0.5} \cdot cm^{-2}$)	1200	1641	2473	1500	1073

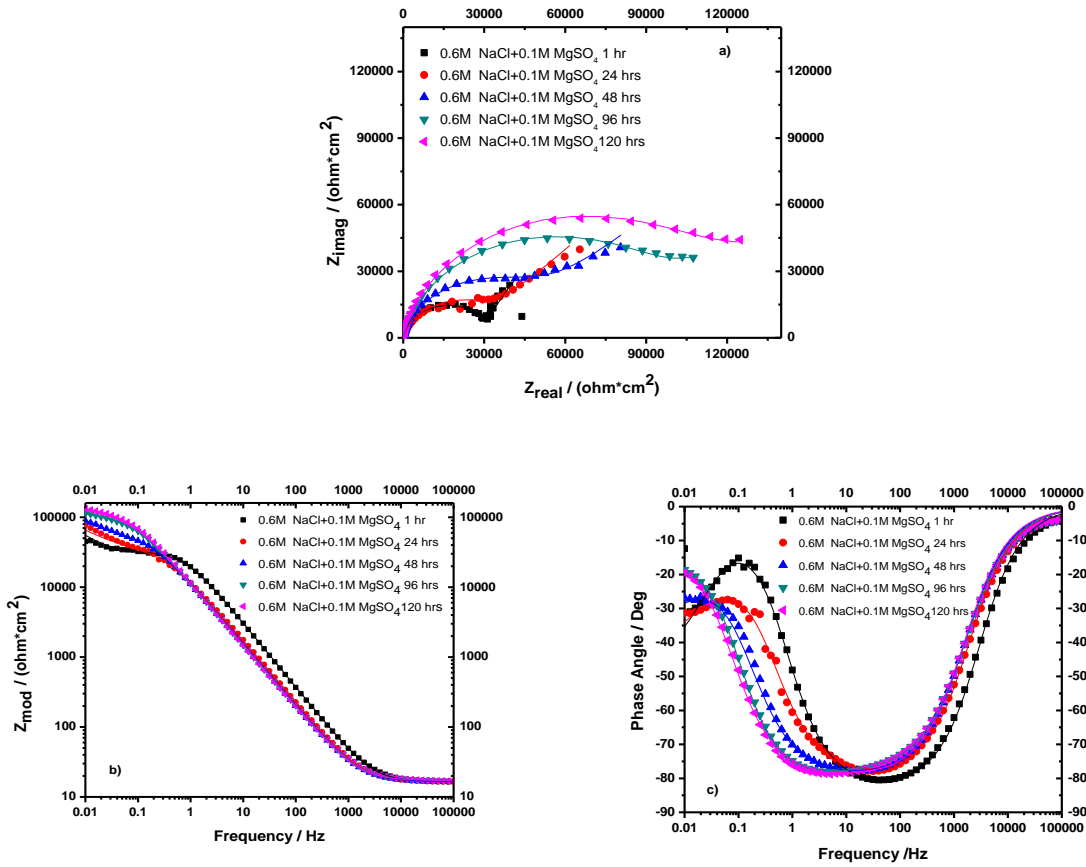


Figure 4.16: a) Nyquist plot as a function of immersion time; b) Bode impedance vs. frequency as a function of immersion time; c) phase angle vs. frequency as a function of immersion time for AA7050 immersed in 0.6M NaCl+0.1M MgSO₄.

Table 4.9: Fitted EIS parameters for AA7050 in 0.6M NaCl+0.1M MgSO₄ solution in different immersion time.

Time (Hr)	1	24	48	96	120
R_s ($ohm \cdot cm^2$)	16.69	16.31	16.62	17.17	17.15
CPE_{film} ($S \cdot s^{\alpha_1}$)	7.124E-6	1.550E-5	1.678E-5	1.746E-5	1.72E-5
α_1	0.921	0.881	0.8834	0.880	0.885
$C_{film,eff}$ ($F \cdot cm^{-2}$)	1.018E-5	2.675E-5	2.863E-5	3.027E-5	2.912E-5
R_{film} ($ohm \cdot cm^2$)	33000	38123	61000	108000	129150
CPE_{dl} ($S \cdot s^{\alpha_2}$)	3.01E-4	1.501E-4	1.62E-4	4.1E-4	4.4E-4
α_2	0.99	0.86	0.92	0.92	0.98
R_{ct} ($ohm \cdot cm^2$)	23404	25000	25656	24211	27800
W ($S \cdot s^{0.5} \cdot cm^{-2}$)	9998	10023	9908	7011	4555

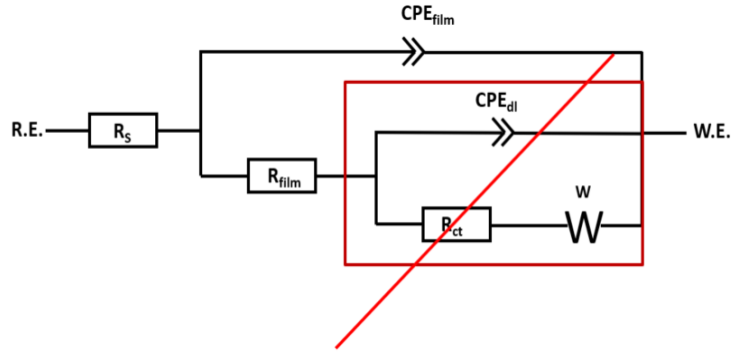


Figure 4.17: Equivalent circuit model for AA7050 in 0.6M NaCl+0.1M ZnSO₄.

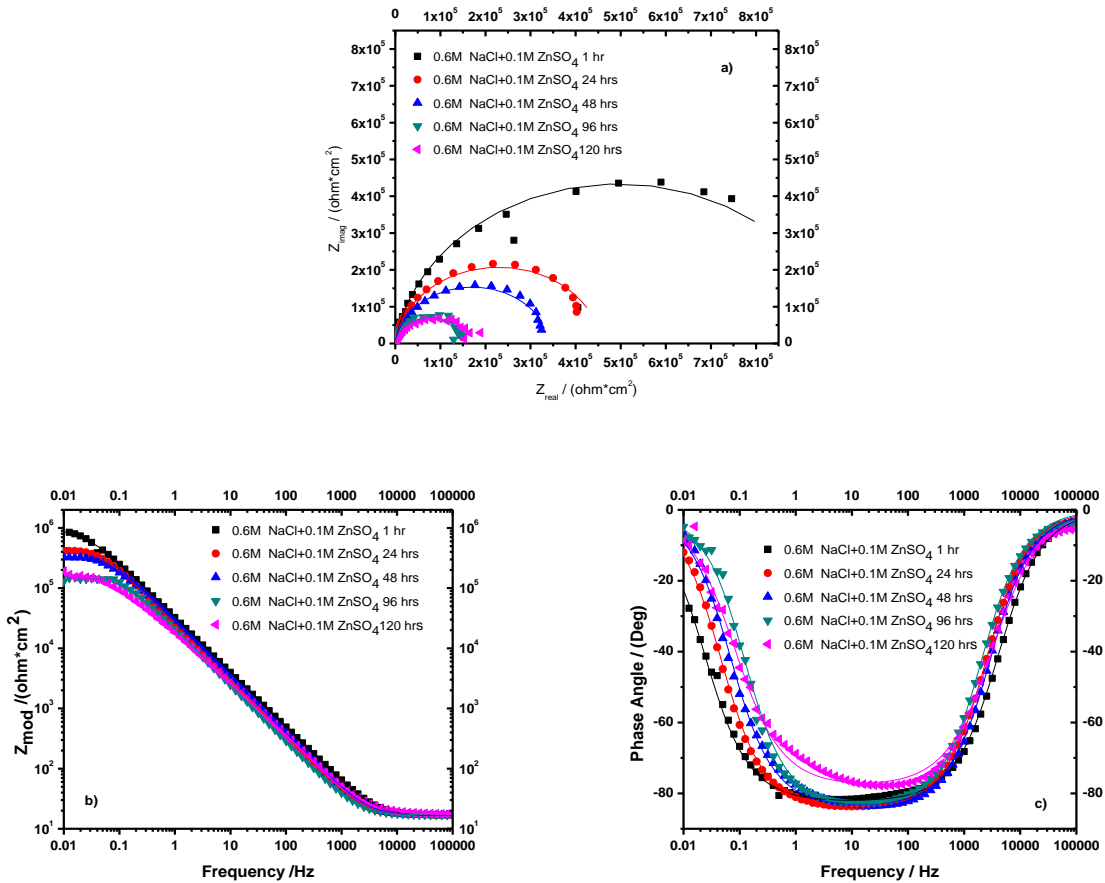


Figure 4.18: a) Nyquist plot as a function of immersion time; b) Bode impedance vs. frequency as a function of immersion time; c) phase angle vs. frequency as a function of immersion time for AA7050 immersed in 0.6M NaCl+0.1M ZnSO₄.

Table 4.10: Fitted EIS parameters for AA7050 in 0.6M NaCl+0.1M ZnSO₄ solution in different immersion time

Time (Hr)	1	24	48	96	120
R_s ($ohm \cdot cm^2$)	16.46	16.91	16.56	16.97	17.02
CPE_{film} ($S \cdot s^{\alpha_1}$)	5.657E-6	6.897E-6	6.328E-6	8.309E-6	1.062E-5
α_1	0.9156	0.9376	0.9324	0.936	0.8683
$C_{film,eff}$ ($F \cdot cm^{-2}$)	2.498E-6	3.761E-6	3.282E-6	4.461E-6	2.997E-6
R_{film} ($ohm \cdot cm^2$)	990000	457384	341585	154737	168403

Comparisons in corrosion product film resistance (R_{film}), film CPE (CPE_{film}) and effective capacitance of film ($C_{eff,film}$) are shown in Figure 4.19. For R_{film} , as immersion time increased, those for 0.6M NaCl and 0.6M NaCl+0.1M MgSO₄ both increased initially and then reached a plateau for the former and kept going up for the latter, whereas that for ZnSO₄ containing solution decreased from the beginning and reached minimum at 96hrs before a slight increase at 120hrs. Nevertheless, the film resistance was always highest for ZnSO₄ containing solution, followed by MgSO₄ containing solution, and pure NaCl solution had the lowest film resistance, which implied that corrosion product showed corrosion protection for the alloy surface when solution contained Mg²⁺ or Zn²⁺. As for CPE_{film} and $C_{eff,film}$, they both increased during the first 24hrs for all three solutions; however, for ZnSO₄ containing solution, $C_{eff,film}$ and CPE_{film} reached minimum at 48hrs before increasing again to the end of 120hrs; for MgSO₄ containing solution, $C_{eff,film}$ and CPE_{film} were almost constant after the first 24hrs; they kept increasing for pure NaCl. It is interesting that the CPE_{film} and $C_{eff,film}$ were the highest in pure NaCl solution, and the lowest for ZnSO₄ containing solution, which indicated the film thickness was the highest for ZnSO₄ solution, whereas surface exposed in pure NaCl solution had the lowest film thickness.

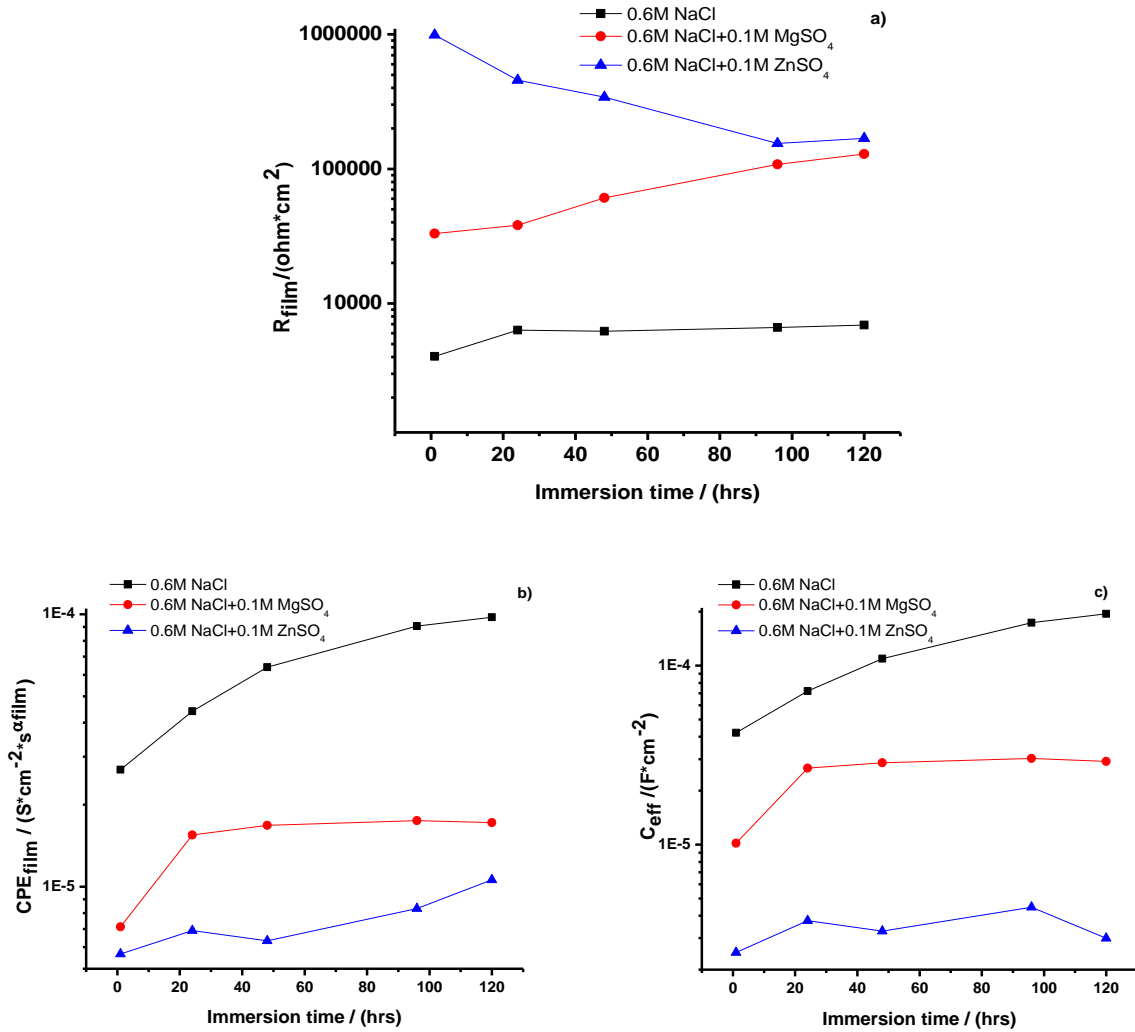


Figure 4.19: a) Comparison of a) R_{film} , b) CPE_{film} and c) $C_{eff, film}$ as a function of immersion time in three different solutions.

4.4.3.5 SEM and EDS Analysis to Evaluate the Efficiency of Corrosion Inhibitive Effect

Comparison of surface morphologies before HNO₃ treatment among three different AA7050-T7451 coupons immersed in 0.6M NaCl, 0.6M NaCl+0.1M MgSO₄, and 0.6M NaCl+0.1M ZnSO₄ for 120hrs respectively is shown in Figure 4.20. For 0.6M NaCl solution, the surface was fully covered by amorphous corrosion product; as for MgSO₄ containing solution, the surface was partially protected by discretely distributed precipitates; in ZnSO₄ containing solution, flake-wise precipitates meshed together to form a “web” which fully covered the entire alloy

surface. After HNO_3 treatment, the real corrosion morphologies for three different solutions were revealed which are shown in Figure 4.21. It can be clearly seen that: without Mg^{2+} or Zn^{2+} , AA7050 surface experienced tremendous amount of localized corrosion, whereas for Mg^{2+} containing solution scenario, only shallow pits were discretely distributed on the surface, and for Zn^{2+} containing solution, there was little or no localized corrosion appeared. This proved that Zn^{2+} provided better corrosion protection than Mg^{2+} at least during 120hrs immersion test.

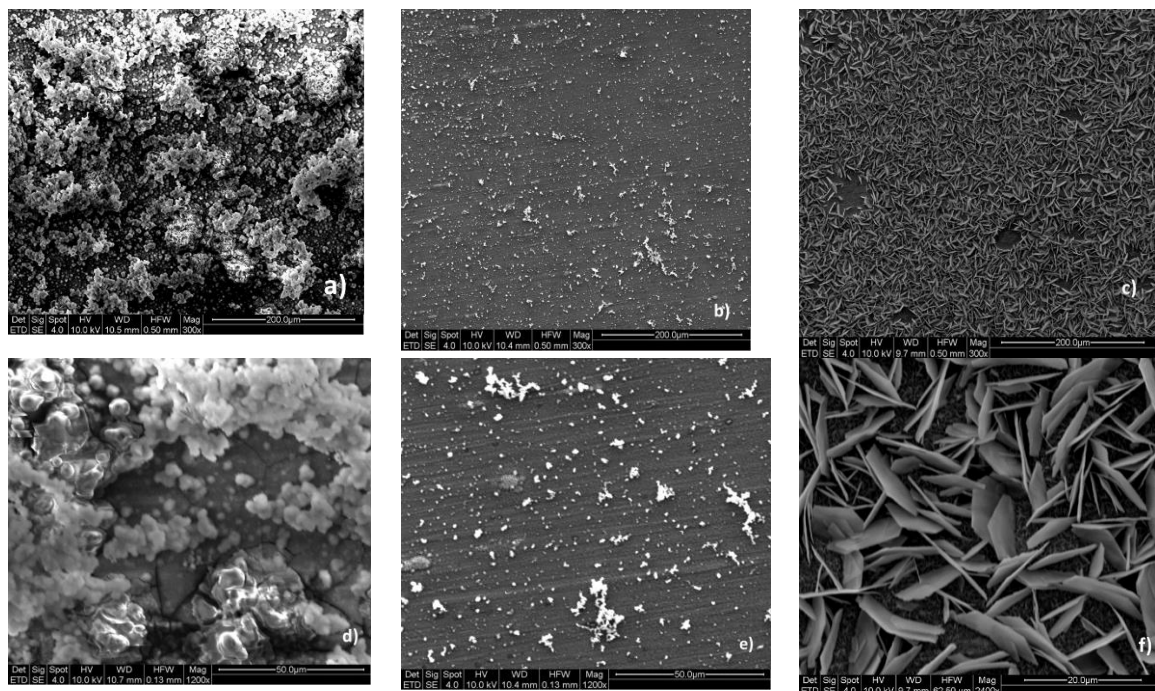


Figure 4.20: a) SEM images of AA7050 surface prior to HNO_3 treatment after 120hr-immersion in a) 0.6M NaCl solution; b) SEM image of AA7050 surface in 0.6M NaCl +0.1M MgSO_4 solution; c) SEM image of AA7050 surface in 0.6M NaCl+0.1M ZnSO_4 solution; d) a zoom-in of a); e) a zoom-in of b); f) a zoom-in of c).

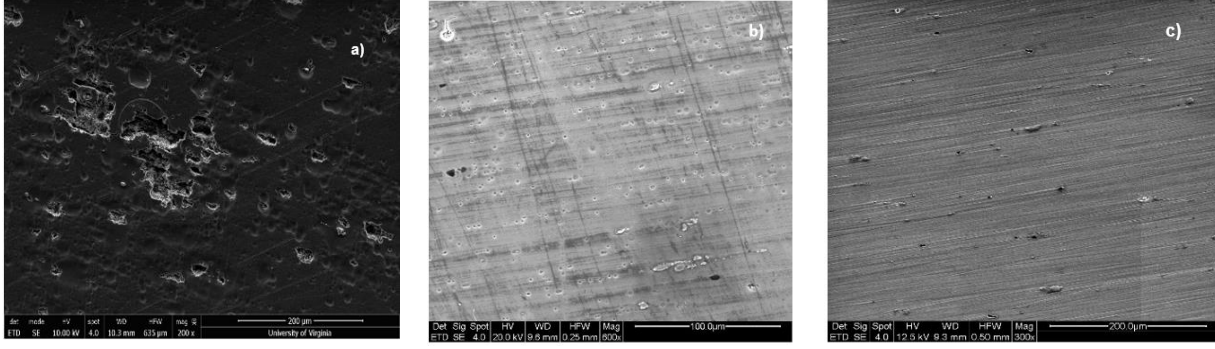


Figure 4.21: SEM image of AA7050 surface with HNO₃ cleaning the surface after 120hr-immersion in a) 0.6M NaCl solution; b) 0.6M NaCl +0.1M MgSO₄ solution; c) 0.6M NaCl+0.1M ZnSO₄ solution.

4.4.4 Discussions

4.4.4.1 Film Quality and Corrosion Resistance Analysis

To evaluate the resistance of film formed by precipitation from either Mg²⁺ or Zn²⁺, $R_{film} * C_{eff, film}$ product was defined. Since $R_{film} = \rho_{film} \frac{\delta_{film}}{A_{film}}$ (ρ_{film} : film resistivity, Film A_{film} : cross section area of film, δ_{film} : film thickness) and $C_{eff, film} = \frac{\epsilon_o \epsilon A_{film}}{\delta_{film}}$, $R_{film} * C_{eff, film} = \rho_{film} \epsilon_o \epsilon$ is a function of film resistivity. A comparison of RC product between Zn²⁺ and Mg²⁺ containing solution in terms of immersion time is shown in Figure 4.22a. RC product for Zn²⁺ was higher than Mg²⁺ containing solution during the first 35hrs, and then it decreased with time and became lower than Mg²⁺, whereas Mg²⁺ experienced an ascending tendency all the time, which implied that the film quality of Mg²⁺ would be better for an immersion time longer than 35hrs. For total corrosion resistance (Figure 4.22b), both Mg²⁺ and Zn²⁺ containing solutions showed larger resistance compared to pure NaCl solution, but again, the total resistance of Zn²⁺ containing solution degraded over time whilst it for Mg²⁺ improved with time increasing, which might infer that Mg²⁺ corrosion inhibitive effect would be better for Zn²⁺ for a very long-time immersion exposure (>120hrs).

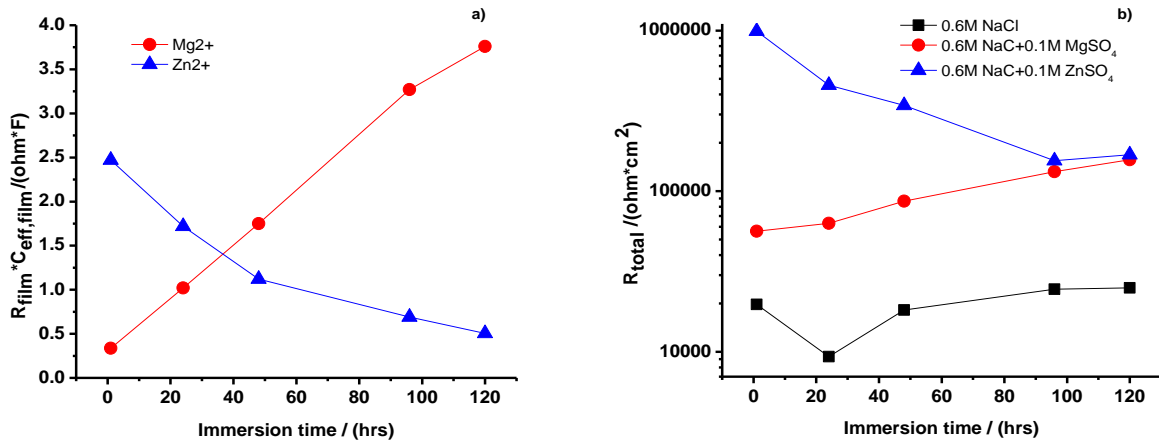
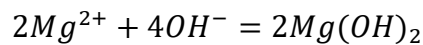
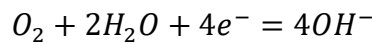


Figure 4.22: a) Comparison of film RC products between Zn²⁺ and Mg²⁺ containing solutions as a function of immersion time; b) Comparison of total resistance between Zn²⁺ and Mg²⁺ containing solutions as a function of immersion time.

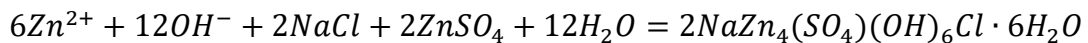
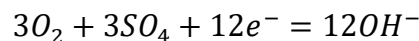
4.4.4.2 Reactions to Form Corrosion Products

When oxygen reduction reaction takes place on Cu-containing intermetallic particle (IMC) of AA7050 during cathodic polarization, in Mg²⁺ containing solution, these electrochemical and chemical reactions proceed in the following sequence:



As a result, Mg(OH)₂ is the main corrosion product at open circuit potential or cathodic polarization in neutral to mild alkaline solution containing Mg²⁺.

Whereas in Zn²⁺ containing solution, these electrochemical and chemical reactions take place in the following sequence:



As a result, $\text{NaZn}_4(\text{SO}_4)(\text{OH})_6\text{Cl}\cdot 6\text{H}_2\text{O}$ is the main corrosion product at open circuit potential or cathodic polarization in neutral to mild alkaline solution containing Zn^{2+} .

4.4.5 Conclusions:

The effect of Mg^{2+} and Zn^{2+} on the cathodic kinetics of AA7050 has been investigated in this work. It has been found that: during cathodic potential regime where ORR is dominant, $\text{Mg}(\text{OH})_2$ and $\text{NaZn}_4(\text{SO}_4)(\text{OH})_6\text{Cl}\cdot 6\text{H}_2\text{O}$ are precipitated on Cu-containing IMCs embedded in AA7050-T7451 in Mg^{2+} and Zn^{2+} containing solutions respectively, forming diffusional barrier to ORR and lowering down the cathodic limiting current density. The decrease in cathodic limiting current density pertinent to ORR is proportional to $\text{Mg}^{2+}/\text{Zn}^{2+}$ concentration. As for the evaluation of corrosion inhibitive effect of these two cations with respect to reduced ORR kinetics, both increases with increased cation concentration, and Zn^{2+} provides better inhibition than Mg^{2+} at the same ion concentration; corrosion inhibitive effect of Mg^{2+} is inferior to Zn^{2+} during the first 120hrs, but would be superior to Zn^{2+} for an immersion exposure period longer than 120hrs.

4.4.6 References

1. J. Zhao, G. Frankel, and R. L. McCreery, *J. Electrochem. Soc.*, **145**, 2258–2264 (1998).
2. M. W. Kendig and R. G. Buchheit, *CORROSION*, **59**, 379–400 (2003).
3. L. Li, K. P. Doran, and G. M. Swain, *Journal of the Electrochemical Society*, **160**, C396–C401 (2013).
4. G. O. Ilevbare and J. R. Scully, *CORROSION*, **57**, 134–152 (2001).
5. J. Zhao, L. Xia, A. Sehgal, D. Lu, R.L. McCreery, G.S. Frankel, *Surface and Coatings Technology*, **140**, 51–57 (2001).
6. A. M. Simões, A.C. Bastos, M.G. Ferreira, Y. Gonzalez-Garcia, S. Gonzalez, R.M. Souto *Corrosion Science*, **49**, 726–739 (2007).
7. D. Battocchi, A. M. Simões, D. E. Tallman, and G. P. Bierwagen, *Corrosion Science*, **48**, 1292–1306 (2006).
8. A.D. King, B. Kannan, and J.R. Scully, *Corrosion*, **70**, 512–535 (2013).
9. A.D. King, B. Kannan, and J.R. Scully, *Corrosion*, **70**, 536–557 (2013).
10. B. Kannan, A. D. King, and J.R. Scully, *Corrosion*, **71**, 1093–1109 (2015).

11. R. J. Santucci, B. Kannan, W. Abbott, and J. R. Scully, *CORROSION*, **73**, 1196–1201 (2017).
12. R. J. Santucci, B. Kannan, and J. R. Scully, *CORROSION*, **74**, 96–111 (2018).
13. M. D. Danford, M. J. Mendrek, and D. W. Walsh, "The Corrosion Protection of 2219-T87 Aluminum by Organic and Inorganic Zinc-Rich Primer", NASA Technical Paper 3534 (1995)
14. R. G. Buchheit, H. Guan, S. Mahajanam, and F. Wong, *Progress in Organic Coatings*, **47**, 174–182 (2003).
15. P. Plagemann, J. Weise, and A. Zockoll, *Progress in Organic Coatings*, **76**, 616–625 (2013).
16. A. Chilukuri, The Ohio State University, Columbus, OH, *Ph.D. Dissertation* (2012)
17. D. Battocchi, A. M. Simões, D. E. Tallman, and G. P. Bierwagen, *Corrosion Science*, **48**, 1292–1306 (2006).
18. B. Kannan, D. Wolanski, and J.R.Scully, *CORROSION*, 2424 (2018).
19. G. Bierwagen, R. Brown, D. Battocchi, and S. Hayes, *Progress in Organic Coatings*, **67**, 195–208 (2010).
20. A. Simões, D. Battocchi, D. Tallman, and G. Bierwagen, *Progress in Organic Coatings*, **63**, 260–266 (2008).
21. A. D. King, J. S. Lee, and J. R. Scully, *J. Electrochem. Soc.*, **163**, C342–C356 (2016).
22. G. Bierwagen, D. Battocchi, A. Simões, A. Stamness, and D. Tallman, *Progress in Organic Coatings*, **59**, 172–178 (2007).
23. G. O. Ilevbare, O. Schneider, R. G. Kelly, and J. R. Scully, *Journal of The Electrochemical Society*, **151**, B453 (2004).
24. G. O. Ilevbare and J. R. Scully, *CORROSION*, **57**, 134–152 (2001).
25. N. Birbilis, M. K. Cavanaugh, and R. G. Buchheit, *Corrosion Science*, **48**, 4202–4215 (2006).
26. M. B. Vukmirovic, N. Dimitrov, and K. Sieradzki, *Journal of The Electrochemical Society*, **149**, B428 (2002).
27. M. A. Jakab, D. A. Little, and J. R. Scully, *Journal of The Electrochemical Society*, **152**, B311 (2005).
28. A. J. Aldykewicz, H. S. Isaacs, and A. J. Davenport, *Journal of The Electrochemical Society*, **142**, 3342 (1995).
29. A. Aballe, M. Bethencourt, F. . Botana, and M. Marcos, *Journal of Alloys and Compounds*, **323–324**, 855–858 (2001).
30. Kiryl A. Yasakau, M.L. Zheludkevich, S.V. Lamaka, and M. G. S. Ferreira, *Journal of Physical Chemistry B*, **110**, 5515-5528 (2006).
31. A. K. Mishra and R. Balasubramaniam, *Corrosion Science*, **49**, 1027–1044 (2007).
32. V. Guillaumin, P. Schmutz, and G. S. Frankel, *Journal of The Electrochemical Society*, **148**, B163 (2001).

33. M. Iannuzzi, T. Young, and G. S. Frankel, *Journal of The Electrochemical Society*, **153**, B533 (2006).
34. K. D. Ralston, T. L. Young, and R. G. Buchheit, *Journal of The Electrochemical Society*, **156**, C135 (2009).
35. M. A. Jakab, F. Presuel-Moreno, and J. R. Scully, *Journal of The Electrochemical Society*, **153**, B244 (2006).
36. O. Lopez-Garrity and G. S. Frankel, *Journal of the Electrochemical Society*, **161**, C95–C106 (2013).
37. M. A. Jakab, F. Presuel-Moreno, and J. R. Scully, *CORROSION*, **61**, 246–263 (2005).
38. R. Krieg, M. Rohwerder, S. Evers, B. Schuhmacher, and J. Schauer-Pass, *Corrosion Science*, **65**, 119–127 (2012).
39. P. Volovitch, C. Allely, and K. Ogle, *Corrosion Science*, **51**, 1251–1262 (2009).
40. F. Thébault, B. Vuillemin, R. Oltra, C. Allely, and K. Ogle, *Electrochimica Acta*, **56**, 8347–8357 (2011).
41. S.-H. Lin and S. C. Dexter, *CORROSION*, **44**, 615–622 (1988).
42. N. C. Hosking, M. A. Ström, P. H. Shipway, and C. D. Rudd, *Corrosion Science*, **49**, 3669–3695 (2007).
43. T. Prosek, D. Thierry, C. Taxén, and J. Maixner, *Corrosion Science*, **49**, 2676–2693 (2007).
44. A. Collazo, X. R. Nóvoa, and C. Pérez, *Electrochimica Acta*, **124**, 17–26 (2014).
45. R. G. Buchheit, H. Guan, S. Mahajanam, and F. Wong, *Progress in Organic Coatings*, **47**, 174–182 (2003).
46. ASTM G-1, “Standard Practice for Preparing, Cleaning, and Evaluating Corrosion Test Specimens” (West Conshohocken, PA: ASTM International, 2001), p. 1-9.
47. N. Birbilis and R. G. Buchheit, *J. Electrochem. Soc.*, **152**, B140–B151 (2005).
48. S.-S. Wang, I.-W. Huang, L. Yang, J. -T. Jiang, J.-F. Chen, S. -L. Dai, D. N. Seidman, G.S. Frankel, and L. Chen, *J. Electrochem. Soc.*, **162**, C150–C160 (2015).
49. N. Birbilis, M. K. Cavanaugh, and R. G. Buchheit, *Corrosion Science*, **48**, 4202–4215 (2006).
50. B. Lafuente, R.T. Downs, H. Yang, N. Stone, “The Power of Databases: The RRUFF Project,” in *Highlights in Mineralogical Crystallography*, eds. T. Armbruster, R.M. Danisi (Berlin, Germany: DeGruyter, 2015).
51. F. Mansfeld, *Electrochimica Acta*, **35**, 1533–1544 (1990).
52. Y. J. Tan, S. Bailey, and B. Kinsella, *Corrosion Science*, **38**, 1545–1561 (1996).
53. H. Shi, E.-H. Han, and F. Liu, *Corrosion Science*, **53**, 2374–2384 (2011).
54. B. Hirschorn, M.E. Orazem, B. Tribollet, V. Vivier, I. Frateur, M. Musiani, *Journal of The Electrochemical Society*, **157**, C452 (2010).
55. B. Hirschorn, M.E. Orazem, B. Tribollet, V. Vivier, I. Frateur, M. Musiani., *Electrochimica Acta*, **55**, 6218–6227 (2010).
56. <https://www.azom.com/properties.aspx?ArticleID=54>

4.5 Part 3: Promotive Effect of Al³⁺ on the Cathodic Kinetics of Aluminum Alloys

4.5.1 Introduction

High strength aluminum alloys (Al alloys) have received wide application in the aerospace and automotive industries for decades. However, these alloys are prone to localized corrosion due to highly heterogeneous microstructures^{1,2}, with susceptibility to pitting and crevice corrosion³⁻⁶, intergranular corrosion⁷⁻⁹, exfoliation corrosion^{10,11}, and environmental assisted cracking¹²⁻¹⁴, depending upon the alloy composition and temper. These localized corrosion behaviors are detrimental to the Al-alloy based structures and there have been a great deal of experimental studies performed aimed at interrogation of the underlying mechanisms as well as development of pertinent test protocols to better quantify these phenomena. Among these experimental protocols, accelerated corrosion test methods are designed to create corrosion morphologies that mimic those observed in service and evaluate the interaction between exposure environment and the degree of localized corrosion in a timely fashion. For exfoliation corrosion, available accelerated testing protocols include ASTM G34¹⁵, ASTM G85¹⁶, and ANCIT¹⁷. For ANCIT test method¹⁷ proposed by Lee and Lifka, there are four major metal ion species which are determined from the solution chemistry of AA7150 exposed in G34 test after 24hrs: Al³⁺, Zn²⁺, Mg²⁺, and Cu²⁺. The corresponding elements are the dominant constituent ones in AA7150. Lee and Lifka found that Al³⁺ was the cation that was most important in the success of the exfoliation corrosion test. However, the role of Al³⁺ in causing severe exfoliation corrosion in susceptible tempers was not explained in their work.

From an electrochemical perspective, the localized corrosion rate of aluminum alloys under open circuit potential conditions can be controlled by either the passivity of the alloys which attenuates the dissolution kinetics, or the rate of the oxygen reduction reaction (ORR) or hydrogen

evolution (HER) rate happening on the alloy surface. Some corrosion inhibitors focus on mitigation of the mass transfer limited cathodic kinetics on Al alloys. Metallic cation-based inhibitors (most of which belong to transition metal group such as lanthanide) form metal oxide/hydroxides on the noble intermetallic particles embedded in the Al matrix, which are the key cathodic sites, to achieve cathodic inhibition goal¹⁸⁻²⁵. However, there has been limited literature pertinent to the effect of four major metallic cations in the ANCIT test on the cathodic kinetics of Al alloys, despite the fact that under corrosion conditions, these metallic ions will be in the highest concentration on the surface.

Recently, Parker and Kelly²⁶ parsed the electrochemical foundation of G34 and ANCIT tests, and discovered that addition of AlCl_3 (~0.224M) significantly increased the hydrogen evolution reaction (HER) rate on both AA2060-T3 and AA2060-T86, which in turn accelerated the localized corrosion of those Al alloys. However, this work lacked a detailed explanation of the means by which the addition of Al^{3+} caused a huge increase in cathodic kinetics. Actually, there are several potential applications of understanding the role of Al^{3+} in localized corrosion behaviors of Al alloys: 1) during the localized corrosion, Al^{3+} will diffuse out from the localized corrosion site into the adjacent solution environment, which can further impact the corrosion behavior of Al alloys; 2) by utilizing the fact that Al^{3+} can increase the cathodic kinetics which in turn increases localized corrosion rate, improved accelerated corrosion testing for Al alloys can be developed by manipulating the content of Al salts; 3) if HER enhancement by Al^{3+} can be extended to the other metal and alloys, one can make use of Al^{3+} for the production of hydrogen.

The overarching goal of this study is to firstly examine the phenomenological effect of Al^{3+} on the cathodic kinetics and corrosion rates on 2xxx, 5xxx and 7xxx series Al alloys, and then

extend the Al³⁺ effect study to pure platinum (Pt) and stainless steel 316L (SS), and parse the underlying mechanism of cathodic kinetics enhancement by Al³⁺.

4.5.2 Experimental Methods

4.5.2.1 Materials Preparations

Three types of Al alloys: AA2024-T351, AA5083-H131 and AA7050-T451 all of which are obtained from ALCOA (Pittsburgh, PA), as well as SS316L (McMaster-Carr Supply Company, Elmhurst IL) were cut into 1" x 1" test coupons. A platinum rotating disk electrode (Pine Research Instrumentation, Inc., Durham, NC) of diameter equal to 0.5 cm was use for the RDE test. The nominal compositions of three types of Al alloys are listed in Table 4.11. All of these specimen were polished to a surface finish of 1200 grit with SiC paper, and subsequently degreased with ethanol followed by deionized water, before experiment.

Table 4.11: Composition of AA7050-T7451, AA5083-H131 and AA2024-T351 (All values in weight percent)

	Si	Fe	Cu	Mn	Mg	Cr	Zn	Ti	Zr	Al
7050	0.12	0.15	2.6	0.1	2.6	0.04	6.7	0.06	0.15	balance
5083	0.1	0.22	0.05	0.7	4.4	0.08	0.02	0.02	N/A	balance
2024	0.093	0.18	4.5	0.62	1.3	0.01	0.1	0.018	0.003	balance

4.5.2.2 Electrochemical Tests

A three-electrode electrochemical cell was used with the alloy specimen as the working electrode (WE) with an exposure area of 1cm² except that Pt disc electrode had surface area=0.2 cm², saturated calomel reference electrode (SCE) as reference electrode (RE), and platinum-niobium mesh as the counter electrode (CE). A Bio-Logic SP-200 (Bio-Logic SAS, Claix, France) potentiostat was utilized with EC-Lab (Version 11.01) software running to record all the electrochemical results. The details of each electrochemical technique will be described in below

Cathodic polarization measurements were performed on AA7050, AA5083, AA2024 and SS316L at scan rate=0.2 mV/s after 1hr open circuit potential (OCP) measurement, starting from OCP to -1.5 V_{SCE} in five different solutions: (1) 0.6M NaCl, (2) 0.57M NaCl+0.01M AlCl₃, (3) 0.45M NaCl+0.05M AlCl₃, (4) 0.3M NaCl+0.1M AlCl₃, and (5) 0.2M AlCl₃. The pH of each solution is listed in Table 4.12. Two additional test solutions of 0.6M NaCl with pH adjusted with HCl were prepared to compare with solution (2) and (4) under the same pH: 0.6M NaCl with pH=3.57 and 0.6M NaCl with pH=3.01. The purpose of performing cathodic polarization from OCP is to avoid the effect of prior anodic dissolution on the surface structure if the scan started above OCP, and only focus on the cathodic characteristic of as-polished samples. To determine the dependence of the polarization resistance (R_p) and corrosion potential (E_{corr}) on the [Al³⁺], full polarization measurements were performed on all Al alloy samples with scan rate=0.2 mV/s, which started at 0.3V below OCP and ended at -0.55 V_{SCE}.

Table 4.12: pH of each test solution

Solution	pH
0.6M NaCl	5.6
0.57M NaCl+0.01M AlCl ₃	3.57
0.45M NaCl+0.05M AlCl ₃	3.2
0.3M NaCl+0.1M AlCl ₃	3.01
0.2M AlCl ₃	2.87

A typical electrochemical impedance spectrum in this part was acquired over the frequency range from 10 kHz to 10 mHz at 10 points per decade with a 10 mV AC amplitude around OCP after 1hr immersion time. AA7050-T7451 were immersed in solution (1)–(5) described above to study the effect of Al³⁺ concentration on interfacial parameters. All the EIS data were fitted by EC-Lab software.

A PINE Instrument ASR rotator (Pine Research Instrumentation, Inc., Durham, NC) was used with a Pt WE. Two types of experiments with RDE configurations were performed: 1) after 10-min stabilization, direct RDE cathodic polarization measurements from $-0.2 V_{SCE}$ to $1.1 V_{SCE}$ with scan rate $=0.2 \text{ mV/s}$ and rotation speeds of $= 100, 200, 500$ and 1000 rpm , in $0.57\text{M NaCl}+0.01\text{M AlCl}_3$, 0.6M NaCl ($\text{pH}=3.57$), $0.3\text{M NaCl}+0.1\text{M AlCl}_3$, and 0.6M NaCl ($\text{pH}=3$), respectively; 2) RDE cathodic polarization measurements starting from OCP to $-1 V_{SCE}$ after 1hr OCP measurement in 0.6M NaCl , 0.6M NaCl ($\text{pH}=3.01$) and $0.3\text{M NaCl}+0.1\text{M AlCl}_3$. One additional test in N_2 -purged de-aerated environment was conducted in the last solution.

4.5.2.3 SEM/EDS Characterizations

A Pt surface after cathodic polarization in Al^{3+} containing solution was characterized by both FEI QUANTA 200 scanning electron microscopes (SEM) with an energy dispersive spectroscopy (EDS) detector (Hillsboro, OR).

4.5.3 Results

A description of the corrosion kinetics of Al alloys in the absence and presence of Al^{3+} , as well as the dependence of mass-transfer limited cathodic kinetics and corrosion resistance of Al alloys on the Al^{3+} concentration will be presented here. Most of the results presented are for AA7050-T7451.

4.5.3.1 Mass Transfer-Limited Cathodic Kinetics and Polarization Resistance of Al Alloys as a Function of $[\text{Al}^{3+}]$

Typical cathodic polarization curves of AA7050-T7451 in pure 0.6M NaCl and $\text{NaCl}+\text{AlCl}_3$ with different $[\text{Al}^{3+}]$ and fixed $[\text{Cl}^-]=0.6\text{M}$ are displayed Figure 4.23a. At first glance, cathodic limiting current density (i_{lim}) increased significantly once $[\text{Al}^{3+}]$ was added to the NaCl, and i_{lim} kept increasing steadily as $[\text{Al}^{3+}]$ increased. A comparison of i_{lim} chosen at a reference

potential $-1.05 \text{ V}_{\text{SCE}}$ as a function of $[\text{Al}^{3+}]$ is shown in Figure 4.23b. A sharp jump in i_{lim} ($\sim 6\times$) when 0.01M $[\text{Al}^{3+}]$ was introduced into pure NaCl solution, followed by a steady increase in i_{lim} with increasing $[\text{Al}^{3+}]$, albeit at a slower rate between 0.05 and 0.1M , until a maximum was reached at 0.2M $[\text{Al}^{3+}]$, which was about 9 times higher than 0.6M NaCl. It is obvious that addition of $[\text{Al}^{3+}]$ can significantly enhance mass transfer limited cathodic kinetics of AA7050. To determine if the effect of $[\text{Al}^{3+}]$ also takes place in the other Al alloys, cathodic polarization curves of AA7050, 5083 and 2024 in 0.6M NaCl and 0.3M NaCl+ 0.1M AlCl_3 were generated and are compared in Figure 4.24. It is clearly seen that, with addition of Al^{3+} into NaCl solution, i_{lim} was significantly enhanced for all three Al alloys, and the order of the degree of i_{lim} was ranked as follows: AA2024>AA7050>AA5083 in both solutions in the presence and absence of Al^{3+} . The fact that AA2024 had highest i_{lim} can be attributed to its high Cu content since Cu-bearing IMCs are believed to be active sites sustaining mass-transfer limited cathodic kinetics¹⁹.

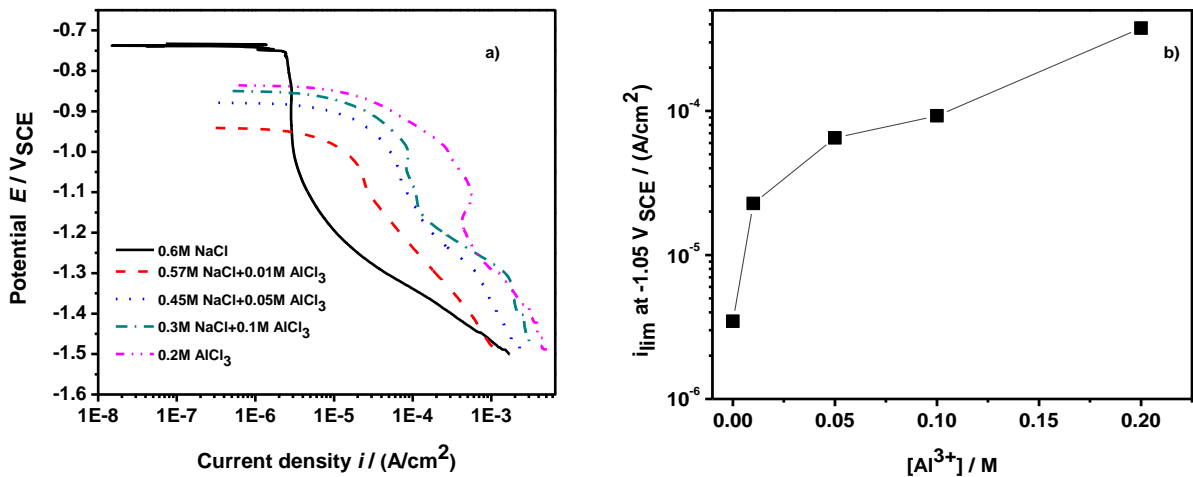


Figure 4.23: a) Comparison of cathodic polarization curves of AA7050 as a function of $[\text{Al}^{3+}]$; b) i_{lim} vs. $[\text{Al}^{3+}]$ at a reference potential $-1.05 \text{ V}_{\text{SCE}}$.

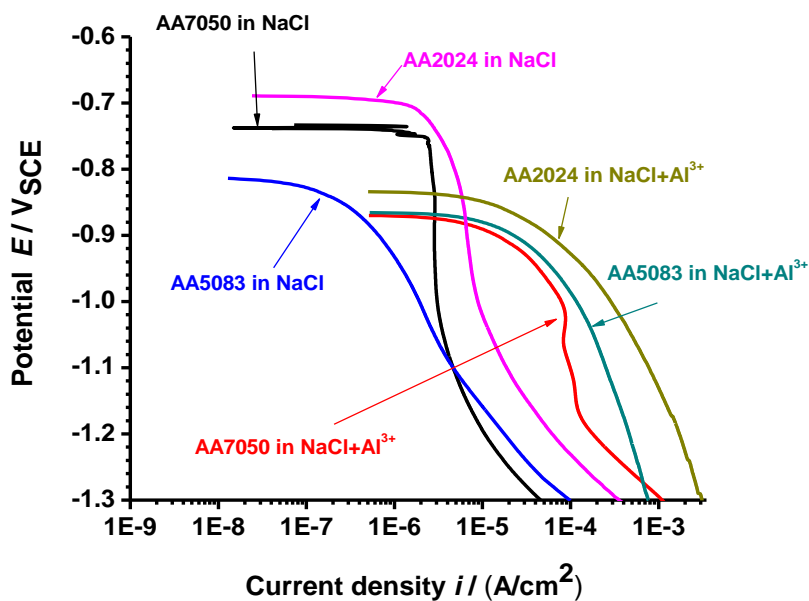
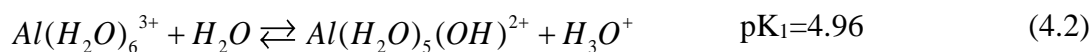


Figure 4.24: Comparisons of cathodic kinetics of AA7050, AA5083 and AA2024 in 0.6M NaCl and 0.3M NaCl+0.1M AlCl₃.

It is known that Al³⁺ can be hydrated with six water molecules to form complex ion Al(H₂O)₆³⁺ in neutral solutions²⁷. This complex ion can undergo a series of complicated hydrolysis reactions, with the dominant reaction being:



The hydrolysis of hydrated Al³⁺ results in an acidic pH in the solution. To distinguish the enhanced cathodic kinetics of Al alloys by adding Al³⁺ from that due to merely low pH of solution, a comparison of cathodic kinetics of AA7050 in 0.6M NaCl (pH=5.6), 0.6M NaCl (pH=3.01), and 0.3M NaCl + 0.1M AlCl₃ (pH=3.01) is displayed in Figure 4.25. By looking at *i_{lim}* at -1.05 V_{SCE} again, that for Al³⁺ containing solution was about twice that for 0.6M NaCl at the same pH, indicating the increase in *i_{lim}* is not solely caused by low pH due to hydrolysis of Al³⁺.

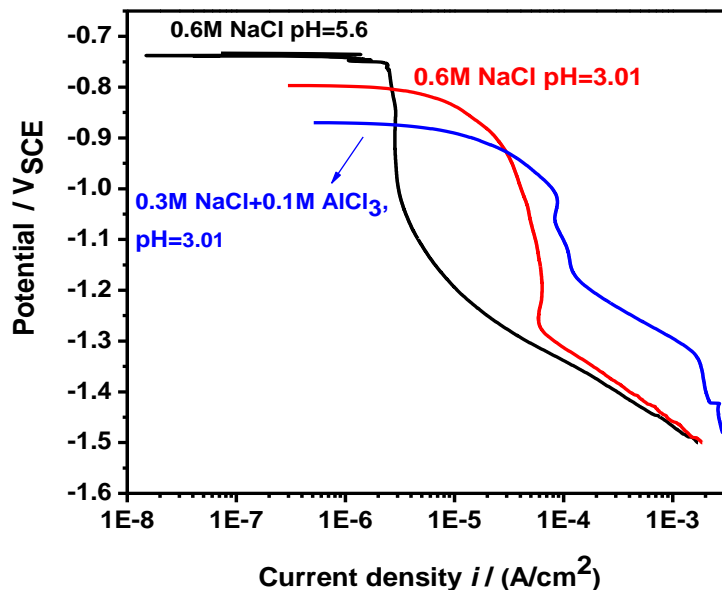


Figure 4.25: A comparison of cathodic kinetics of AA7050 in 0.6M NaCl (pH=5.6), 0.6M NaCl (pH=3.01), and 0.3M NaCl + 0.1M AlCl₃ (pH=3.01).

As for the effect of [Al³⁺] on the polarization resistance, a comparison of full polarization curves of AA7050 as a function of [Al³⁺] is shown in Figure 4.26a. R_p , E_{corr} and i_{corr} (calculated by EC-lab software) for each solution in Figure 4.26a are listed in Table 4.13. It can be seen that R_p fell suddenly from 19820 ohm*cm² to 3785 ohm*cm² when adding 0.01M [Al³⁺], followed by a gradual decrease as [Al³⁺] increased until reaching a minimum in 0.2M AlCl₃, which was only about 11% of that in 0.6M NaCl. The i_{corr} values showed the reversal trend due to its reciprocal relation with R_p , starting from 7.15E-7 A/cm² to 1.21E-5 A/cm² with increasing [Al³⁺]. Interestingly, E_{corr} first dropped from -0.742 V_{SCE} to -0.939 V_{SCE} when introducing 0.01M [Al³⁺] into NaCl solution, and then rose with increasing [Al³⁺]. This behavior can be explained by Figure 4.26b. When solution changes from a to b, application of Mixed Potential Theory demonstrates that anodic/ dissolution kinetics of AA7050 was enhanced due to addition of [Al³⁺], and the resultant E_{corr} moved in negative direction assuming cathodic kinetics either stayed

unchanged or changed less than the anodic kinetics. However, the mass transfer limited cathodic kinetics was significantly increased as $[Al^{3+}]$ increased further, such that cathodic kinetics became more dominant than anodic kinetics regarding the change in E_{corr} , with the resultant E_{corr} switched to move in more positive direction as keeping increasing $[Al^{3+}]$. This also implies that a significant $[Al^{3+}]$ ($\sim 0.05M$) is needed in order to maintain a high corrosion rate of Al alloys controlled by enhanced cathodic kinetics.

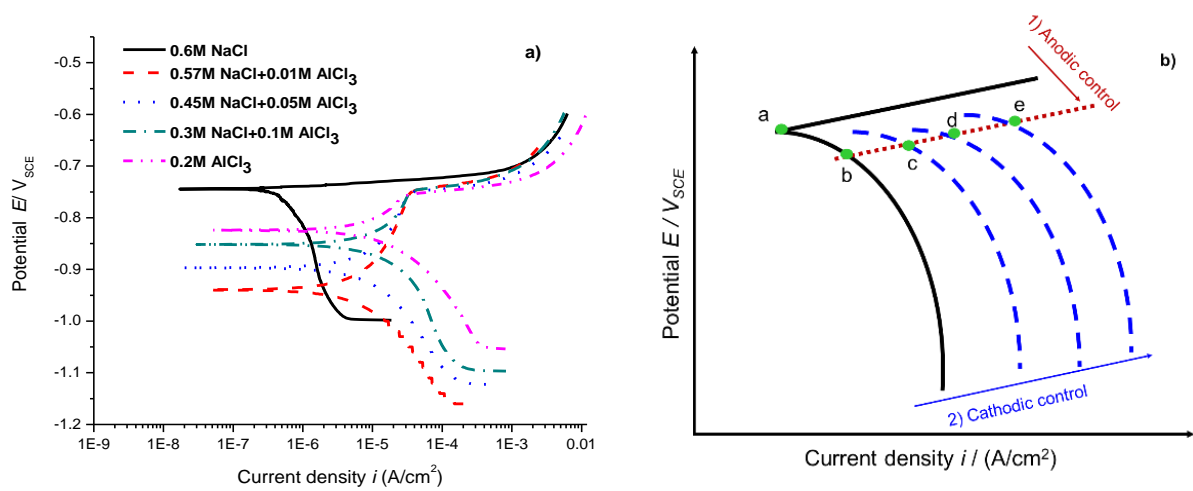


Figure 4.26: a) A comparison of full polarization curves of AA7050 as a function of $[Al^{3+}]$; b) schematic polarization curve to show the controlling factors for E_{corr} based on the Mixed Potential Theory.

Table 4.13: A list of Fitted Electrochemical Parameters for AA7050 as a function of $[Al^{3+}]$ in solutions.

	Solution	$R_p(ohm \cdot cm^2)$	$E_{corr}(V_{SCE})$	$i_{corr}(A/cm^2)$
a	0.6M NaCl	19820	-0.742	7.15E-7
b	0.57M NaCl+0.01M $AlCl_3$	3785	-0.939	6.89E-6
c	0.45M NaCl+0.05M $AlCl_3$	3485	-0.897	7.48E-6
d	0.3M NaCl+0.1M $AlCl_3$	2805	-0.852	9.30E-6
e	0.2M $AlCl_3$	2158	-0.823	1.21E-5

4.5.3.2 EIS Study

In order to better understand the electrochemical mechanism of the effect of $[Al^{3+}]$ on the corrosion behavior of Al alloys and evaluate passive oxide film quality as a function of $[Al^{3+}]$, EIS analyses were performed on AA7050-T7451. Figure 4.27 shows the corresponding Nyquist and Bode plots for the different solutions. It is clearly seen that an inductive loop appeared in the low frequency regime in Al^{3+} containing solution, and as a result, two types of equivalent circuit models were incorporated as shown in Figure 4.28. The equivalent circuit model in Figure 4.28a was used to fit data in 0.6M NaCl, and that in Figure 4.28b was used for the NaCl+AlCl₃ solutions to take in account the inductive loop, which might be caused relaxation of absorbed intermediate in the oxide film during HER²⁸⁻³¹. Also, a Warburg impedance element was used in both models, to account for mass transfer of protons to the oxide/electrode interface in the low frequency regime. At high frequency regime, both models have CPE behavior attributed to the passive oxide film, in order to estimate the effective capacitance values from the CPE, Hirschorn *et al.*^{32,33} derived the mathematical relation between constant phase element (CPE) and effective capacitance for oxide film thickness which was used in Part 2 of this chapter as well

$$C_{eff} = gQ(\rho_{\delta}\epsilon\epsilon_0)^{1-\alpha} \quad (4.1)$$

Where C_{eff} is the effective capacitance, ρ_{δ} is the film resistivity, ϵ is the dielectric constant for the film, ϵ_0 is the vacuum permittivity (8.852E-12 F/m), and g is a dimensionless number which is a function of α : $g = 1 + 2.88(1 - \alpha)^{2.375}$. For ρ_{δ} and ϵ , it is assumed that the oxide film is mainly alumina with film resistivity = 1E+12 *ohm · m* and $\epsilon=9.1$ (Table 4.7). All of the fitted EIS parameters are listed in Table 4.14: *Fitted EIS parameters as a function of [Al3+] for AA7050*. Based on these fitted parameters, two factors can be evaluated: $R_{film}C_{eff, film}$ product to evaluate oxide film quality, and $R_{total}=R_{film}+R_{ct}+R_{Loop}$, to evaluate total corrosion resistance. The reason RC

product can be used to evaluate oxide film quality is that: $R_{film} = \rho_{film} \frac{\delta_{film}}{A_{film}}$ (ρ_{film} : film resistivity, A_{film} : cross section area of film, δ_{film} : film thickness) and $C_{eff,film} = \frac{\epsilon_o \epsilon A_{film}}{\delta_{film}}$, so $R_{film} * C_{eff,film} = \rho_{film} \epsilon_o \epsilon$ is only a function of film resistivity assuming the dielectric constant is unchanged. Plots in which $R_{film} \times C_{eff,film}$ as well as R_{total} vs. $[Al^{3+}]$ are shown in Figure 4.29. The RC product declined dramatically with small addition of Al^{3+} , which might be attributed to hydration of oxide film under anodic control when Al^{3+} just introduced into NaCl. Higher Al^{3+} concentration led to small increases in RC, possibly due to build-up of aluminum oxide/hydroxide on the alloy surface till Al^{3+} concentration. As for the total resistance, it decreased with increasing Al^{3+} concentration with the largest decrease occurring at the smallest Al^{3+} concentrations, echoing the tendency of polarization resistance calculated from previously, indicating that Al alloy is more prone to localized corrosion as increasing $[Al^{3+}]$.

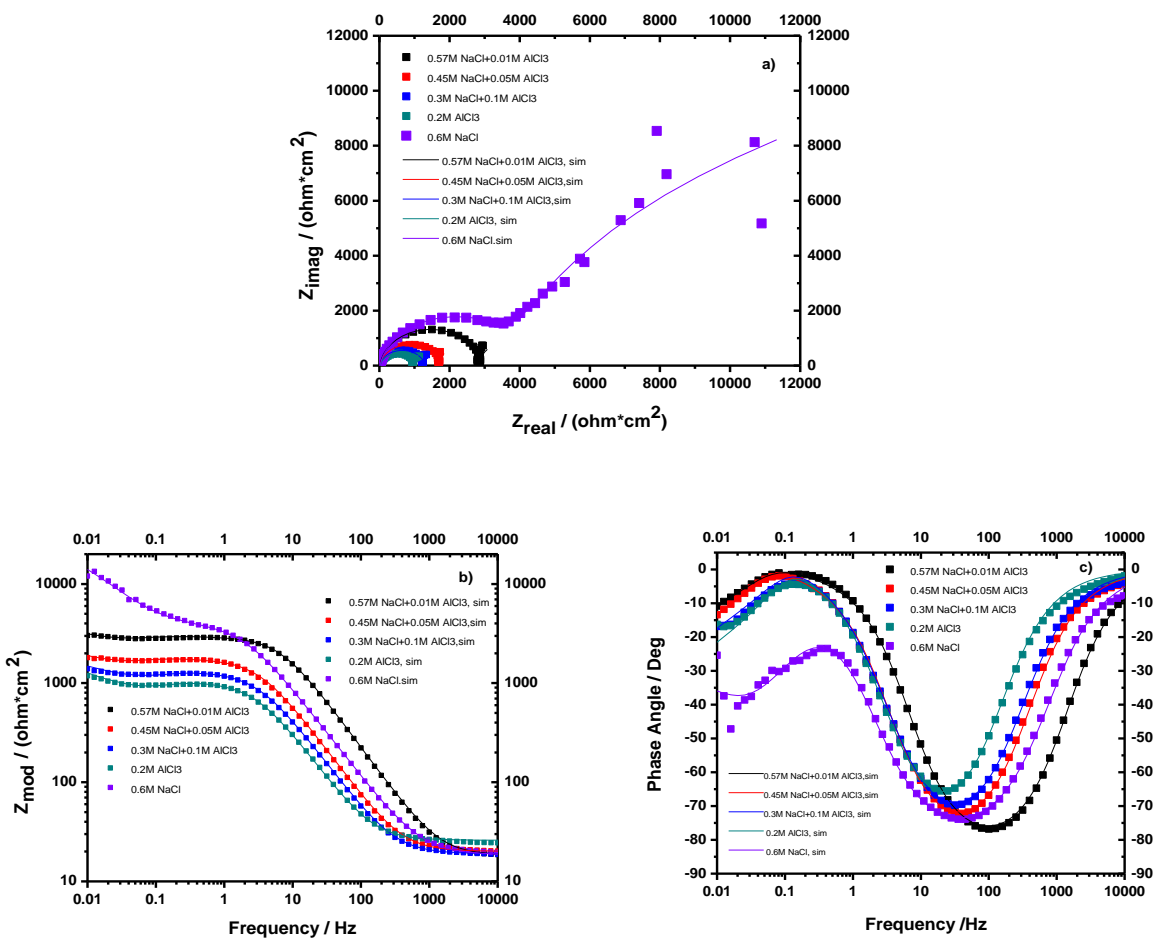


Figure 4.27: a) Nyquist Plots of AA7050 as a function of $[Al^{3+}]$; b) Bode impedance vs. Frequency as a function of $[Al^{3+}]$; c) phase angle vs. Frequency as a function of $[Al^{3+}]$.

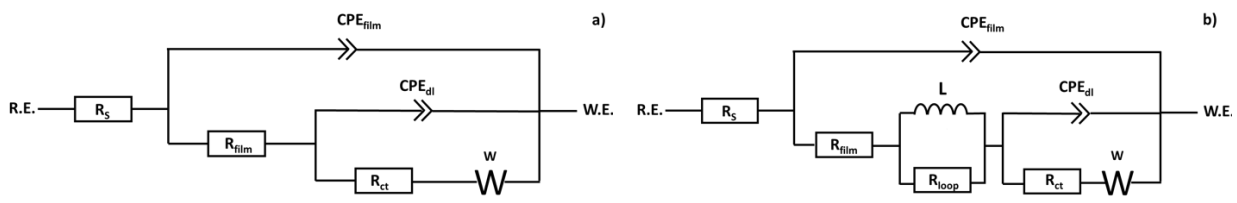


Figure 4.28: a) equivalent circuit model to fit data in 0.6M NaCl solution; b) in NaCl+AlCl₃ solution.

Table 4.14: Fitted EIS parameters as a function of $[Al^{3+}]$ for AA7050

	0.6M NaCl	+0.01M AlCl ₃	+0.05M AlCl ₃	+0.1M AlCl ₃	0.2M AlCl ₃
R_s ($\text{ohm} \cdot \text{cm}^2$)	18.57	18.5	20.1	19	26
CPE_{film} ($S \cdot s^{\alpha_1}$)	2.685E-5	1.01E-5	3.40E-5	5.00E-5	6.75E-5
α_{film}	0.9002	0.945	0.933	0.92	0.931
$C_{\text{film,eff}}$ ($F \cdot \text{cm}^{-2}$)	3.804E-5	1.218E-5	4.301E-5	6.617E-5	8.599E-5
R_{film} ($\text{ohm} \cdot \text{cm}^2$)	4037	2760		840	713
L_{loop} (H)	N/A	165	210	330	300
R_{loop} ($\text{ohm} \cdot \text{cm}^2$)	N/A	121.5	251	459	265
CPE_{dl} ($S \cdot s^{\alpha_2}$)	5.51E-6	1.05E-2	8E-3	6.7e-3	5.98E-3
α_{dl}	0.827	0.991	0.75	0.7	0.69
R_{ct} ($\text{ohm} \cdot \text{cm}^2$)	15682	1221	1115	1000	601
W ($S \cdot s^{0.5} \cdot \text{cm}^{-2}$)	1200	160	120	115	120

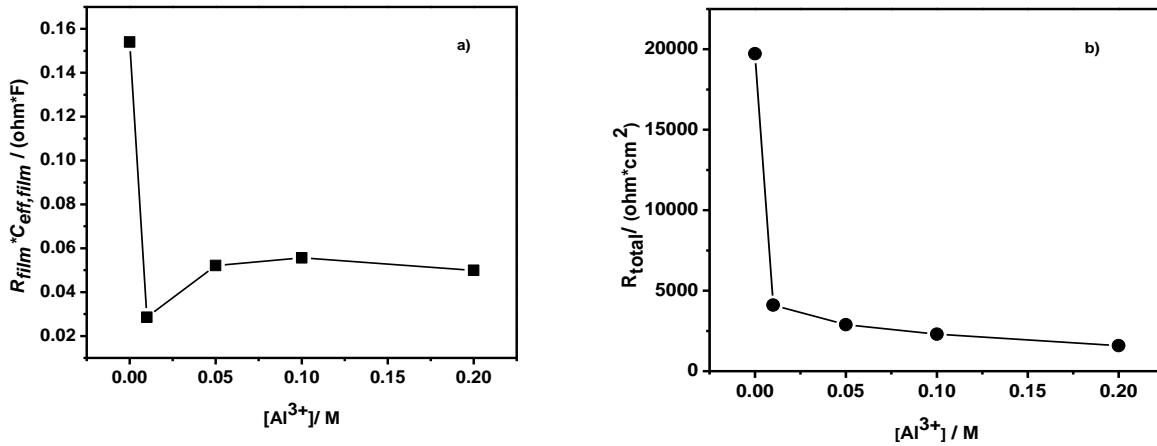


Figure 4.29: a) $R_{\text{film}}C_{\text{eff, film}}$ product vs. $[Al^{3+}]$ and b) R_{total} vs. $[Al^{3+}]$ for AA7050 from EIS analysis.

4.5.3.3 Effect of Al^{3+} on Cathodic Kinetics of Pt and SS

Several previous studies have investigated the effect of cathodic polarization on the corrosion of pure Al. Lin and Hebert^{34,35} found that the hydrated oxide film transformed into hydroxide and became an ohmic conductor with high conductivity at cathodic potential $\sim -1.7 V_{SCE}$, resulting in higher cathodic charge and enhanced corrosion rate. Moon and Pyun^{36,37} studied the electrochemical behavior of Al after prior cathodic polarization, showing that the observed

enhanced corrosion rate was caused by the dissolution of native oxide film due to prior cathodic polarization (and alkalization of the surface). However, both of their studies indicate that cathodic charge changed the property of oxide film which in turn accelerate the corrosion rate. Here, we wanted to show that the enhanced cathodic kinetics or corrosion rate is not limited in the Al alloy system, but can be also extended to the other metals and alloys, of which Pt and SS were utilized as two examples in this study.

Cathodic polarization curves of SS316L in three different solutions are shown in Figure 4.30a. Similar phenomenon observed with the Al alloys, SS316L showed enhanced mass transfer limited cathodic kinetics in the presence of Al^{3+} compared to that in 0.6M NaCl with natural pH, and 0.6M NaCl with adjusted to the same pH, proving again that this enhancement was contributed to the Al^{3+} ion, not only the low solution pH due to hydrolysis of Al^{3+} . However, it is still difficult to distinguish the ORR limiting current density from effects on HER. Another group of cathodic polarization curves of Pt in the three same solutions as SS 316L tests, plus one additional test of 0.3M NaCl+0.1M AlCl_3 in deaerated solution, are displayed in Figure 4.30b. Because the i_{lim} in 0.6M NaCl pH=5.6 for Pt is attributed to ORR only, this can be utilized to distinguish HER diffusion limited potential region from ORR one in both 0.6M NaCl pH=3, and 0.3M NaCl+0.1M AlCl_3 quiescent solutions: $0.2 V_{\text{SCE}} \sim -0.3 V_{\text{SCE}}$ is attributed to ORR, and $-0.5 V_{\text{SCE}} \sim -0.9 V_{\text{SCE}}$ is attributed to HER. It is clearly seen that the i_{lim} pertinent to ORR in both 0.6M NaCl pH=3.01 and 0.3M NaCl+0.1M AlCl_3 solutions were almost identical to that in 0.6M NaCl with natural pH, proving that adding Al^{3+} has negligible effect to ORR related diffusional cathodic kinetics. By comparing i_{lim} in 0.3M NaCl+0.1M AlCl_3 quiescent and deaerated solutions, one can see that: i_{lim} in deaerated solution was only about 40% of that in quiescent solution, since the reduced ORR-related current density resulted in a lower total current density due to deaeration. However, i_{lim}

pertinent to HER was still about 40 times higher than that in 0.6M NaCl with same pH, proving that Al^{3+} is the dominant factor contributing significant enhancement in HER diffusional cathodic kinetics. This finding also implies that the interaction between Al^{3+} and native oxide film on the Al alloy surface is not the contributing factor to the enhancement of cathodic kinetics, but the change in solution property is the one when introducing Al^{3+} into NaCl system.

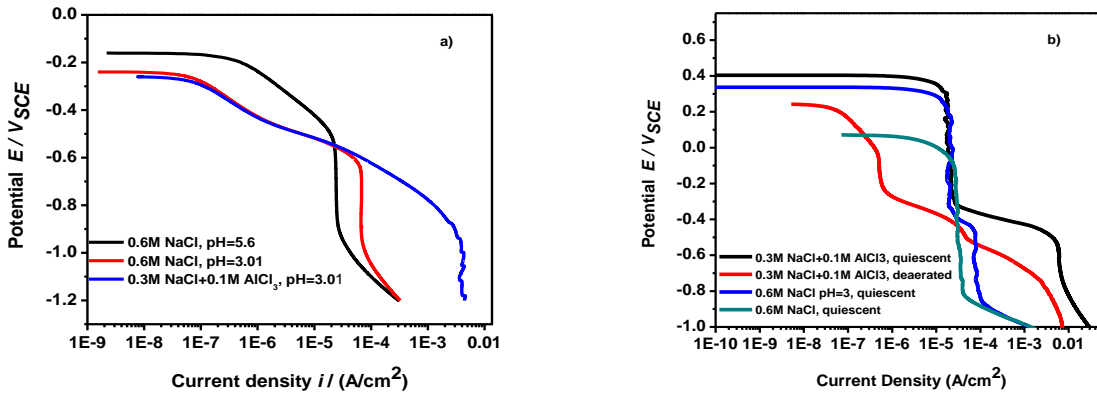


Figure 4.30: Comparison of cathodic polarization curves of a) SS316L, and b) Pt in 0.6M NaCl (natural pH), 0.6M NaCl (pH=3.01), and 0.3M NaCl+0.1M AlCl_3 (pH=3.01, additional test in deaerated solution for Pt).

4.5.4 Discussions

According to Fick's 1st Law, the theoretical diffusion limited current density assuming one-dimensional diffusion can be expressed as

$$i_{\text{lim,theoretical}} = \frac{nFD(C_{\text{bulk}} - C_{\text{surface}})}{\delta} \quad (4.3)$$

where n is the number of electrons transferred during electrochemical reaction, D is the diffusivity of reacting species, C_{bulk} and C_{surface} are the concentration of reacting species at the bulk solution and electrode surface respectively, and δ is the diffusion layer thickness. In this section, a deconstruction of Equation 4.3 will be performed to target the dominant parameter controlling the increased HER related diffusion current density.

4.5.4.1 Formation of Aluminum Oxide/Hydroxide Film on the Surface as Diffusional Barrier to HER

A very thin layer of white film was formed after cathodic polarization of Pt in Al^{3+} containing solution, and SEM/EDS was then utilized to look at the film morphology and composition. Typical SEM and EDS images of Pt after cathodic polarization in 0.3M NaCl+0.1M AlCl_3 are displayed in Figure 4.31. In SEM image, the film consists of loosely packed irregularly shaped flakes, and the composition of film consists of Al and O, implying some type of aluminum oxide/hydroxide was formed on the Pt surface, Lin and Hebert³⁴ found that aluminum hydroxide can be existed on the Al surface even in an acidic environment (0.1M HCl). However, the detailed composition and chemical structure of this film is beyond the study scope in this work.

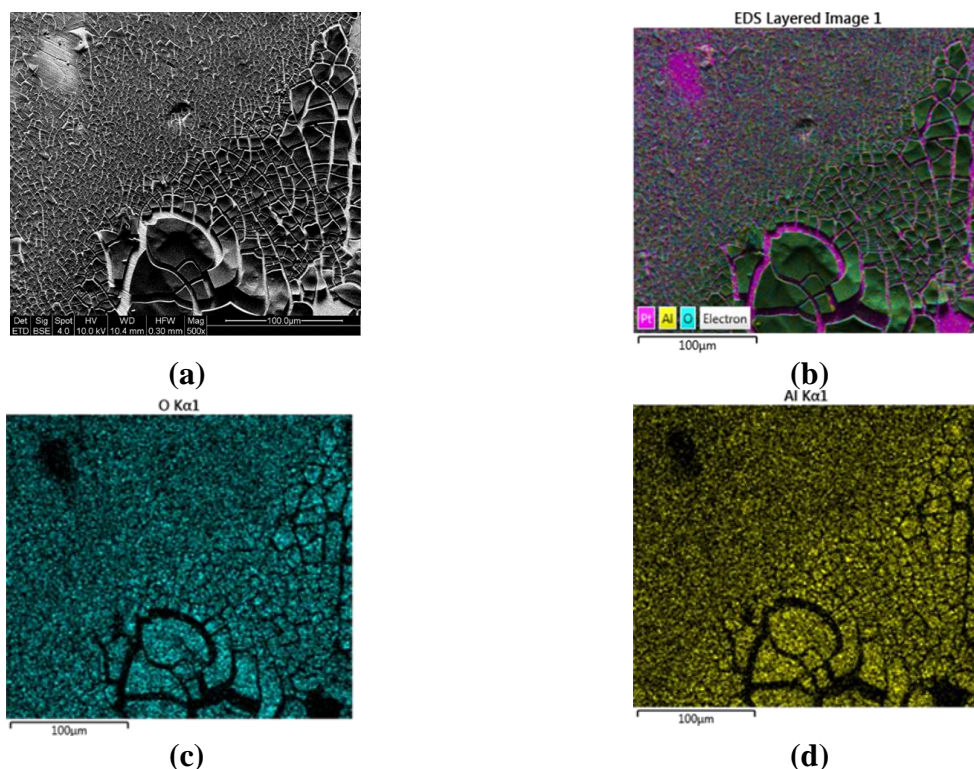


Figure 4.31: a) SEM image , b) layered EDS map, c) O elemental EDS map and d) Al elemental map of film covered on the Pt surface after cathodic polarization in 0.3M NaCl+0.1M AlCl_3 solution.

To discern the role of this film in mass transfer limited cathodic kinetics, continuous cathodic polarization measurement was performed on Pt in 0.3M NaCl+0.1M AlCl₃, in which after one scan, Pt was allowed to rest in the test solution for 5mins, and then scan from OCP to the final potential was conducted. This procedure was repeated three times. The measured cathodic polarization scans are shown in Figure 4.32. After the formation of aluminum oxide/hydroxide film on the surface during the 1st scan, both i_{lim} at ORR region and HER region were decreased, which indicates that the formed film is diffusional barrier to both ORR and HER. According to Equation 4.3, the real diffusion layer thickness $\delta = \delta_{natural_convection} + \delta_{film}$, where $\delta_{natural_convection}$ ³⁸⁻⁴⁰ is the critical natural convection boundary layer thickness in quiescent solution, and δ_{film} is the film thickness. Once film forms the surface, the diffusion layer thickness increased from $\delta_{natural_convection}$ to $\delta_{natural_convection} + \delta_{film}$, resulting in a lower limiting current density. However, both $i_{lim, ORR}$ and $i_{lim, HER}$ were almost the same in 2nd and 3rd scan, which implies that the film covered Pt surface might not be a good substrate for future film deposition such that the accumulation of film thickness was negligible after the 1st scan.

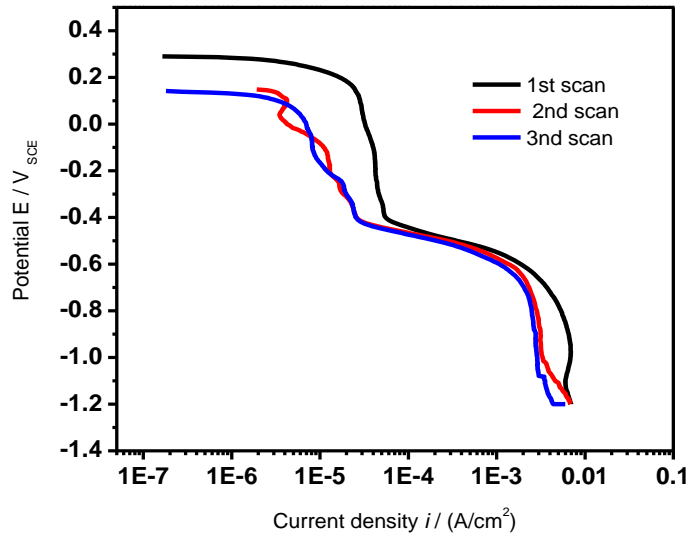


Figure 4.32: Repeated cathodic polarization scans of Pt in 0.3M NaCl+0.1M AlCl₃.

4.5.4.2 Mechanism of Enhanced Proton Diffusivity (Grotthuss Mechanism)

To investigate the diffusivity of the proton in the Al³⁺-containing solution and compare it with that in purely acidified NaCl solution, RDE tests were performed on Pt in both 0.6M NaCl pH 3.01 and 0.3M AlCl₃+0.1M AlCl₃ (pH=3.01) with rotation speeds of = 100, 200, 500 and 1000 rpm (Figure 4.33). Reference potentials of =-0.7 V_{SCE} and -0.8 V_{SCE} were selected for NaCl, and NaCl+AlCl₃ solutions respectively to develop Levich analysis⁴¹. Levich plots for Pt in these two solutions are shown in Figure 4.34. Based on the fitting, the expression of Levich equation for each solution are: i_{lim} (at -0.7 V_{SCE})= 0.00454+0.00153* $\omega^{0.5}$ for 0.6M NaCl (pH=3.01) solution, and i_{lim} (at -0.8 V_{SCE})= 0.00454+0.00153* $\omega^{0.5}$ for 0.3M NaCl+0.1M AlCl₃. Because Levich equation is expressed as

$$i_{lim} = 0.620 \cdot nFD_{H^+}^{2/3} \nu^{-1/6} C_{H^+} \omega^{0.5} \quad (4.4)$$

where D is the diffusivity of proton at 25°C , ν is the kinematic viscosity of solution, C_{H^+} is the bulk concentration of proton assuming fast HER at the electrode/electrolyte interface such that $C_{\text{surface}, \text{H}^+}$ is zero. and ω is the rotation speed of the RDE. Assuming two solutions have the same ν and C_{H^+} , the ratio of slope in each Levich expression is equal to

$$\left[\frac{D_{\text{H}^+}(\text{Al}^{3+})}{D_{\text{H}^+}(\text{no Al}^{3+})} \right]^{2/3} = \frac{1.53E-3}{1.781E-4} \quad (4.5)$$

Hence $D_{\text{H}^+}(\text{Al}^{3+}) : D_{\text{H}^+}(\text{no Al}^{3+})$ is about 25, which means diffusivity in Al^{3+} containing solution is 24 times higher than pure NaCl solution under the same pH value.

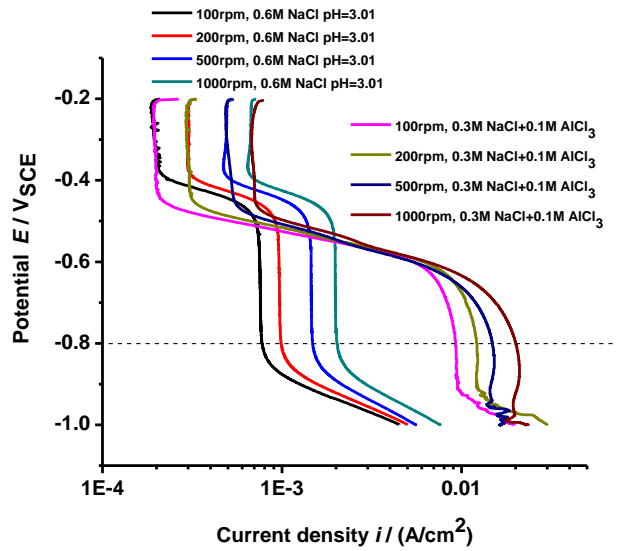


Figure 4.33: RDE tests of Pt in both 0.6M NaCl pH3.01 and 0.3M $\text{AlCl}_3+0.1\text{M AlCl}_3$ (pH=3.01) with rotation speed= 100, 200, 500 and 1000 rpm respectively.

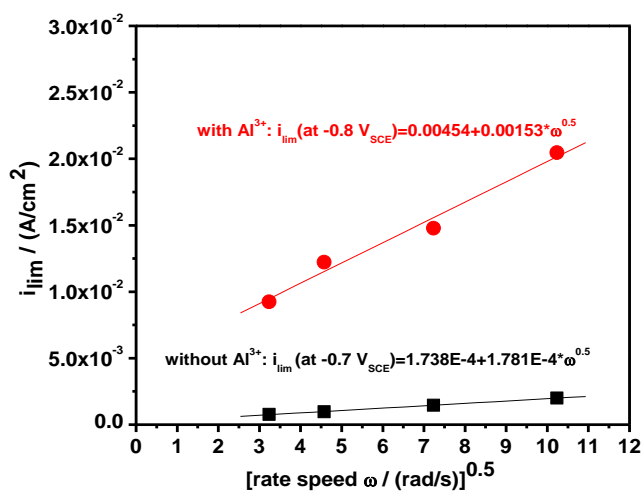


Figure 4.34: Levich Plots for Pt in 0.6M NaCl pH3.01 and 0.3M AlCl₃+0.1M AlCl₃ (pH=3.01).

A mechanism based on Grotthuss Theory^{42,43} is proposed to explain the large increased proton diffusivity in Al³⁺ containing solution. In this theory, proton transport along chains of hydrogen bonds in water involving hopping or tunneling of the proton from one molecule to the next. In pure acidified NaCl solution, the transport of proton can be illustrated in Figure 4.35a. Protons from the bulk solution, move along the proton chains in water system, and reach the electrode surface to undergo reaction. The Grotthuss Theory can be also applied into Al³⁺ containing solution⁴⁴. When Al³⁺ is introduced into the system (Figure 4.35b), for example, the Al³⁺ coordinates with O at location 1), such that the center of electronic cloud moves from the O toward Al³⁺, such that the bonding energy between O and H is lower than in Figure 4.35a. As a result, the proton will transport more easily in Al³⁺ containing solution, leading to a higher diffusivity.

Lastly, a brief comparison is illustrated to explain why Al³⁺ has distinct effect from Zn/Mg²⁺ in terms of cathodic kinetics of Al alloys. Hydrolysis of Al³⁺ can easily occur in water-

based solution, providing excessive proton and resulting in acidic solution environment according to Equation 4.2. However, the hydrolysis of either Mg^{2+} or Zn^{2+} can only occur to a small degree before massive precipitation reaction taking place. The stability constants⁴⁵ ($\log_{10}\beta$) to form $Al(H_2O)_5(OH)^{2+}$, $Mg(OH)^+$ and $Zn(OH)^+$ which are major species from hydrolysis reaction in corresponding water-based solutions are:- 4.95, -9.00, and -39.82 respectively. It should be noted that more positive stability constant indicates more availability of hydrolysis product as well as proton, thus it explains why Al^{3+} solution is more acidic to Zn/Mg^{2+} solution (e.g., pH for 0.3M NaCl+0.1M $AlCl_3$ is 3, that for 0.6M NaCl +0.1M $ZnSO_4$ is 5.5, and that for 0.6M NaCl+0.1M $MgSO_4$ is 5.8) and HER is the dominant reaction in Al^{3+} solution but ORR is the one in Zn/Mg^{2+} solution due to solution pH difference at the same cation concentration. Furthermore, suppose one adjusts the pH of Zn/Mg^{2+} solution same as Al^{3+} solution assuming identical metallic cation concentration, due to the relatively low value of stability constant of both $Mg(OH)^+$ and $Zn(OH)^+$ compared to $Al(H_2O)_5(OH)^{2+}$, the availability of $Mg(OH)^+$ and $Zn(OH)^+$ in each pertinent solution is too rare to substantially affect the bonding energy between hydrogen and oxygen in the water molecules among a large scale according to Grotthuss Theory, thus contribution to increased proton diffusivity by adding Zn/Mg^{2+} is negligible compared to Al^{3+} . To summarize, Al^{3+} can promote cathodic kinetics of Al alloy due to large stability constant of major hydrolysis product $Al(H_2O)_5(OH)^{2+}$ as well as significantly increased proton diffusivity based on Grotthuss Theory. Based on this framework, one can infer that Fe^{3+} would show the similar behavior as Al^{3+} which can promote HER cathodic kinetics, whereas the behavior of Fe^{2+} would resemble Zn^{2+}/Mg^{2+} which can inhibit ORR cathodic kinetics, since the stability constants⁴⁵ of major hydrolysis product $FeOH^{2+}$ (from Fe^{3+} solution) and $FeOH^+$ (from Fe^{2+} solution) are -2.38 and -9.32 respectively.

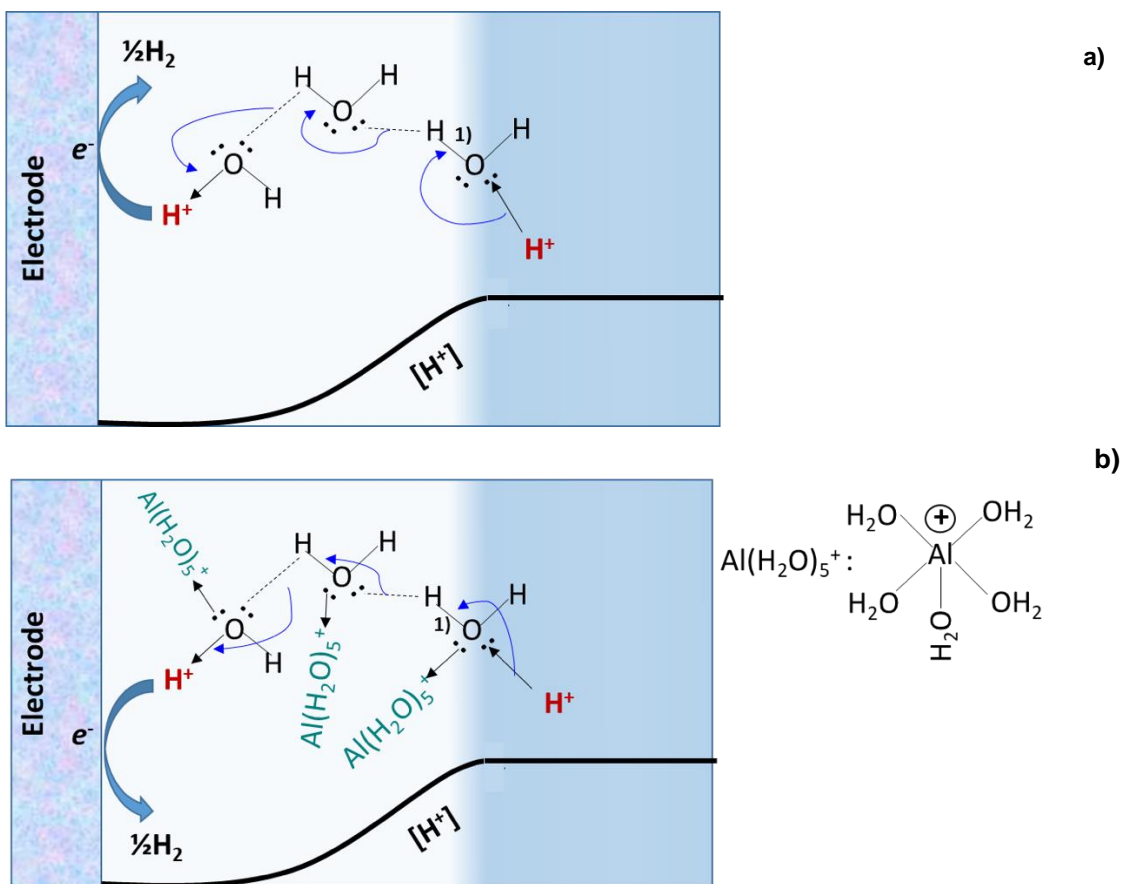


Figure 4.35: Proton Transport in: a) purely acidified NaCl solution and b) Al^{3+} containing solution based on Grotthuss Theory^{42,43}.

4.5.5 Conclusions

The effect of Al^{3+} on the cathodic kinetics of Al alloys has been explored in this study. It has been found that: addition of Al^{3+} into NaCl solution can significantly increase the diffusion limited cathodic kinetics of Al alloys, and this increase is also proportional to $[Al^{3+}]$. The same phenomenon was also observed on Pt and SS316L, which indicates that this enhancement in cathodic kinetics is not related the surface structure of Al alloy, and HER diffusion limited kinetics are increased rather than ORR kinetics as a result. Based on rigorous electrochemical studies on Pt, it shows that: according to the Grotthuss Theory in which Al^{3+} can facilitate transport of proton, although addition of Al^{3+} can precipitate oxide/hydroxide film on Pt which acts as diffusional barrier to HER during cathodic polarization, greatly enhanced proton diffusivity due to Al^{3+}

overwhelms the barrier effect of precipitate film, and then significantly increases cathodic limiting current density.

4.5.6 References

1. J. R. Davis, *Corrosion of Aluminum and Aluminum Alloys*, ASM International, (1999).
2. R. T. Foley, *Corrosion*, **42**, 277–288 (1986).
3. G. S. Chen, M. Gao, and R. P. Wei, *CORROSION*, **52**, 8–15 (1996).
4. Z. Szklarska-Smialowska, *Corrosion Science*, **41**, 1743–1767 (1999).
5. M. Shao, Y. Fu, R. Hu, and C. Lin, *Materials Science and Engineering: A*, **344**, 323–327 (2003).
6. S. Furuya and N. Soga, *CORROSION*, **46**, 989–993 (1990).
7. M.L.C. Lim, J. R. Scully, and R.G. Kelly, *Corrosion*, **69**, 35–47 (2012).
8. X. Zhao, G. S. Frankel, B. Zoofan, and S. I. Rokhlin, *CORROSION*, **59**, 1012–1018 (2003).
9. T. Ramgopal, P. I. Gouma, and G. S. Frankel, *CORROSION*, **58**, 687–697 (2002).
10. M. Keddam, C. Kuntz, H. Takenouti, D. Schustert, D. Zuili, *Electrochimica Acta*, **42**, 87–97 (1997).
11. F.-H. Cao, Z. Zhang, J.-F. Li, Y.-L. Cheng, J.-Q. Zhang, C.-N. Cao, *Materials and Corrosion*, **55**, 18–23 (2004).
12. R. J. Gest and A. R. Troiano, *CORROSION*, **30**, 274–279 (1974).
13. N. E. C. Co and J. T. Burns, *International Journal of Fatigue*, **103**, 234–247 (2017).
14. S. Kim, J. T. Burns, and R. P. Gangloff, *Engineering Fracture Mechanics*, **76**, 651–667 (2009).
15. ASTM G34-1, “Standard Test Method for Exfoliation Corrosion Susceptibility in 2XXX and 7XXX Series Aluminum Alloys” (West Conshohocken, PA: ASTM International, 2001), p. 1-7.
16. ASTM B117-18, “Standard Practice for Operating Salt Spray (Fog) Apparatus” (West Conshohocken, PA: ASTM International, 2001), p. 1-12
17. S. Lee and B. Lifka, in *New Methods for Corrosion Testing of Aluminum Alloys*, V. Agarwala and G. Ugiansky, Editors, p. 1-1–19, West Conshohocken, PA, ASTM International (1992)

18. M. A. Jakab, F. Presuel-Moreno, and J. R. Scully, *CORROSION*, **61**, 246–263 (2005).
19. M. A. Jakab, F. Presuel-Moreno, and J. R. Scully, *Journal of The Electrochemical Society*, **153**, B244 (2006).
20. G. O. Ilevbare and J. R. Scully, *CORROSION*, **57**, 134–152 (2001).
21. E. Akiyama and G. S. Frankel, *J. Electrochem. Soc.*, **146**, 4095–4100 (1999).
22. M. Iannuzzi, T. Young, and G. S. Frankel, *Journal of The Electrochemical Society*, **153**, B533 (2006).
23. A. K. Mishra and R. Balasubramaniam, *Corrosion Science*, **49**, 1027–1044 (2007).
24. R.G. Buchheit, H. Guan, S. Mahajanam, and F. Wong, *Progress in Organic Coatings*, **47**, 174–182 (2003).
25. Kiryl A. Yasakau, Mikhail L. Zheludkevich, and Sviatlana V.Lamaka, and Mario G. S. Ferreira, .
26. M. Parker and R. Kelly, *CORROSION* (2018)
27. C. R. Frink and M. Peech, *Inorg. Chem.*, **2**, 473–478 (1963).
28. F. Mansfeld, *CORROSION*, **37**, 301–307 (1981).
29. A. Yurt, S. Ulutas, and H. Dal, *Applied Surface Science*, **253**, 919–925 (2006).
30. H. J. W. Lenderink, M. V. D. Linden, and J. H. W. De Wit, *Electrochimica Acta*, **38**, 1989–1992 (1993).
31. M. Metikoš-Huković, R. Babić, and Z. Grubač, *Journal of Applied Electrochemistry*, **32**, 35–41 (2002).
32. B. Hirschorn, M.E. Orazem, B. Tribollet, V. Vivier, I. Frateaur, M. Musiani., *J. Electrochem. Soc.*, **157**, C458–C463 (2010).
33. B. Hirschorn, M.E. Orazem, B. Tribollet, V. Vivier, I. Frateaur, M. Musiani, *Electrochimica Acta*, **55**, 6218–6227 (2010).
34. C.-F. Lin and K. R. Hebert, *Journal of The Electrochemical Society*, **141**, 104 (1994).
35. C.-F. Lin, M. D. Porter, and K. R. Hebert, *Journal of The Electrochemical Society*, **141**, 96 (1994).
36. S.-M. Moon and S.-I. Pyun, *Corrosion Science*, **39**, 399–408 (1997).
37. S.-M. Moon and S.-I. Pyun, *CORROSION*, **54**, 546–552 (1998).

38. A. Nishikata, Y. Ichihara, Y. Hayashi, and T. Tsuru, *J. Electrochem. Soc.*, **144**, 1244–1252 (1997).
39. O. Dolgikh, A. C. Bastos, A. Oliveira, C. Dan, and J. Deconinck, *Corrosion Science*, **102**, 338–347 (2016).
40. C. Liu, J. Srinivasan, and R. G. Kelly, *J. Electrochem. Soc.*, **164**, C845–C855 (2017).
41. V. G. Levich, *Physicochemical hydrodynamics.*, Prentice-Hall, Englewood Cliffs, N.J., (1962).
42. T. Miyake and M. Rolandi, *J. Phys.: Condens. Matter*, **28**, 023001 (2016).
43. V. Grozovski, S. Vesztergom, G. Lang, and P. Broekmann, *J. Electrochem. Soc.*, **164**, E3171–E3178 (2017).
44. S. Dong, W. Shi, J. Zhang, and S. Bi, *ACS Earth Space Chem.*, **2**, 269–277 (2018).
45. P. Brown, and C. Ekberg, *Hydrolysis of Metal Ions*, 2nd ed., 2016.

4.6 Part 4: Effect of Solution Chemistry on Galvanic Coupling between AA7050-T7451 and SS316L: Experimental Approach and Modeling Validation

4.6.1 Introduction

Connections between aluminum (Al) alloy-based components and stainless steel (SS) fasteners are frequently encountered in aircraft architecture. Such galvanic couple arrangements exacerbate the corrosion susceptibility of Al alloy when a thin electrolyte is develops on the surface during atmospheric exposure. The galvanic-coupling-induced corrosion damage can be alleviated by applying a coating system in which the coating can provide corrosion prevention to mitigate

the interaction between the Al alloy and SS fastener. There has been extensive research on the use of metal-rich primers, such as magnesium-rich primer (MgRP)¹⁻⁵ to provide sacrificial anode-based cathodic protection to prevent corrosion damage of the aluminum alloy substrates. At the same time, metallic cations (Mg^{2+}) produced from open circuit and sacrificial anodic dissolution, as well as ions (Al^{3+} , Zn^{2+}) from the dissolution of the substrate (i.e., AA7050 under inadequate protection of the primer due to coating breakdown), can diffuse into the solution and impact the galvanic behavior between the Al alloy and SS fastener. The distribution of this pH across the galvanic couple is crucial as pH is known to affect the electrode potentials of corroding interfaces⁶, the speciation of ions, the formation of corrosion products⁷, and the thermodynamic driving force for redox reactions⁸. There is a limited number of studies on the effect of relevant cation ions on the galvanic corrosion between an Al alloy and SS fastener, and better understanding of this effect, together with pH effect, can provide complementary information on the corrosion prevention mechanism of these metal-rich primers.

In Part 2&3 of this chapter, the effects of Zn^{2+} , Mg^{2+} and Al^{3+} on the cathodic kinetics of AA7050 have been carefully studied. These two studies were used to illustrate the scenario in which metal rich primer coated AA7050 substrate has no galvanic coupling with SS316L such that metal richer primer is the anode and AA7050 substrate is the cathode, thus the pertinent metallic cations come from either self-dissolution of AA substrate or anodic dissolution of the primer due to sacrificial-anode protection. However, the objective of the study in this part is to study effect of solution chemistry (metal cations and pH) on the galvanic coupling between SS316L and AA7050 without and with protection of MgRP (Figure 4.36).

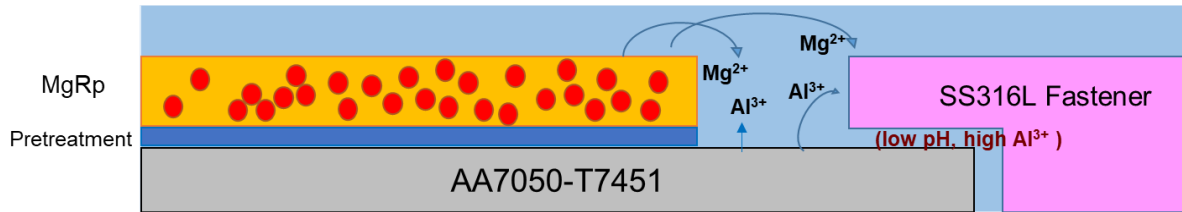


Figure 4.36: A schematic diagram to show the solution chemistry environment between a generic SS316L fastener and MgRP coated AA7050-T7451.

4.6.2 Experimental Approach

4.6.2.1 Electrochemical Kinetics Measurements

Potentiodynamic polarization curve measurements were performed on AA7050-T7451, SS316L and 99.99% pure Mg after 1hr open circuit potential measurement with scan rate =0.2 mV/s. Three types of test solutions were prepared: 1) 0.6M NaCl with adjusted pH=3, 4, and 5.5; 2) 0.6M NaCl+ 0.01, 0.05 and 0.1 M MgSO₄, pH of each solution was adjusted to 3, 4, and 5.5 respectively; 3) 0.6M NaCl+0.005, 0.025 and 0.05M Al₂(SO₄)₃ with adjusted pH=3. The latter two types of solution were used to study the effect of metal cation (Mg²⁺/Al³⁺) on the galvanic corrosion between AA7050 and SS316L. These experimentally determined electrochemical kinetics were used as boundary conditions in the modeling work.

4.6.2.2 Scanning Vibrating Electrode Technique (SVET)

Scanning vibrating electrode technique (SVET) was utilized to determine current distribution at the galvanic coupling surface. SVET is a powerful technique to provide local current map at the sample surface by measuring voltage drop in solution, the measured current density can be expressed as⁹

$$i = -\kappa E = -\kappa \frac{\nabla V}{\nabla r} \quad (4.6)$$

The current density i between two points is a function of solution conductivity κ , voltage difference ∇V and distance between two points ∇r . In this study, scanning vibrating electrode measurements were carried out using a probe with a $125 \mu\text{m}$ diameter Pt micro-disc electrode. The probe vibration frequency and amplitude were set at 140 Hz and $30 \pm 5 \mu\text{m}$ respectively. SVET was performed above a galvanic coupling between SS316L and AA7050-T7451 with confined solution volume (solution height=1cm). The galvanic coupling in which a round SS part was fixed at the center of a square AA7050 coupon embedded in epoxy shown in Figure 4.37. SVET was tested in three different solutions: 1) 0.6M NaCl pH=5.6; 2) 0.6M NaCl+0.1M MgSO_4 with pH=4; 3) 0.6M NaCl+0.05M $\text{Al}_2(\text{SO})_4$ with pH=3.

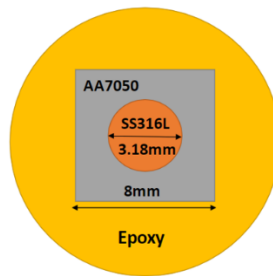


Figure 4.37: Dimension of galvanic coupling between SS316L and AA7050-T7451 for SVET measurements.

4.6.2.3 Characterizations

Optical microscope Hirox KH8700 was used to characterize the corrosion damage of SVET samples after tests at the surface. Scanning electron microscope FEI LV 200 was utilized to better characterize localized corrosion on the AA7050 in the vicinity of SS316L/AA7050 interface.

4.6.2.4 Secondary Current Distribution Modeling

A 2-D steady state secondary current distribution model with Laplace's Equation as governing equation was applied to simulate potential and current density distributions at the

surface of galvanic coupling between SS316L and AA7050 with and without interaction of MgRP. Two sets of modeling studies were performed: 1) SS316L and AA7050 galvanic coupling only (Figure 4.38a), and 2) half of galvanic coupling was covered by MgRP (Figure 4.38b). In this model, two assumptions were made: 1) solution conductivity was maintained at 5.5 S/m all the time; 2) MgRP was considered as pure Mg. Experimentally determined electrochemical kinetics mentioned previously were used as boundary conditions. Details of mathematical development in this modeling framework have been discussed in previous chapters.

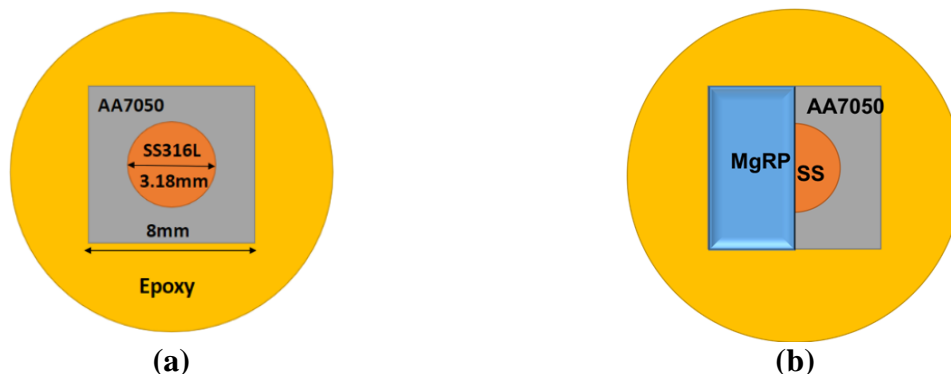


Figure 4.38: a) Geometry setup for the 1st set of modeling, typical of SVET sample's geometry; b) geometry setup for the 2nd set of modeling, the dimension was identical to a), but half of the surface was covered by MgRP.

4.6.3 Results and Discussions

4.6.3.1 Determination of Appropriate pH Range for Test Solutions

Distributions of pertinent stable species as a function of pH during metal cation hydrolysis were generated for Mg^{2+} (Figure 4.39a) and for Al^{3+} (Figure 4.39b) by OLI software. It shows that when $pH > 5.5$, more than 50% of $[Mg^{2+}]$ precipitates out as $Mg(OH)_2$, whereas Al^{3+} is overwhelmed by different hydroxyl-aluminum species once the pH was beyond 4. As a result, in order to accurately determine the effect of Mg^{2+}/Al^{3+} , pH range from 3 to 5.5 was chosen for 0.6M NaCl+ $MgSO_4$ and pH=3 was chosen for 0.6M NaCl+ $Al_2(SO_4)_3$.

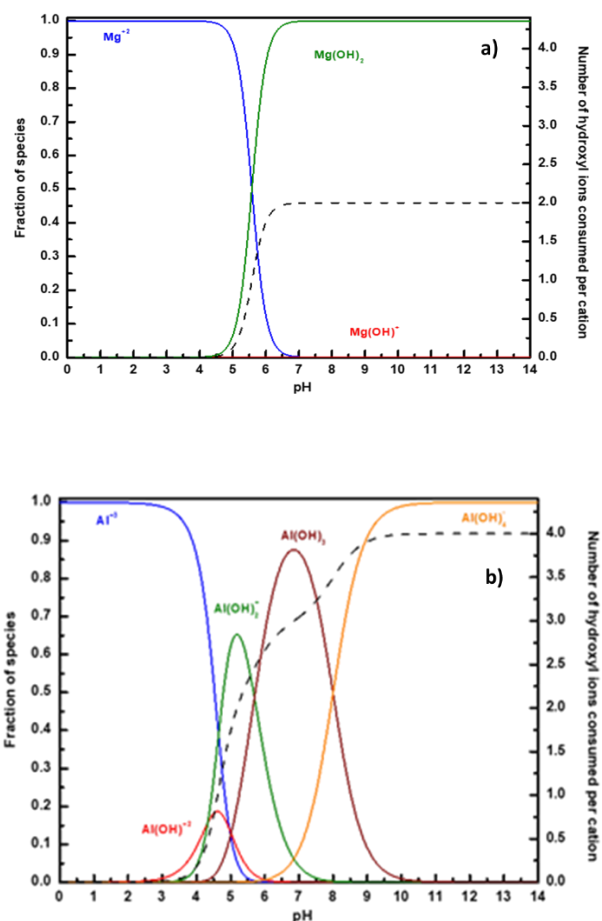


Figure 4.39: Distributions of pertinent stable species as a function of pH during metal cation hydrolysis were generated for a) Mg^{2+} and b) for Al^{3+} by OLI software.

4.6.3.2 Galvanic Coupling Current Density as a Function of Cation Concentration and pH

Comparisons of polarization curves of SS316L and AA7050 as a function of Mg^{2+} concentration for different pHs are shown in Figure 4.40a-c. Assuming cathode-to-anode area ratio is 1:1, the interaction between cathodic and anodic polarizations defines the galvanic current density ($i_{galvanic}$), a plot in which galvanic coupling current density ($i_{galvanic}$) vs. $[Mg^{2+}]$ for different pH is displayed in Figure 4.40d based the information from Figure 4.40a-c. It shows that: higher pH (pH=4 and 5.5) experienced lower $i_{galvanic}$ than lower pH (pH=3) for every $[Mg^{2+}]$. When pH=3, $i_{galvanic}$ was almost constant ($\sim 5.6E-5$ A/cm²) till $[Mg^{2+}] = 0.01M$, and then increased to $\sim 7.8E-5$

A/cm² at [Mg²⁺]=0.05M before decreasing to ~6.9E-5 A/cm² at [Mg²⁺]=0.1M. As for higher pH group, i_{galvanic} steadily decreased over [Mg²⁺]: $i_{\text{galvanic}} = \sim 2.7\text{E-}5$ A/cm² for pH=5.5 and $\sim 1.5\text{E-}5$ A/cm² for pH=4 at [Mg²⁺]=0, and then i_{galvanic} decreased to $\sim 1.3\text{E-}5$ A/cm² for pH=5.5 and to $\sim 7.5\text{E-}6$ A/cm² for pH=4 at [Mg²⁺]=0.1M. It is also noticed that pH=4 had lowest i_{galvanic} at all [Mg²⁺]. It can be concluded that: galvanic corrosion inhibitive effect of Mg²⁺ can be only effective when pH was between 4 and 5.5 (mild acidic environment); Mg²⁺ showed the most inhibitive effect at pH=4 among all pHs from 3 to 5.5 and its effect became more significant as [Mg²⁺] increased.

For the effect of Al³⁺, comparisons of polarization curves of SS316L and AA7050 as a function of [Al³⁺] at pH=3 are shown in Figure 4.41a. polarization curves of SS316L and AA7050 at neutral 0.6M NaCl (pH=5.6) are also displayed as reference to compare with those at pH=3. It is clearly seen that: cathodic kinetics of SS316L increased with increasing [Al³⁺] due to enhanced hydrogen-evolution-reaction (HER) related kinetics discussed in Part 3 of this chapter; the E_{corr} of AA7050 showed the same trend as Figure 4.23. Following the same routine, i_{galvanic} vs. [Al³⁺] was plotted in Figure 4.41b. i_{galvanic} doubled when 0.6M NaCl was acidified from 5.5 to 3 with no [Al³⁺], and it then became twice higher than that for 0.6M NaCl pH=3 when only 0.005M Al₂(SO₄)₃ was added into 0.6M NaCl. However, the increase in i_{galvanic} became steadily once the [Al³⁺] > 0.05M, although the highest i_{galvanic} at [Al³⁺] = 0.1 M was still about 5 times that at 0.6M NaCl pH=3. It can be concluded that: [Al³⁺] showed promotive effect on galvanic corrosion largely due to enhanced HER cathodic kinetics at acidic environment, and the promotive effect increased with increasing [Al³⁺].

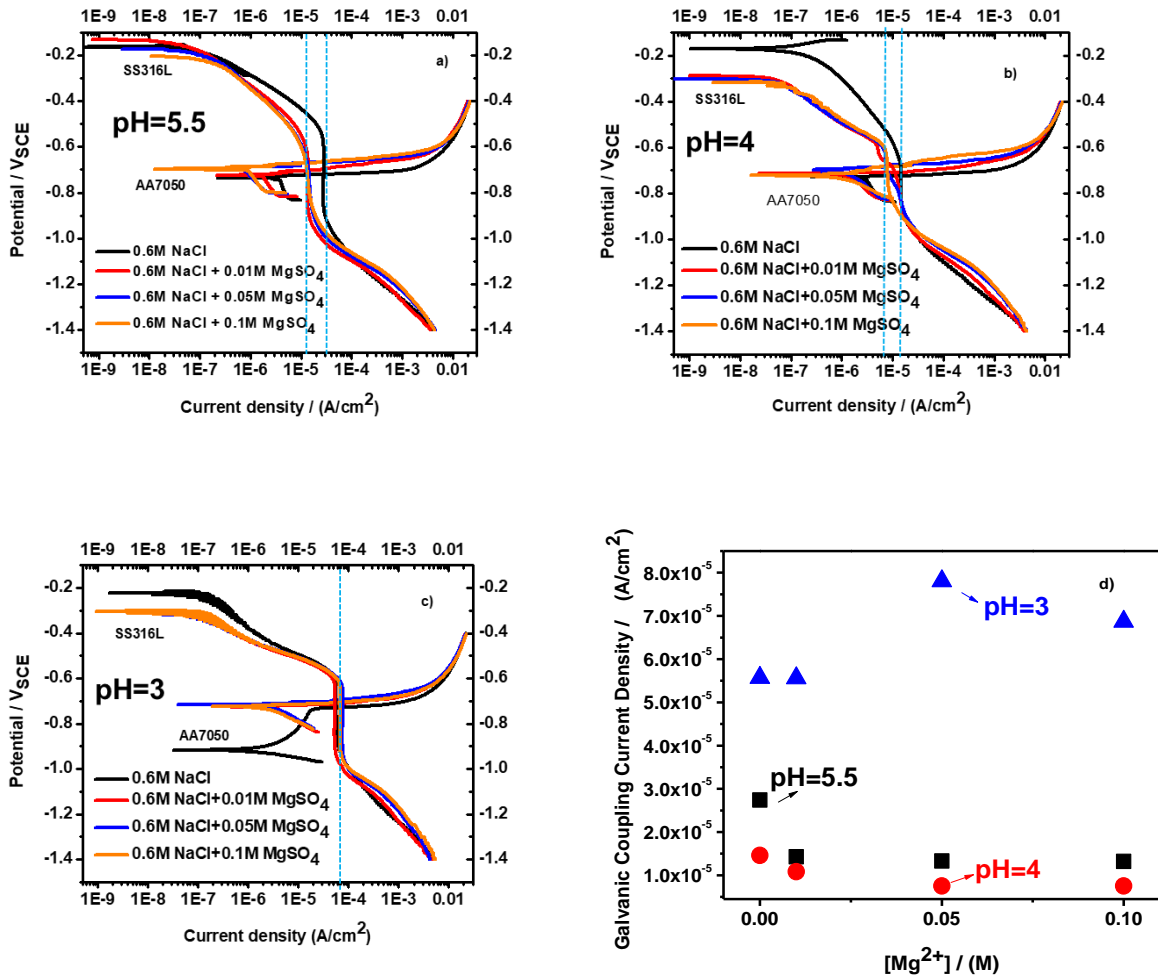


Figure 4.40: Comparisons of polarization curves of SS316L and AA7050 as a function of [Mg²⁺] at a) pH=5.5, b) pH=4 and c) pH=3; d) comparison of galvanic coupling current density vs. [Mg²⁺] for different pHs.

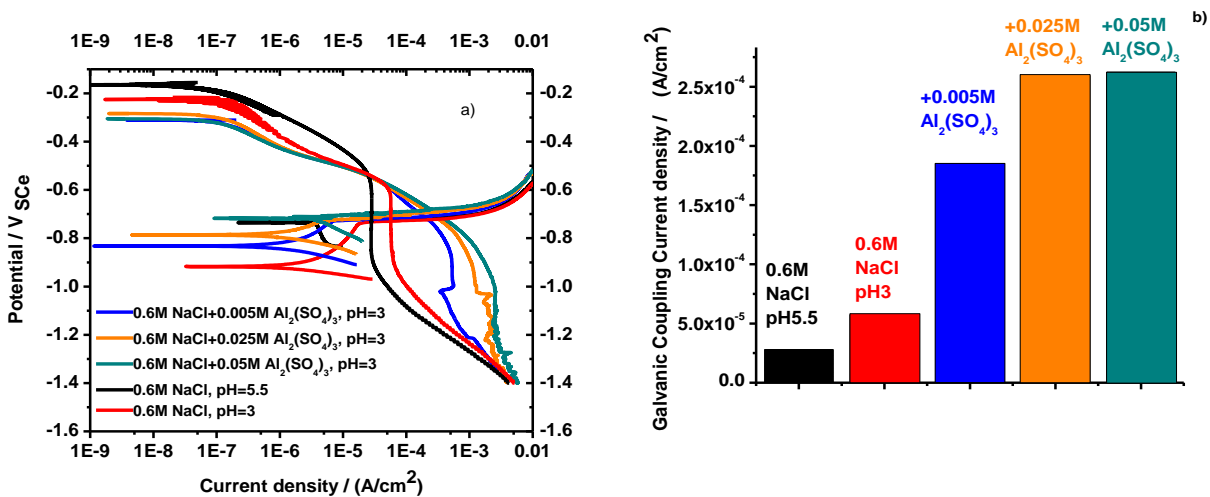


Figure 4.41: a) Comparisons of polarization curves of SS316L and AA7050 as a function of [Al³⁺] at pH=3; b) comparison of galvanic coupling current density vs. [Mg²⁺] at pH=3.

4.6.3.3 SVET Measurements and Microscope Characterizations to Compare Corrosion Damages in Different Solution Environments

Based on the electrochemical kinetics study, both Mg²⁺ and Al³⁺ showed maximum inhibitive/promotive effect when their concentration was 0.1M. To compare the galvanic damage in different solution chemistry environments, SVET measurements were performed in (1) 0.6M NaCl pH=5.6; (2) 0.6M NaCl+0.1M MgSO₄ with pH=4; (3) 0.6M NaCl+0.05M Al₂(SO)₄ with pH=3. The corresponding SVET measurements over time in these solutions are shown in Figure 4.42-Figure 4.44 respectively. In the SVET measurement, red color indicated anodic current density whereas blue represented cathodic current density. The black circle in each SVET measurement result represented the location of SS part artificially.

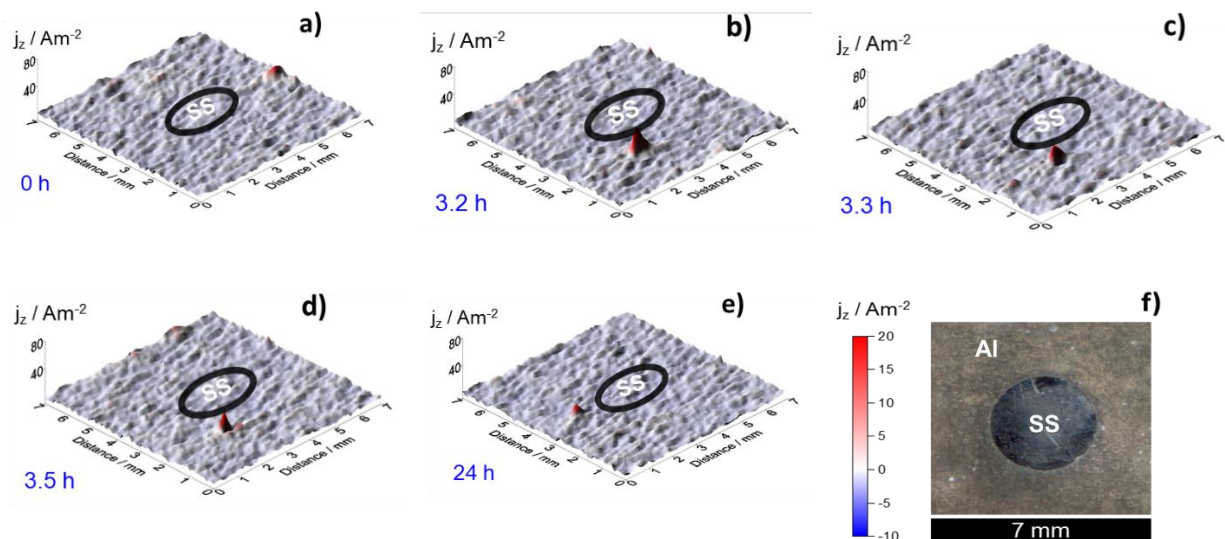


Figure 4.42: SVET measurement in 0.6M NaCl pH=5.6 solution at a) 0 hrs, b) 3.2 hrs, c) 3.3 hrs, d) 3.5 hrs, and e) 24hrs. f) optical micrograph of galvanic coupling after 24hr-SVET measurement.

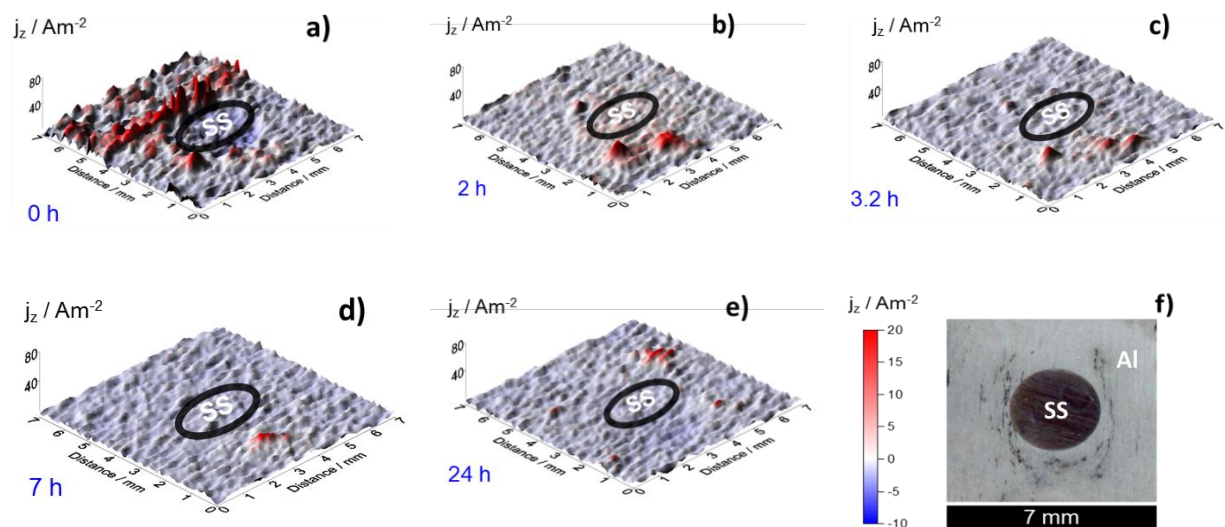


Figure 4.43: SVET measurement in 0.6M NaCl+0.05M $\text{Al}_2(\text{SO}_4)_3$ pH=3 solution at a) 0 hr, b) 2 hrs, c) 3.2 hrs, d) 7 hrs, and e) 24 hrs. f) optical micrograph of galvanic coupling after 24hr-SVET measurement.

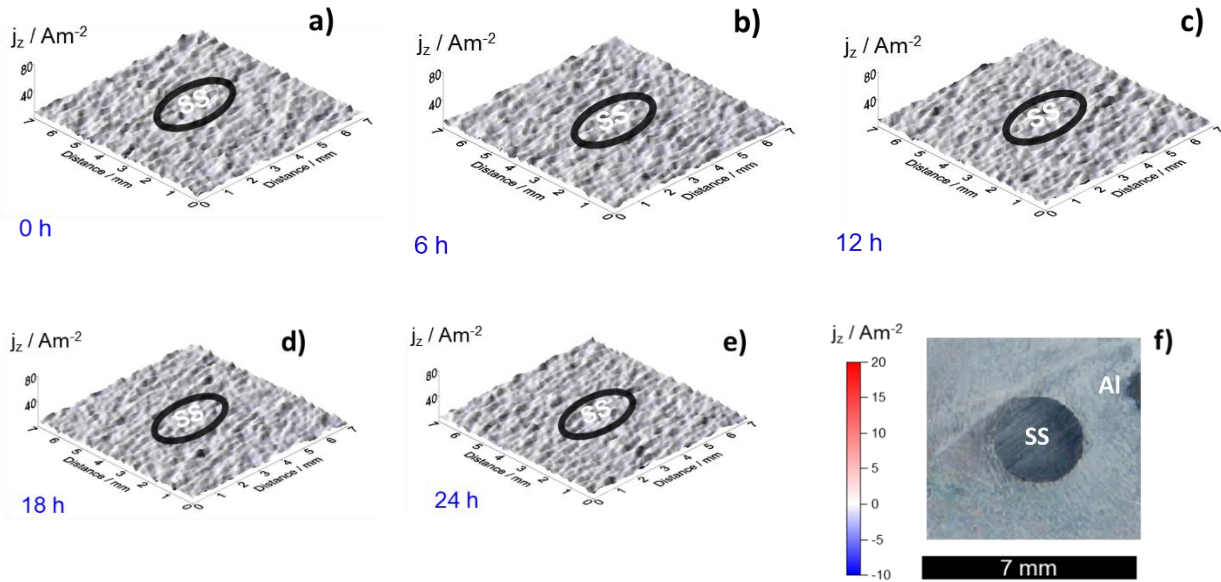


Figure 4.44: SVET measurement in 0.6M NaCl+0.1M MgSO_4 pH=4 solution at a) 0 hr, b) 6 hrs, c) 12 hrs, d) 18 hrs, and e) 24 hrs. f) optical micrograph of galvanic coupling after 24hr-SVET measurement.

From the SVET measurements, it can be seen that: in 0.6M NaCl (pH=5.6) solution (Figure 4.42), anodic current density peaks only appeared in a few discrete small localized areas and peak magnitude decayed over exposure time; in 0.6M NaCl+0.05M $\text{Al}_2(\text{SO}_4)_3$ solution (Figure 4.43), much higher anodic current peaks spread over a larger area around the SS316L/AA7050 interface at the early stage, and then decayed dramatically over time but still more intensive than neutral NaCl solution. The optical micrograph in Figure 4.43f indicates a number of corrosion fissures distributed around the interface area; in 0.6M NaCl+0.1M MgSO_4 solution (Figure 4.44), anodic current peaks barely appeared during the entire immersion time. The following SEM images shown in Figure 4.45 provided better characterization of corrosion damages on the AA7050 surface. For 0.6M NaCl (pH=5.6) environment, a few corrosion fissures were distributed near the interface, and lots of small corrosion pits were distributed in the bulk part; for the 0.6M NaCl+0.05M $\text{Al}_2(\text{SO}_4)_3$ environment, larger corrosion fissures were distributed on the AA7050 surface with increasing number of density when the distance was closer to the interface; however

for 0.6M NaCl+0.1M MgSO₄ environment, barely any corrosion features appeared in either interface or bulk part. These combined characterization studies confirmed that Al³⁺ in acidic environment promoted galvanic corrosion damage, whereas Mg²⁺ in mild acidic environment inhibited galvanic corrosion damage between SS316L and AA7050 without coated MgRP.

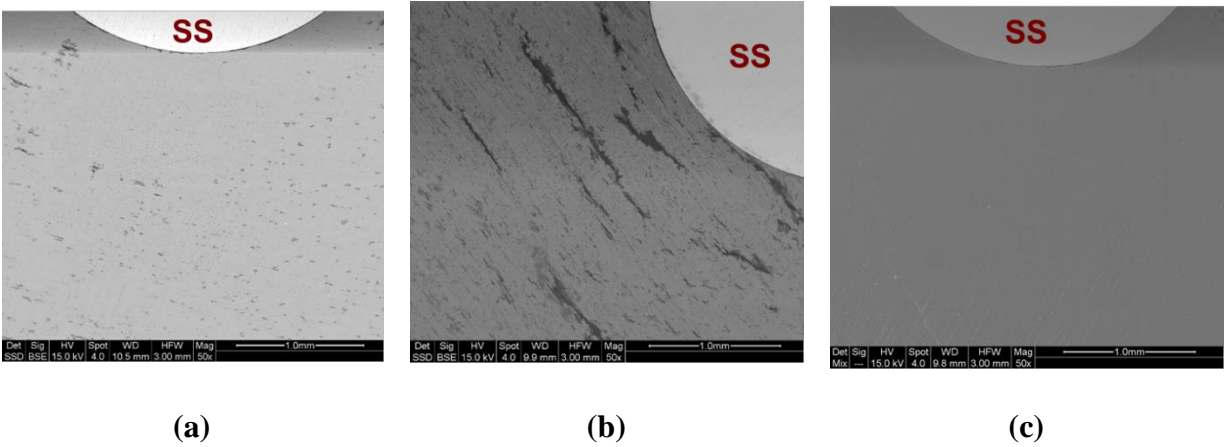


Figure 4.45: SEM characterizations of corrosion damage on the surface in the vicinity of SS316L/AA7050 interface after 24-hr SVET tests for a) 0.6M NaCl pH=5.6, b) 0.6M NaCl+0.05M Al₂(SO₄)₃ pH=3, and c) 0.6M NaCl+0.1M MgSO₄ pH=4.

4.6.3.4 FEM Modeling Study to Show the Effect of Solution Chemistry on the Galvanic Corrosion distributions

Modeling studies here are aimed to compare with SVET measurement results for bare SS316L/AA7050 galvanic couple shown Figure 4.38a and extend this modeling work to predict the current density distribution for the SS316L/AA7050 galvanic couple with half surface coated by MgRP shown in Figure 4.38b (which has not been studied experimentally yet).

For the bare galvanic coupling configuration, the boundary conditions used in the simulation or this configuration are displayed in Figure 4.46, which are cathodic kinetics of SS316L and anodic kinetics of AA7050 in three SVET test solutions. Comparison of current density distributions in three different solution environments along the distance from center to the

edge is displayed in Figure 4.46b. Current density along either SS or AA was almost constant in all solutions, and the magnitude of anodic current density along AA7050 followed this order: 0.6M NaCl+0.05M $\text{Al}_2(\text{SO}_4)_3$ > 0.6M NaCl pH=5.6 > 0.6M NaCl+0.1M MgSO_4 . The average anodic current density for Al^{3+} containing solution was about 60 times higher than the neutral NaCl solution, and 240 times higher than the Mg^{2+} containing solution. To validate the modeling prediction, A comparison of average anodic current density ($i_{\text{anodic,avg}}$) over the entire AA7050 surface by SVET as a function of immersion time in three solutions is shown in Figure 4.47a. It can be seen that: Al^{3+} containing solution had the highest $i_{\text{anodic,avg}}$ at the very beginning before experiencing a sharp decrease and then reaching a plateau over time; neutral NaCl solution had increase in $i_{\text{anodic,avg}}$ in the first 3hrs and then showed the same tendency as Al^{3+} containing solution; Mg^{2+} containing solution however barely displayed any anodic current density over the entire immersion time. It should be noted here that: steady state modeling results predicted nearly constant current density distribution over time whereas SVET measurement showed decays in $i_{\text{anodic,avg}}$ over time. One can explain this discrepancy as follows: during SVET test, due to the change in solution chemistry and build-up of corrosion product, the measured $i_{\text{anodic,avg}}$ thus decreased with time, whereas modeling work used electrochemical kinetics as boundary conditions which assumed solution chemistry environment was constant over time, resulting in constant $i_{\text{anodic,avg}}$ from modeling prediction. Nevertheless, if the maximum $i_{\text{anodic,avg}}$ from SVET was compared with modeling prediction for three different solutions (Figure 4.47b), one can see that the modeling prediction compared well SVET results. Both modeling and experimental results showed that addition of Al^{3+} resulted in the most severe corrosion damage, and Mg^{2+} resulted in the least severe corrosion damage.

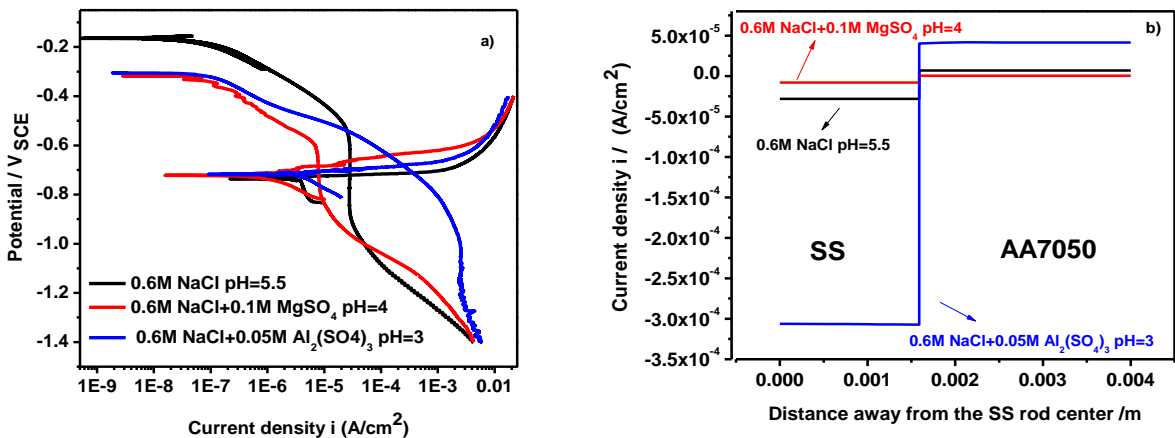


Figure 4.46: a) Boundary conditions used for bare galvanic coupling configuration shown in Figure 4.38a in three different SVET test solutions; b) comparison of current density distributions along the distance from the SS rod center to the AA7050 edge in three different solutions.

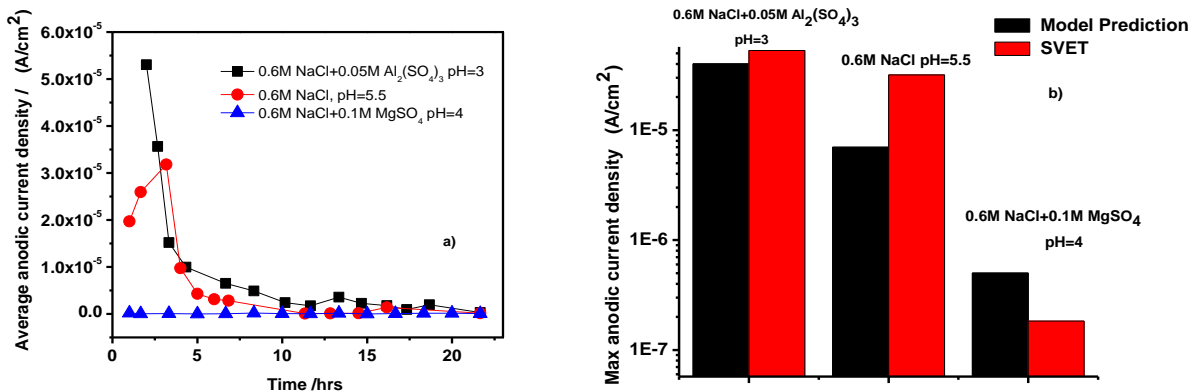


Figure 4.47: a) Comparison of average anodic current density from SVET as a function of immersion time for three different solutions; b) comparison of maximum anodic current density between modeling prediction and SVET results for three different solutions.

As for half-coated galvanic coupling configuration, potential distribution rather than current distribution provided more useful information to discern the protective abilities of MgRP in three different solutions. Boundary conditions used in each solution are displayed in Figure 4.48a-c. Potential distributions along the distance from the left edge of MgRP to the right edge of AA7050 (Figure 4.48d) for three different solutions are shown in Figure 4.49a. One can see that Al^{3+} containing solution had the most positive potential $\sim -0.78 \text{ V}_{\text{SCE}}$, followed by Mg^{2+} containing

solution (~ -1.17 V_{SCE}) and neutral NaCl solution (~ -1.25 V_{SCE}). If these potential values were labelled in the electrochemical kinetics (boundary conditions) diagrams shown in Figure 4.49b-d, one can see that potential of AA7050 almost reached its corrosion potential, indicating AA7050 was least protected by MgRP in Al³⁺ containing solution (Figure 4.49c); There was a little difference in terms cathodic overpotential of AA7050 between Mg²⁺ containing solution (Figure 4.49d) and neutral 0.6M NaCl (Figure 4.49b). The second type of modeling study indicates that Al³⁺ could interfere the performance of MgRP and resulted in the least protection to AA7050.

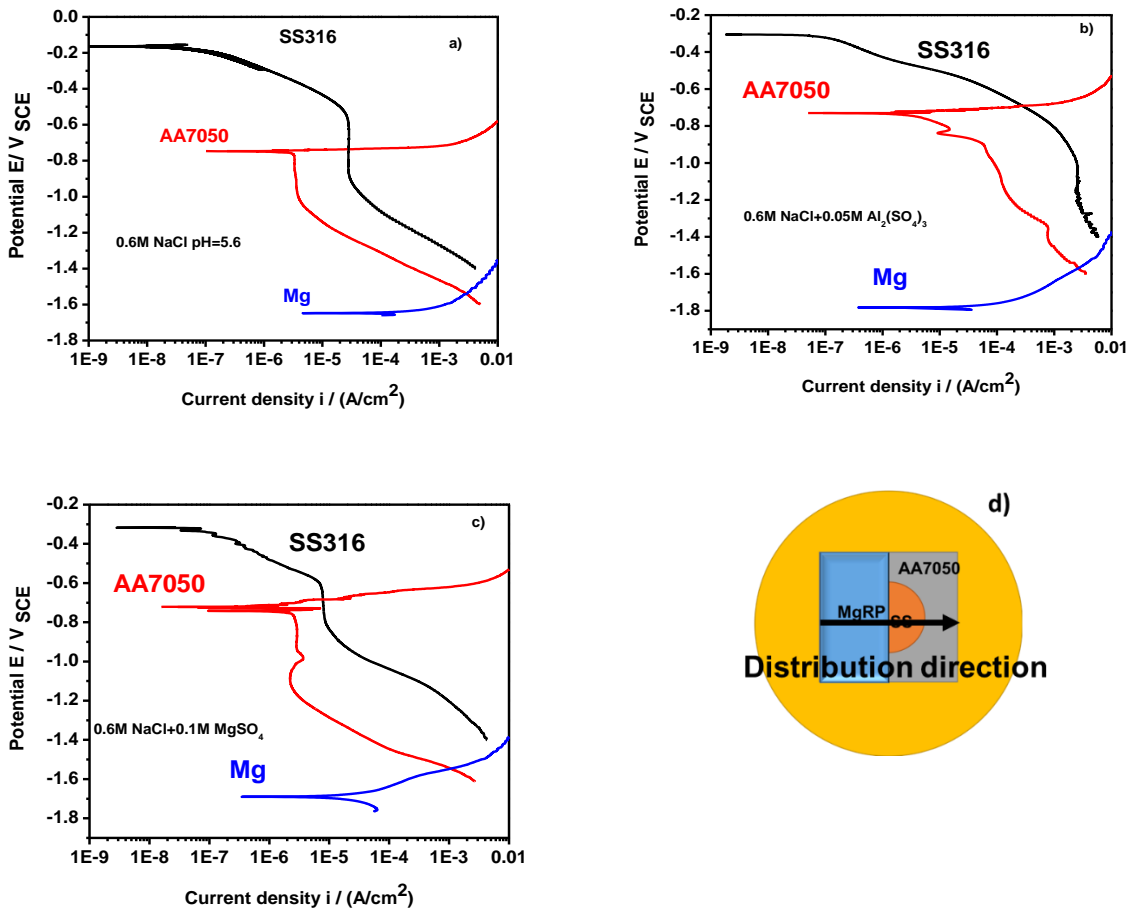


Figure 4.48: Boundary conditions for half-coated galvanic coupling in a) 0.6M NaCl pH=5.6, b) 0.6M NaCl+0.05M Al₂(SO₄)₃ pH=3, and c) 0.6M NaCl+0.1M MgSO₄ pH=4; d) direction for potential distribution along the galvanic coupling surface.

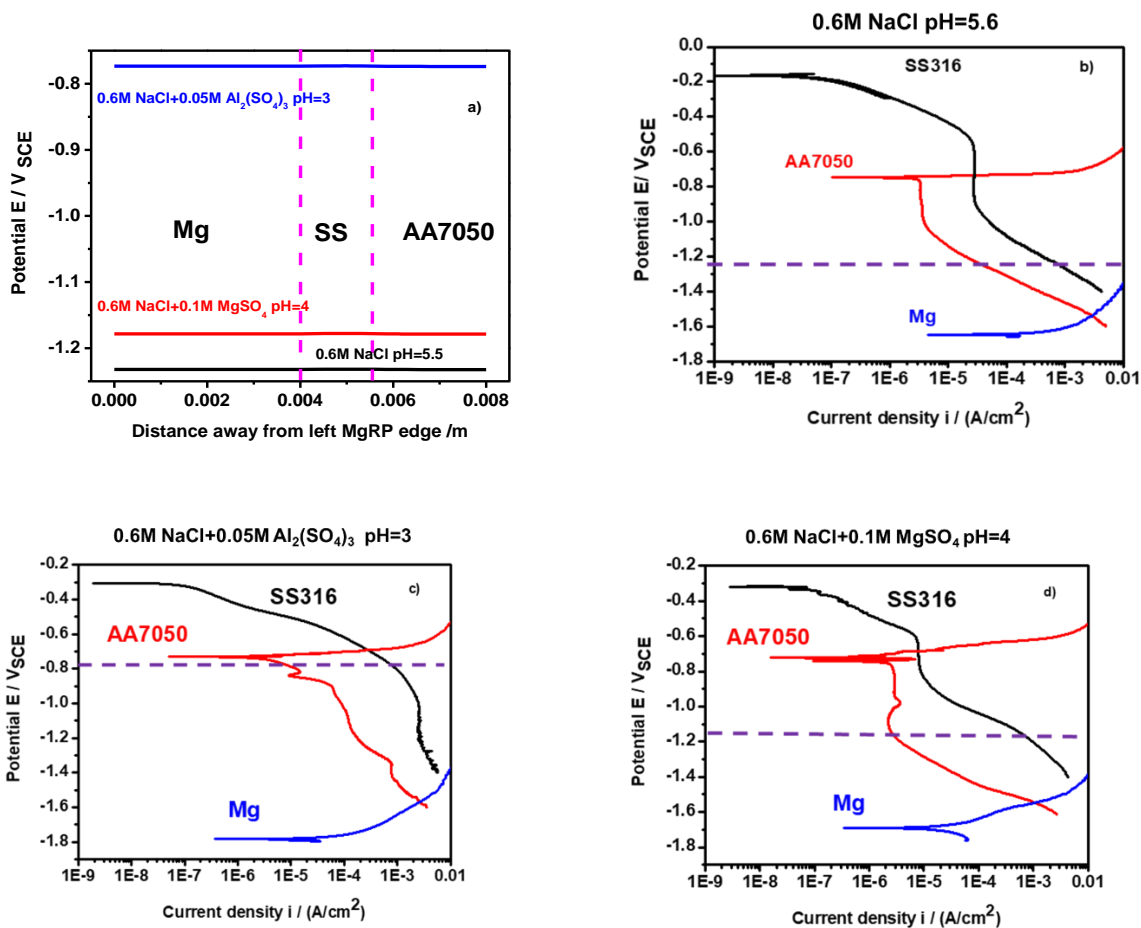


Figure 4.49: a) Potential distributions along the distance from the left edge of MgRP to the right edge of AA7050 (Figure 4.48d) for three different solutions; display of the simulated potential on AA7050 (dashed line) over the electrochemical kinetics diagram in b) 0.6M NaCl pH=5.6, c) 0.6M NaCl+0.05M $\text{Al}_2(\text{SO}_4)_3$ pH=3, and d) 0.6M NaCl+0.1M MgSO_4 pH=4.

4.6.4 Conclusions

This combined experimental and modeling study investigated the effect of Mg^{2+} , Al^{3+} and pH on the electrochemical and galvanic corrosion distributions in the AA7050/SS316L system without and with MgRP. It can be concluded that:

- Addition of Al^{3+} or Mg^{2+} into NaCl solution significantly affects galvanic corrosion between AA7050/SS316L. Al^{3+} is corrosion accelerator since it can boost both the cathodic kinetics of cathode SS and corrosion rate of AA7050, and Mg^{2+} is corrosion inhibitor due

to its inhibition effect on both cathodic kinetics of cathode SS and corrosion rate of AA7050.

- pH affects the inhibitive effect of Mg^{2+} : corrosion inhibitive effect is the most significant in pH=4.
- Promotive/inhibitive effect of cation increases with cation concentration.
- The addition of Al^{3+} mitigates the protection of AA7050 from MgRP, and brings the potential up to near-OCP region of AA7050.

4.6.5 References

1. B. Kannan., A. D. King, and J.R. Scully, *Corrosion* 71 (2015): pp. 1093–1109.
2. R.J. Santucci, B. Kannan, W. Abbott, and J.R. Scully, *CORROSION* 73 (2017): pp. 1196–1201.
3. A.D. King, B. Kannan, and J.R. Scully, *CORROSION* 70 (2014): pp. 536–557.
4. A.D. King, J.S. Lee, and J.R. Scully, *J. Electrochem. Soc.* 163 (2016): pp. C342–C356.
5. D. Battocchi, A.M. Simões, D.E. Tallman, and G.P. Bierwagen, *Corrosion Science* 48 (2006): pp. 1292–1306.
6. Tada, E., K. Sugawara, and H. Kaneko, *Electrochimica Acta* 49 (2004): pp. 1019–1026.
7. A. Pardo, M.C. Merino, A.E. Coy, R. Arrabal, F. Viejo, and E. Matykina, *Corrosion Science* 50 (2008): pp. 823–834.
8. M. -C Zhao, M. Liu, G.-L. Song, and A. Atrens, *Corrosion Science* 50 (2008): pp. 3168–3178.
9. A.C. Bastos, M.C. Quevedo, O.V. Karavai, and M.G. Ferreira, *J. Electrochem. Soc.* 164 (2017): pp. 973–C990.

4.7 Acknowledgements

The financial support from Office of Naval Research (ONR) via Grants N00014-14-1-0012 and N00014-17-1-2033, Sea-Based Aviation Program, William Nickerson, Program Manager is gratefully acknowledged. Dr. Piyush Khullar (AA5083 cathodic kinetics study), Dr. Veronica N. Rafla (XCT measurements), Mr R.J. Santucci (AA7050 electrochemical kinetics study), Dr. Carol Glover (SVET measurement), Dr. Marybeth Parker and Mr. Victor Yang from the University of Virginia are also acknowledged for the study collaboration and discussion.

5. The Effect of Materials Properties (Oxide Film Composition and Thickness) on the Corrosion Kinetics of the Materials Involved in the Galvanic Couple

Summary:

From the study in previous chapters, cathodic kinetics of SS316L cathode is the dominant factor affecting the galvanic coupling current density and galvanic coupling potential based on Mixed Potential Theory assuming cathode-to-anode area ratio equal to 1:1, due to its large diffusion limited potential window. Materials properties, especially surface properties such as passive oxide film composition and thickness of stainless steel can further impact its diffusion limited cathodic kinetics together with the other variables (electrolyte layer thickness, solution chemistry and etc.). Although there are several previous studies in literature to illustrate the qualitative relation between oxide film composition and cathodic kinetics of stainless steel, they fail to develop a thorough quantitative description of the dependence of cathodic limiting current density on the content of pertinent element(s) in oxide film and oxide film thickness. The purposes of the study in this chapter are: (1) to delineate the condition at which the effect of oxide film becomes comparable to that of electrolyte layer thickness for the diffusion limited cathodic kinetics of SS in a simulated thin film electrolyte environment; (2) to develop a quantitative description between oxide film thickness and cathodic limiting current density; (3) to investigate the dependence of oxide film properties on the diffusion limited cathodic kinetics for two types of stainless steels with different alloying element contents.

5.1 Abstract

In a typical galvanic coupling between AA7050 and SS316L, the cathodic kinetics of SS316L can significantly impact the galvanic corrosion damage due to the fact that the galvanic coupling potential is always located at diffusion limited potential range of SS316L. This study is aimed at investigating the effect of surface treatment, oxide film thickness, and oxide film composition at different pre-oxidation potentials on the cathodic kinetics especially ORR kinetics of stainless steel. The study was performed by a number of electrochemical (RDE, CV, chronoamperometry and EIS) techniques and XPS surface analysis. From this study, it shows that the cathodic kinetics of SS at ORR potential region is determined by a combined effect of oxide film composition, film thickness and resistivity as well as the competition over cathodic limiting current density between oxide film and electrolyte layer thickness.

5.2 Introduction

Stainless steels (SS) are considered as good candidate materials for a variety of functional and structural applications in automotive, aviation & aerospace, energy, and construction industries. However, corrosion issues always come along with the application of stainless steel in these areas, and limit its service lifespan. One of critical corrosion factors is oxygen reduction reaction (ORR). When SS experiences localized corrosion such as pitting or crevice corrosion, the propagation of corrosion within the cavity is largely supported by the SS outside the cavity as external cathode where ORR takes place¹⁻⁴. Another corrosion scenario where ORR can be a controlling factor to the degree of corrosion damage is galvanic corrosion, especially when the galvanic coupling potential is located within of diffusion limited cathodic potential region of cathode SS, this is frequently occurred in the galvanic coupling system such as aluminum alloy (AA)/SS⁵⁻⁷, and Zinc or Zinc alloy/SS⁸⁻¹¹. Development of a thorough understanding of the

electrochemical role of SS in the corrosion system can help come up with pertinent mitigation strategy to reduce its susceptibility to localized corrosion damage.

When a typical stainless steel is exposed to atmosphere, a protective passive oxide film is usually formed to resist further oxidation of bulk steel. This inherent mild corrosion resistance comes from the oxidation of the major alloying element chromium and some other elements^{12,13}. The composition and structure of this passive oxide film is complicated, and there is numerous literature research effort for it. As for the chemical composition and structure, a number of researchers¹³⁻²⁰ indicated that the oxide film has bilayer structure in which the outer layer consists of iron and nickel oxide whereas the inner layer is enriched in chromium oxide. However Marcus and his coworkers²¹⁻²³ argued that a stable passive film should have bilayer structure with chromium hydroxide as outer layer and mixed chromium and iron oxides as inner layer, and this argument is also supported by Phadnis *et al.*²⁴ and Raja *et al.*²⁵ The properties of oxide film on SS can further impact its electrochemical kinetics, especially ORR kinetics concerned in this study.

In neutral solution, oxygen reduction reaction (ORR) has two pathways^{26,27}: (1) direct reduction via 4-electron transfer



or (2) two-step indirect reduction via 2-electron transfer at each step



The type of ORR pathway is highly dependent on the oxide film property of steel. Early studies for pure iron showed that: 2-electron pathway proceeds with passive/oxide-covered iron whereas bare/oxide-free iron undergoes 4-electron pathway²⁷⁻²⁹, and the number of electron transferred is also dependent on the potential²⁷. However, Jovancicevic and Bockris²⁸ indicated that ORR rate is

higher on passive iron surface than bare iron one due to the catalytical effect of oxide film on ORR (e.g., ORR current was about 100 times higher at pH=7), whereas Zecevic *et al.*²⁷ argued that ORR rate is faster for the less oxidized or pre-reduced iron surface than passivated surface due to more Fe²⁺ sites available at less oxidized surface. As for stainless steel, Le Bozec *et al.*²¹ investigated the dependence of ORR on the surface treatment for SS 316L and 904L, and found that ORR rate is highest on cathodically pre-reduced surface, followed by mechanically polished surface and then anodically passivated surface, the surface chemically treated with HF/HNO₃ has the lowest ORR rate. On pre-reduced and polished surface, ORR follows the 4-electron, and a combined 4-electron and 2-electron pathways respectively, and they are both under mass-transfer limited control. On passivated surface, the pathway had been not clear (which might be different from passivated iron) and implied that it might be dependent on the presence of Fe(III) oxides and the resultant number of Fe (II) sites after Fe(III) reduction, but ORR is lower due to limited access of the oxygen to the electrode/oxide interface or change in film conductivity. The chemical treated surface however impedes the ORR due to possible lack of iron oxide to support ORR. Gojkovic *et al.*³⁰ also indicated that the discrepancy in ORR rate between stainless steel and iron especially at passivated state is Cr-enriched oxide film structure of stainless steel which results in lower content of Fe oxide assuming ORR takes place only at Fe oxide, this discrepancy leads to a lower ORR current density on SS.

However, there has been rare number of studies focusing on a quantitative relation among oxide film composition, oxidized potential and ORR kinetics for different types of stainless steels. Furthermore, little or no previous studies have developed a quantitative description between oxide film thickness and ORR-related cathodic limiting current density. In this chapter, three different types of studies were performed: (1) rotating disk electrode (RDE) technique was applied to

investigate the effect of surface treatment on the ORR cathodic kinetics; (2) a number of electrochemical methods were utilized to study the effect of pre-oxidation potential on the ORR kinetics between SS304L and SS316L, and surface characterization technique X-ray photoelectron spectroscopy (XPS) was applied to determine the oxide film composition at each pre-oxidation potential to correlate this information to electrochemical characterization.

5.3 Hypothesis

For the surface treatment, SS treated by HNO_3 should have lowest cathodic limiting current density since it has the thickest oxide film created by HNO_3 ; for the oxide film composition study, the cathodic kinetics due to ORR should be higher for SS316L at all the potentials since it has Mo in the oxide film which has catalytic effect on ORR based on literature.

5.4 Methodology

5.4.1 Effect of Surface Treatment

5.4.1.1 Surface Treatment

Three different surface treatments were performed on SS316L prior to RDE test: (1) cathodically pre-reduction at $-1 \text{ V}_{\text{SCE}}$ for 10 mins; (2) 1.5-hr immersion at open circuit potential (OCP) in 0.6M NaCl solution; (3) chemical treatment with HNO_3 on the surface for 1hr. For surface treatment (3), the sample surface was then rinsed with ethanol followed by de-ionized water.

5.4.1.2 RDE Test

RDE tests were performed for Pt, and SS316L disk electrodes with three different surface treatments mentioned above in 0.6M NaCl solution. The RDE cell configuration was described in Chapter 3. Cathodic polarization measurements were performed for each sample at 0.2 mV/s scan

rate after 1hr OCP, starting from 0.05 V above OCP and ending at $-1.2 V_{SCE}$ with rotation speed ranging from 10 to 1440rpm.

5.4.2 Comparative Study of Effect of Pre-Oxidation Potential Between SS316L and SS314L

5.4.2.1 Materials Preparation

304L and 316L stainless steel test coupons were both cut from the 3"x 5" plates acquired from McMaster Carr. These coupons were polished up to a 1200 grit surface finish with silicone carbide paper, and then rinsed with acetone and deionized water ($18.1 M\Omega \cdot cm$, <5 ppb TOC) respectively, followed by using zero grade compressed air to dry the surface. The composition of these two types of stainless steels are listed in Table 5.1.

Table 5.1: Composition of SS304L and SS316L in Atomic Weight Percent (%)

	Cr	Ni	Mn	Mo	Si	N	P	C	S	Fe
SS304L	19.01	8	1.27	N/A	0.35	0.053	0.030	0.021	0.001	Balance
SS316L	17.23	10.16	1.75	2.25	0.46	0.071	0.039	0.019	0.028	Balance

5.4.2.2 Electrochemical Test

All the experiments were measured by a Gamry Ref 600 Potentiostat. Gamry Framework and Gamry Analyst software were used to monitor the measurements and perform EIS data fitting respectively. Since two different reference electrodes were used, all the potentials were converted in terms of SCE for better comparison of experimental results. It should be noted that the potential difference between saturated Hg/HgSO₄ and saturated calomel electrode is 0.4V.

For the determination of cathodic kinetics of two types of SS coupons, the WE surface was pre-reduced at $-1.0 V_{SCE}$ for 30mins before 1hr open circuit potential (OCP) measurement, then followed by cathodic scan starting at OCP and ending at $-1.0 V_{SCE}$ with a scan rate= 0.5 mV/s. The cathodic polarization curve measurements were performed in both 0.3 M Na₂SO₄ and 0.6M NaCl

respectively. The purpose of this comparison was to ensure the mass transfer limited cathodic current density (kinetics) due to oxygen reduction reaction (ORR) in these two solutions were nearly identical. The anodic kinetics of these two types of SSs were only measured in 0.3M Na₂SO₄ after 1 hr OCP measurement, starting from OCP to 2 V_{SCE} at the same scan rate. The purpose of measuring anodic kinetics is to determine the passive/transpassive region of two SSs in chloride-free solution environment.

In potentiostatic experiment, the SS coupons were held at different anodic oxide potentials equal to 0, 0.4, 0.9 and 1.4 V_{SCE} as well as corrosion potential individually for 2 hrs. after 30 mins cathodic pre-reduction at -1.0 V_{SCE}. Each of these samples was taken out of the electrochemical cell immediately right after the galvanostatic experiment and put into XPS chamber within 10mins for post characterization of oxide film properties at different oxidation potentials, in order to mitigate the formation of unwanted air-formed passive oxide film on the SS surface.

In cyclic voltammetry experiment, after 30mins cathodic pre-reduction, the SS samples were initially charged at different anodic oxidation potentials same to the above potentiostatic experiment for 2hrs, and then scanned to -1 V_{SCE} in negative direction before scanning back to the corresponding anodic oxidation potential in the positive direction, at scan rate equal to 0.5 mV/s for three times. The plots for post analysis were taken from the last cycle.

For the EIS experiment setup, the SS samples again experienced 30-min cathodic pre-reduction followed by 2-hr potentiostatic hold at different anodic oxidation potentials, then the EIS experiment was performed at each anodic oxidation potential, in the frequency range from 10 kHz to 5 mHz at 10 points per decade and a 10 mV AC amplitude around the anodic oxidation potential.

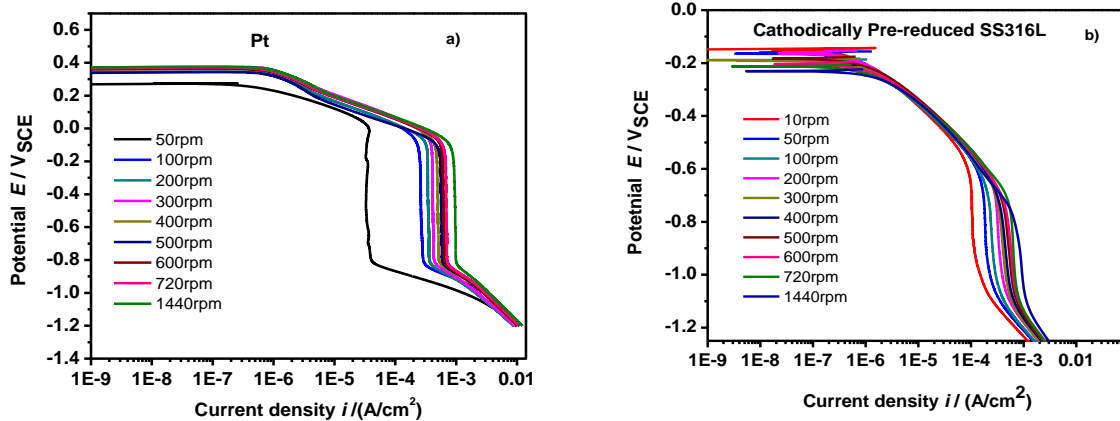
5.4.2.3 XPS Characterizations

For XPS surface analysis, a PHI VersaProbe III spectrometer was used with a Mg $K\alpha$ X-ray source (1253.6 eV) and 55eV pass energy. Survey spectra were firstly performed in order to identify major elements appeared on the oxide film formed at different oxidation potentials: Fe 2p, Cr 2p, Ni 2p, Mo 3d, and O 1s. Then the depth profiles at different sputtering time intervals were monitored in order to obtain distributions of pertinent elements across the surface layer at a given sputtering time period equal to 360 seconds (6 mins) with Ar^+ energy of 3 keV over a 3 x 3 mm² area.

5.5 Results and Discussions

5.5.1 RDE Studies to Investigate the Effect of Surface Treatment on ORR Cathodic Kinetic

Cathodic polarization curves of Pt (reference material), and SS316L with three different surface treatments are shown in Figure 5.1a-d. Cathodic kinetics especially ORR diffusion limited cathodic kinetics of Pt were used as upper limit values for those of SS316L in this study.



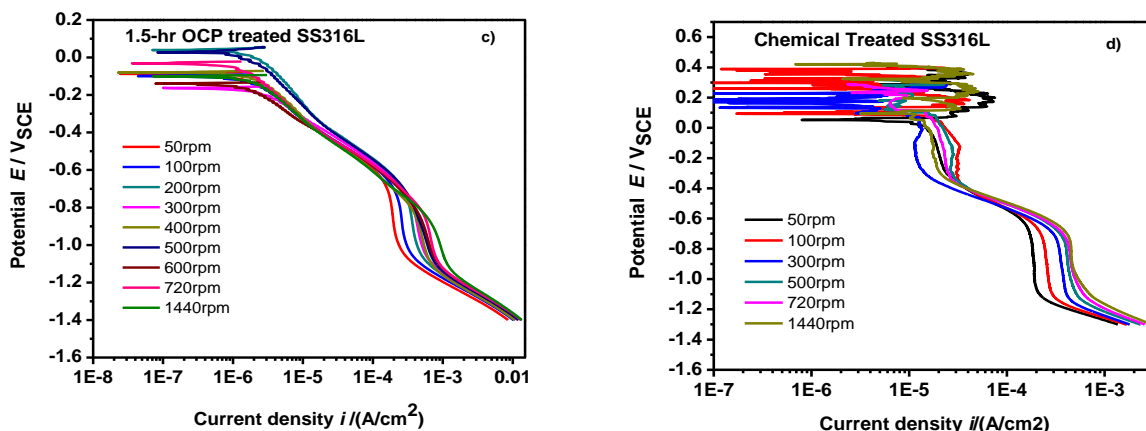


Figure 5.1: Cathodic polarization curves of a) Pt, b) cathodically pre-reduced SS316L, c) 1.5-hr OCP treated SS316L and d) chemical treated SS316L in 0.6M NaCl as a function of rotation speed.

A reference potential $= -0.85 \text{ V}_{\text{SCE}}$ at ORR diffusion limited potential region for all electrodes is selected to make Levich plot in which cathodic limiting current density (i_{lim}) at the selected reference potential vs. reciprocal of boundary layer thickness for Pt and SS316L of different surface treatments (Figure 5.2). The details of Levich analysis is discussed in Chapter 3. Additionally, theoretical lines based on Fickian 1st law are also shown in Figure 5.2: solid line represents ORR via 4-electron transfer, and dash line represents that via 2-electron transfer. It can be seen that Pt data all falls on the solid line, indicating 4-electron ORR took place on Pt. When the simulated electrolyte layer $\geq 36 \mu\text{m}$, i_{lim} for all the electrodes align along the solid line, which infers 4-electron ORR took place on all the electrode surfaces, and electrolyte layer thickness was still the dominant factor controlling the i_{lim} ; Once the electrolyte layer $< 36 \mu\text{m}$, there is discrepancy in i_{lim} between Pt and all the SS316Ls, and discrepancy becomes larger as the electrolyte layer continues to decrease. For SS316L, the degree of deviation from Pt at thinner electrolyte layer regime follows this order: cathodic-preduction $<$ 1.5-hr OCP $<$ chemical treatment, especially for chemical treated SS316L, the trend line is closer to theoretical dash line for 2-electron transfer

ORR. Actually, Le Bozec *et al.*²¹ investigated the dependence of ORR on the surface treatment for SS 316L and 904L, and found that ORR rate in seawater environment is highest on cathodically pre-reduced surface, followed by mechanically polished surface and then anodically passivated surface, the surface chemically treated with HF/HNO₃ has the lowest ORR rate. On pre-reduced and polished surface, ORR follows the 4-electron, and a combined 4-electron and 2-electron pathways respectively, and are both under mass-transfer limited control, whereas HNO₃ treated surface inhibits ORR due to enrichment in Cr³⁺ species in oxide film (not larger thickness as stated in the hypothesis). Those explain why chemical treated SS316L surface had lowest i_{lim} closer to dash line (2-electron transfer ORR), whereas cathodic pre-reduced SS316L had highest i_{lim} among three SS samples and closer to the solid line (4-electron transfer ORR). This comparison also implies the effect of oxide film became significant under very thin electrolyte thickness.

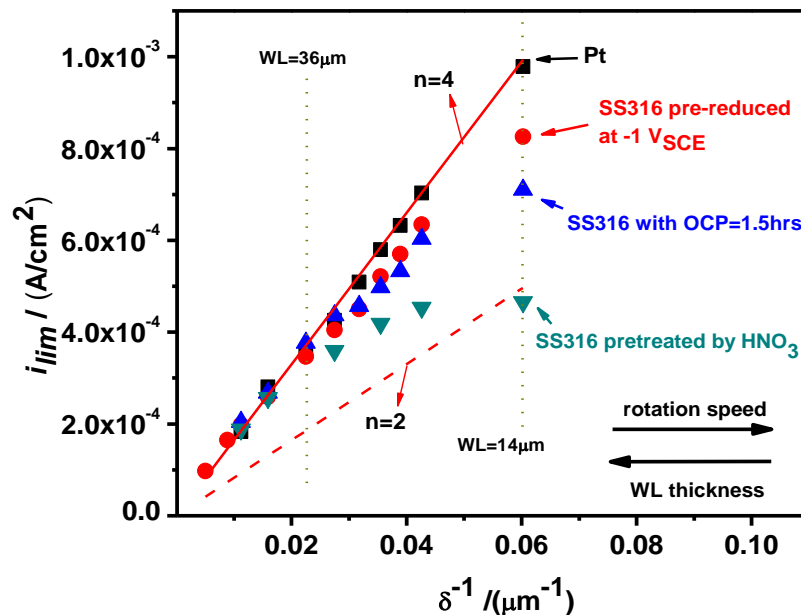


Figure 5.2: Levich plots for Pt and SS316L with three different surface treatments in which i_{lim} is a function of reciprocal of simulated electrolyte layer thickness.

5.5.2 Comparative Study of Effect of Pre-Oxidized Potential on Cathodic ORR Kinetics Between SS316L and SS314L

5.5.2.1 Determination of Pertinent Electrochemical Kinetics of SSs in Na₂SO₄ Solution

To determine the cathodic kinetics especially diffusion limited region in Na₂SO₄ pertinent to 0.6M NaCl, one can express the cathodic limiting current density for ORR via one-dimensional Nernst-Fickian Equation (Equation 5.4):

$$i_{lim,ORR} = \frac{nFD_{O_2}(C_{bulk,O_2} - C_{surface,O_2})}{\delta} \quad (5.4)$$

where n is the number of transferred for ORR, D_{O_2} is the diffusivity of dissolved oxygen [O_2], C_{bulk, O_2} and $C_{surface,O_2}$ are the concentration of O_2 at the bulk solution and electrode surface respectively, and δ is the diffusion layer thickness. Assuming n is the same for ORR taken place at SS surface in both Na₂SO₄ and NaCl solution, and fast electrochemical reaction of ORR at the electrolyte/electrode interface such that $C_{surface, O_2}$ is equal to zero, $i_{lim, ORR}$ in two solutions should be identical as long as $D_{O_2}C_{bulk,O_2}$ product is the same. OLI Analyzer software (version 9.6) was applied to calculate theoretical product values in two solutions. Plot of $D_{O_2}C_{bulk,O_2}$ product as a function of Na₂SO₄ concentration, and the reference value of product in 0.6M NaCl solution are displayed in Figure 5.3a. The intersection of 0.6M NaCl horizontal line and Na₂SO₄ slope determines the equivalent Na₂SO₄ concentration, which is equal to 0.3M and has a product value of 4.5E-10 mol*s/m. To validate the accuracy of theoretical calculations by OLI software, cathodic kinetics of SS304L and SS316L in both 0.3M Na₂SO₄ and 0.6M NaCl are shown in Figure 5.3b, together with cathodic kinetics of Platinum (Pt) in 0.3M Na₂SO₄ solution. $i_{lim, ORR}$ in 0.3M Na₂SO₄ were nearly identical to those in 0.6M NaCl for both SS304L and SS316L, and there was barely any difference between two types of SSs in terms of $i_{lim, ORR}$, proving the accuracy of theoretical calculation. It should be noted that the $i_{lim,ORR}$ for SSs are supposed to be less than that for Pt, which

was also demonstrated in the plot as well ($i_{lim, ORR}$ for SS was about 90% of that for Pt). A comparison of full electrochemical kinetics of two types of SSs in 0.3M Na₂SO₄ solution is shown in Figure 5.4. It is clearly seen that except the fact that E_{corr} of SS316L was 0.087 V higher than SS304L, the breakdown potential of two SSs were almost identical which were about 1.14 V_{SCE}.

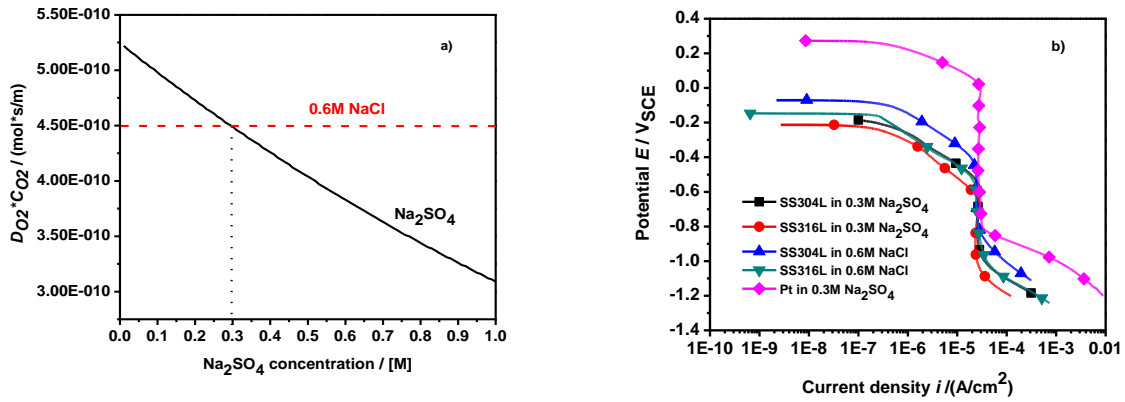


Figure 5.3: Theoretical calculation of $D_{O_2} C_{bulk, O_2}$ product as a function of [Na₂SO₄] and that in 0.6M NaCl; b) cathodic kinetics of SS304L and SS316L in 0.3M Na₂SO₄ and 0.6M NaCl, as well as Pt in 0.3M Na₂SO₄.

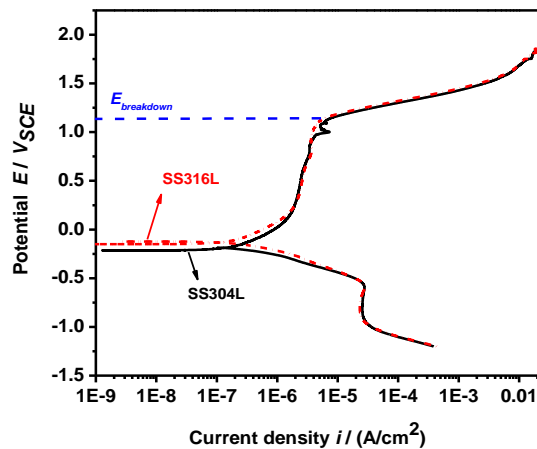


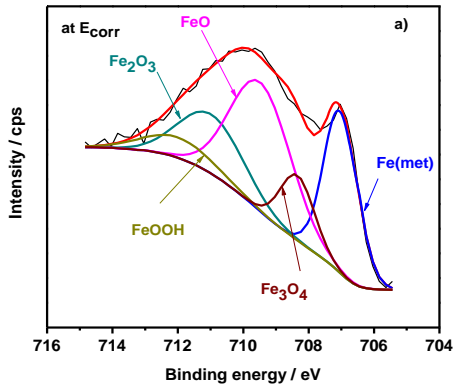
Figure 5.4: Comparison of full electrochemical kinetics of SS304L and SS316L in 0.3M Na₂SO₄.

5.5.2.2 XPS Characterization to Precisely Determine the Oxide Film Composition at Each Pre-oxidization Potential

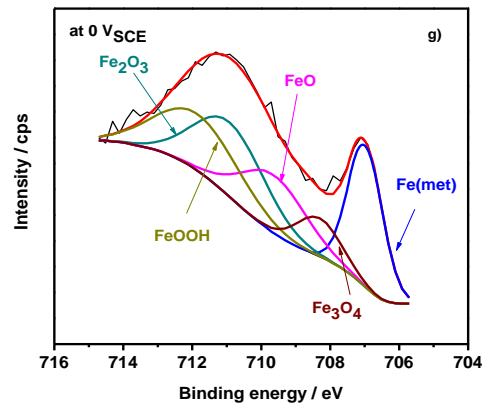
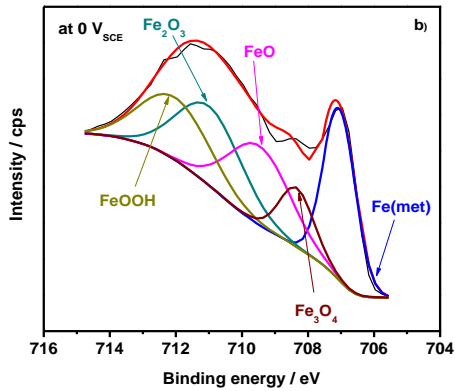
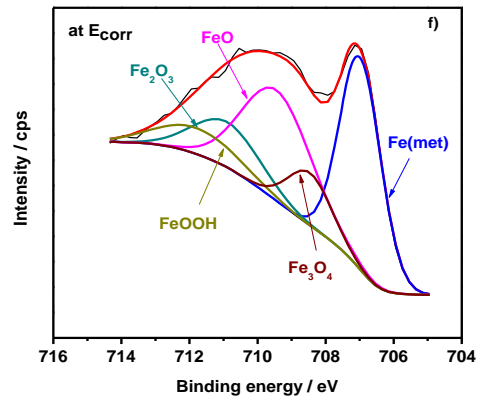
Five different oxidation potentials were chosen for potentiostatic testing to grow oxide film for 2hrs prior to XPS analysis: E_{corr} , 0, 0.4, 0.9 and 1.4 V_{SCE} . Based on Figure 5.4, 1.4 V_{SCE} is located at transpassive region, whereas 0, 0.4 and 0.9 V_{SCE} are still in the passive region for both SS304L and SS316L. XPS spectra analysis of oxide film of both SS304L and SS316L after 2-hr pre-oxidization at differential potentials are Figure 5.5-Figure 5.8, in which metallic and oxidation states of Fe 2p_{3/2}, Cr 2p_{3/2}, Ni 2p_{3/2} and Mo 3d are presented. Deconvolution of these elements in different states are based on the binding energies listed in Table 5.2³³⁻³⁵. For Fe 2p_{3/2} of both SS304L and 316L, metallic Fe, Fe²⁺ and Fe³⁺ oxidized compounds were major species in the oxide film at lower oxidation potentials from E_{corr} to 0.4 V_{SCE} , whereas at medium oxidation potential 0.9 V_{SCE} , Fe²⁺ and Fe³⁺ oxidized compounds were primary species; at high oxidation potential (transpassive region), only Fe³⁺ oxidized compounds were major species, especially FeOOH. It is also noticed that Fe₃O₄ only appeared in lower and medium oxidation potential in this study. Actually for pure iron, Fe₃O₄ is formed at lower oxidation potential to provide pseudo-passivity for iron and it transformed into γ -Fe₂O₃ when the applied potential is more anodic^{17,36}. For Cr 2p_{3/2} of both SS304L and 316L, Cr³⁺ oxide and hydroxide were dominant species in the oxide film at lower oxidation potentials from E_{corr} to 0.4 V_{SCE} ; at medium oxidation potential 0.9 V_{SCE} , although Cr³⁺ oxide and hydroxide were major species, Cr⁶⁺ oxide began to appear in oxide film, and then it became the most dominant species followed by Cr³⁺ oxide and hydroxide at higher oxidation potential 1.4 V_{SCE} ; For Ni 2p_{3/2}, metallic Ni and NiO were two major species in the oxide film at lower oxidation potentials; Ni(OH)₂ took over NiO and became the dominant species together with metallic Ni at medium oxidation potential, and then turned into the only dominant

species at transpassive potential $1.4V_{SCE}$. As for Mo $3d$ which only appeared in SS316L, metallic Mo and Mo^{6+} were major in oxide film during potentials from E_{corr} to $0.4V_{SCE}$, and then Mo^{6+} oxide became the most available species at 0.9 and $1.4 V_{SCE}$.

SS304L



SS316L



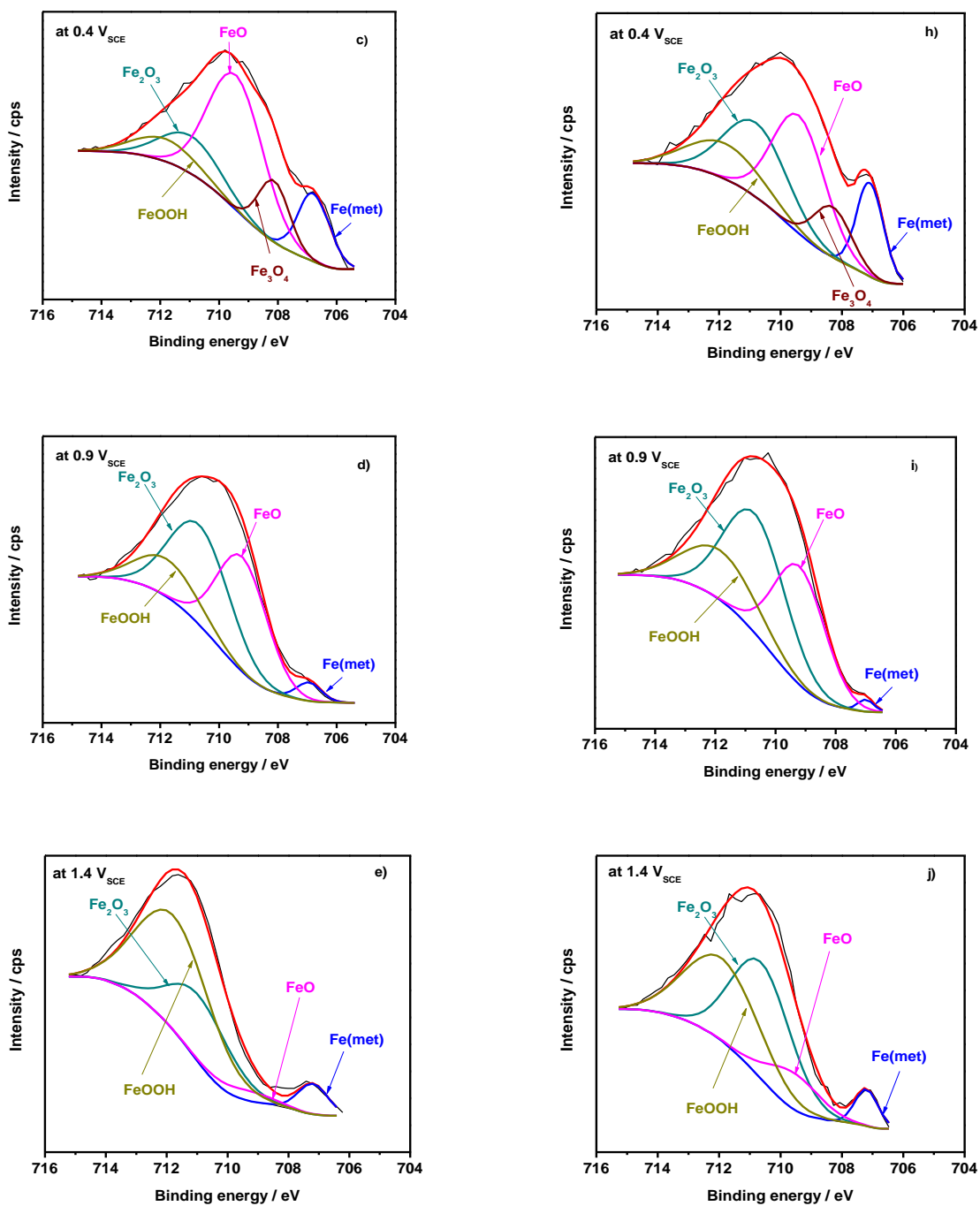
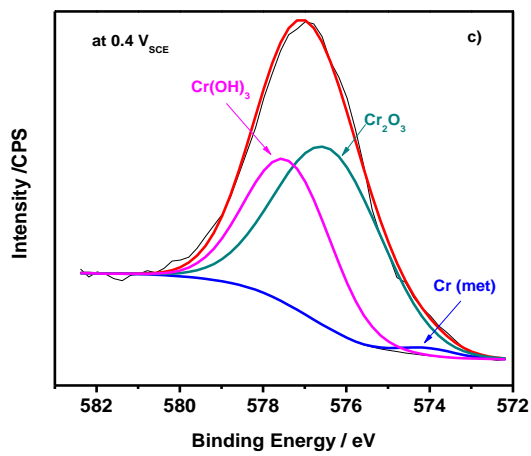
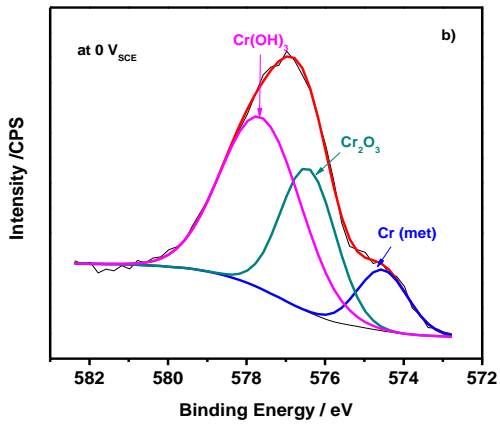
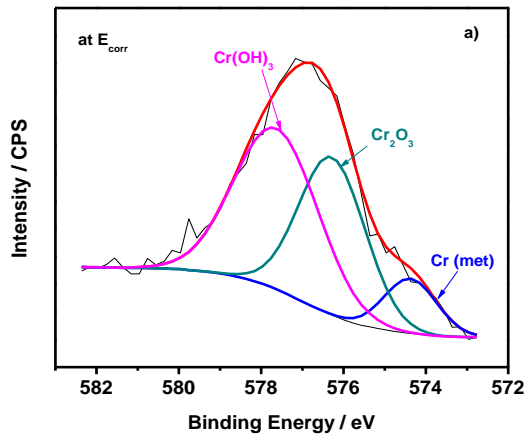
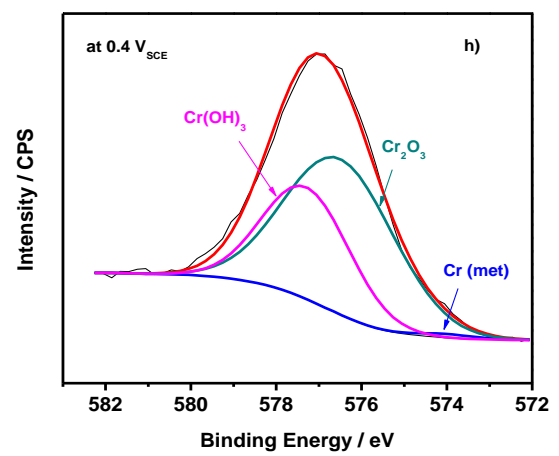
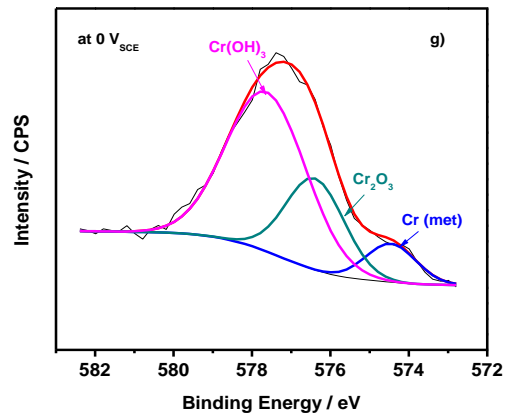
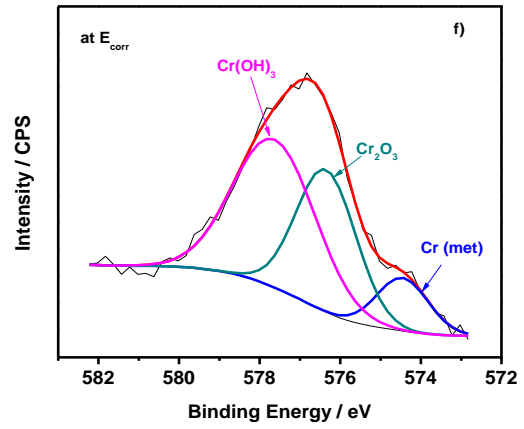


Figure 5.5: XPS spectra and deconvolution of Fe 2p_{3/2} at pre-oxidation potential a) E_{corr} ; b) $0 V_{\text{SCE}}$; c) $0.4 V_{\text{SCE}}$; d) $0.9 V_{\text{SCE}}$ and e) $1.4 V_{\text{SCE}}$ for SS304L and f) E_{corr} ; g) $0 V_{\text{SCE}}$; h) $0.4 V_{\text{SCE}}$; i) $0.9 V_{\text{SCE}}$ and j) $1.4 V_{\text{SCE}}$ for SS3316L.

SS304L



SS316L



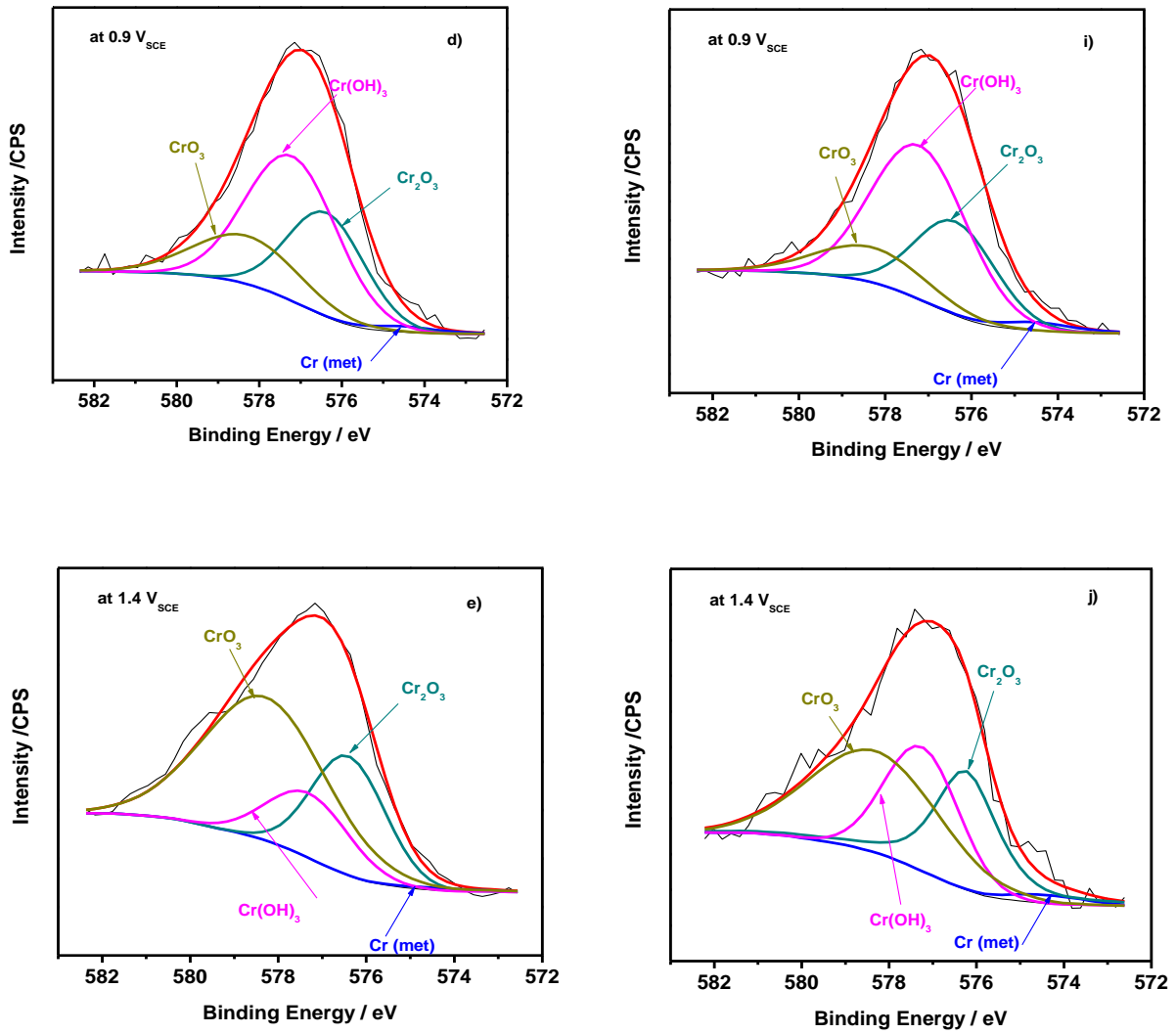
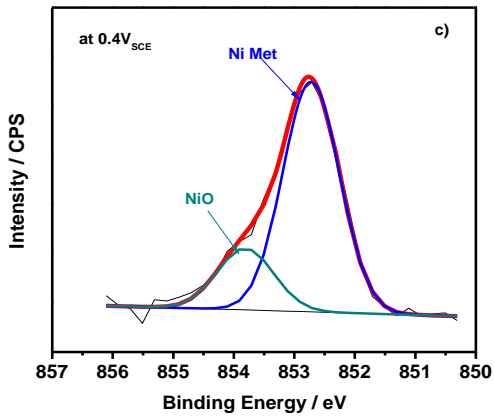
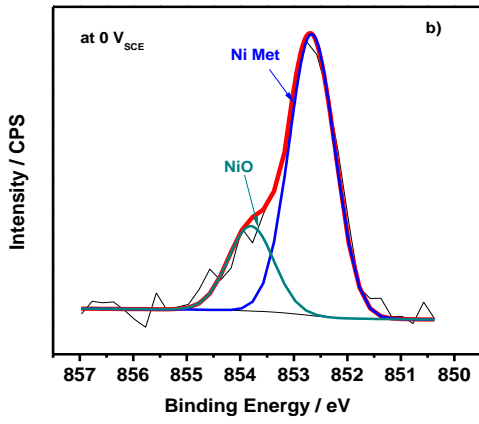
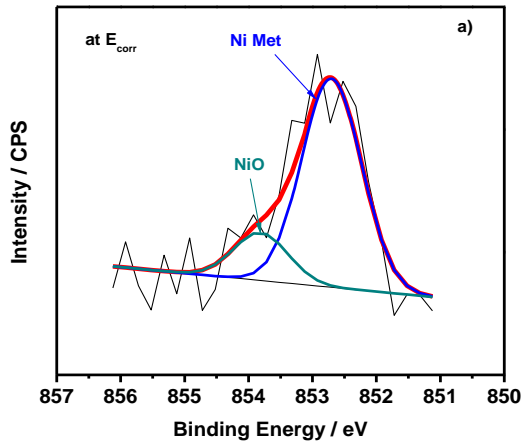
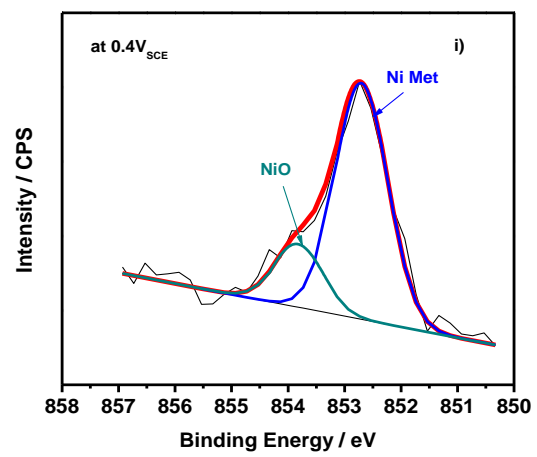
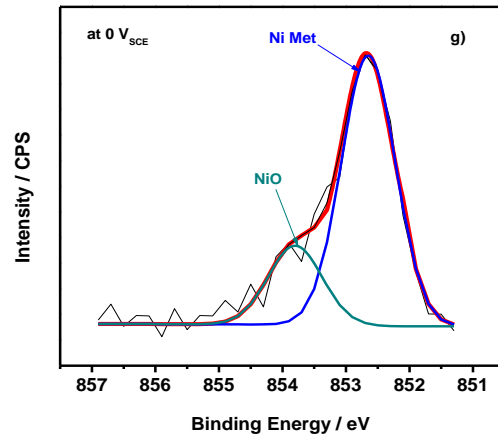
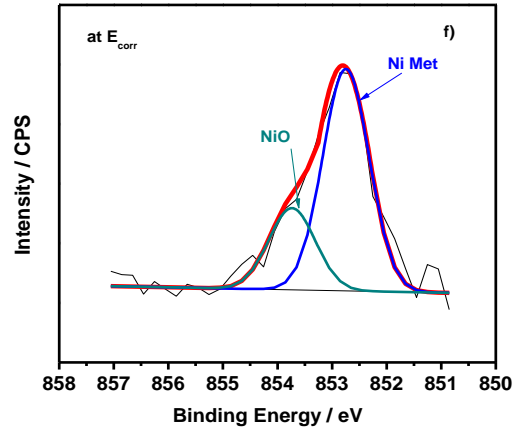


Figure 5.6: XPS spectra and deconvolution of Cr $2p_{3/2}$ at pre-oxidation potential a) E_{corr} ; b) $0 V_{\text{SCE}}$; c) $0.4 V_{\text{SCE}}$; d) $0.9 V_{\text{SCE}}$ and e) $1.4 V_{\text{SCE}}$ for SS304L and f) E_{corr} ; g) $0 V_{\text{SCE}}$; h) $0.4 V_{\text{SCE}}$; i) $0.9 V_{\text{SCE}}$ and j) $1.4 V_{\text{SCE}}$ for SS3316L.

SS304L



SS316L



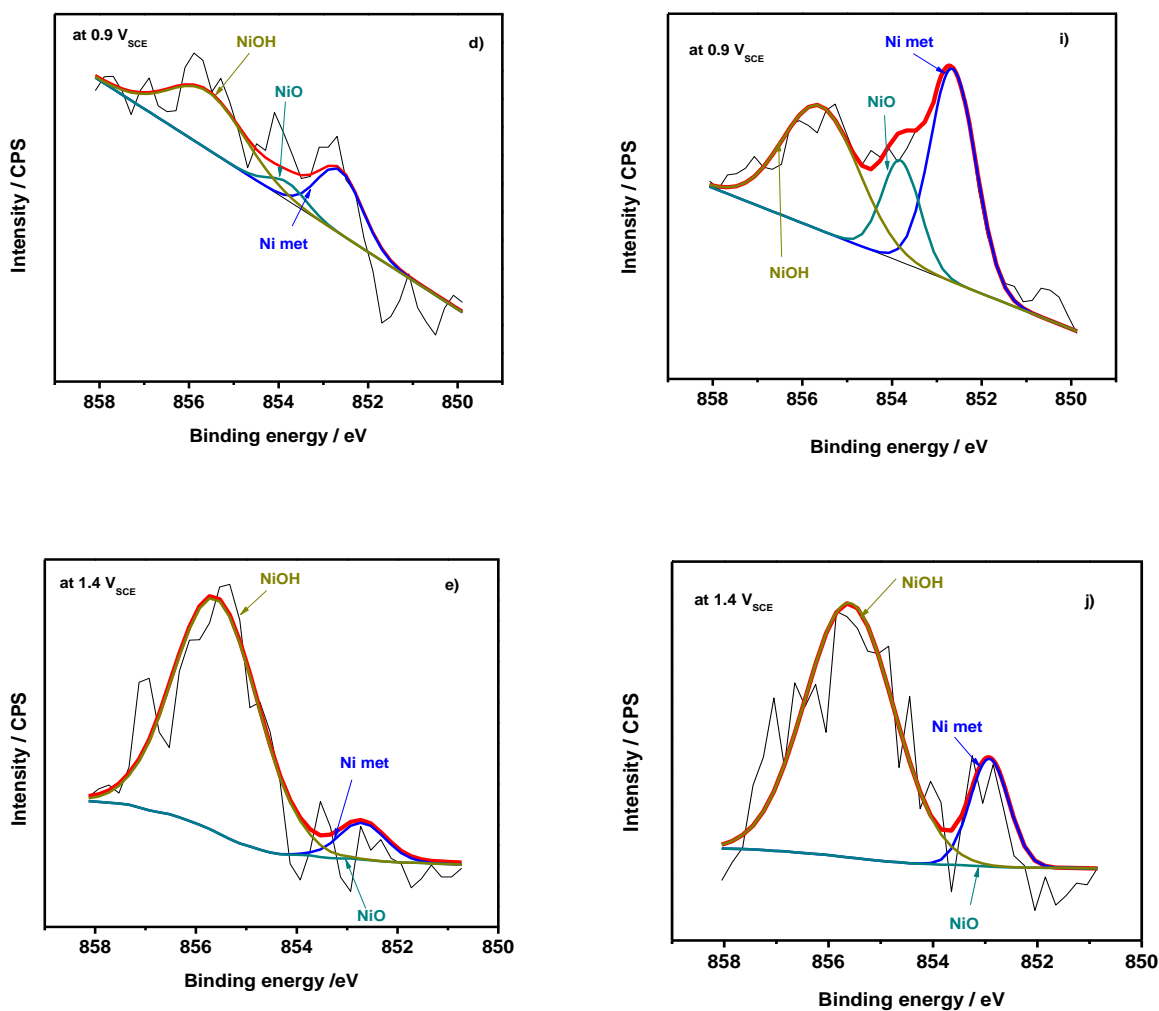


Figure 5.7: XPS spectra and deconvolution of Ni 2p_{3/2} at pre-oxidation potential a) E_{corr}; b) 0 V_{SCE}; c) 0.4 V_{SCE}; d) 0.9 V_{SCE} and e) 1.4 V_{SCE} for SS304L and f) E_{corr}; g) 0 V_{SCE}; h) 0.4 V_{SCE}; i) 0.9 V_{SCE} and j) 1.4 V_{SCE} for SS3316L.

SS316L

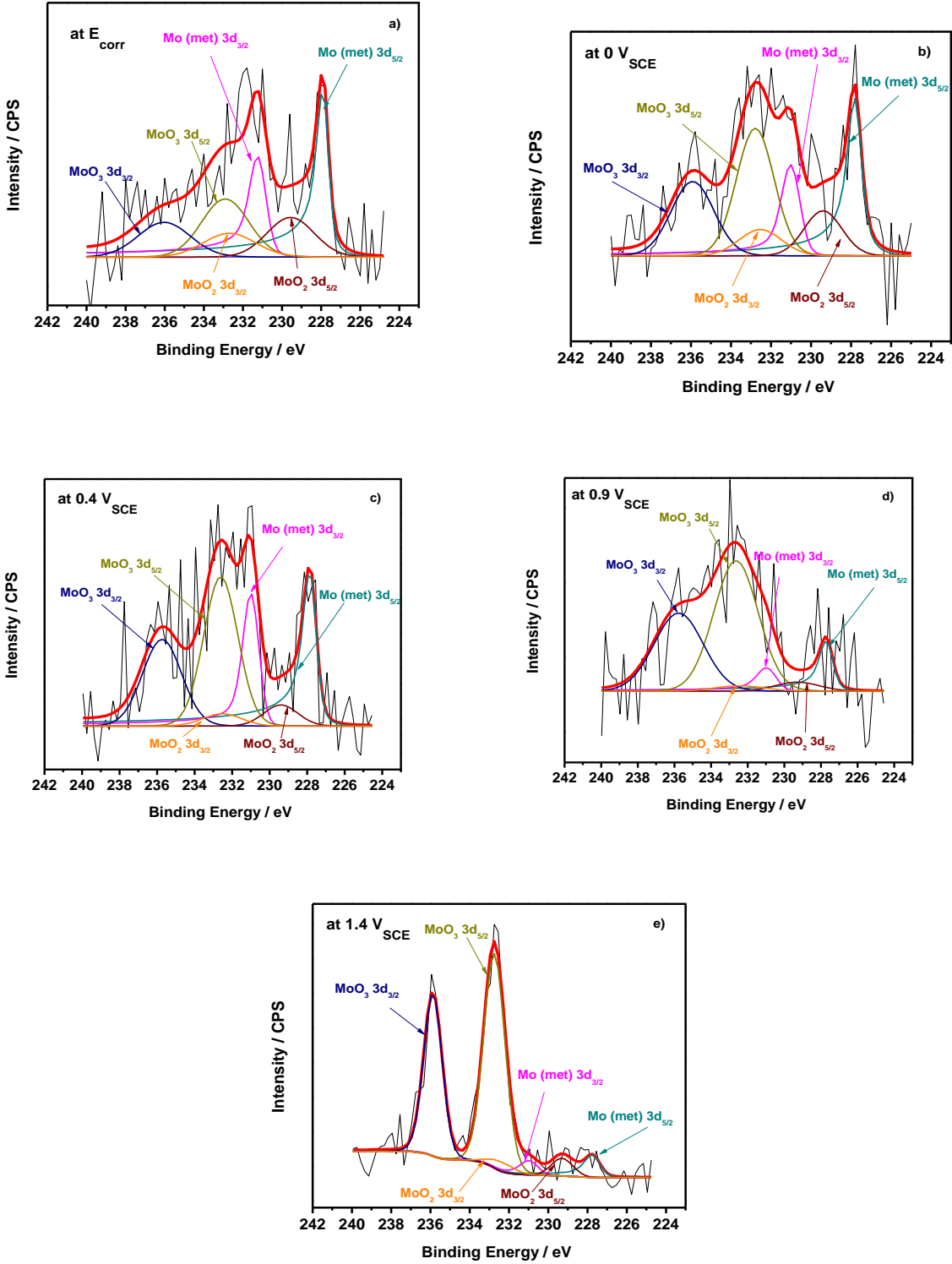


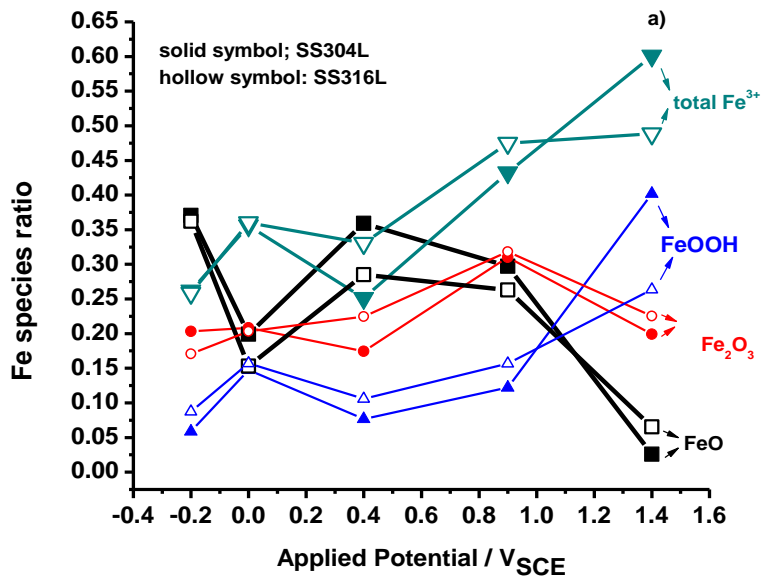
Figure 5.8: XPS spectra and deconvolution of Mo 3d at pre-oxidation potential a) E_{corr} ; b) 0 V_{SCE}; c) 0.4 V_{SCE}; d) 0.9 V_{SCE} and e) 1.4 V_{SCE} for SS316L.

Table 5.2: List of binding energies for different states of each primary element appeared in the oxide film of steels³³⁻³⁵.

Element	Peak	Binding Energy (eV)
Fe	2p _{3/2}	Fe (met): 707; Fe₃O₄ : 708.3; FeO : 709.4; Fe₂O₃ :710.9; FeOOH : 711.8
Cr	2p _{3/2}	Cr (met): 574.4; Cr₂O₃ :576.3; Cr(OH)₃ : 577.1; CrO₃ : 578.3
Ni	2p _{3/2}	Ni (met):852.7; NiO : 853.8; Ni(OH)₂ :855.6
Mo	3d _{5/2}	Mo (met):228.1; MoO₂ : 229.81; MoO₃ : 233.15
	3d _{3/2}	Mo (met): 231.33; MoO₂ : 232.90; MoO₃ : 236.28

To better discern the distribution of each oxidized Fe species as a function of oxidation potential, comparisons of ratio of each oxidized Fe species to the total amount of all oxidized species (Fe+Cr+Ni+Mo) between SS314L and SS316L are shown in Figure 5.9a. In these comparisons, FeO, Fe₂O₃, FeOOH and total Fe³⁺ (Fe₂O₃+FeOOH) are considered, while Fe₃O₄ is deconstructed as FeO·Fe₂O₃, half amount of which is FeO and the rest is Fe₂O₃. For each SS, it shows that: FeO had the highest ratio at E_{corr}, and it then decreased at 0 V_{SCE} before reaching the second highest ratio at 0.4 V_{SCE}. After that, FeO ratio kept decreasing during medium and high oxidation potential regions. Fe₂O₃ ratio was fluctuated although it reached highest at 0.9 V_{SCE}, whereas FeOOH ratio increased with applied potential except a secondary peak appeared at 0 V_{SCE}. For total Fe³⁺ ratio, it was lower than Fe²⁺(FeO) at E_{corr} and 0.4 V_{SCE}, but higher once the potential was beyond 0.4V_{SCE} and increased with applied potential. At 0 V_{SCE}, the total Fe³⁺ ratio was surprisingly higher than Fe²⁺ as well. By comparing SS304L and SS316L, it shows that: SS316L had on average higher Fe³⁺ and lower Fe²⁺ ratios than SS304L at all applied potentials except transpassive potential 1.4 V_{SCE}. In spite of some fluctuations, the overall results agree well with Lorang *et al*¹⁷'s work, in which Fe²⁺ ratio decreased whereas Fe³⁺ one increased as potential became more anodic. Following the same routine, comparisons of Cr oxidized species between SS304L and SS316L are shown in Figure 5.9b. It can be seen that: for each SS, total Cr³⁺ ratio (Cr₂O₃+Cr(OH)₃) initially increased from E_{corr} to 0 V_{SCE} and then decayed over increased applied

potential, reaching minimum at transpassive potential 1.4 V_{SCE} ; whereas Cr^{6+} (CrO_3) ratio maintained at zero until 0.9 V_{SCE} , and then increased to maximum at transpassive potential 1.4 V_{SCE} . SS304L averagely had slightly higher Cr^{3+} than SS316L except at transpassive potential, while it always had higher Cr^{6+} ratio than SS316L once Cr^{6+} species appeared. For Mo species which only appeared in SS316L (Figure 5.9c), it shows that: MoO_2 ratio maintained at low content below 1% at all potentials, MoO_3 increased steadily till 0.9 V_{SCE} except that the second maximum peak showed up at 0 V_{SCE} , and then peaked at transpassive potential with ratio~ 9%.



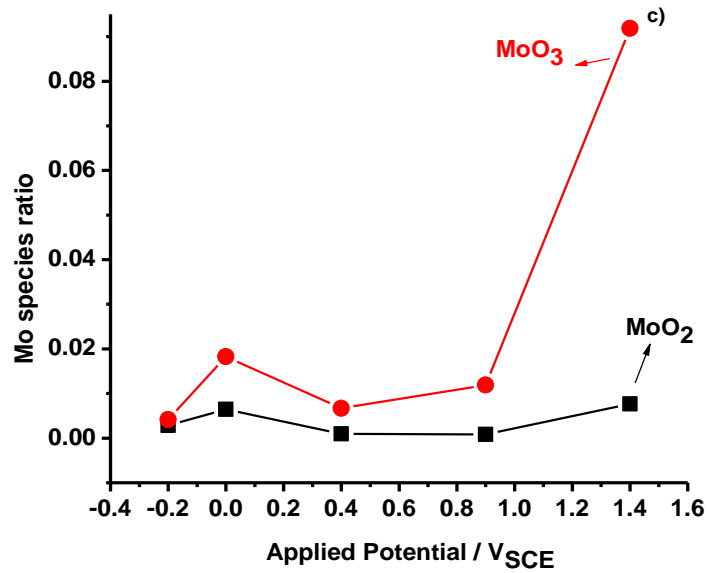
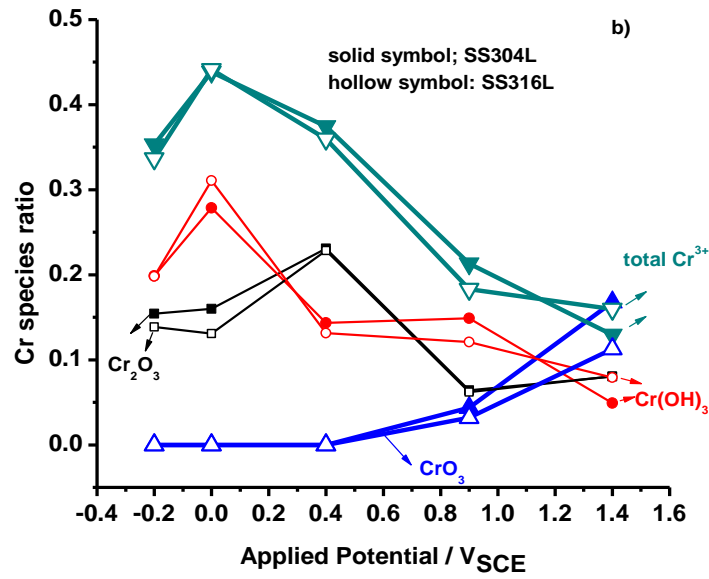


Figure 5.9: Comparisons of ratio of each oxidized a) Fe and b) Cr species to the total amount of all oxidized species (Fe+Cr+Ni+Mo) between SS314L and SS316L as a function of applied potential; c) Mo species ratio vs. applied potential for SS316L.

To investigate the oxide film thickness at each oxidation potential, depth profiling was performed by Ar⁺ sputtering. Data was recorded at every 30 seconds. In order to convert sputtering time into estimated depth, sputtering rate which was approximately equal to 1nm/min ($\frac{1}{60}$ nm/s) was incorporated from Donik *et al.*'s XPS depth profiling work for duplex stainless steel³⁷, as a result, the estimated sputtering-through depth during 6mins was 6nm. Comparisons of depth profile in terms of ratio of Fe 2p_{3/2} (sum of metallic and oxide species) to the sum of Fe 2p_{3/2} and Cr 2p_{3/2} as a function of applied potential for SS304L and SS316L are displayed in Figure 5.10a and 5.10b respectively. For both SS304L and SS316L, as increasing applied potential, the oxide film thickness increased as well in both figures if one defines the first depth to reach a constant Fe 2p_{3/2} ratio as oxide film thickness. At transpassive potential 1.4 V_{SCE}, the pertinent film thickness was largest, which could be attributed to continuous thickening of porous FeOOH. The estimated oxide film thickness as a function of applied potential between SS304L and SS316L are plotted in Figure 5.10c, these two sets of data are also compared with work by Nicic and Macdonald³⁸, in which oxide film thickness of SS316L as a function of passive potential in borate buffer solution was estimated by single frequency EIS technique. For our study, SS304L and SS316L had the same oxide film thickness at potentials from E_{corr} (both ~-0.2 V_{SCE}) to 0.9 V_{SCE}, and oxide film thickness of SS304L was 0.5 nm higher than SS316L at transpassive potential 1.4V; by linear fitting, the oxide film growth rate for SS304L was about 1.7 nm/V, which was slightly higher than SS316L which was ~ 1.4 nm/V, but both were lower than Nicic and Macdonald's estimation of 2.2 nm/ V.

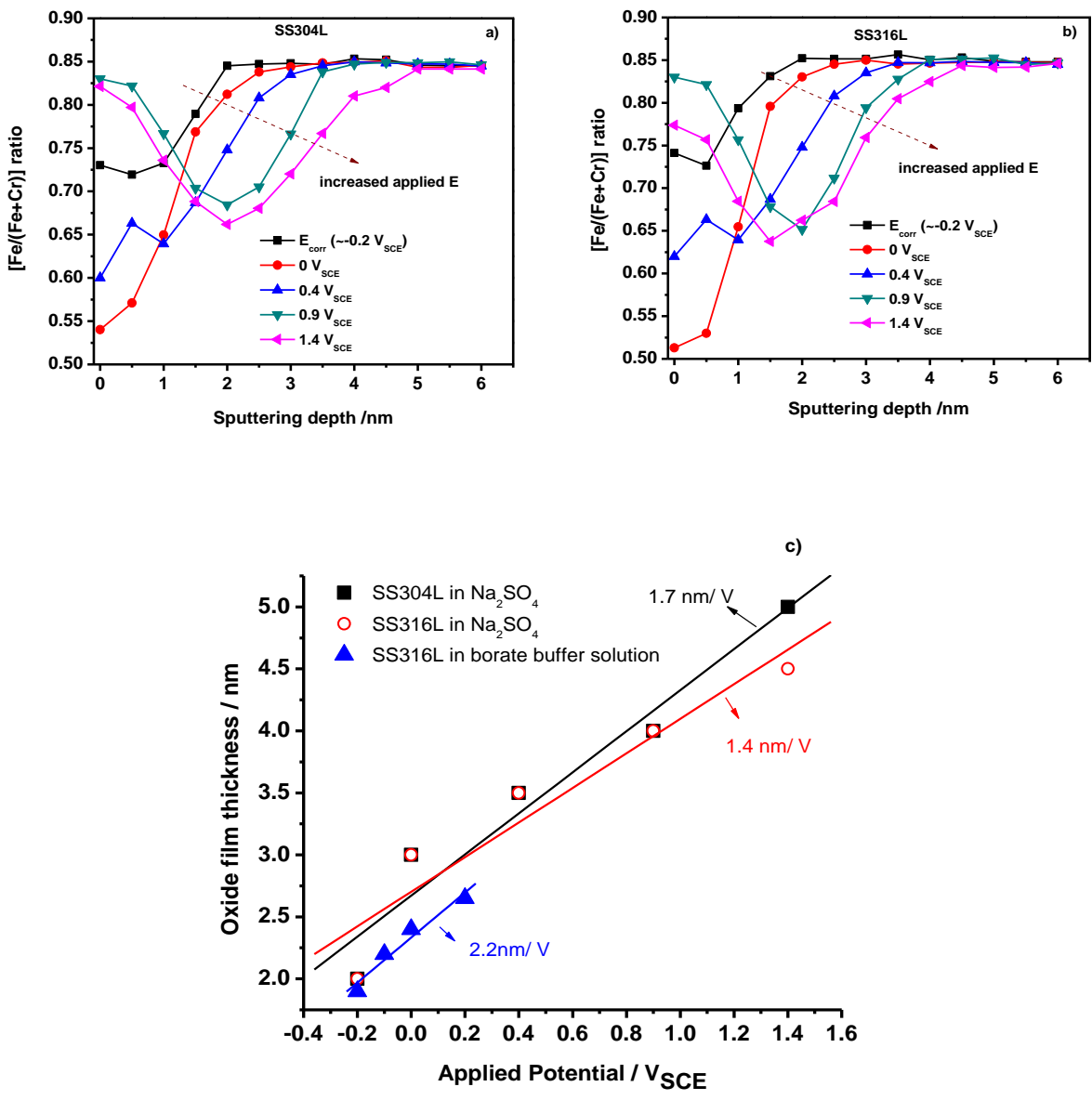


Figure 5.10: Comparison of depth profile in terms of ratio of Fe 2p $_{3/2}$ to the sum of Fe 2p $_{3/2}$ and Cr 2p $_{3/2}$ as a function of applied potential for a) SS304L and b) SS316L; c) comparison of oxide film thickness vs applied potential for 304L(solid square) and 316L(hollow circle) from this study and SS316L from Nicic and Macdonald's work³⁸ (solid triangle).

5.5.2.3 Cyclic Voltammetry to Investigate the Dependence of ORR Limiting Current Density on Pre-Oxidization Potential

Cyclic voltammetry measurements at a 0.5 mV/s scan rate for two types of SSs were performed to study the effect of pre-oxidization potential on the ORR diffusion limited kinetics. The CVs for SS304L and SS316L were plotted in E-log|i| fashion with smaller potential window from -0.5 to -1.2 V_{SCE} for the better observation of $i_{lim, ORR}$, which are shown in Figure 5.11a and 5.13b, respectively. They were also compared to the cathodic kinetics directly scanned from OCP to -1.2 V_{SCE} in negative direction displayed in Figure 5.3b. Noting that the CV started from negative direction and then reversed to positive direction, the cathodic current densities in the potential range from -0.6 to -1V_{SCE} in the negative direction were all higher than the positive direction at all pre-oxidation potential for both SS304L and SS316L. A reference potential -0.8V_{SCE} was selected to plot $i_{cathodic}(-0.8V_{SCE})$ as a function of pre-oxidation potential for both SS304L and SS306L which is displayed in Figure 5.12. $i_{cathodic}$ for Pt at -0.8 V_{SCE} obtained from Figure 5.3b was also plotted in Figure 5.12, representing the highest $i_{lim, ORR}$ can be obtained in 0.3 M Na₂SO₄ solution. For $i_{cathodic}$ at different pre-oxidation potentials, those at negative direction were both higher than positive direction, this is due to the extra contribution from reduction of Fe³⁺ oxide to Fe²⁺ oxide which happened simultaneously with ORR during the negative scan, such that the $i_{cathodic}$ at pre-oxidation potential=-1.4 V_{SCE} in negative direction was even higher than $i_{lim, ORR}$ for Pt, this also implied that $i_{cathodic}$ at -0.8V_{SCE} in positive direction can be equivalent to $i_{lim, ORR}$ for that pre-oxidation potential since there was no Fe³⁺-to-Fe²⁺ reduction during the scan in the positive direction. For each SS, $i_{lim, ORR}$ dropped significantly quickly when SS was pre-oxidized from OCP to 0V_{SCE}, and then increased with increasing pre-oxidation potential except a plateau from 0 to 0.4V_{SCE} for SS316L. By comparing two SSs, $i_{lim, ORR}$ for SS316L was always larger than

SS304L except at $0.4V_{SCE}$, and the largest difference appeared for $1.4V_{SCE}$, at which $i_{lim,ORR}$ for SS316L was about 1.3 times that for SS304L. The detailed relationship between the oxide film composition at each pre-oxidation potential and the resultant $i_{lim,ORR}$ will be delineated in Section 5.5.2.5.

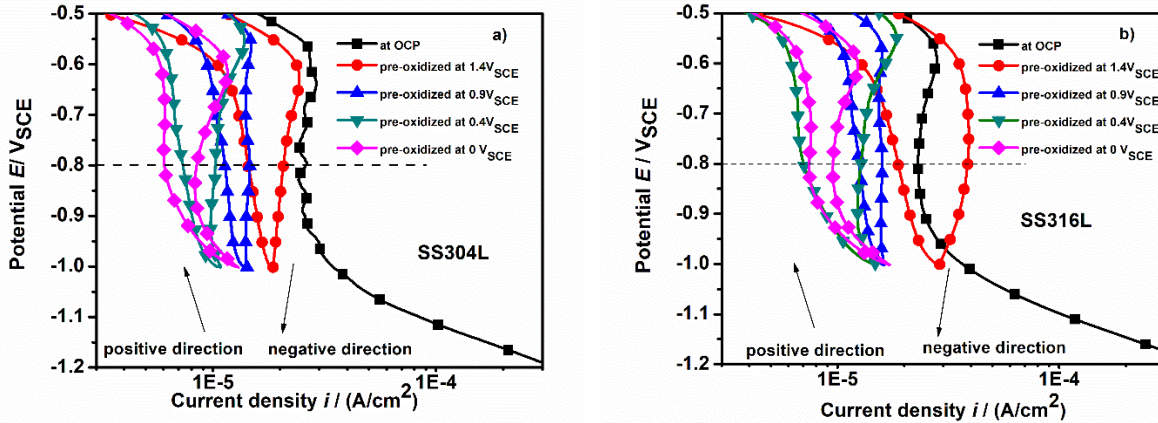


Figure 5.11: a) Comparisons of cathodic kinetics of SS304L in negative and positive directions as a function of applied potential; b) comparisons of cathodic kinetics of SS316L in negative and positive directions at a function of applied potential.

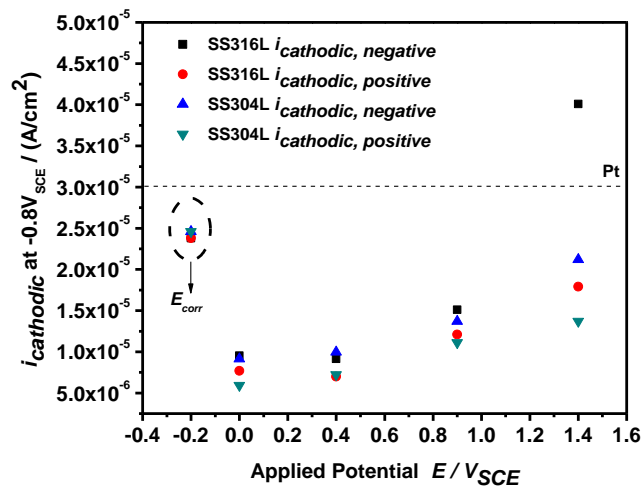


Figure 5.12: Comparison of $i_{cathodic}$ at $-0.8V_{SCE}$ in both negative and positive direction as a function of applied potential for both SS304L and SS316L.

5.5.2.4 EIS Analysis to Determine Corrosion Resistance of Stainless Steels at Different Pre-Oxidization Potential

To evaluate oxide film capacitance and corrosion resistance of each stainless steel at different pre-oxidation potential, EIS analysis was performed. Two types of equivalent circuit models were utilized to fit EIS data shown in Figure 5.13. It should be noted that the second model (Figure 5.13b) better fitted the EIS spectrum at 1.4 V_{SCE}—due to change in film structure at this transpassive potential. Corresponding Bode impedance and phase angle vs. frequency for SS304L and SS316L are plotted in Figure 5.14. At high frequency regime, both models have CPE behavior attributed to the passive oxide film, in order to estimate the effective capacitance values from the CPE, Equation 5.5 is utilized

$$C_{eff} = gQ(\rho_{\delta}\epsilon\epsilon_0)^{1-\alpha} \quad (5.5)$$

Details of this equation has been illustrated in Chapter 4. For ρ_{δ} and ϵ , one can use the value for the oxide film on Fe17Cr steel³⁹ with film resistivity = 4.5 ohm · m and $\epsilon=12$. The EIS parameters pertinent to this study are effective film capacitance $C_{film, eff}$, film resistance R_{film} and charge transfer resistance R_{ct} . Values of these pertinent EIS parameters for both SS304L and SS316L are listed in Table 5.3. Comparisons of $C_{film,eff}$, total corrosion resistance ($R_{film}+R_{ct}$) as well as $R_{film}C_{film,eff}$ product between SS304L and SS316L are shown in Figure 5.15.

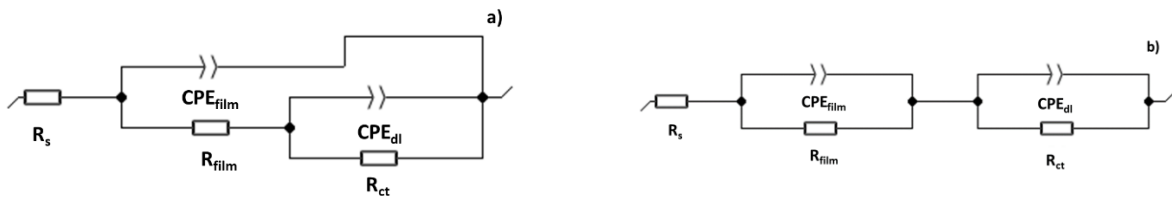


Figure 5.13: Equivalent circuit models used to fit EIS data of SS304L and SS316L at a) applied potential= E_{corr} , 0, 0.4, and 0.9V_{SCE}; b) 1.4 V_{SCE}.

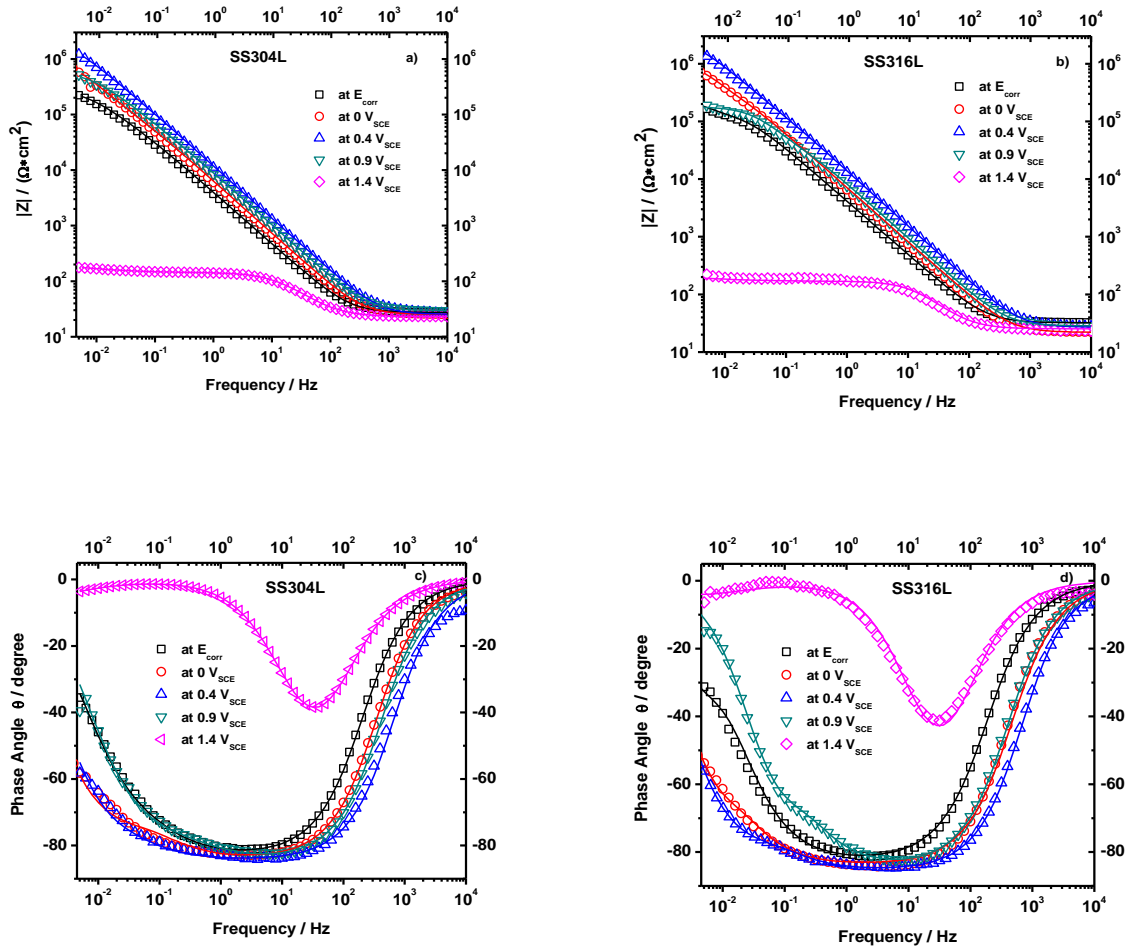


Figure 5.14: a) Bode Impedance response and b) phase angle response of SS304L in 0.3M Na₂SO₄ for different applied potentials; c) Bode Impedance response and d) phase angle response of SS316L in 0.3M Na₂SO₄ for different applied potentials. All solid lines represented the fit using the equivalent circuit models in **Figure 5.13**.

Table 5.3: List of values of $C_{film, eff}$, R_{film} and R_{ct} . for both SS304L and SS316L in 0.3M Na₂SO₄.

		Applied Potential				
		E_{corr}	$0 V_{SCE}$	$0.4 V_{SCE}$	$0.9 V_{SCE}$	$1.4 V_{SCE}$
$C_{film, eff}$ ($F \cdot cm^{-2}$)	SS304L	9.463E-6	7.331E-6	4.115E-6	5.507E-6	1.251E-5
	SS316L	8.127E-6	6.104E-6	4.440E-6	5.919E-6	2.612E-5
R_{film} ($ohm \cdot cm^2$)	SS304L	107927	223872	1098000	97598	120
	SS316L	163977	593288	639347	74198	144.4
R_{ct} ($ohm \cdot cm^2$)	SS304L	203645	1283000	1414000	535345	101.3
	SS316L	112462	685492	2329000	104779	47.2

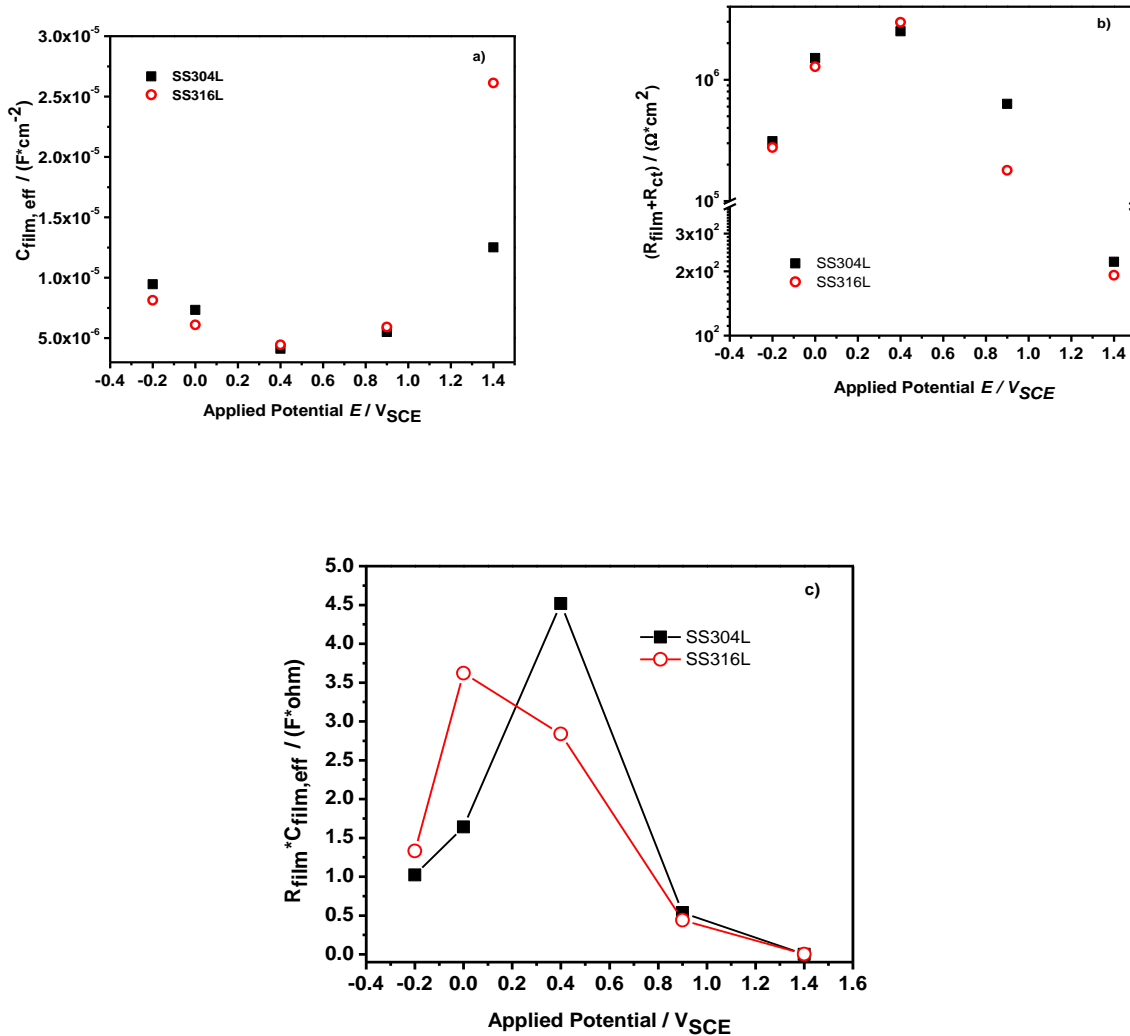


Figure 5.15: Comparison of a) effective oxide film capacitances ($C_{film,eff}$), b) total resistance ($R_{film}+R_{ct}$) and c) $R_{film}C_{film,eff}$ product between SS304L and SS316L as a function of applied potential.

For effective film capacitance (Figure 5.15a), it decreased as applied potential increased from E_{CORR} to $0.4 V_{SCE}$, these might be attributed to accumulation of Cr^{3+} oxide/hydroxide making pre-reduced surface less defective; $C_{film,eff}$ then increased when the potential become more anodic, due to more availability of high oxidation state of Mo and Cr species⁴, Especially for SS316L, its $C_{film,eff}$ was about twice that of SS304L, since SS316L had Mo^{6+} oxidized species besides Cr^{6+} species, whereas SS304L only had Cr^{6+} species at transpassive potential $1.4 V_{SCE}$. As for the total

corrosion resistance (Figure 5.15b), the highest values appeared at $0.4V_{SCE}$ followed by that at $0 V_{SCE}$, this was caused by high content of protective Cr^{3+} species in the oxide film which was observed by XPS analysis. The lowest values both appeared at transpassive potential $1.4V_{SCE}$, due to destruction of passive oxide film structure. SS304L averagely had higher resistance than SS316L except at $0.4 V_{SCE}$. Lastly, for $R_{film}C_{film,eff}$ product (Figure 5.15c) which can be used to evaluate film resistivity as discussed in Chapter 4, it was highest at $0 V_{SCE}$ for SS316L and at $0.4 V_{SCE}$ for SS304L, whereas both stainless steels had the lowest products at $1.4 V_{SCE}$, implying that oxide film at that potential might have very porous structure.

5.5.2.5 Discussion of the Effect of Oxide Film Composition at Ascending Pre-oxidation Potential on Cathodic Kinetics of SS Based on Electrochemistry and XPS Characterization

It is indicated in literature that reduction of Fe^{3+} oxide to Fe^{2+} oxide in the oxide film takes place at $\sim -0.6 V_{SCE}$, which is within the potential range of ORR, whereas the reverse oxidation reaction is at $\sim -0.4 V_{SCE}$ ^{20,21,27,28}. The oxidation of Cr^{3+} to Cr^{6+} in the oxide film takes place at $\sim 0.63 V_{SCE}$ ²⁰, that is why Cr^{6+} oxidized species can be observed in potential only at 0.9 and $1.4 V_{SCE}$ from XPS analysis. Recall from Figure 5.12 that cathodic current densities ($i_{cathodic}$) at $-0.8 V_{SCE}$ (a typical potential for diffusion limited ORR cathodic kinetics) scanning in negative potential were all bigger than in positive direction for both types of stainless steels, this is because both Fe^{3+} -to- Fe^{2+} reduction as well as diffusion limited ORR kinetics contributed to the total current densities in the negative direction, whereas only diffusion limited ORR kinetics took place in the positive direction.

It is noticed that except at E_{Corr} , the overall trend of change in $i_{cathodic}$ from both negative and positive directions ascended with increasing applied potential, this is due to the decrease in Cr^{3+} content in the oxide film which highly inhibits ORR²¹. Although at passive potential range

from 0 to 0.4 V_{SCE}, Fe²⁺ were very high in oxide film which is linked to the active site for ORR^{21,40}, the effect of Cr³⁺ overwhelmed Fe²⁺ such that lower Cr³⁺ amount in the oxide film resulted in higher *i*_{cathodic} due to ORR. For *i*_{cathodic} at E_{corr}, the oxide film compositions at this potential for two types of stainless steels were both high in Cr³⁺ and Fe²⁺, but still had the highest *i*_{cathodic} for SS304L and the secondly highest *i*_{cathodic} for SS316L in negative scan direction, this can be attributed to lowest oxide film thickness (Figure 5.10) and relatively low film resistivity (Figure 5.15c) at E_{corr}. In the RDE study for the effect of surface treatment discussed earlier, at relatively thick electrolyte region, if oxide film thickness was very thin (~2nm), the effect of electrolyte layer thickness overwhelmed the effect of oxide film in terms of ORR kinetics such that the effect of surface treatment which altered the oxide film composition was negligible to ORR kinetics. However, if the oxide film thickness of stainless steel became comparable to that of air-formed oxide film on the Al alloys, the effect of oxide film thickness would matter the ORR kinetics. As seen in this study, when applied potential increased, the corresponding oxide film thickened, resulting in discrepancy in *i*_{cathodic} even in quiescent solution condition shown in Figure 5.12.

It is also noticed that *i*_{cathodic} at 1.4 V_{SCE} for SS316L in negative direction was even higher than theoretical ORR limiting current density measured by Pt and *i*_{cathodic} for SS304L at the same applied potential, this enhancement in *i*_{cathodic} might have three folds: 1) the amount of Fe³⁺ oxidized species was highest, leading to a highest Fe³⁺-to-Fe²⁺ reduction current density; 2) SS316L had the lowest corrosion resistance and its oxide film had the lowest resistivity at that potential; 3) more availability of higher oxidation state of Mo (Mo⁶⁺) can show catalytical effect to ORR⁴. Combining these three factors, *i*_{cathodic} at 1.4 V_{SCE} for SS316L was highest in negative scan direction.

In conclusion, i_{cathodic} at ORR potential region is a complicated function of oxide film composition, thickness, and resistivity as well as electrolyte layer thickness.

5.6 Conclusions:

In this chapter, the effect of oxide film properties (thickness, composition, resistivity and etc.) on the cathodic kinetics of stainless steel were investigated. It can be concluded that

- When the passive oxide film is thin (~2nm), the effect of electrolyte layer thickness overwhelms that of oxide film thickness in terms of ORR cathodic kinetics as long as electrolyte layer thickness is larger than 36 μm in 0.6M NaCl; below this critical electrolyte layer thickness, the effect of oxide film becomes comparable to that of electrolyte layer thickness and has lower cathodic limiting current density compared to the scenario in which only electrolyte layer thickness matters at the same electrolyte layer thickness.
- At the same electrolyte layer thickness (<36 μm), magnitude of cathodic limiting current density after three different surface treatment follows this order: cathodically-pre-reduction > immersion at OCP for 1.5hrs > chemical treatment by HNO_3 .
- From the study of effect of oxide film thickness on cathodic limiting current density on Al alloy 1100, cathodic limiting current density is inversely proportional to oxide film thickness within a certain thickness range; once the oxide film thickness is beyond a critical value (~138 nm in this study), cathodic limiting current density becomes independent of oxide film thickness.
- The effect of oxide film properties at ascending pre-oxidation potential on the cathodic kinetics during ORR potential range of SS304L and SS316L was investigated: for both steels, as oxidation potential increases, the amount of Cr^{3+} in oxide film initially increases from corrosion potential to 0~0.4 V_{SCE} , and then decreases with increasing potential and

oxidized to Cr^{6+} once the potential is higher than $0.63\text{V}_{\text{SCE}}$; the amount of Fe^{3+} in general increases with ascending potential; the oxide film thickness also increases with increasing potential; at transpassive potential, although film has the largest thickness but its resistivity is lowest. A higher Fe^{3+} content in the oxide film during oxidation stage will result in a larger cathodic current density due to larger Fe^{3+} -to- Fe^{2+} reduction current density during the scan in the negative potential direction, and provide more Fe^{2+} sites available for larger ORR cathodic kinetics during the scan in the reverse direction, since active Fe^{2+} site is believed to facilitate ORR. After transpassive pre-potential, SS316L has even larger cathodic current density than Pt SS304L at the same condition during the scan in the negative potential direction due to more availability of Mo^{6+} species and highest Fe^{3+} content in the oxide film, as well as lowest film resistivity and total corrosion resistance.

5.7 Acknowledgements

The financial support from Office of Naval Research (ONR) via Grants N00014-14-1-0012 and N00014-17-1-2033, Sea-Based Aviation Program, William Nickerson, Program Manager is gratefully acknowledged. Ms. Cathy Dukes from NMCF at the University of Virginia are also acknowledged for the XPS technical assistance.

5.8 References

1. F. Cui, F. J. Presuel-Moreno, and R. G. Kelly, *Corrosion Science*, **47**, 2987–3005 (2005).
2. Z. Y. Chen, F. Cui, and R. G. Kelly, *J. Electrochem. Soc.*, **155**, C360–C368 (2008).
3. Z. Y. Chen and R. G. Kelly, *J. Electrochem. Soc.*, **157**, C69–C78 (2010).
4. X. Zhang, Z. Qin, D. Zagidulin, J. J. Noël, and D. W. Shoesmith, *J. Electrochem. Soc.*, **164**, C911–C917 (2017).
5. C.A. Matzdorf, W.C. Nickerson, B.C. Rincon Troconis, G.S. Frankel, L. Li, R.G. Buchheit *CORROSION*, **69**, 1240–1246 (2013).

6. Z. Feng and G.S. Frankel, *CORROSION*, **70**, 95–106 (2013).
7. V. Rafla, A.D. King, S. Glanvill, A. Parsons, A. Davenport, J.R. Scully, *Corrosion*, **71**, 1171–1176 (2015).
8. X. G. Zhang, *J. Electrochem. Soc.*, **143**, 1472–1484 (1996).
9. X. G. Zhang and E. M. Valeriotte, *Corrosion Science*, **34**, 1957–1972 (1993).
10. A. M. Simões, A.C. Bastos, M.G. Ferreira, Y. Gonzalez-Garcia, S. Gonzalez, R.M. Souto, *Corrosion Science*, **49**, 726–739 (2007).
11. A. G. Marques, M. G. Taryba, A. S. Panão, S. V. Lamaka, and A. M. Simões, *Corrosion Science*, **104**, 123–131 (2016).
12. G. Okamoto, *Corrosion Science*, **13**, 471–489 (1973).
13. A. R. Brooks, C. R. Clayton, K. Doss, and Y. C. Lu, *J. Electrochem. Soc.*, **133**, 2459–2464 (1986).
14. D. Shintani, T. Ishida, H. Izumi, T. Fukutsuka, Y. Matsuo, and Y. Sugie, *Corrosion Science*, **50**, 2840–2845 (2008).
15. M. da Cunha Belo, M. Walls, N.E. Hakiki, J. Corset, E. Picquenard, G. Sagon, D. Noel, *Corrosion Science*, **40**, 447–463 (1998).
16. M. F. Montemor, M. G. S. Ferreira, N. E. Hakiki, and M. Da Cunha Belo, *Corrosion Science*, **42**, 1635–1650 (2000).
17. G. Lorang, M. D. C. Belo, A. M. P. Simões, and M. G. S. Ferreira, *J. Electrochem. Soc.*, **141**, 3347–3356 (1994).
18. M. Da C. Belo, B. Rondot, F. Pons, J. L. Héricy, and J. P. Langeron, *J. Electrochem. Soc.*, **124**, 1317–1324 (1977).
19. Z. Feng, X. Cheng, C. Dong, L. Xu, and X. Li, *Corrosion Science*, **52**, 3646–3653 (2010).
20. A. Kocijan, Č. Donik, and M. Jenko, *Corrosion Science*, **49**, 2083–2098 (2007).
21. N. Le Bozec, C. Compere, M. L'Her, A. Laouenan, D. Costa, and P. Marcus, *Corrosion Science*, **43**, 765–786 (2001).
22. W. P. Yang, D. Costa, and P. Marcus, *J. Electrochem. Soc.*, **141**, 111–116 (1994).
23. W. P. Yang, D. Costa, and P. Marcus, *J. Electrochem. Soc.*, **141**, 2669–2676 (1994).
24. S. V. Phadnis, A. K. Satpati, K. P. Muthe, J. C. Vyas, and R. I. Sundaresan, *Corrosion Science*, **45**, 2467–2483 (2003).

25. V. S. Raja, A. Devasenapathi, P. Veluchamy, and H. Minoura, *CORROSION*, **55**, 1119–1126 (1999).
26. H. S. Wroblowa, Yen-Chi-Pan, and G. Razumney, *Journal of Electroanalytical Chemistry and Interfacial Electrochemistry*, **69**, 195–201 (1976).
27. S. Zečević, D. M. Dražić, and S. Gojković, *Journal of Electroanalytical Chemistry and Interfacial Electrochemistry*, **265**, 179–193 (1989).
28. V. Jovancicevic and J. O. Bockris, *J. Electrochem. Soc.*, **133**, 1797–1807 (1986).
29. E. J. Calvo and D. J. Schiffrin, *Journal of Electroanalytical Chemistry and Interfacial Electrochemistry*, **243**, 171–185 (1988).
30. S. L. Gojković, S. K. Zečević, M. D. Obradović, and D. M. Dražić, *Corrosion Science*, **40**, 849–860 (1998).
31. T. D. Burleigh and A. T. Smith, *J. Electrochem. Soc.*, **138**, L34–L35 (1991).
32. M. A. Heine and M. J. Pryor, *J. Electrochem. Soc.*, **110**, 1205–1214 (1963).
33. C. D. Wagner, *Handbook of X-ray Photoelectron Spectroscopy: A Reference Book of Standard Data for Use in X-ray Photoelectron Spectroscopy*, p. 208, Perkin-Elmer, (1979).
34. H. Luo, C. F. Dong, K. Xiao, and X. G. Li, *Applied Surface Science*, **258**, 631–639 (2011).
35. R.-H. Jung, H. Tsuchiya, and S. Fujimoto, *Corrosion Science*, **58**, 62–68 (2012).
36. M. Cohen, D. Mitchell, and K. Hashimoto, *J. Electrochem. Soc.*, **126**, 442–444 (1979).
37. Č. Donik, D. Mandrino, and M. Jenko, *Vacuum*, **84**, 1266–1269 (2010).
38. I. Nicic and D. D. Macdonald, *Journal of Nuclear Materials*, **379**, 54–58 (2008).
39. B. Hirschorn et al., *J. Electrochem. Soc.*, **157**, C458–C463 (2010).
40. M. Stratmann and J. Müller, *Corrosion Science*, **36**, 327–359 (1994).

6. The Effect of Geometric Parameters on the Extent of Localized Corrosion of AA7050-T7451 Galvanically Coupled to SS316L Fastener

Summary:

As introduced earlier in Section 1.2.3, the fastener-hole configuration involves a galvanic coupling induced crevice between SS fastener and AA7050 based component. The geometric parameters such as area ratio of cathode to anode, and crevice geometry (crevice length and width) can also have a significant impact on the extent of localized corrosion along AA7050 in the crevice. For cathode-to-anode area ratio, a great number of previous research studies have been performed to investigate the galvanic corrosion between two dissimilar materials as a function of area ratio quantitatively, but mainly focused on simply geometry in which the exposure surfaces of anode and cathode are connected in a flush manner. As for crevice geometry, little or no previous work has been investigated for the crevice formed inside a galvanic coupling, let alone a quantitative description of the extent of galvanic-coupling induced crevice corrosion as a function of crevice geometric parameters. The study scope in this chapter has two objectives: (1) to investigate the electrochemical and corrosion distributions in the crevice formed in galvanic coupling between AA7050 and SS316L as a function of cathode-to-anode area ratio experimentally and numerically; (2) to explore the effect of crevice geometry on the galvanic-coupling induced crevice corrosion of AA7050, and examine if the typical crevice scaling law is also valid for the crevice between the galvanic couple.

6.1 Abstract

Geometry of galvanic couple is of great importance to affect the electrochemical and corrosion distributions inside. In this chapter, two pertinent geometric parameters were investigated: cathode-to-anode area ratio and crevice geometry. For the area ratio, a combined

modeling and experimental approach was developed to investigate its effect on the crevice corrosion of AA7050 with a galvanic-coupling induced crevice configuration. It has been found that: higher area ratio ($>1:1$) geometry leads to more severe corrosion focused at the crevice mouth, resulting in larger potential and pH variation from crevice center to mouth as well as higher anodic current density; lower area ratio ($1:1$) shows very limited corrosion and little to no change in electrochemical and pH distributions.

For the crevice geometry, the effect of electrolyte layer thickness (WL) above the external SS cathode surface, crevice solution chemistry and crevice wall conditions on the crevice scaling law were investigated by developing a thorough modeling study combining pertinent external variables discussed in previous chapters, and whether or not the scaling law can be held in galvanic-coupling induced crevice was also examined. From this study, it shows that the validity of scaling law depends on the crevice solution chemistry and internal cathode wall condition; L_{crit}^2/G is more applicable to galvanic-coupling induced crevice than L_{crit}/G , but L_{crit}^2/G varies with WL and internal SS wall condition.

6.2 Hypothesis

For the aspect of the area ratio, larger cathode: anode ratio results in more corrosion damage, and the corrosion damage is preferably located at the SS/AA interface and then decays as the distance moves away from the interface due to ohmic drop.

As for the crevice geometry, crevice scaling law can be still held for galvanic coupling induced crevice, and the ratio value is constant regardless of changes in external variables (e.g., WL, crevice solution chemistry and crevice wall condition).

6.3 Part 1: Effect of Cathode-to-Anode Area Ratio on Potential, Current and pH Distribution in the Crevice Formed in Galvanic Coupling Between AA7050-T7451 and SS316L

6.3.1 Introduction:

The study of galvanic corrosion of aerospace aluminum alloys is of great importance due to frequent interaction between Al-alloy based structure and noble component such as noble fastener. The galvanic coupled Al-alloy based structure can experience an accelerated localized corrosion rate compared to self-corrosion without galvanic interaction, since external cathode current from noble materials can greatly support dissolution activity of Al-alloy. The degree of galvanic corrosion damage can be dictated by many factors, one of them is area ratio of cathode to anode.

Mansfeld and his co-workers^{1,2} developed a careful study of area relationships in galvanic corrosion between Al alloys (AA2024 and AA7075) and copper in 3.5% NaCl solution, and generalized an analytical expression of dissolution rate (r_A) of these Al alloys as

$$r_A = k_3 i_g^A \left(1 + \frac{A^C}{A^A}\right)$$

where k_3 is constant, i_g^A is galvanic current density, $\frac{A^C}{A^A}$ is cathode-to-anode area ratio. A similar expression was also proposed by Liao *et al.*³, in which they investigated the dependence of galvanic-coupling induced pitting on area ratio between model alloys representing two types of intermetallic compounds (IMCs) in Al alloys and pure Al. However, their expression of dissolution rate is based on the average galvanic current density across the entire anode surface, which might be valid for the area in the vicinity of galvanic couple interface or the entire galvanic assembly is fully immersed in solution, but not always true for scenario involving a galvanic assembly under

a thin layer of electrolyte, in which ohmic drop in electrolyte can lead to variation in dissolution rate along the surface. Song and his co-workers^{4,5} used both multi-electrode galvanic corrosion assembly (GCA) technique and boundary element method simulation tool to study the galvanic corrosion between magnesium and steel as a function of area ratio, and they indicated that the highest galvanic corrosion current density appeared at the interface, and then decayed quickly to zero within 1 to 2cm away from the interface, and highest galvanic corrosion current density at the interface can be intensified as cathode-to-anode area ratio increased. Nevertheless, all of these previous works only focused on the geometry in which the anode was simply connected to the cathode with a flush surface, there is little or no research study by far investigating the dependence of galvanic-coupling induced localized corrosion on the area ratio with a crevice geometry between two dissimilar materials.

The objective of Part 1 in this chapter is to use a complementary numerical and experimental approach to study how the area ratio of cathode to anode affects potential, current density and pH distribution within a simulated crevice formed between SS316L cathode and AA7050-T7451 anode, and determine the correlation between area ratio and galvanic corrosion distribution quantitatively.

6.3.2 Experimental Approaches

6.3.2.1 Preparation of Crevice Formed Between SS316L and AA7050-T7451

Crevice assemblies between SS316L and AA7050-T7451 are illustrated in Figure 6.1. Each AA7050 sample had a fixed surface area of 1" x 1" and was embedded in epoxy. For the SS316 samples, all the surfaces of each sample were exposed. Observing from top view (Figure 6.1b), the width and thickness of SS plate was fixed at 1" and 1/4" respectively, and the length was varied in a way such that the area ratio of SS316 to AA7050 changed from 1:1 to 8:1. The galvanic

couples were assembled together by electrically isolated SS316L fasteners (Figure 6.1c), leaving the crevice gap width formed in between around 150~200 μm as measured by scanning electron microscope (SEM). All of the crevice assemblies were full immersed into 0.6M NaCl solutions for up to 8 weeks, and pH distributions and localized corrosion damages were measured afterwards.

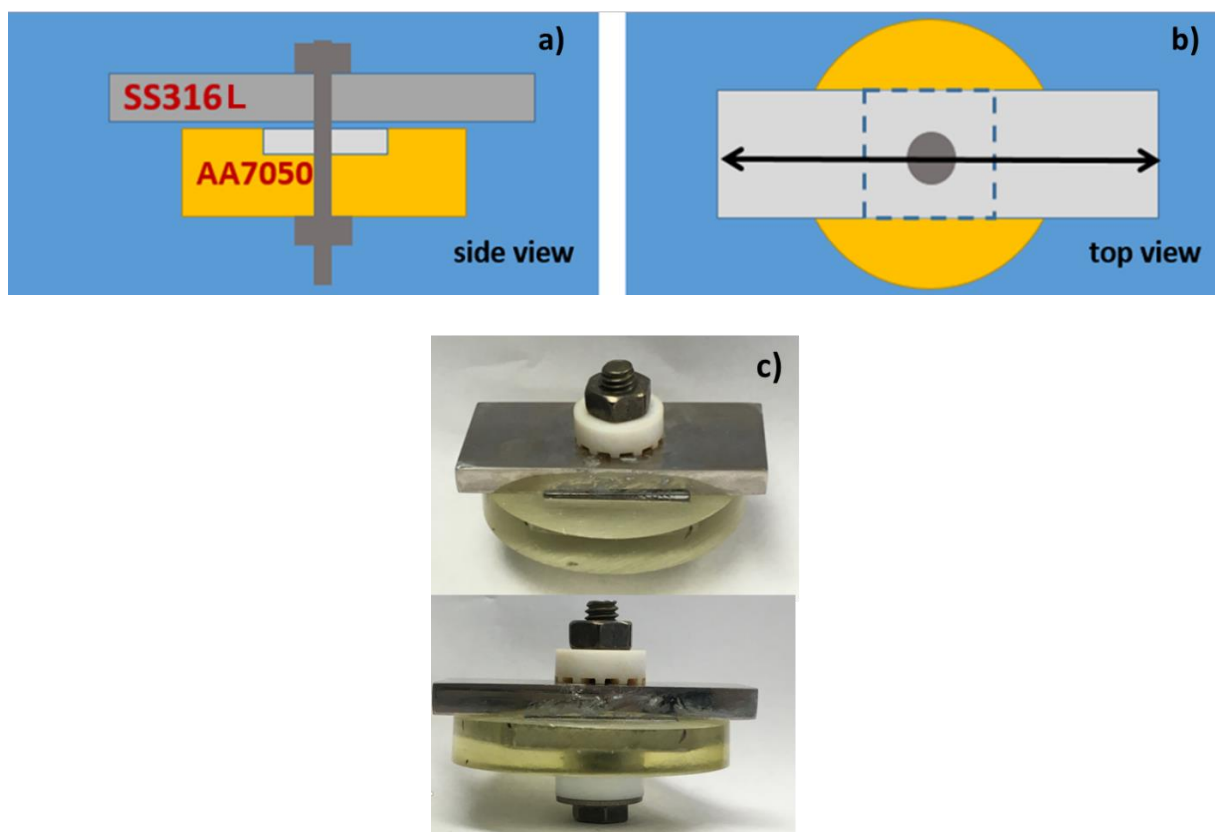


Figure 6.1: A schematic representation of crevice assembly between AA7050 and SS 316L from a) side view and b) from top view, and c) snapshot of testing crevice assembly.

6.3.2.2 Electrochemical Kinetics Measurement for Boundary Condition in FEM Modeling

SS316L, AA7050-T7451 and 99.9%wt pure Cu were used in electrochemical kinetics measurement. They were prepared into 1" x 1" square coupons and grounded to a surface finish of 600 grit with silicon carbide paper. All the electrochemical measurements were conducted using a Bio-Logic™ SP200 potentiostat in a three-electrode cell configuration with test coupon as the working electrode (WE, exposure area=1cm²), a platinum-niobium mesh as the counter electrode

(CE), and a saturated calomel electrode (SCE) as the reference electrode (RE). Potentiodynamic polarization measurements were performed at a scan rate= 0.167 mV/s after 1-hour open circuit potential (OCP) stabilization, starting from 0.1V above OCP and ending at -1.8 V_{SCE}. Three types of testing solutions were prepared for polarization curve measurements: (1) deaerated 0.5M NaCl with adjusted pH=4 by HCl to simulate the most occluded region within the crevice; (2) deaerated 0.5M NaCl with adjusted pH=8 by NaOH to simulate the near-crevice mouth region; (3) 0.5 M NaCl with unadjusted pH=5.6 to simulate bulk solution. These experimentally determined electrochemical kinetics were used as boundary conditions in the modeling.

6.3.2.3 Secondary Current Distribution Model to Simulate Electrochemical Distribution in Crevice

a 3-D steady state secondary current distribution module in COMSOLTM Ver.5.2 was applied to simulate potential and current density distributions in the crevice, the governing equation is Laplace's Equation. The modeling geometry used is shown in Figure 6.2. The simulation domain is electrolyte with constant electrolyte conductivity 5.5 S/m. It should be noticed that electrochemical kinetics in either quiescent or de-aerated solution with different pH were enforced on corresponding parts in order to simulate the realistic crevice solution environment.

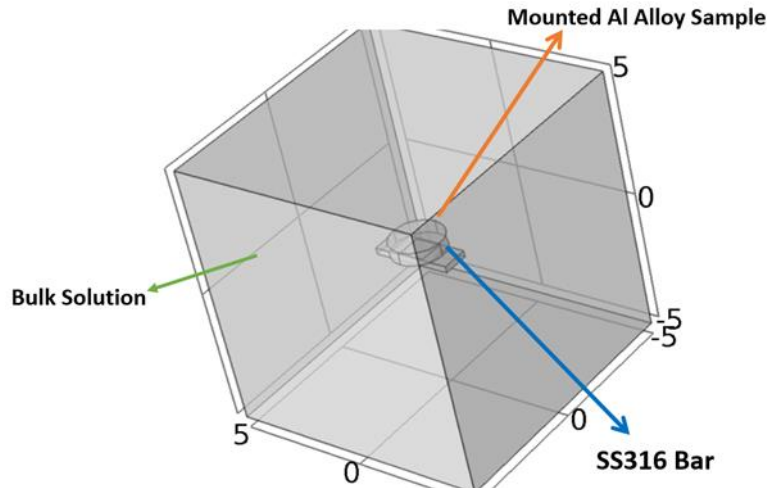


Figure 6.2: Geometry Setup of Crevice Assembly in COMSOL™.

6.3.3 Results and Discussions

6.3.3.1 pH Distribution and Corrosion Damage as a Function of Area Ratio from 8-week Immersion Test.

The pH and corrosion damages were measured after the 8-week full immersion exposure. Figure 6.3 shows pH distributions in the crevice for case of area ratio=1:1 and 8:1. In the case of area ratio=1:1, the pH was around 6~7 for most of the area of the crevice, except for pH=8 in some localized regions. When the area ratio increased to 8:1, the pH was between 7 and 8 along the edges of crevice mouth, and pH ranged from 4 to 5 inside the crevice. Optical profilometry was used to obtain corrosion damage profiles. Maximum damage from the profilometry was measured to characterize the effect of area ratio on corrosion damage, e.g., the maximum damage for area ratio=8:1 shown in Figure 6.4. From comparison of maximum corrosion depth for different area ratios in Figure 6.5, it can be seen that increasing area ratio of cathode to anode caused more severe corrosion damage, and maximum corrosion depth for area ratio=8:1 ($\sim 750 \mu\text{m}$) was about 50 times that for area ratio=1:1 ($\sim 15 \mu\text{m}$).

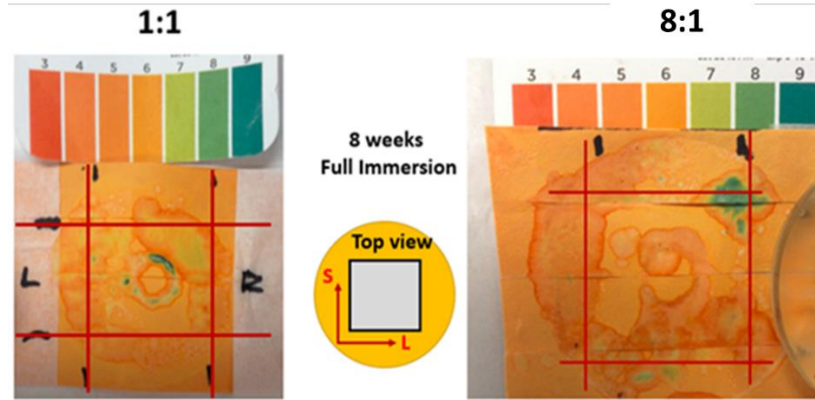


Figure 6.3: pH distribution in the crevice for area ratio =1:1 and 8:1 after 8-week testing.

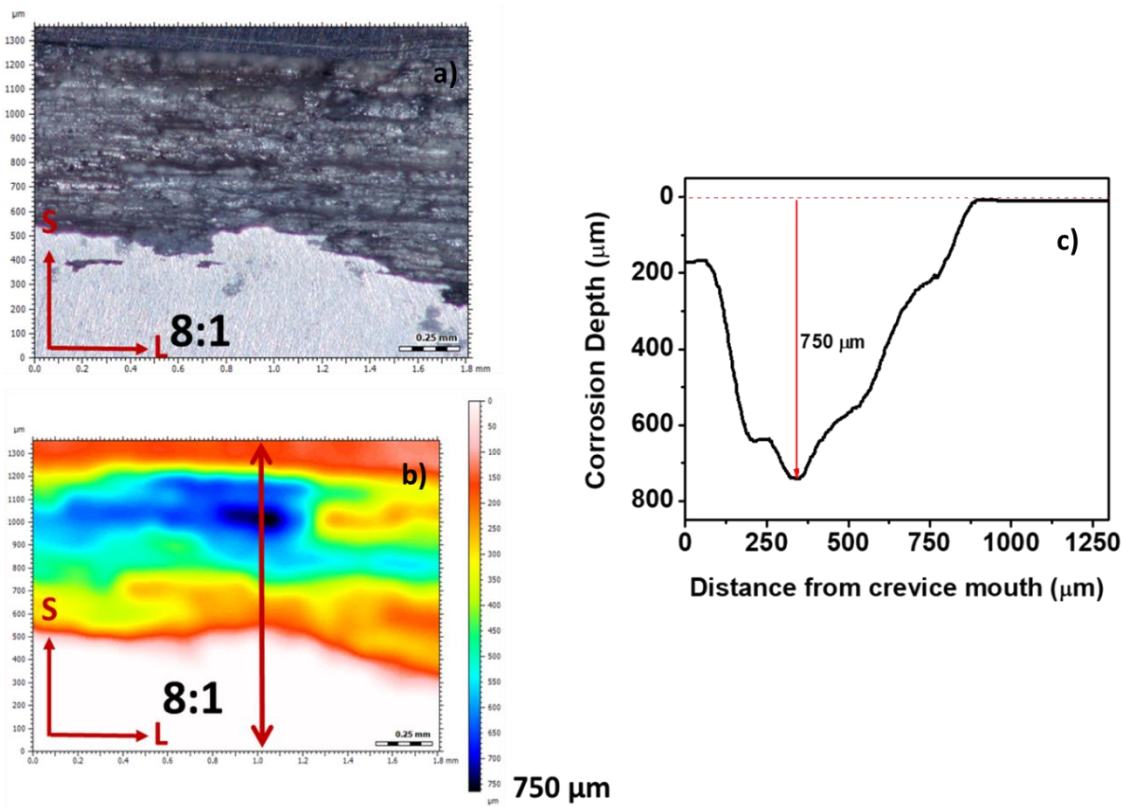


Figure 6.4: a) Optical profilometry of corrosion distribution around the crevice mouth when area ratio=8:1; b) False color expression of a); c) Corrosion depth profile along the direction in b).

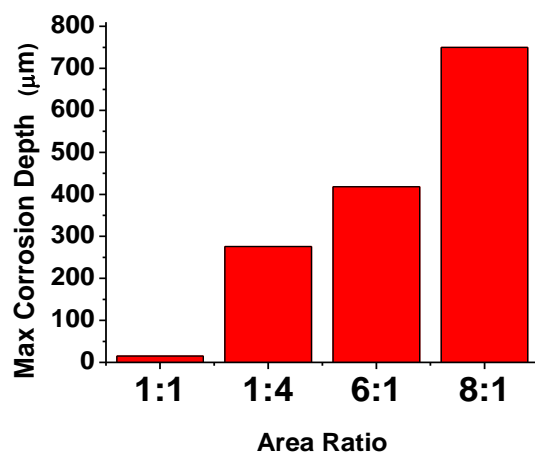


Figure 6.5: Comparison of maximum corrosion depth for area ratio ranging from 1:1 to 8:1

6.3.3.2 Electrochemical Distribution as a Function of Area Ratio from Modeling Study

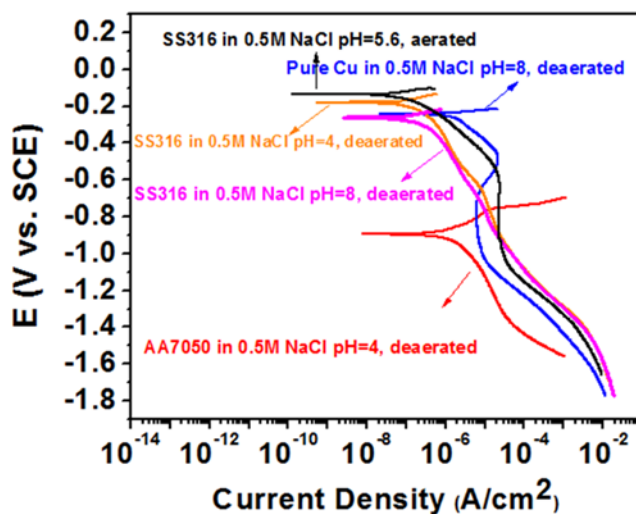


Figure 6.6: Boundary conditions used in the modeling study.

Electrochemical kinetics of AA7050, SS316L and Cu in pertinent solutions representative of different crevice solution environments are displayed in Figure 6.6. It should be noted here that de-aerated condition was enforced within the crevice while the quiescent condition was enforced outside the crevice, and different pH values were imposed in accordance with the pH distributions for different area ratios in experimental part. The effect of replated copper from corrosion had been

also considered into modeling because copper replating just outside the crevice was observed when the area ratio was $>1:1$ (shown in Figure 6.7), the main source of replated Cu is Cu remnant after dealloying of Mg and Al from Cu-containing IMCs (e.g., Al_2CuMg). Once the Cu remnant is mechanically detached and dissolved at its corrosion potential, it will replate on the Al-alloy again^{6,7} Figure 6.8 shows the locations of different boundary conditions on AA7050 and SS316L, respectively.

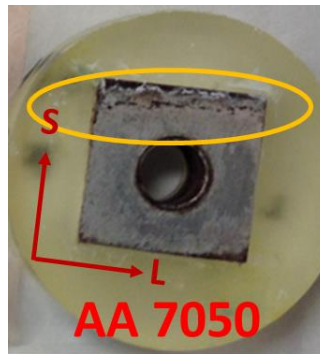


Figure 6.7: An example to show Cu (within the yellow circle) replated on AA7050 after 8-week immersion testing when area ratio of cathode to anode is 8:1.

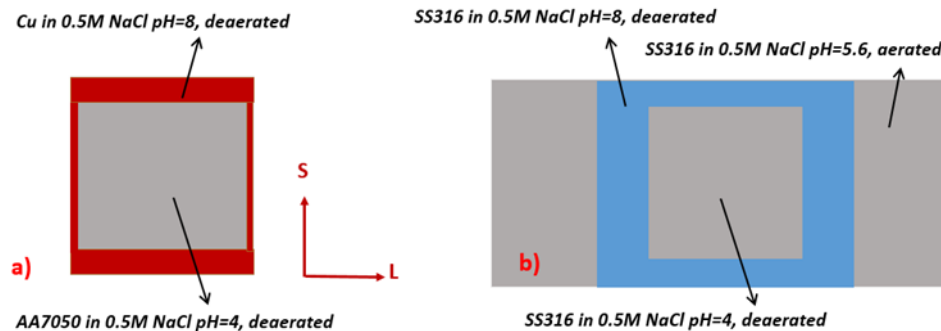


Figure 6.8: Boundary conditions setup for a) AA7050 side; b) SS316L side.

Outputs from the modeling are potential and current density distributions. Potential distributions for different area ratios are displayed in Figure 6.9. It can be clearly seen that higher area ratio led to larger potential difference from the center of the crevice to the mouth. For current density distributions in Figure 6.10, the anodic current density increased as a function of both

distance from the crevice center and area ratio. In order to quantitatively describe corrosion damage, comparisons between different area ratios were made in terms of ratio of the maximum anodic current density from the modeling and that of maximum corrosion depth from the experiment shown in Table 6.1. It indicates that the modeling captures relative severity of attack from the experiment.

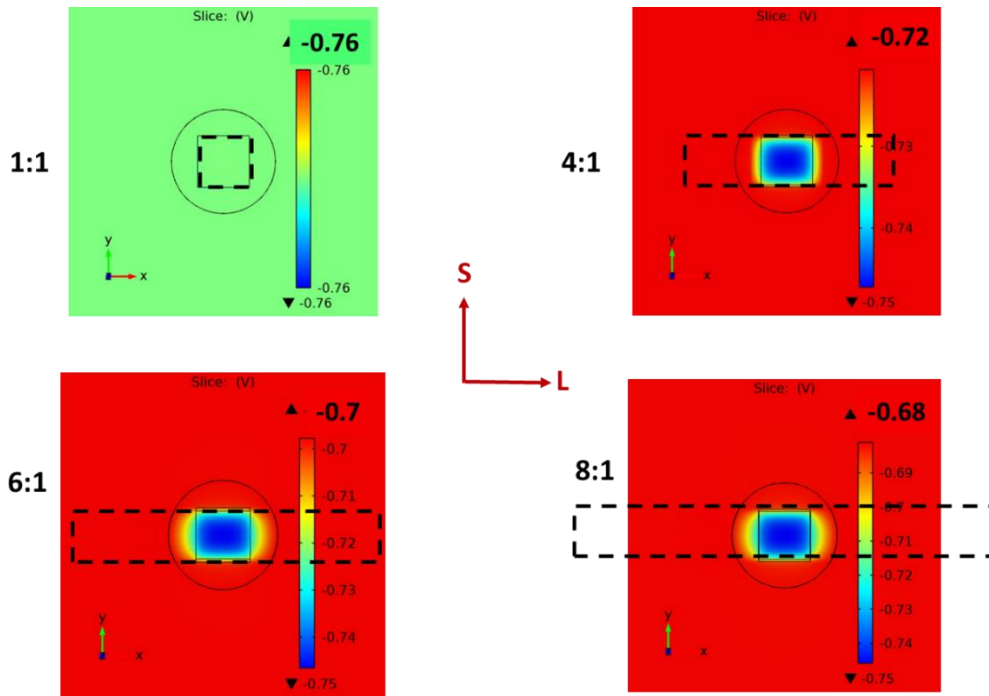


Figure 6.9: Comparison of potential distributions for different area ratios.

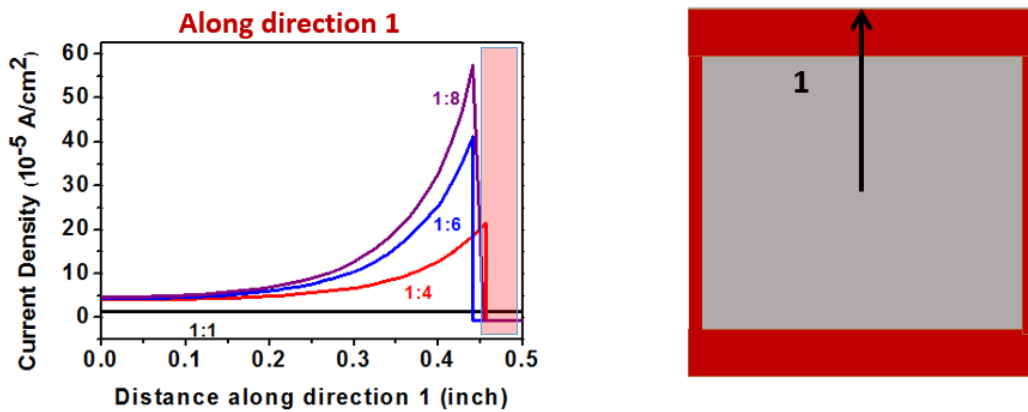


Figure 6.10: Current density vs. distance along the direction 1 as a function of area ratio.

Table 6.1: Comparison between different area ratios in terms of ratio of max anodic current density (from modeling) and maximum corrosion depth (from measurement)

	Ratio of Max Anodic i	Ratio of Max Corr. Depth
8:1 vs. 4:1	2.75	2.72
6:1 vs. 4:1	1.89	1.53

6.3.4 Conclusions

From this study of localized corrosion distribution within the galvanic-coupling induced crevice, it can be concluded that: (1) higher area ratio (>1:1) geometry leads to more severe corrosion focused at the crevice mouth, resulting in larger potential and pH variation from crevice center to mouth as well as higher anodic current density; (2) lower area ratio (1:1) shows very limited corrosion and little to no change in electrochemical and pH distributions.

6.4 Part 2: A Modeling Study of Exploring the Scaling Law in the Galvanic-Coupling Induced Corrosion of AA7050-T7451

6.4.1 Introduction

Scaling law or scaling factor is one important criterion to describe the effect of crevice geometry on the electrochemical and corrosion distributions in the crevice during crevice corrosion propagation. It can help determine the geometry condition in which the crevice corrosion can occur for an engineering alloy. Since the dimension of a typical crevice is generally on the order of millimeters in crevice length and microns in crevice gap width, it is of great difficulty to reproduce this dimension experimentally, a scaling law has come up to scale up this dimension to a

measurable size. The scaling law¹¹ describes how the crevice geometry can be scaled such that the electrochemical and corrosion distributions remain constant on a normalized length scale. For instance, if crevice corrosion attack takes place at 1 mm inside a crevice with 1 cm length, for the same material with larger crevice length equal to 10 cm, the corresponding corrosion attack will happen at 10 mm. Diffusion barrier to relevant chemical species due to confined crevice geometry as well as large crevice solution ohmic resistance are main causes to the existence of scaling law. In general, scaling law can be expressed as a ratio containing two pertinent crevice geometric parameters

$$\text{scaling law} = \frac{L^2}{G} \text{ or } \frac{L}{G}$$

where G is the crevice gap width, and L can be either the total crevice length^{8,9}, or distance from the crevice mouth to the site which receives the most severe attack in the crevice¹⁰. Particularly for the latter case, the scaling law is still valid even the rest of crevice is active beyond the most severe attack site, and L can be also described as x_{crit} . A Schematic representation of crevice geometry is illustrated in Figure 6.11.

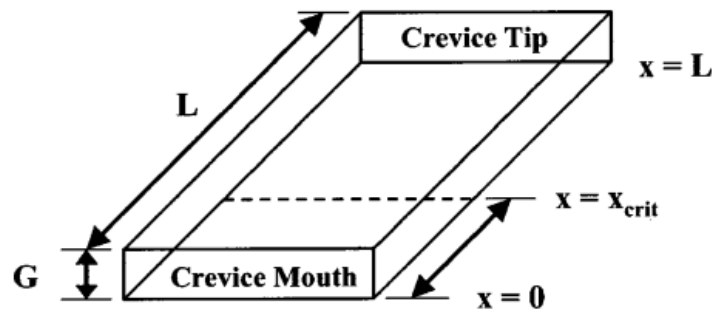


Figure 6.11: A schematic representation of a generic crevice geometry involving two pertinent crevice geometric parameters¹².

Both Lee *et al.*¹² and Vankeerberghen¹³ explored the effect of crevice geometry on the susceptibility of a crevice to crevice corrosion by investigating the existence and form of a scaling

factor that related depth and gap to susceptibility. Lee *et al.* combined FEM modeling and experimental methods to rigorously study the most two commonly proposed scaling laws: x_{crit}/G and x_{crit}^2/G , where x_{crit} is d_c referred by Xu and Pickering¹⁴. Microfabrication method was used to construct crevice formers of rigorously controlled dimensions. This method was used in crevice corrosion experiments on Ni200 in 0.5 M H₂SO₄ to measure x_{crit} . A two-dimensional steady state FEM modeling based on the Laplace Equation was used in this work. A comparison of the two scaling laws x_{crit}/G and x_{crit}^2/G is displayed in Figure 6.12. From these comparisons, it was concluded that a quadratic scaling factor (x_{crit}^2/G) was more applicable to the Ni/H₂SO₄ crevice system, with the result most apparent at short times and small gaps. This was also the same scaling factor for Al crevice in 0.05 M NaCl demonstrated by Vankeerberghen's work¹³. The model also reproduced the experimentally observed failure of the scaling law at large gaps where the x_{crit} was located at much greater depths than would be expected from the scaling law.

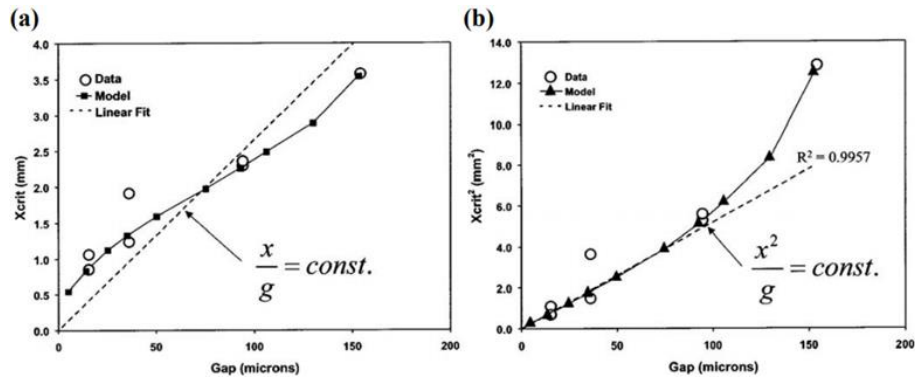


Figure 6.12: Comparison of modeling and experimental results for Ni200 in 0.5M H₂SO₄: a) for linear scaling law; b) quadratic scaling law¹².

However, most of previous research for crevice corrosion only focused on the crevice of same material formed by an inert crevice former, there is little or no research effort on the crevice formed between a galvanic coupling. In general, a typical galvanic coupling assembly does not always physically contact with one surface flush with the other, the geometry can be very complicated. In this study, a noble stainless steel fastener is galvanically coupled with an

aluminum alloy (Al alloy) based plate with a fastener-hole configuration displayed in Figure 1.1 and Figure 1.2. The localized corrosion of Al alloy in the crevice can be sustained by both cathode current from external SS cathode due to ORR, and that from internal SS cathode in the crevice due to either ORR or HER or combined. In this study, the effect of electrolyte layer thickness (WL) above the external SS cathode surface, crevice solution chemistry and crevice wall conditions on the crevice scaling law were investigated by developing a thorough modeling study combining pertinent external variables discussed in previous chapters, and whether or not the scaling law can be held in galvanic-coupling induced crevice was also examined.

6.4.2 Experimental Approaches

6.4.2.1 Electrochemical Kinetics Determination for Boundary Conditions in Modeling

SS316L and AA7050-T7451 were used in electrochemical kinetics measurement. They were prepared into 1" x 1" square coupons and ground to a surface finish of 600 grit with silicon carbide paper. All the electrochemical measurements were conducted using a Bio-LogicTM SP200 potentiostat in a three-electrode cell configuration with test coupon as the working electrode (WE, exposure area=1cm²), a platinum-niobium mesh as the counter electrode (CE), and a saturated calomel electrode (SCE) as the reference electrode (RE). Potentiodynamic polarization measurements were performed at a scan rate= 0.167 mV/s after 1-hour open circuit potential (OCP) stabilization. For SS 316L the scan started from OCP and ended at -1.2 V_{SCE}, whereas the scan for AA7050 started from -1.1 V_{SCE} and ended at -0.55 V_{SCE}. Besides regular flat cell configuration to measure electrochemical kinetics of SS316L in quiescent solution, rotating disk electrode technique which setup has been explained in Chapter 3 was also utilized to simulate the electrochemical kinetics of SS316L in thin film electrolyte condition, two rotation speeds 10 and 40 rpm were applied to simulate electrolyte layer thickness equal to 200 and 100 μm respectively.

Three types of testing solution were prepared for polarization curve measurements: (1) quiescent and agitated 0.6M NaCl with adjusted pH=10 by NaOH for SS316L to represent solution environment under different WL thickness for external SS cathode; (2) deaerated 0.6M NaCl with adjusted pH=4 by HCl to simulate crevice solution environment for SS316L and AA7050, the selection of pH=4 was based on the experimental determination by Alavi and Cottis¹⁵ when they measured the pH of crevice solution formed in AA7475; (3) 0.54M +0.02M AlCl₃ with adjusted pH=4 to simulate Al³⁺ containing crevice solution environment for SS316L and AA7050 due to Al alloy dissolution, the [Al³⁺]=0.02 M was chosen from Vankeerberghen¹³'s work for Al crevice corrosion. These experimentally determined electrochemical kinetics were used as boundary conditions in the modeling.

6.4.2.2 FEM Modeling Setup

An axisymmetric 2-D steady state secondary current distribution module in COMSOL™ Ver.5.2 was applied to simulate potential and current density distributions in the crevice, the governing equation was Laplace's Equation. The simulation domain was electrolyte with constant electrolyte conductivity=5.5 S/m. The generic modeling geometry used is shown in Figure 6.13. A conformal electrolyte layer (WL) was applied along the external surface of galvanic coupling. Dimension of half of SS316L fastener (axisymmetry) is assigned in this figure. The plate thickness T_{plate} , the crevice gap width (G), and WL were variables in the modeling. As for boundary condition assignment, black boundary represents external SS cathode, green one represents internal SS cathode, red one represents AA in the crevice, the yellow one represents electrically isolated corrosion coating. It should be noted that the coating thickness was negligible in this modeling work. Four different cases were investigated in the study with boundary condition

assignment illustrated in Table 6.2. In the simulation, parametric sweep was performed in the following way: T_{plate} from 10 mm to 40 mm, G from 10 to 100 μm , and WL from 2,000 to 100 μm .

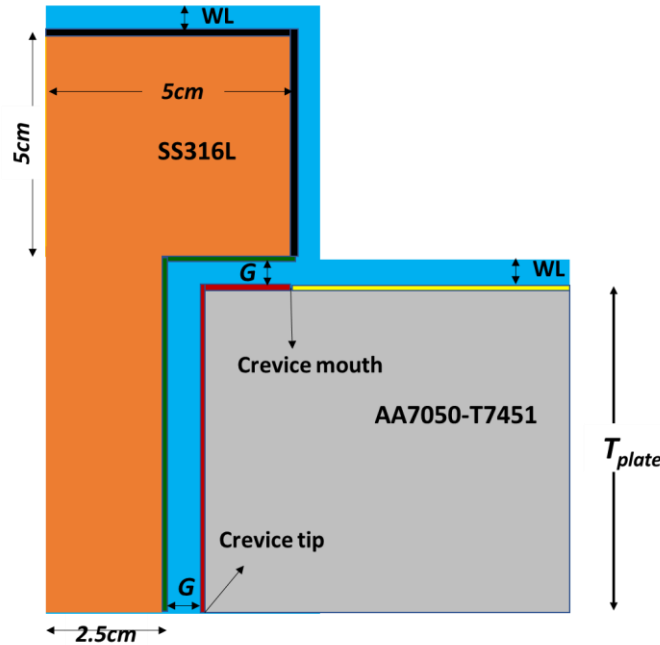


Figure 6.13: A schematic geometry of axisymmetric galvanic coupling between SS316L fastener and AA7050-T7451 plate in the modeling.

Table 6.2: Boundary condition assignments for four different modeling case studies.

Case #	Boundary Description	Boundary Condition Assignments
1	No Al^{3+} containing crevice solution, passive SS crevice wall	Black: 0.6 M NaCl (pH=10) Green: electrically insulated Red: 0.6M NaCl (pH=4) Yellow: electrically insulated
2	No Al^{3+} containing crevice solution, active SS crevice wall	Black: 0.6 M NaCl (pH=10) Green & Red: 0.6M NaCl (pH=4) Yellow: electrically insulated
3	Al^{3+} containing crevice solution, passive SS crevice wall	Black: 0.6 M NaCl (pH=10) Green: electrically insulated Red: 0.6M NaCl (pH=4) Yellow: electrically insulated
4	Al^{3+} containing crevice solution, active SS crevice wall	Black: 0.6 M NaCl (pH=10) Green & Red: 0.54M NaCl+0.02M AlCl_3 (pH=4) Yellow: electrically insulated

6.4.3 Results and Discussions

6.4.3.1 Electrochemical Kinetics of SS316L and AA7050 in Different Solution Environments

Measured electrochemical kinetics of SS 316L and AA7050-T7451 in different solutions are shown in Figure 6.14a. For AA7050-T7451, although addition of Al^{3+} increased E_{corr} by 0.02 V compared to that in no Al^{3+} containing solution at the same pH and $[Cl^-]$, the breakdown potential ($E_{crit} \approx -0.75 V_{SCE}$, below which AA7050 becomes passive) and corresponding current density ($i_{crit} \approx 2.5E-6 A/cm^2$, highest passive current density) were nearly identical, together with same anodic kinetics beyond E_{crit} . For SS316L, as electrochemical kinetics obtained from RDE both had higher cathodic limiting current density (i_{lim}) than quiescent condition in 0.6M NaCl pH=10 solution, and i_{lim} increased with higher rotation speed (smaller WL) due to shorter diffusion path of dissolved oxygen which has been discussed in Chapter 3. When solution was deaerated and acidified to pH=4, the i_{lim} was reduced by ~100 times compared to alkaline, quiescent solution, owing to greatly depressed ORR cathodic kinetics and weak HER cathodic kinetics at pH=4; By adding Al^{3+} while still maintaining same $[Cl^-]$ and pH in the solution, cathodic kinetics of SS316L was greatly enhanced due to extremely high proton diffusivity in Al^{3+} containing solution discussed in Chapter 4. It should be noted that the pH assumption for the crevice solution in this study is different from Part 1 in Chapter 4 in which alkaline crevice solution was assumed in the most occluded region. These experimentally determined electrochemical kinetics were used as boundary conditions in the modeling. Boundary conditions for Case 1&2 and those for Case 3&4 are shown in Figure 6.14b and 6.14c respectively. Based on Mixed Potential Theory, it can be seen that galvanic coupling potential between AA7050 and external SS cathode ($E_{galv,ext}$) was highest, followed by E_{crit} and then galvanic coupling potential between AA 7050 and internal SS cathode ($E_{galv,int}$) in Case 1&2, whereas potentials followed this order in case 3&4: $E_{galv,int} > E_{galv,ext} > E_{crit}$.

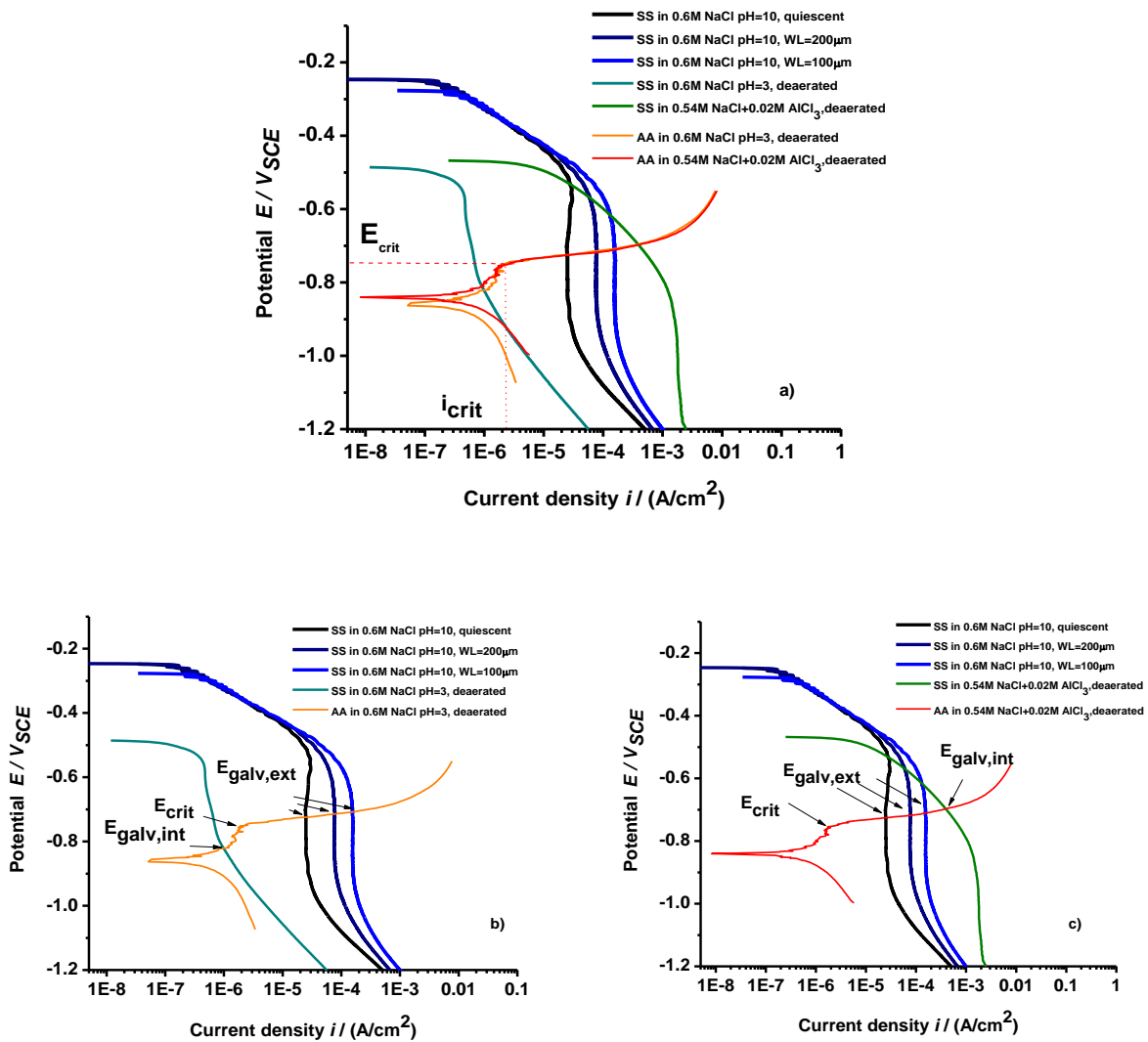


Figure 6.14: a) Electrochemical kinetics of SS316L and AA7050-T7451 in different solutions; b) boundary conditions in Case 1&2; c) boundary conditions in Case 3&4.

6.4.3.2 Example to Show the Effect of Gap Width (G) on Electrochemical Distribution

This example is to illustrate the effect of crevice gap width (G) on potential and current density distributions along the AA7050 in the crevice. Geometry setup in this example was: $T_{plate}=10\text{mm}$, $WL=1000\ \mu\text{m}$, G varied from 10 to 100 μm . Boundary conditions were those in Case 1 in which internal SS crevice wall was passive. Potential and anodic current density distributions along the AA in the crevice are shown in Figure 6.15.

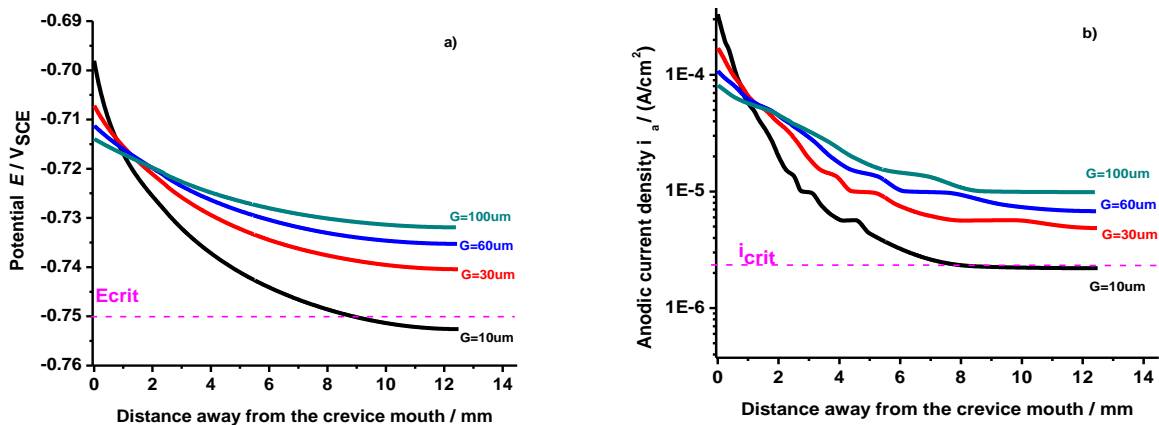


Figure 6.15: a) Potential distributions and b) anodic current density distributions along the AA7050 in the crevice as a function of G when $T_{plate}=10$ mm and $WL= 1000 \mu m$ in Case 1: internal passive SS wall.

From these comparisons, it can be seen that smaller G led to a more positive potential (higher anodic dissolution current density) at the crevice mouth and a more negative potential and (lower anodic dissolution current density) at the tip, resulting in a wider potential distribution. This phenomenon was caused by higher ohmic drop across the crevice solution due to smaller gap width. It is also noticed that at this geometric configuration, the entire crevice was active when $G \geq 30 \mu m$, whereas it became partially passive for the crevice location beyond 9.5 mm away from the crevice mouth at $G = 10 \mu m$, based on the E_{crit} .

6.4.3.3 Effect of Electrolyte Layer Thickness (WL) and SS Crevice Wall Condition on Electrochemical Distributions Without Al^{3+}

The effect of electrolyte layer thickness on the potential and current density distributions for Case 1 and Case 2 are demonstrated in Figure 6.16. The geometry setup in this section is: $T_{plate} = 20$ mm, $G= 50 \mu m$ and WL changed from 2000 μm down to 100 μm . Firstly, modeling results for both potential and current density distributions were nearly identical when $WL \geq 1000 \mu m$ for both cases, hence those for $WL= 1000 \mu m$ were used only instead of showing repetitive results for

any WL larger than 1000 μm . It can be seen from Figure 6.16 that smaller electrolyte thickness resulted in more positive potential (higher anodic current density) at both crevice mouth and tip in Case 1 where internal SS crevice wall was fully passive, this can be explained by higher $E_{\text{galv,ext}}$ and larger galvanic current density at the crevice mouth resulted from enhanced ORR cathodic kinetics at smaller WL. For Case 2, at the crevice mouth, smaller WL led to more positive potential and higher anodic current density like Case 1, however, at the crevice tip, smallest WL (100 μm) had the most negative and lowest anodic current density among all the WLs. The pertinent discussion will be presented in Section 6.4.3.4. By comparing potential and current density at the same WL between Case 1 and Case 2, it can be seen that Case 2 which had internal active SS wall, led to more positive potential and higher anodic current density than Case 1 which had passive SS wall in the near-crevice tip region (which distance away from the crevice mouth was beyond $\sim 15\text{mm}$). This can be explained by the fact that more cathode current from internal active SS wall to sustain crevice corrosion of AA7050 in Case 2 besides that from external SS cathode, resulting in higher anodic dissolution current along AA7050 compared to the cathode current only from external SS cathode in Case 1.

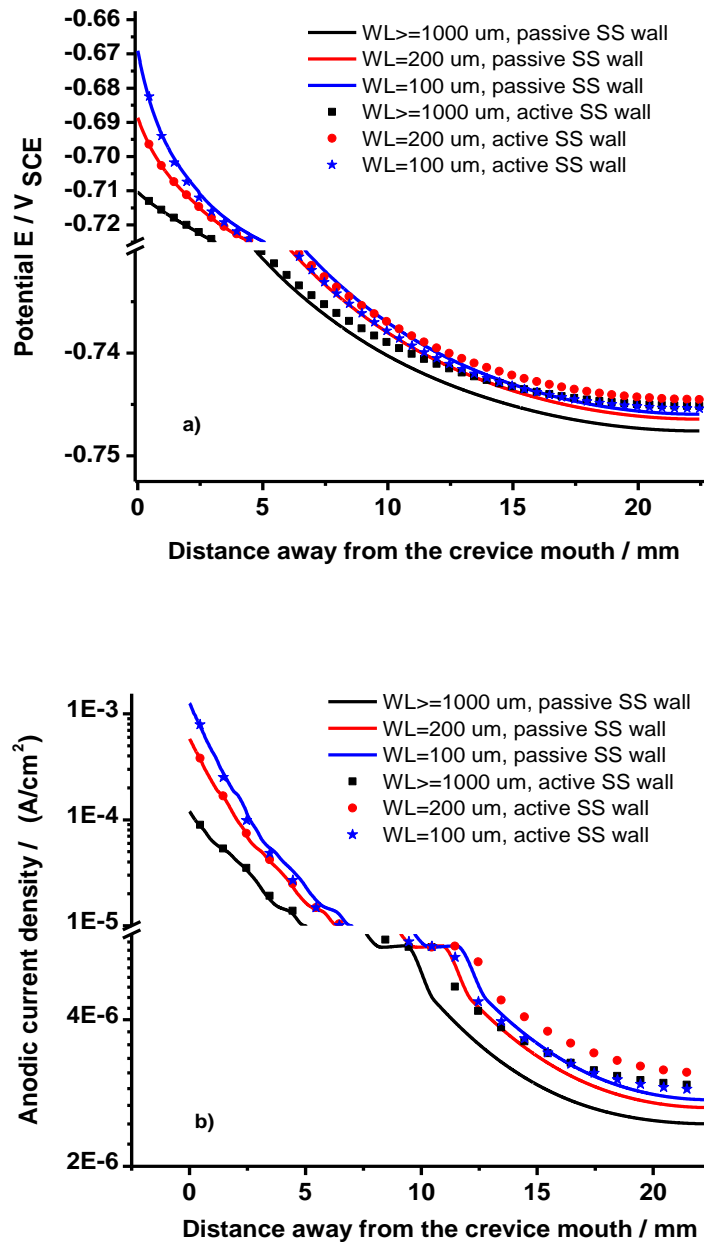


Figure 6.16: Comparison of a) potential distribution and b) anodic current density distribution along the AA7050 in the crevice as a function of WL between Case 1: passive SS wall and Case 2: active SS wall.

6.4.3.4 Validation of Scaling Law

To validate if scaling law exists for galvanic-coupling induced crevice and determine whether L/G or L^2/G is the more suitable scaling law for this type of crevice, a series of simulations

were performed to find out the value of critical crevice length (L_{crit}) below which the entire crevice was active at a certain crevice gap G in a given WL and internal SS wall condition. It should be noted that L_{crit} in this study is different from the typical L_{crit} described by Pickering *et al.*^{8,9} and Lee *et al.*¹¹: in their study, either Ni or SS experiences passive-to-active transition as potential moves to negative direction due to ohmic drop, whereas AA7050 experiences reverse transition as potential drops down. That said, L_{crit} in their study represents a critical value beyond which crevice begins to corrode, whereas that in our study represent a critical value beyond which active crevice begin to passivate. An example of comparisons of simulated results and linear fit between two types of scaling law is demonstrated in Figure 6.17, in which WL was equal to 1,000 μm and internal SS wall was passive. It shows that linear fit for L_{crit}^2/G has $R^2=0.9947$, which is larger than $R^2=0.9323$ for L_{crit}/G . Noting that R^2 is a statistical measure of how close the data to the fitted regression line, larger R^2 indicates that the model explains the variability of the response data around its mean better. A full list of comparison between L_{crit}^2/G and L_{crit}/G in terms of R^2 values in different WL and internal SS wall conditions is shown in Table 6.3. By this comparison, it has been found that L_{crit}^2/G is more applicable to galvanic-coupling induced crevice than L_{crit}/G

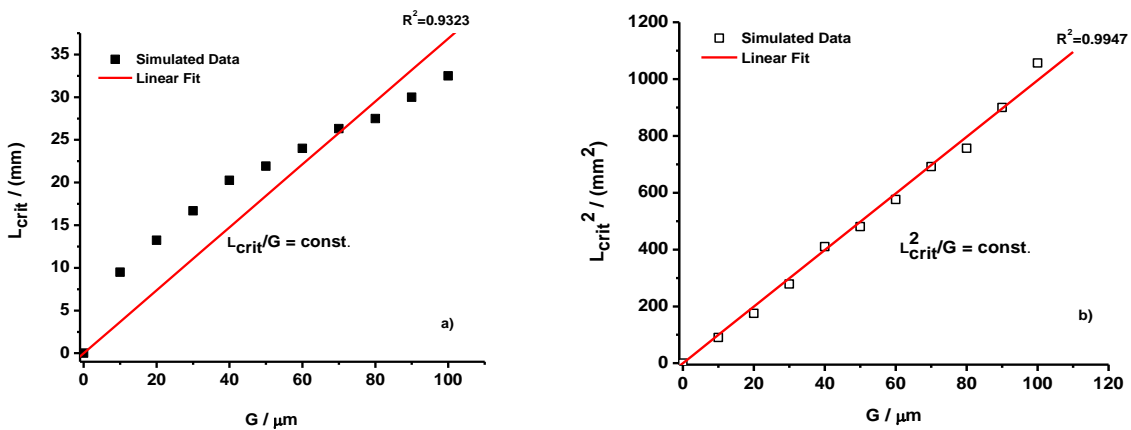


Figure 6.17: Comparison of simulated data and linear fit as a function of G plotted on a) linear scale L_{crit} and b) quadratic scale L_{crit}^2 .

Table 6.3: A list of comparisons between L_{crit}^2/G and L_{crit}/G in terms of R^2 values in different WL and internal SS wall conditions.

	Passive Wall			Active Wall		
	WL:1000 μm	WL:200 μm	WL:100 μm	WL:1000 μm	WL:200 μm	WL:100 μm
L_{crit}/G	0.9323	0.9303	0.9291	0.9283	0.9268	0.9296
L_{crit}^2/G	0.9947	0.9986	0.9991	0.9988	0.9994	0.9990

Comparisons of L_{crit}^2/G as a function of WLs for two different internal SS wall conditions are shown in Figure 6.18. It shows that the slope for L_{crit}^2/G increased as WL decreased for passive SS wall condition, which indicates L_{crit} became larger for smaller WL as crevice gap G went up. Whereas for active SS wall condition, this behavior was only valid when $WL \geq 200 \mu\text{m}$; once $WL = 100 \mu\text{m}$, L_{crit} was even smaller than the scenario when WL was equal or greater than $1000 \mu\text{m}$. By comparing L_{crit} between two internal SS wall conditions at the same WL, active wall scenario always had larger L_{crit} than passive wall one as discussed earlier, except $WL = 100 \mu\text{m}$ at which slope had no change. These abnormal behaviors at $WL = 100 \mu\text{m}$ can be explained in Figure 6.19 which is a deconstruction of Figure 6.16a: when the internal SS wall was passive (Figure 6.19a), there was no galvanic coupling between AA7050 and internal SS cathode, although degree of potential drop was higher for $WL = 100 \mu\text{m}$ than $WL \geq 200 \mu\text{m}$, the beginning potential at the crevice mouth was more positive due to largely enhanced ORR kinetics at $WL = 100 \mu\text{m}$, such that the potential along the crevice was always higher; when the internal SS wall was active (Figure 6.19b), there was another galvanic coupling between AA7050 and internal SS cathode besides one between AA7050 and external SS cathode, the exposure area of internal SS cathode was almost equal to that of AA7050 such that internal SS cathode had the tendency to push the potential towards $E_{galv,int} \sim -0.822 \text{ V}_{SCE}$. This potential-drop factor due to internal galvanic coupling was more prominent for $WL = 100 \mu\text{m}$ at which potential distribution became more negative (lower current density) than $WL = 200 \mu\text{m}$ when distance away from the crevice mouth was around 5mm,

and than $WL \geq 1000 \mu\text{m}$ when distance away from the crevice mouth was about $\sim 15\text{mm}$, as shown in Figure 6.19b. This resulted in a smaller critical crevice length for $WL=100 \mu\text{m}$ when the internal SS wall was active.

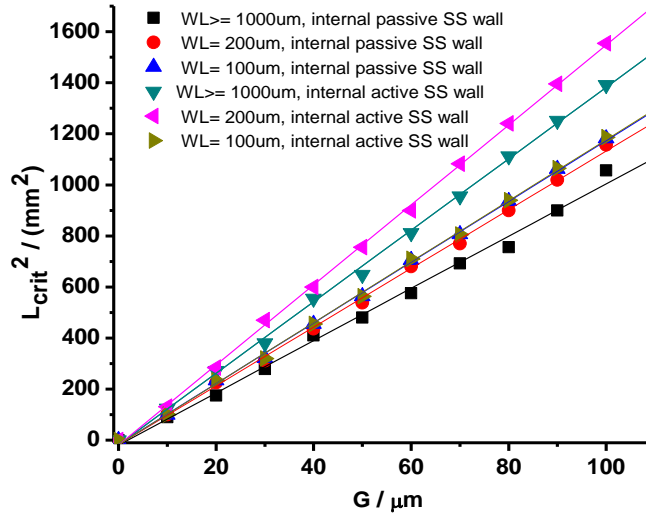


Figure 6.18: Comparisons of L_{crit}^2/G as a function of WLs for two different internal SS wall conditions.

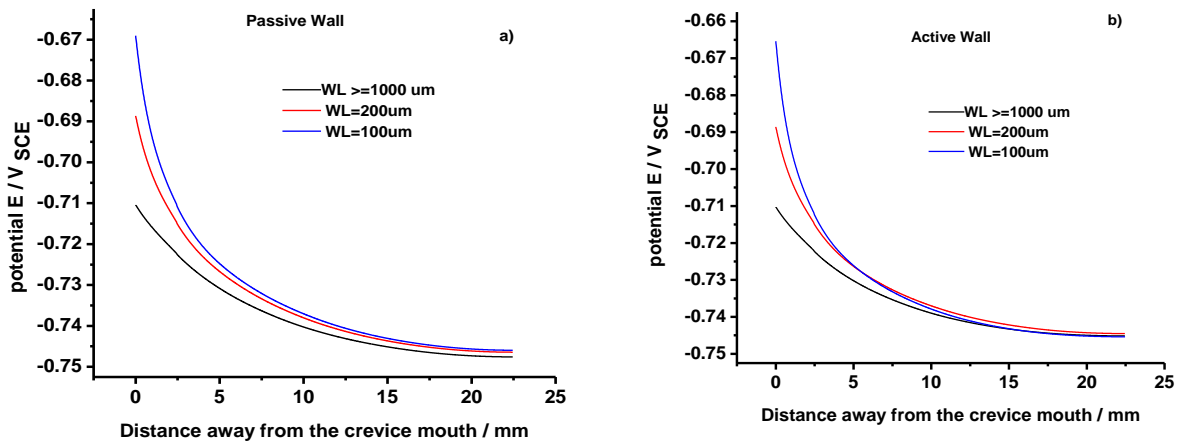


Figure 6.19: Comparison of potential distributions along AA7050 in the crevice as a function of WL when the internal SS wall is a) passive and b) negative. This figure has the same geometry configuration as **Figure 6.16**.

6.4.3.5 Effect of Al^{3+} in Crevice Solution

Due to same E_{crit} value and anodic kinetics beyond E_{crit} , Case 3 (passive crevice wall) won't be discussed here since simulation results in terms of scaling law in Case 3 were identical to Case 1. However simulation for Case 4 (active crevice wall) showed that the potential at crevice tip was pinned at $\sim -0.696 V_{SCE}$ regardless of change in WL, G or T_{plate} . An extreme example for Case 4 is shown in Figure 6.20. In this example, T_{plate} was set to be 150mm with $G=10 \mu m$ which were aimed to create large ohmic drop in the crevice solution. Surprisingly, the potential for both WL=100 and 1000 μm dropped quickly around the crevice mouth and then maintained along the rest of the crevice at $\sim -0.696 V_{SCE}$ which was equal to $E_{galv,int}$ in Figure 6.14c. Since cathodic current density at $E_{galv,int}$ was much higher than $E_{galv,ext}$ even at WL=100 μm , when the internal SS cathode was active, the crevice corrosion of AA7050 was dominantly supported by internal SS cathode such that the potential along the majority of crevice was equal to $E_{galv,int}$. As a result, the entire AA7050 in the crevice was corrosion-active all the time when Al^{3+} was in solution with an internal active SS wall. This also implies that scaling law is not valid in Case 4. Modeling study for scaling law also overturned our hypothesis in which scaling law is constant regardless of changes in external variables.

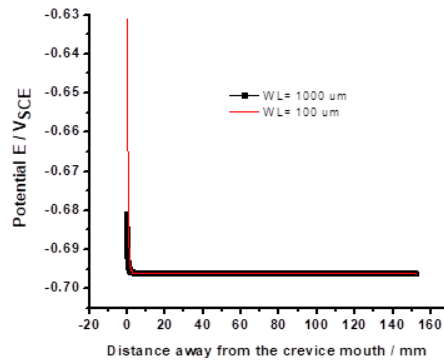


Figure 6.20: Comparison of potential distributions along AA7050 between WL=1000 and 100 μm when $T_{plate}=150$ mm and $G=10 \mu m$ in Case 4.

6.4.4 Conclusions

This study investigated the scaling law for a galvanic-coupling induced crevice between SS316L and AA7050-T7451. The effect of electrolyte layer thickness on the external SS cathode, crevice solution chemistry and wall condition of internal SS cathode were considered in the study. It is concluded that:

- Smaller WL for the thin electrolyte layer above the external SS cathode as well as tighter crevice gap results in higher anodic current density (more corrosion damage) at the near-crevice mouth region.
- Scaling law is valid for Case 1, 2 and 3, but not for 4. It is also found that L_{crit}^2/G is more applicable to galvanic-coupling induced crevice than L_{crit}/G , but L_{crit}^2/G varies with WL and internal SS wall condition. Active SS wall condition and smaller WL generally lead to a higher L_{crit}^2/G as long as $WL \geq 200 \mu\text{m}$.

6.5 Acknowledgements

The financial support from Office of Naval Research (ONR) via Grants N00014-14-1-0012 and N00014-17-1-2033, Sea-Based Aviation Program, William Nickerson, Program Manager is gratefully acknowledged.

6.6 References

1. F. Mansfeld, *Corrosion* 27 (1971): pp. 436–442.
2. F. Mansfeld, and J.V. Kenkel, *Corrosion Science* 15 (1975): pp. 239–250.
3. C.-M. Liao, and R.P. Wei, *Electrochimica Acta* 45 (1999): pp. 881–888.
4. J.X. Jia, G. Song, and A. Atrens, *Corrosion Science* 48 (2006): pp. 2133–2153.
5. G. Song, *Advanced Engineering Materials* 7 (n.d.): pp. 563–586.

6. D.Y.Jung, I. Dumler, and M. Metzger, *J. Electrochem. Soc.* 132 (1985): pp. 2308–2312.
7. N. Murer, N.A. Missert, and R.G. Buchheit, *J. Electrochem. Soc.* 159 (2012): pp. C265–C276.
8. Y. Xu, M. Wang, and H.W. Pickering, *J. Electrochem. Soc.* 140 (1993): pp. 3448–3457.
9. M. Wang, H.W. Pickering, and Y. Xu, *J. Electrochem. Soc.* 142 (1995): pp. 2986–2995.
10. M. Watson, and J. Postlethwaite, *Corrosion* 46 (1990): pp. 522–530.
11. L. DeJong, University of Virginia, Charlottesville, M.S. Thesis (1999)
12. J.S. Lee, M.L. Reed, and R.G. Kelly, *J. Electrochem. Soc.* 151 (2004): pp. B423–B433.
13. M. Vankeerberghen, *CORROSION* 60 (2004): pp. 707–717.
14. Y. Xu, and H.W. Pickering, *J. Electrochem. Soc.* 140 (1993): pp. 658–668.
15. A. Alavi, and R.A. Cottis, *Corrosion Science* 27 (1987): pp. 443–451.

7 Summary and Recommended Future work

7.1 Summary

This dissertation utilized a combined modeling and experimental approach to develop a fundamental understanding of the effect of environmental, material and geometric variables on the electrochemical (potential, current density) and corrosion distributions in the galvanic coupling between AA7050-T7451 and stainless steel with a simulated fastener-hole configuration, and demonstrate the capability of Laplace-Equation based FEM modeling approach to estimate and predict corrosion distribution with accurately defined electrochemical kinetics as boundary conditions.

To validate the robustness of our modeling approach, a Laplace-Equation based modeling coupled with mathematically fitted electrochemical kinetics from experiment as boundary conditions was applied to simulate galvanic corrosion between Zn plate and SS 316 rods under thin layer electrolyte condition. The effect of geometric, electrolytic parameters on the corrosion distribution had been examined. The modeling results were then compared with experimental results from a four-day modified B117 test by adding sodium persulfate to predict the thickness of thin film electrolyte during the test from modeling. Major conclusions from this chapter are: (1) for geometric parameters, galvanic corrosion between Zn plate and SS rods can be intensified by increased number of cathode rod (SS) and shorter spacing between two adjacent SS rods; (2) for electrolytic parameters, the high ohmic resistance due to thin WL and low solution conductivities can decrease the cathode current delivery power from the SS cathode; (3) for a combined effect of both geometric and electrolytic parameters, the lowest electrolytic ohmic resistance from shortest spacing resulted in more interaction between two SS rods and the Zn portion in between, and the galvanic corrosion became more significant as WL went below $800\ \mu\text{m}$, due to the enhanced mass

transfer limited cathodic kinetics from SS cathode to provide more cathode current to maintain the corrosion of Zn; (4) $WL=3,500\sim 4,000\ \mu\text{m}$ would be the appropriate WL range formed on the sample surface during modified B117 salt fog testing; (5) the robustness of Laplace-Equation based modeling is highly dependent on the boundary conditions, experimentally determined electrochemical kinetics as boundary conditions are the most appropriate choice since they can truly reflect the electrochemical response of anode/cathode to the surrounding solution environment.

In the study of the effect of electrolyte layer thickness, the total cathodic current capacity of a surface on the electrolyte film thickness and cathode size in a galvanic couple to support the corrosion of AA7050 were accessed. It spans the range of WL thickness from full immersion conditions (where the total cathode current scales with cathode size) to the thin film regime in which the WL is the diffusion boundary layer thickness. In order to fully assess the transition from thin film to thick film condition, an understanding of the natural convection layer thickness is required. The natural convection layer defines the upper limit for true thin film behavior for atmospheric corrosion, and it can be experimentally determined by combining RDE experiments with data from quiescent conditions. For the conditions studied here, the natural convection boundary layer was found to be close to $800\ \mu\text{m}$. Electrolyte layer domains were delineated by three limits which described, in order of decreasing film thickness: (1) transition in exposure condition from full immersion to thick film, (2) the hydrodynamic boundary layer due to natural convection which defined the upper limit of the thin film regime, and (3) the relative dominance of ohmic resistance over mass transport in determining the total current output. This study also showed that for sufficiently thin films, this total current was independent of the size of the cathode and the nature of kinetics at the electrochemical interface, being solely driven by the ohmic resistance in solution.

In the study of the solution chemistry effect, the effect of solution pH, conductivity, pertinent cation species (Al^{3+} , Zn^{2+} and Mg^{2+}) on the electrochemical and galvanic corrosion distributions between SS316L and AA7050 was well studied. For the aspect of solution pH and conductivity, a FEM based modeling approach with experimentally determined electrochemical kinetics as boundary conditions was used to simulate potential and current density distributions in the galvanic coupling with a simulated fastener-hole configuration based on different pH and conductivity assumptions in the solution. It shows that the acidic crevice solution at the mouth leads to more severe corrosion at the occluded site of the crevice than mild alkaline crevice solution. It has been indicated that linear conductivity assumption is good enough to represent the effect of varying conductivity on electrochemical distributions and reflect corrosion behavior along the anode if one focus on the study of anode only, implying that conductivity might be a secondary factor affecting electrochemical distributions in the galvanic coupling; but the estimation of conductivity function should be within a reasonable range (1~17 S/m in this study). As for the aspect of pertinent metallic cation, Zn^{2+} and Mg^{2+} show inhibitive effect due to formation of precipitate on Cu-containing IMCs embedded in the AA7050 surface thus impeding ORR activity; whereas Al^{3+} shows promotive effect on HER cathodic kinetics due to enhanced proton diffusivity, this effect is not only observed on Al alloys, but also on Pt and stainless steel. The cation study for the galvanic couple indicates that: addition of Al^{3+} or Mg^{2+} into NaCl solution significantly affects galvanic corrosion between AA7050/SS316L. Al^{3+} is corrosion accelerator, and Mg^{2+} is corrosion inhibitor.

The effect of oxide film properties (thickness, composition, resistivity and etc.) on the cathodic kinetics of stainless steel were investigated. It can be concluded that: (1) when the passive oxide film is thin (~2nm), the effect of electrolyte layer thickness overwhelms that of oxide film

thickness in terms of ORR cathodic kinetics as long as electrolyte layer thickness is larger than 36 μm ; below this critical electrolyte layer thickness, the effect of oxide film becomes comparable to that of electrolyte layer thickness and has lower cathodic limiting current density compared to the scenario in which only electrolyte layer thickness matters; (2) at the same electrolyte layer thickness ($<36 \mu\text{m}$), magnitude of cathodic limiting current density after three different surface treatment follows this order: cathodically-pre-reduction > immersion at OCP for 1.5hrs > chemical treatment by HNO_3 ; (3) the effect of oxide film properties at ascending pre-oxidation potential on the cathodic kinetics during ORR potential range of SS304L and SS316L was investigated: for both steels, as oxidation potential increases, the amount of Cr^{3+} in oxide film initially increases from corrosion potential to $0\sim 0.4 V_{\text{SCE}}$, and then decreases over increasing potential and is oxidized to Cr^{6+} once the potential is higher than $0.63V_{\text{SCE}}$; the amount of Fe^{3+} in general increases with ascending potential; the oxide film thickness also increases with increasing potential; at transpassive potential, although film has the largest thickness but its resistivity is lowest. A higher Fe^{3+} content in the oxide film during oxidation stage will result in a larger cathodic current density due to larger Fe^{3+} -to- Fe^{2+} reduction current density during the scan in the negative potential direction, and provide more Fe^{2+} sites for larger ORR cathodic kinetics during the scan in the reverse direction, since active Fe^{2+} site is believed to facilitate ORR. After transpassive pre-potential, SS316L has even larger cathodic current density than Pt SS304L at the same condition during the scan in the negative potential direction due to more availability

of Mo^{6+} species and highest Fe^{3+} content in the oxide film, as well as lowest film resistivity and total corrosion resistance.

At last, in the study of geometric parameter effects, the area ratio of cathode to anode, and crevice geometry were investigated. In the study of area ratio, a galvanic crevice former between AA7050 and SS316L was utilized to evaluate the dependence of pH and dissolution current density of AA7050 on the cathode-to-anode ratio. It can be concluded from this study that: higher area ratio geometry leads to more severe corrosion focused at the crevice mouth, resulting in larger potential and pH variation from crevice center to mouth as well as higher anodic current density. In the study of the scaling law for a galvanic-coupling induced crevice between SS316L and AA7050-T7451, the effect of electrolyte layer over the external SS cathode surface, crevice solution chemistry and wall condition of internal SS cathode were considered in the study. It is concluded that: scaling law is valid for the crevice with passive internal SS wall, as well as one with active internal SS wall but with no Al^{3+} presented in the crevice solution. It is also found that L_{crit}^2/G is more applicable to galvanic-coupling induced crevice than L_{crit}/G , but L_{crit}^2/G varies with WL and internal SS wall condition. Active SS wall condition and smaller WL generally lead to a higher L_{crit}^2/G as long as $\text{WL} \geq 200 \mu\text{m}$.

7.2 Recommended Future Work

- The boundary conditions in our Laplace-Equation based modeling approach will be modified in a way such that they can be adapted in response to change in solution chemistry, electrode properties over time; we will also relax the modeling constraints in Laplacian framework into full Nernst-Planck -Equation based one, and then compare the results between these two different approaches.
- For the corrosion simulation in thin film electrolyte condition, we will extend the current framework in which electrolyte layer thickness remains static, to a more realistic scenario in which the film thickness becomes a

- dynamic representative of wet and dry cycling. Furthermore, to validate the electrochemical distributions in thin film electrolyte condition, multielectrode array (MEA) and scanning Kelvin probe (SKP) will be utilized to determine current and potential distributions in the galvanic corrosion system.
- Further experimental exploration of interaction between metal-rich primer (MgRP, ZnRP, and AlRP) coated AA7050 and SS316L will be continued, focusing on the determination of corrosion solution composition in a thin film electrolyte condition after a certain period of exposure time by inductive coupled plasma-optical emission spectroscopy (ICP-OES), and then a new modeling setup with the consideration of metal-rich primer in the realistic corrosion solution determined by ICP-OES will be developed.
- A point defect model will be developed in order to delineate oxygen diffusion within the oxide film and oxygen reduction reaction at the oxide/metal interface on stainless steel during cathodic polarization within the ORR potential range.
- Microfabrication technique will be utilized to experimentally generate crevice formed by AA7050 and SS316L and then experimentally validate the scaling law and compare with modeling results.